UNIVERSITY OF SOUTHAMPTON

FACULTY OF NATURAL AND ENVIRONMENTAL SCIENCES

School of Chemistry

Sensitivity Enhancement and Field-Dependent Relaxation in Singlet Nuclear Magnetic Resonance

by

Ing. Jiří Bočan

Thesis for the degree of Doctor of Philosophy

May 2013

UNIVERSITY OF SOUTHAMPTON

ABSTRACT

FACULTY OF NATURAL AND ENVIRONMENTAL SCIENCES
Chemistry

Doctor of Philosophy

SENSITIVITY ENHANCEMENT AND FIELD-DEPENDENT RELAXATION IN SINGLET NUCLEAR MAGNETIC RESONANCE

by Jiří Bočan

Nitrous oxide (N_2O), also known as “laughing” gas, is a well known compound used in medicine as a mild anaesthetic, or in engineering as a powerful oxidizer providing high output of engines. Recently, its ^{15}N doubly-labelled isotopologue attracted attention in singlet NMR due to its long singlet relaxation time ranging between 7 minutes, when dissolved in blood, up to 26 minutes in degassed dimethyl sulfoxide (DMSO).

Singlet NMR deals with nuclear singlet states, which are exchange antisymmetric quantum states of coupled pairs of spin-1/2 nuclei with zero total nuclear spin quantum number. These states are nonmagnetic and immune to exchange-symmetric relaxation processes such as intramolecular direct dipolar relaxation. Their lifetimes may be up to an order of magnitude longer than conventional relaxation times T_1 and T_2. Besides various fields of NMR, singlet states find potential application also in MRI. The direct medical application of $^{15}N_2O$ as a MRI tracer is, however, complicated by a poor detection sensitivity resulting from the low ^{15}N magnetogyric ratio, low solubility in liquids at room temperature and atmospheric pressure, and limitations of ^{15}N signal enhancement by means of physical methods for dissolved $^{15}N_2O$.

This thesis addresses two topics related to singlet NMR of $^{15}N_2O$ – sensitivity enhancement and magnetic-field dependent relaxation. The NMR signal decay in liquid phase is often dominated by static magnetic field inhomogeneity, described by the time constant T_2', which is much faster than the transverse relaxation, characterized by T_2. Repeated refocusing by a multiple spin-echo (MSE) train maintains the ^{15}N signal for extended times of several T_2. Acquisition of the signal during the whole MSE sequence followed by a proper processing either by matched weighting or singular value decomposition, may lead to the signal-to-noise ratio (SNR) enhancement by up to an order of magnitude under favourable circumstances. The SNR enhancement is a function of T_2, T_2', and the spectral resolution.

The procedure of the SNR enhancement in combination with methods of singlet NMR was used to investigate in detail low-field $^{15}N_2O$ singlet relaxation. The $^{15}N_2O$ relaxation measurements were extended to field strengths up to the spectrometer high field. The observed relaxation dependencies were described by a general theory, which represents relaxation as a time-dependent exchange of populations of the field-dependent energy eigenstates. In particular, spin-rotation relaxation in low field was discussed.

“You will recognize your own path

when you come upon it,

because you will suddenly have

all the energy and imagination

you will ever need.”

— Jerry Gillies

Contents

List of Figures

List of Tables

Declaration of Authorship

I, Jiří Bočan, declare that this thesis:

Sensitivity Enhancement and Field-Dependent Relaxation in
Singlet Nuclear Magnetic Resonance

and the work presented in the thesis are both my own, and have been generated by me as the result of my own original research.

I confirm that:

- this work was done wholly or mainly while in candidature for a research degree at this University;
- where any part of this thesis has previously been submitted for a degree or any other qualification at this University or any other institution, this has been clearly stated;
- where I have consulted the published work of others, this is always clearly attributed;
- where I have quoted from the work of others, the source is always given. With the exception of such quotations, this thesis is entirely my own work;
- I have acknowledged all main sources of help;
- where the thesis is based on work done by myself jointly with others, I have made clear exactly what was done by others and what I have contributed myself;
- parts of this work have been published as:

  J. Bocan, G. Pileio, and M. H Levitt. Sensitivity enhancement and low-field spin relaxation in singlet NMR. *Phys. Chem. Chem. Phys.*, 14(46):16032-16040, 2012.

Signed: ....   Date: ....

Acknowledgements

At the first place, I would like to express my deep gratitude and thanks to Professor Malcolm Levitt. He was truly the best supervisor I have ever had. For inviting me to the Great Britain, for his immense knowledge and understanding of NMR, for his support, patient guidance and encouragement, for his inspiring suggestions and useful critique. But also for his human values, for learning me to separate, what really matters in the life from the rest, and for allowing me to let go of what no longer serves me. Still, there are many other lessons I will, hopefully, understand and appreciate one day.

I owe my very special thanks and gratitude to Ing. Miloslav Vobecký for his longtime and unremitting friendship, encouragement, support, and trust, whenever I wanted to give up. He always knew how to ignite the fire within me for the rest of the “journey”.

Wholehearted thanks belong to Marina Carravetta for being more than just my advisor. I wish I could cooperate more with her. And also to Professor Richard Brown for learning me to answer “I am very well!”, while smiling, whenever someone asks me, how I am. And really feel this way afterwards.

I wish to thank Giuseppe Pileio, for his initial help in the laboratory, for providing the $^{15}N_2O$ sample, and together with Maria Concistrè and Salvatore Mamone for spicing up my life with an authentic essence of Calabria. Personal thanks belong to Michael Tayler (Radboud University Nijmegen, The Netherlands) and Irene Marco-Rius (University of Cambridge) for their ceaseless curiosity, for spending time together, and also for reminding me important lessons from the past.

Many thanks belong also to other, former and current, members of Malcolm’s group, namely Andrea Sauerwein, Elisa Carignani, Rangeet Bhattacharyya, Riddhiman Sarkar, Ole Johannessen, Pär Hakensson, Gabriele Stevanato, Soumya Roy, Benno Meier, Samuel Mitchell, and Graeme Finch. Outside the group, to Ilya Kuprov and members of his own group, namely to Zenawi Welderufael, Dmitry Savostyanov, Gary Wall, and Andreas Biternas, for their fresh and unorthodox computational approach to NMR. Finally also to

Mark Denning and Ibraheem Haies from Marina's group.

Thought impossible to express in words, I owe my deepest gratitude and thankfulness to my parents, Jiří and Marie for being the best, most supportive, encouraging, patient, and loving teachers and guides throughout my whole life. Without them, my current life would not be this wonderful and adventurous experience.

✿ Thank you! ✿

Chapter 1

Introduction

This thesis encloses a 35-month project in the NMR group of Professor Malcolm Levitt at the University of Southampton.

In the light of the newest developments in singlet NMR, till 2012, it was believed that one of the most promising candidates for singlet MRI is $^{15}N_2O$ dissolved in blood. However, several obstacles related to the sensitivity of the method prevented direct application. First, $^{15}N_2O$ is a gas with a limited solubility, though blood has slightly better properties compared to other ordinary solvents. Secondly, a very low $^{15}N_2O$ concentration is expected after redistribution of the enriched sample in the blood stream. Thirdly, the ^{15}N magnetogyric ratio is approximately ten times lower than that of hydrogen ^{1}H, which results in a proportionally weaker signal. The search for a means of sensitivity enhancement is, and especially in NMR always was, particularly pressing.

An easy and readily available way to enhance the sensitivity of NMR, translated into the signal-to-noise ratio (SNR) in frequency spectra, is provided by solution NMR itself. In such a case, the NMR signal may ideally live for a long time, which is comparable to the longitudinal relaxation time constant T_1. Possible magnetic field inhomogeneity effects, which speed up the signal decay, may be overcome by using multiple refocussing by means of the spin-echo pulse sequence, the so-called multiple spin-echo (MSE) sequence. The MSE signal, acquired during a prolonged scan, may be processed afterwards in a way that allows the SNR enhancement compared to an ordinary free-induction decay signal. Therefore, a combination of $^{15}N_2O$ singlet NMR together with the MSE pulse sequence may provide the desired enhancement in sensitivity.

An additional piece of information, which $^{15}N_2O$ as an alternative MRI tracer might provide, and which is extracted from the human body in a completely noninvasive way through observing NMR signals, is hidden in the relaxation of $^{15}N_2O$. Once the MSE method was developed, its application to singlet relaxation in the case of weak ^{15}N signals was obvious.

1.1 Thesis Outline

The whole text is divided into eight chapters. Chapter 1 provides the main ideas and the motivation behind this project, and overviews the thesis.

Chapter 2 introduces a geometrical vector model of magnetization, which is shown to be an useful tool for visualization of basic and even more complicated NMR experiments. Relationships presented in this chapter will be exploited later in Chapter 6, in order to evaluate the effects of various pulse imperfections during the MSE experiment. The rigorous quantum mechanical formalism, and singlet and triplet states, are introduced afterwards.

Chapter 3 provides the reader with an overview of singlet NMR. Inclusion of the singlet state into ordinary NMR experiments brings several advantages. This branch of NMR has widened significantly since 2004, when the singlet state was prepared purely by means of NMR for the first time. The basic techniques of singlet NMR, as well as examples of singlet state applications, are summarized.

Chapter 4 is dedicated to Fourier transformation, the essence of modern magnetic resonance spectroscopy (MRS). Since the whole procedure of MSE signal processing was programmed by hand, without using any commercially available software package, basic methods of the NMR signal processing will be presented. Special care is given to signal and noise in NMR, and to derivation of a matched filter in general. Other important subjects included are the methods of the SNR enhancement, particularly singular value decomposition (SVD). SVD will be used as one of the means for MSE signal processing.

Chapter 5 starts with a brief introduction to nitrogen NMR, and presents ^{15}N samples used for the experimental work. A summary of their properties, mainly various relaxation time constants, is provided.

Chapter 6 is devoted to the MSE pulse sequence. A short overview of the spin-echo sequence, a fundamental building block of pulse sequences in modern NMR, is followed by detailed treatment of the preferred CPMG spin-echo sequence. Taken into account are basic interference effects, which may occur during the prolonged pulse trains. The matched filter corresponding to the MSE signal will be derived. Due to knowledge of the specifications of the matched filter, a realistic theoretical model, predicting the SNR enhancement, will be presented. The description of experimental procedures for processing the MSE signal will follow. Finally, experimental evidence of the SNR enhancement after MSE signal processing will be provided, and the achieved results will be compared to the theoretical predictions.

Chapter 7 discusses the formal theory of relaxation with emphasis on the singlet state. The field-cycling experiments will be described, which were used for study of the field-dependent relaxation of $^{15}N_2O$ dissolved in liquid phase in the full range of magnetic fields, which are reachable in the laboratory. The observations are explained by using a phenomenological field-dependent relaxation model, which will be presented in full detail. Finally, experimental results will be compared to the model-based predictions and also with the dedicated literature.

Concluding Chapter 8 will bring the thesis to an end. It will summarize the achieved findings and will foreshadow possible prospects for application of the presented methods.

Chapter 2

Basics of Nuclear Magnetic Resonance

2.1 Classical Description

2.1.1 Nuclear Magnetism

Nuclear magnetism is a consequence of the existence of a nuclear spin angular momentum $\boldsymbol{I}$. This vector quantity, first observed in the electron [1], is purely quantum mechanical, without a classical counterpart. Amongst the mass and the electric charge, the spin is a fundamental property of all subatomic particles, including the proton or the neutron, as well as objects built from them. The magnitude of $\boldsymbol{I}$ is given by [2]:

$$|\boldsymbol{I}| = \sqrt{I(I+1)}\,\hbar \tag{2.1}$$

where $\hbar = h/2\pi$ is the reduced Planck constant [3]. A nuclear spin quantum number I may be either integer or half-integer, ranging from 0 up to 10 [4]. For solution NMR, the most important nuclei are those with $I = 1/2$ (spin-1/2 nuclei), mainly the stable isotopes ^{1}H, ^{13}C or ^{15}N. Nuclei with spin zero are undetectable by means of NMR. Nuclei with spin $I > 1/2$ are called quadrupolar nuclei. Their nonspherical electric charge distribution gives rise to an electric quadrupole moment, which causes very rapid relaxation and makes their observation difficult.

In the presence of a significant direction, $\boldsymbol{I}$ is quantized. In NMR, such a direction is determined by a strong static magnetic field $\boldsymbol{B}_0$. $\boldsymbol{B}_0 = B_0\,\boldsymbol{e}_z$ is conventionally aligned along the z-axis of a right-handed Cartesian coordinate system, represented by an orthogonal set of unit vectors $(\boldsymbol{e}_x, \boldsymbol{e}_y, \boldsymbol{e}_z)$. Quantum mechanics restricts that only one of the $\boldsymbol{I}$ components may be determined at a time, while the other two remain indeterminate. By convention, values of the z-component of $\boldsymbol{I}$ are given by [2]:

$$I_z = m\hbar \tag{2.2}$$

where m is a magnetic quantum number, having $(2I+1)$ discrete values between $-I$ and $+I$.

Spin interactions with magnetic fields are described by means of a nuclear magnetic moment $\boldsymbol{\mu}$, related to $\boldsymbol{I}$ through [2]:

$$\boldsymbol{\mu} = \gamma \boldsymbol{I} \tag{2.3}$$

where γ is a magnetogyric ratio, a constant characteristic for each nucleus with nonzero spin. It may be either positive or negative. Consequently, the vector $\boldsymbol{\mu}$ is either parallel or antiparallel to $\boldsymbol{I}$. The γ ratio also determines the size of the Larmor frequency:

$$\omega_0 = -\gamma B_0 \tag{2.4}$$

and the sense of precession of $\boldsymbol{I}$ and the derived magnetic moments in the given field $\boldsymbol{B}_0$.

The interaction energy E of the moment $\boldsymbol{\mu}$ placed in the field $\boldsymbol{B}$ is equal to:

$$E = -\boldsymbol{\mu} \cdot \boldsymbol{B} = -\gamma \boldsymbol{I} \cdot \boldsymbol{B} = -\gamma |\boldsymbol{I}||\boldsymbol{B}| \cos\alpha \tag{2.5}$$

where the dot product is defined by Eq. (A.3), and α is the angle between the two vectors. Assuming that $\boldsymbol{B} = \boldsymbol{B}_0$ and $|\boldsymbol{I}|\cos\alpha = I_z$, and using Eq. (2.2), there exist $(2I+1)$ equally spaced energy levels:

$$E_m = -\gamma I_z B_0 = -\gamma m \hbar B_0 \tag{2.6}$$

called the Zeeman levels in analogy with the Zeeman effect in optical spectroscopy [5, 6]. The thermal-equilibrium population of each level is governed by the Boltzmann distribution. Assuming a total number N of observed nuclei, the relative population of the mth level is given by [2]:

$$\frac{N_m}{N} = \frac{\exp(-E_m/k_\mathrm{B}T)}{\sum\limits_{m=-I}^{I} \exp(-E_m/k_\mathrm{B}T)} = \frac{\exp(\gamma m \hbar B_0/k_\mathrm{B}T)}{\sum\limits_{m=-I}^{I} \exp(\gamma m \hbar B_0/k_\mathrm{B}T)} \approx \frac{1}{2I+1}\left(1 + \frac{\gamma m \hbar B_0}{k_\mathrm{B}T}\right) \tag{2.7}$$

k_B is the Boltzmann constant [3], and T is the thermodynamic temperature. The final approximate expression is obtained by the Maclaurin series expansion of the exponential function around $E_m/k_\mathrm{B}T \sim 10^{-5} \ll 1$ up to the linear term.

A bulk nuclear magnetic moment (magnetization) $\boldsymbol{M}$ is obtained by the vector sum over $\boldsymbol{\mu}_i$ of all individual nuclei:

$$\boldsymbol{M} = \sum_{i=1}^{N} \boldsymbol{\mu}_i \tag{2.8}$$

By using Eqs. (2.2), (2.3) and (2.7), the equilibrium value M_0 of the z-component of $\boldsymbol{M}$ in the field $\boldsymbol{B}_0$ is given by:

$$M_0 = \gamma\hbar \sum_{m=-I}^{I} m N_m \approx \frac{N\gamma\hbar}{2I+1} \sum_{m=-I}^{I} m \left(1 + \frac{\gamma m \hbar B_0}{k_\mathrm{B} T}\right) = \frac{N\gamma^2\hbar^2 I(I+1)}{3k_\mathrm{B}T} B_0 = \chi_0 B_0 \tag{2.9}$$

χ_0 is the nuclear contribution to the magnetic susceptibility [7], experimentally first determined for the proton [8]. The susceptibility dependence on the inverse of temperature is known as the Curie law [2].

2.1.2 Bloch Equations and Vector Model

A classical description of magnetization was formulated by Bloch [9]. His vector model and associated equations are valid for an idealized sample containing isolated noninteracting spins-1/2. Despite its simplicity, many terms introduced within this approach are routinely used in NMR until today.

The behaviour of the magnetization $\boldsymbol{M}(t)$ in a magnetic field $\boldsymbol{B}(t)$ is given by the set of Bloch equations [10]:

$$\frac{\mathrm{d}\boldsymbol{M}(t)}{\mathrm{d}t} = \gamma \boldsymbol{M}(t) \times \boldsymbol{B}(t) - \mathsf{R}\left[\boldsymbol{M}(t) - \boldsymbol{M}_0\right] \tag{2.10}$$

where the cross product is defined in Eq. (A.4). A relaxation matrix, R, given by:

$$\mathsf{R} = \begin{pmatrix} 1/T_2 & 0 & 0 \\ 0 & 1/T_2 & 0 \\ 0 & 0 & 1/T_1 \end{pmatrix} \tag{2.11}$$

consists of longitudinal and transverse relaxation time constants T_1 and T_2, respectively, see Section 2.1.4.

As explained in Section 2.1.4, a strong static longitudinal field $\boldsymbol{B}_0$ is used to establish the steady equilibrium magnetization $\boldsymbol{M}_0$. In order to manipulate it, another magnetic field, a radiofrequency (rf) transverse magnetic field $\boldsymbol{B}_\mathrm{rf}(t)$ is applied along the x-axis:

$$\boldsymbol{B}_\mathrm{rf}(t) = 2B_1 \cos\left(\omega_\mathrm{rf} t + \varphi\right) \boldsymbol{e}_x \tag{2.12}$$

$2B_1$ is the rf field amplitude, ω_rf is an angular frequency of a rotating frame as explained below, and φ is an initial phase of the rf field. The linearly oscillating motion of $\boldsymbol{B}_\mathrm{rf}(t)$

may be decomposed into two counter-rotating components:

$$\boldsymbol{B}_{\mathrm{rf}}(t) = \boldsymbol{B}_{\mathrm{rf}}^{+}(t) + \boldsymbol{B}_{\mathrm{rf}}^{-}(t) \tag{2.13}$$

where:

$$\boldsymbol{B}_{\mathrm{rf}}^{\pm}(t) = B_1\left[\cos(\omega_{\mathrm{rf}}t + \varphi)\,\boldsymbol{e}_x \pm \sin(\omega_{\mathrm{rf}}t + \varphi)\,\boldsymbol{e}_y\right] \tag{2.14}$$

Only the resonant component is retained, which rotates in the same sense as $\boldsymbol{\mu}$. The non-resonant component is responsible for the Bloch-Siegert shift, which is of order $(B_1/2B_0)^2$ and may usually be neglected [2, 11].

The time dependence of $\boldsymbol{B}_{\mathrm{rf}}(t)$ makes the description of the rf field effects on the spin system complicated. Simplification is provided by transforming all relationships into the rotating frame:

$$\boldsymbol{B}(t) = \mathsf{R}_z(\omega_{\mathrm{rf}}t)\,\tilde{\boldsymbol{B}}(t) \tag{2.15}$$

$$\boldsymbol{M}(t) = \mathsf{R}_z(\omega_{\mathrm{rf}}t)\,\tilde{\boldsymbol{M}}(t) \tag{2.16}$$

The rotating frame rotates about the laboratory frame z-axis with the angular frequency ω_{rf}, which may be expressed by a rotation matrix $\mathsf{R}_z(\phi)$ defined by Eq. (B.3). A tilde is used to distinguish rotating frame quantities from those in the laboratory frame. A time independent effective magnetic field, experienced by nuclei within the rotating frame, is then:

$$\tilde{\boldsymbol{B}} = (B_1\cos\varphi, B_1\sin\varphi, \Delta B_0)^{\mathsf{T}} \tag{2.17}$$

A superscript "T" denotes the column vector, see Eq. (A.1), and ΔB_0 is a reduced (offset) field:

$$\Delta B_0 = B_0 + \omega_{\mathrm{rf}}/\gamma \equiv -\Omega/\gamma \implies \Omega = \omega_0 - \omega_{\mathrm{rf}} \tag{2.18}$$

Ω is a resonance offset in the rotating frame. The magnitude of the effective field $\tilde{\boldsymbol{B}}$ is given by:

$$\tilde{B} = \sqrt{(B_1)^2 + (\Delta B_0)^2} \tag{2.19}$$

The angle θ between the z-axis and the vector $\tilde{\boldsymbol{B}}$ is defined by the following equivalent expressions:

$$\sin\theta = \frac{B_1}{\tilde{B}} = \frac{\omega_1}{\omega_{\mathrm{nut}}} \iff \cos\theta = \frac{\Delta B_0}{\tilde{B}} = \frac{\Omega}{\omega_{\mathrm{nut}}} \iff \tan\theta = \frac{B_1}{\Delta B_0} = \frac{\omega_1}{\Omega} \tag{2.20}$$

where ω_1 is the rf field strength:

$$\omega_1 = -\gamma B_1 \tag{2.21}$$

and ω_{nut} is, by convention, a positive nutation frequency [12]:

$$\omega_{\text{nut}} = |\gamma \tilde{B}| \tag{2.22}$$

with which the magnetization $\boldsymbol{M}$ rotates around the field $\tilde{\boldsymbol{B}}$.

By using Eqs. (2.15) and (2.16), and assuming $\boldsymbol{M}_0 = \tilde{\boldsymbol{M}}_0$, the Bloch equations (2.10) transform into the rotating frame accordingly:

$$\frac{\mathrm{d}\tilde{\boldsymbol{M}}(t)}{\mathrm{d}t} = \gamma \tilde{\boldsymbol{M}}(t) \times \tilde{\boldsymbol{B}} - \mathbf{R}\left[\tilde{\boldsymbol{M}}(t) - \boldsymbol{M}_0\right] \tag{2.23}$$

If not specified otherwise, the rotating frame will be used by default and the tilde will be left out from now on.

2.1.3 Radiofrequency Pulses

The detection of a NMR signal is based on Faraday's law of electromagnetic induction [13]. A NMR sample is surrounded by a wire coil. The time varying bulk magnetization induces an electromotive force, and consequently an electric current in the coil and an attached circuitry.

The only nonzero mean component at equilibrium is $\boldsymbol{M}_0$, which does not vary with time. Application of an rf pulse, i.e., the additional field $\boldsymbol{B}_{\text{rf}}(t)$ with the frequency ω_{rf} close to the Larmor frequency ω_0, and the phase φ for a time interval τ_{p}, disturbs the equilibrium magnetization. In result, $\boldsymbol{M}_0$ rotates by the flip angle:

$$\beta = \omega_{\text{nut}} \tau_{\text{p}} \tag{2.24}$$

around the direction of $\tilde{\boldsymbol{B}}$ at the frequency ω_{nut}. The β_φ pulse transforms $\boldsymbol{M}_0$ as follows [2]:

$$\boldsymbol{M}(t) = \mathbf{R}(\beta, \varphi, \theta)\, \boldsymbol{M}_0 \tag{2.25}$$

where the composite rotation is given by [2]:

$$\mathbf{R}(\beta, \varphi, \theta) \equiv \mathbf{R}_z(\varphi)\, \mathbf{R}_y(\theta)\, \mathbf{R}_z(\beta)\, \mathbf{R}_y(-\theta)\, \mathbf{R}_z(-\varphi) \tag{2.26}$$

Its explicit form is provided in Eq. (B.6). The similarity transformation $\mathbf{R}_y(\theta)\, \mathbf{R}_z(\beta)\, \mathbf{R}_y(-\theta)$ represents nutation around the direction of $\tilde{\boldsymbol{B}}$ by the angle β, and $\mathbf{R}_z(\varphi) ... \mathbf{R}_z(-\varphi)$ represents the rotation of the rf field $\boldsymbol{B}_{\text{rf}}$, originally aligned along the x-axis, by the angle φ in the transverse plane. The conventional labelling of the pulse phase is the following:

$$\varphi = \{0, \pi/2, \pi, 3\pi/2\} \iff \{x, y, -x, -y\} \tag{2.27}$$

As an example, a simple one-pulse experiment is assumed. The β_φ pulse of a strong rf field $|\omega_1| \gg |\Omega|$, $\theta \approx \pi/2$ is applied to the equilibrium magnetization $\boldsymbol{M}_0$:

$$\boldsymbol{M}(0) = \boldsymbol{M}_0 \xrightarrow{\mathsf{R}(\beta,\varphi,\pi/2)} \begin{cases} M_x(\tau_\mathrm{p}) = M_0 \sin\beta \sin\varphi \\ M_y(\tau_\mathrm{p}) = -M_0 \sin\beta \cos\varphi \\ M_z(\tau_\mathrm{p}) = M_0 \cos\beta \end{cases} \tag{2.28}$$

and the tilted magnetization is left to precess freely. Solution of (2.23) gives:

$$\boldsymbol{M}(\tau_\mathrm{p}) \xrightarrow{\substack{\text{free}\\ \text{precession}}} \begin{cases} M_x(t) = -M_0 \sin\beta \sin(\Omega t - \varphi)\, \mathrm{e}^{-t/T_2} \\ M_y(t) = -M_0 \sin\beta \cos(\Omega t - \varphi)\, \mathrm{e}^{-t/T_2} \\ M_z(t) = M_0 \left[1 - (1 - \cos\beta)\, \mathrm{e}^{-t/T_1}\right] \end{cases} \tag{2.29}$$

The transverse magnetization, obtained by combining $M_x(t)$ and $M_y(t)$ from (2.29), is recorded through the quadrature detection method as the NMR signal [14]:

$$M^-(t) = M_x(t) - \mathrm{i}M_y(t) = \mathrm{i}M_0 \sin\beta \exp[\mathrm{i}(\Omega t - \varphi) - t/T_2] \tag{2.30}$$

The signal of amplitude $M_0 \sin\beta$ oscillates with the offset angular frequency Ω, and is exponentially damped with the transverse relaxation time constant T_2.

In general, rf pulses may be categorized according to the relative strength of the rf field ω_1 with respect to the resonance offset Ω [15]. Assume that there exist several coupled spins of the same isotope in the sample, each characterized by its own chemical shift, each pair having a characteristic coupling constant. The corresponding frequency spectrum will display multiplets of peaks at offsets Ω_i for the given frequency ω_rf. The rf pulse is called hard or nonselective, when $|\omega_1| \gg |\Omega_i|$ for all i. A weak rf-field of either constant or modulated amplitude or phase may be used to excite only one multiplet belonging to a certain nucleus, while leaving the rest of the resonances untouched [16–22]. This is a semi-selective pulse. When only one specific resonance is excited, such a pulse is called selective [23, 24].

2.1.4 Longitudinal and Transverse Relaxation Experiments

Both the longitudinal and transverse relaxation time constants were introduced phenomenologically by Bloch [9, 25]. Though they were introduced for the purpose of the classical description of magnetization by means of the vector model, they are still valid characteristics of individual nuclear centers.

The T_1 constant describes reestablishment of the thermal-equilibrium population distribution after its perturbation. This process is connected with the transfer of excess energy from excited nuclei to their surroundings. The value of T_1 depends on the observed isotope as well as on the sample properties as, e.g., its temperature T, viscosity η or self-diffusion coefficient D. Oxygen dissolved within the sample may shorten T_1 as well [14, 26].

Several methods exist for T_1 determination [10, 14, 26]. The one used in this work is the inversion recovery method [27, 28]. Its basic pulse sequence is shown in Figure 2.1(a). Using Eqs. (2.28) and (2.29), the thermal equilibrium magnetization $\boldsymbol{M}_0$ is inverted by a hard π_x pulse of duration τ_p:

$$\boldsymbol{M}(0) = \boldsymbol{M}_0 \xrightarrow{\mathsf{R}(\pi,0,\pi/2)} \boldsymbol{M}(\tau_\mathrm{p}) = -\boldsymbol{M}_0 \tag{2.31}$$

and left to relax towards equilibrium during a τ interval. Assume that $\tau_\mathrm{p} \ll \tau$, then:

$$\boldsymbol{M}(\tau_\mathrm{p}) \longrightarrow \boldsymbol{M}(\tau) = \boldsymbol{M}_0 \left(1 - 2\,\mathrm{e}^{-\tau/T_1}\right) \tag{2.32}$$

After the relaxation interval, another hard $(\pi/2)_x$ pulse converts the longitudinal magnetization into transverse magnetization, which is detected:

$$M^-(t) = \mathrm{i}M_0\,[1 - 2\exp(-\tau/T_1)]\exp[\mathrm{i}(\Omega t - \varphi) - t/T_2] \tag{2.33}$$

When the same experiment is repeated for different values of τ, the T_1 value may be determined from a plot of signal intensity vs. τ interval, shown in Figure 2.1(b). T_1 may also be estimated from the zero-crossing time $\tau_\mathrm{zc} = T_1 \ln 2$.

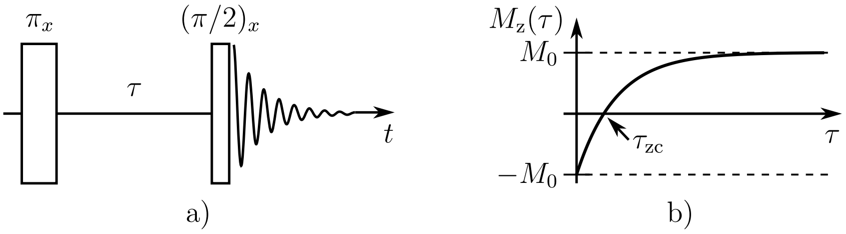

a) b)

Figure 2.1: The inversion recovery experiment. a) The rf pulse sequence. b) The longitudinal magnetization recovery after inversion as a function of the τ interval. The magnetization strength is zero for $\tau = \tau_\mathrm{zc}$.

The inversion recovery method is advantageous because of its simplicity. It does not use magnetic field gradients as, e.g., saturation recovery [10, 29]. However, thermal equilibrium magnetization has to be reestablished before repeating the experiment. In practice, it takes between 3 and 5 T_1-intervals, which makes the method impractical in the case of long T_1 values.

Transverse relaxation, characterized by the T_2 time constant, is not connected with any energy transfer. Its cause is a gradual loss of synchrony during the precession of individual spins due to magnetic field fluctuations on the microscopic scale. This homogeneous decay is irreversible and results in the NMR signal fading away, see Eq. (2.29). The value of T_2 depends on the sample phase, possible spin exchange taking place inside the sample, and the molecular size as related to the respective molecular dynamics. In the liquid phase, $T_2 \leq T_1$ is the usual case [14].

Besides the homogeneous decay characterized by T_2, the inhomogeneous decay exists as well. On the one hand, it is caused by a macroscopic B_0 field inhomogeneity over the sample volume due to, e.g., instrumental imperfections or a nonuniform sample susceptibility. On the other hand, transport processes (diffusion) contribute, too. The inhomogeneous decay is reversible by means of a spin-echo method, which is treated in detail in Section 6.1. Assuming the inhomogeneous decay is described by a time constant T_2', then both T_2 and T_2' combine into an apparent transverse relaxation time constant T_2^* given by:

$$\frac{1}{T_2^*} = \frac{1}{T_2} + \frac{1}{T_2'} \tag{2.34}$$

Neither T_2' nor T_2^* bear any meaningful information about the studied spin system as they are solely a result of the above mentioned processes within the sample volume. T_2^* is, however, related to the full-width at half-maximum (FWHM) of the observed spectral peaks, see Eq. (4.23), instead of the ideal T_2.

2.1.5 Drawbacks of the Classical Approach

The Bloch approach to describe the classical evolution of nuclear magnetization was very successful. Though it was originally suited only for isolated spins-1/2, either in its simplest form or due to various *ad hoc* extensions, it allowed the explanation of different effects in NMR such as chemical shifts, reaction kinetics, or diffusion [10, 26].

The inability to handle the internuclear couplings and its restriction to the description of magnetization as a 3D vector hindered the classical model from universal use. It cannot explain strong spin-spin coupling effects, evolution of the coupled spin system after application of nonselective rf pulses, individual processes responsible for apparent T_1 and T_2 relaxation, or magnetization transfer via forbidden transitions in general [2]. In order to understand the nature of these and numerous other phenomena, the full quantum-mechanical treatment of a realistic ensemble of interacting spins, with all the essential properties taken into account, has to be used.

2.2 Quantum-Mechanical Approach

2.2.1 From Individual Spins to the Spin Ensemble

The wavefunction formalism represents an intermediate step between the classical and full quantum mechanical treatment of the spin system. It is capable of describing systems of a few spins, but introduces important terms and concepts used in more advanced approaches [2, 30].

Any state of the spin system is fully characterized by a wavefunction $\Psi(t,\tau)$. In Dirac formalism, the wavefunction is represented by a ket $|\Psi(t,\tau)\rangle$ or its complex conjugate, a bra $\langle\Psi(t,\tau)|$. It is a function of time t and other relevant variables τ, and is normalized to unity:

$$\langle\Psi(t,\tau)|\Psi(t,\tau)\rangle = \int_{-\infty}^{+\infty} \mathrm{d}\tau\, \Psi^{*}(t,\tau)\Psi(t,\tau) = 1 \tag{2.35}$$

When concentrating only on the time-dependence of $|\Psi(t,\tau)\rangle$, and using the natural units ($\hbar = 1$), time evolution of the spin system is described by the Schrödinger equation:

$$\frac{\partial}{\partial t}|\Psi(t)\rangle = -\mathrm{i}\hat{H}(t)\,|\Psi(t)\rangle \tag{2.36}$$

where $\hat{H}(t)$ is the Hamiltonian operator, which incorporates processes influencing the spin system evolution. A detailed solution of (2.36) is provided in Appendix C. The solution for a time-independent Hamiltonian is equal to, see Eq. (C.3):

$$|\Psi(t)\rangle = \hat{U}(t,0)\,|\Psi(0)\rangle \tag{2.37}$$

where $\hat{U}$ is the propagation operator (propagator) of the system between the time-points t_1 and t_2 defined by:

$$\hat{U}(t_2,t_1) = \exp[-\mathrm{i}\hat{H}(t_2 - t_1)] \quad \text{for} \quad t_1 \le t_2 \tag{2.38}$$

The propagator is a unitary operator (A.10), which obeys the following relationships:

$$\hat{U}(t,t) = \hat{E} \tag{2.39}$$

$$\hat{U}^{-1}(t_2,t_1) = \hat{U}(t_1,t_2) \tag{2.40}$$

$$\hat{U}(t_3,t_1) = \hat{U}(t_3,t_2)\,\hat{U}(t_2,t_1) \tag{2.41}$$

where $\hat{E}$ is the identity operator, and $t_1 \le t_2 \le t_3$.

Formal integration of (2.36) for a time-dependent Hamiltonian is difficult to evaluate in practice, and is replaced by an iterative scheme leading to the time-ordered exponential (C.10):

$$|\Psi(t)\rangle = \hat{\hat{T}} \exp\left[-\mathrm{i}\int_{t_0}^{t} \mathrm{d}t'\, \hat{H}(t')\right] |\Psi(t_0)\rangle \tag{2.42}$$

where $\hat{\hat{T}}$ is the Dyson time-ordering superoperator. If the continuous Hamiltonian $\hat{H}(t)$, considered within a time interval $t_A \leq t_B$, may be approximated by a series of piecewise constant Hamiltonians $\hat{H}_i(t)$ within time intervals $t \in [t_i, t_{i+1}]$, where $t_A \equiv t_0 \leq t_1 \leq \ldots \leq t_k \equiv t_B$, then, using Eq. (2.41), the solution of (2.36) is simply [30]:

$$|\Psi(t)\rangle = \hat{U}_{k-1}(t_k, t_{k-1}) \cdot \ldots \cdot \hat{U}_0(t_1, t_0)\, |\Psi(0)\rangle \tag{2.43}$$

Every quantum mechanical observable quantity A has associated a Hermitian operator $\hat{A}$, satisfying the eigenvalue equation [2]:

$$\hat{A}|\psi_i\rangle = \lambda_i|\psi_i\rangle \quad \text{or} \quad \langle\psi_i|\hat{A}^{\dagger} = \lambda_i^{*}\langle\psi_i| \tag{2.44}$$

$|\psi_i\rangle$ is the eigenfunction (eigenstate) and λ_i is the corresponding eigenvalue. The dagger denotes adjoint operation, see Eq. (A.8). Hermiticity (A.9) of $\hat{A}$ implies $\lambda = \lambda^{*}$ is real.

In a system of N distinct spins I_i, there exist $\mathcal{N}$ different energy eigenstates $|\psi_i\rangle$, each having an energy E_i:

$$\hat{H}|\psi_i\rangle = E_i|\psi_i\rangle \tag{2.45}$$

where $\mathcal{N}$ is given by:

$$\mathcal{N} = \prod_{k=1}^{N}(2I_k + 1) \tag{2.46}$$

The time-independent eigenstates are orthonormal:

$$\langle\psi_i|\psi_j\rangle = \delta_{i,j} = \begin{cases} 1 & \text{if } i = j \\ 0 & \text{if } i \neq j \end{cases} \tag{2.47}$$

The symbol $\delta_{i,j}$ is the Kronecker delta. A complete set of $\mathcal{N}$ eigenstates forms a basis (eigenbasis), common for all observable operators. Any wavefunction may be expressed as a linear combination of the eigenstates [31]:

$$|\Psi(t)\rangle = \sum_{j=1}^{\mathcal{N}} c_j(t)\mathrm{e}^{\mathrm{i}\phi_j}|\psi_j\rangle \tag{2.48}$$

Here $\mathrm{e}^{\mathrm{i}\phi_j}$ is the phase of the jth eigenstate, which is not provided by solution of (2.36). It uniquely determines $|\psi_j\rangle$, which solves (2.36) as well. The coefficients $c_j(t)$ are generally complex, time-dependent and normalized:

$$\sum_{j=1}^{\mathcal{N}} c_j^{*}(t)c_j(t) = \sum_{j=1}^{\mathcal{N}} |c_j(t)|^2 = \sum_{j=1}^{\mathcal{N}} p_j = 1 \tag{2.49}$$

The coefficients $c_j(t)$ quantify the contribution of the eigenstate $|\psi_j\rangle$ to $|\Psi(t)\rangle$. Their square denotes the probabilities p_j. Therefore, Eq. (2.49) expresses that the sum over probabilities of all possible states is equal to one.

The operator $\hat{A}$ may be expressed in the form of a $\mathcal{N} \times \mathcal{N}$ matrix in the considered basis. The matrix elements are given by:

$$A_{ij} = \langle\psi_i|\hat{A}|\psi_j\rangle = \int_{-\infty}^{+\infty} \mathrm{d}\tau\, \psi_i^* \hat{A} \psi_j \tag{2.50}$$

An expectation value of the observable A, when the system is in the state $|\Psi(t)\rangle$, is then given by:

$$\langle A\rangle = \langle\Psi(t)|\hat{A}|\Psi(t)\rangle \tag{2.51}$$

Despite its usefulness, the wavefunction formalism cannot be extended to describe bigger molecules or even macroscopic spin ensembles [30]. Firstly, since the whole system is described by only one wavefunction, inclusion of all degrees of freedom for all spins makes it a very complicated and an enormously sizable object. Secondly, for an NMR sample containing $\sim 10^{20}$ spins, it is unlikely that all spins of the ensemble would be in the same pure state described by a single state wavefunction. All these difficulties may be overcome by means of the density operator formalism [32, 33].

2.2.2 Spin Density Operator

Assume first an idealized spin ensemble in a pure state, described by the single wavefunction $|\Psi(t)\rangle$. The density operator is defined as [10]:

$$\hat{\rho}(t) = |\Psi(t)\rangle\langle\Psi(t)| = \sum_{i,j=1}^{\mathcal{N}} c_i(t) c_j^*(t) \mathrm{e}^{\mathrm{i}(\phi_i - \phi_j)} |\psi_i\rangle\langle\psi_j| \tag{2.52}$$

The density operator $\hat{\rho}(t)$ is the projection operator:

$$\hat{\rho}(t)|\Phi(t)\rangle = |\Psi(t)\rangle\langle\Psi(t)|\Phi(t)\rangle = \lambda_\Phi |\Psi(t)\rangle \tag{2.53}$$

The eigenvalue λ_Φ denotes an amount of $|\Phi(t)\rangle$ contained in $|\Psi(t)\rangle$. The matrix form of the density operator in the given eigenbasis is a $\mathcal{N} \times \mathcal{N}$ density matrix:

$$\rho_{mn}(t) = \langle\psi_m|\hat{\rho}(t)|\psi_n\rangle = \sum_{i,j=1}^{\mathcal{N}} c_i(t) c_j^*(t) \mathrm{e}^{\mathrm{i}(\phi_i - \phi_j)} \langle\psi_m|\psi_i\rangle\langle\psi_j|\psi_n\rangle = c_m(t) c_n^*(t) \mathrm{e}^{\mathrm{i}(\phi_m - \phi_n)} \tag{2.54}$$

The diagonal elements, $\rho_{mm}(t)$, give the probability that the spin ensemble is in the eigenstate $|\psi_m\rangle$:

$$\rho_{mm}(t) = c_m(t) c_m^*(t) = |c_m(t)|^2 = P_m \tag{2.55}$$

P_m is called the population of the eigenstate $|\psi_m\rangle$, and is associated with the operator $|\psi_m\rangle\langle\psi_m|$. The existence of nonzero off-diagonal elements:

$$\rho_{mn}(t) = c_m(t)c_n^*(t)\mathrm{e}^{\mathrm{i}(\phi_m - \phi_n)}\,,\ m \neq n \tag{2.56}$$

implies that the wavefunction $|\Psi(t)\rangle$ contains a coherent superposition (coherence) of the eigenstates:

$$c_m(t)\mathrm{e}^{\mathrm{i}\phi_m}|\psi_m\rangle + c_n(t)\mathrm{e}^{\mathrm{i}\phi_n}|\psi_n\rangle \tag{2.57}$$

This means that the evolution of different spin sub-ensembles is correlated to the coherence $|\psi_m\rangle\langle\psi_n|$, of which $\rho_{mn}(t)$ is the complex amplitude.

The coherences correspond to transitions between the corresponding eigenstates. The difference in the (total) magnetic quantum numbers of the eigenstates $|\psi_r\rangle$ and $|\psi_s\rangle$:

$$p = m_r - m_s \tag{2.58}$$

denotes the p-quantum coherence. Only the transitions with $p = \pm 1$ (single quantum coherences) give rise to the observable NMR signal. Coherences with $p \neq \pm 1$ may only be observed indirectly [10].

As a consequence of the interactions of individual spins with their surroundings, the spin ensemble is in a mixed state. Different states, characterized by the wavefunctions $|\Psi^\lambda(t)\rangle$, are populated with probabilities p^λ by sub-ensembles of the spins. A generalized form of the density operator is then [10]:

$$\begin{aligned}\hat{\rho}(t) &= \sum_\lambda p^\lambda |\Psi^\lambda(t)\rangle\langle\Psi^\lambda(t)| \\ &= \sum_\lambda p^\lambda \sum_{i,j=1}^{\mathcal{N}} c_i^\lambda(t) c_j^{\lambda *}(t)\mathrm{e}^{\mathrm{i}(\phi_i^\lambda - \phi_j^\lambda)}|\psi_i\rangle\langle\psi_j| \\ &= \sum_{i,j=1}^{\mathcal{N}} \overline{c_i(t)c_j^*(t)\mathrm{e}^{\mathrm{i}(\phi_i - \phi_j)}}|\psi_i\rangle\langle\psi_j|\end{aligned} \tag{2.59}$$

Also the probabilities p^λ obey Eq. (2.49). The overbar denotes the ensemble average.

The trace (A.14) of the density operator is given by:

$$\mathrm{Tr}\{\hat{\rho}(t)\} \equiv \sum_{j=1}^{\mathcal{N}} \rho_{jj}(t) = \sum_{j=1}^{\mathcal{N}} \overline{|c_j(t)|^2} = \sum_{j=1}^{\mathcal{N}} P_j = 1 \tag{2.60}$$

Different results are obtained for the trace of $\hat{\rho}^2(t)$. For a spin ensemble in a pure state:

$$\mathrm{Tr}\{\hat{\rho}^2(t)\} = \mathrm{Tr}\{|\Psi(t)\rangle\langle\Psi(t)|\Psi(t)\rangle\langle\Psi(t)|\} = \mathrm{Tr}\{|\Psi(t)\rangle\langle\Psi(t)|\} = \mathrm{Tr}\{\hat{\rho}(t)\} = 1 \tag{2.61}$$

Knowledge of the behaviour of any sub-ensemble means knowledge of the behaviour of the ensemble. The ensemble in a general mixed state obeys:

$$\mathrm{Tr}\{\hat{\rho}^2(t)\} < 1 \tag{2.62}$$

This means that knowledge of the behaviour of sub-ensembles says nothing about the ensemble as a whole. If $\hat{\rho}^2(t) = \hat{\rho}(t)$, the density operator is idempotent [10].

The time evolution of the density operator may be derived as follows, taking into account Eqs. (2.36) and (2.52):

$$\begin{aligned}\frac{\partial}{\partial t}\hat{\rho}(t) &= \frac{\partial}{\partial t}|\Psi(t)\rangle\langle\Psi(t)| \\ &= \left[\frac{\partial}{\partial t}|\Psi(t)\rangle\right]\langle\Psi(t)| + |\Psi(t)\rangle\left[\frac{\partial}{\partial t}\langle\Psi(t)|\right] \\ &= -\mathrm{i}\hat{H}(t)\hat{\rho}(t) + \mathrm{i}\hat{\rho}(t)\hat{H}(t) \\ &= -\mathrm{i}[\hat{H}(t), \hat{\rho}(t)]\end{aligned} \tag{2.63}$$

where $[\cdot,\cdot]$ is the commutator (A.17). Eq. (2.63) is called the Liouville-von Neumann equation. Its solution may be written in the most general form using Eq. (2.37):

$$\hat{\rho}(t) = |\Psi(t)\rangle\langle\Psi(t)| = \hat{U}(t,0)|\Psi(0)\rangle\langle\Psi(0)|\hat{U}^{-1}(t,0) = \hat{U}(t,0)\,\hat{\rho}(0)\,\hat{U}^{-1}(t,0) \tag{2.64}$$

The expectation value of the observable A is given by:

$$\langle A\rangle = \mathrm{Tr}\{\hat{\rho}(t)\,\hat{A}\} = \mathrm{Tr}\{\hat{A}\,\hat{\rho}(t)\} \tag{2.65}$$

where Eqs. (2.50), (2.51), (2.59), and (2.60), and the relationship (A.16) were taken into account.

2.2.3 Superoperators

As shown in Section 2.2.2, the density operator formalism often involves commutators or double-sided multiplications. As a consequence, the description of complex NMR experiments eventuates in extensive expressions, which may also become computationally demanding [30]. A simplification of the formalism is possible by introducing superoperators [34].

In analogy with operators, represented by $\mathcal{N}\times\mathcal{N}$ matrices, which act on the wavefunctions, represented by $\mathcal{N}\times 1$ vectors, the superoperators are represented by $\mathcal{N}^2\times\mathcal{N}^2$ matrices, and act on such operators. The operators are rearranged column-wise into $\mathcal{N}^2\times 1$ column supervectors, and the application of the superoperators simplifies into matrix-vector multiplication.

Assume a complete basis $\{\hat{B}_i\}$ of $\mathcal{N}^2$ orthogonal operators with the trace metric defined by the scalar product [10]:

$$\left(\hat{B}_i\middle|\hat{B}_j\right) = \begin{cases} \mathrm{Tr}\{\hat{B}_i^\dagger \hat{B}_i\} & \text{for } i = j \\ 0 & \text{for } i \neq j \end{cases} \tag{2.66}$$

where $\left(\cdot\middle|\cdot\right)$ is called the Liouville bracket, which is defined by [34]:

$$\left(\hat{A}\middle|\hat{B}\right) = \mathrm{Tr}\{\hat{A}^\dagger \hat{B}\} = \sum_{i,j=1}^{\mathcal{N}} \hat{A}^\dagger_{ji}\hat{B}_{ij} = \sum_{ij=1}^{\mathcal{N}^2} \hat{A}^*_{ij}\hat{B}_{ij} \tag{2.67}$$

The first sum is appled to the operator matrix representations and the second sum is applied to the supervectors of the operators $\hat{A}$ and $\hat{B}$. Any operator $\hat{A}$, including $\hat{\rho}$, may be expanded in this basis:

$$\hat{A} = \sum_{i=1}^{\mathcal{N}^2} a_i \hat{B}_i \tag{2.68}$$

where the mixing coefficients a_i are given by:

$$a_i = \frac{\left(\hat{B}_i\middle|\hat{A}\right)}{\left(\hat{B}_i\middle|\hat{B}_i\right)} = \frac{\mathrm{Tr}\{\hat{B}_i^\dagger \hat{A}\}}{\mathrm{Tr}\{\hat{B}_i^\dagger \hat{B}_i\}} \tag{2.69}$$

The matrix representation of the superoperator, which is denoted by a double hat, in a suitable orthonormal operator basis $\{\hat{B}_i\}$, where $\left(\hat{B}_i\middle|\hat{B}_i\right) = 1$, is then:

$$\hat{\hat{S}}_{ij} = \left(\hat{B}_i\middle|\hat{\hat{S}}\middle|\hat{B}_j\right) = \mathrm{Tr}\{\hat{B}_i^\dagger \hat{\hat{S}} \hat{B}_j\} \tag{2.70}$$

Similarly with the operators, the superoperators may be Hermitian or unitary.

Several important classes of superoperators, which are used in the rest of the text, will be introduced now.

2.2.3.1 Commutation Superoperators

The commutation superoperator $\hat{\hat{C}}$ generates the commutator of two operators [10]:

$$\hat{\hat{C}}\hat{A} = [\hat{C}, \hat{A}] = \hat{C}\hat{A} - \hat{A}\hat{C} \tag{2.71}$$

The matrix representation of the superoperator $\hat{\hat{C}}$ is constructed from the matrix representations of the operator $\hat{C}$ and unity operator $\hat{E}$ as follows:

$$\hat{\hat{C}} = \hat{C} \otimes \hat{E}^\mathsf{T} - \hat{E} \otimes \hat{C}^\mathsf{T} \tag{2.72}$$

where the symbol $\otimes$ denotes the Kronecker product (A.18). If $\hat{C}$ is Hermitian, $\hat{\hat{C}}$ is Hermitian as well.

Commutation superoperators are often associated with Hamiltonians and involve different combinations of spin operators $\hat{I}$. An important example is the Liouvillian $\hat{\hat{L}}(t)$, which simplifies the Liouville-von Neumann equation (2.63):

$$\frac{\partial}{\partial t}\hat{\rho}(t) = -\mathrm{i}\,[\hat{H}(t), \hat{\rho}(t)] \equiv -\mathrm{i}\hat{\hat{L}}(t)\hat{\rho}(t) \tag{2.73}$$

2.2.3.2 Cyclic Commutation

A special case of the commutation superoperator is the double-commutator superoperator [10]:

$$\hat{\hat{C}}_2\,\hat{\hat{C}}_1\,\hat{A} = \hat{\hat{C}}_2\,[\hat{C}_1, \hat{A}] = [\hat{C}_2, [\hat{C}_1, \hat{A}]] \tag{2.74}$$

Two operators $\hat{A}$ and $\hat{B}$ commute cyclically, if [31]:

$$\hat{\hat{A}}\hat{\hat{A}}\hat{B} = \hat{B} \tag{2.75}$$

The product $\hat{\hat{A}}\hat{B}$ gives rise to another operator $\mathrm{i}\hat{C}$. By using all three operators, the cyclic commutation relationships may be rewritten as follows:

$$\hat{\hat{A}}\hat{B} \equiv [\hat{A}, \hat{B}] = \mathrm{i}\hat{C} \iff {}_{\hat{C}}\overset{\hat{A}}{\circlearrowleft}{}_{\hat{B}} \tag{2.76}$$

A generalized form of Eq. (2.75) is given by [31]:

$$\hat{\hat{A}}^k\hat{B} = \begin{cases} \hat{\hat{A}}\hat{B} & \text{for odd } k \\ \hat{B} & \text{for even } k \end{cases} \tag{2.77}$$

from which an important equivalence may be derived:

$$\begin{aligned} \exp\left(-\mathrm{i}\theta\hat{\hat{A}}\right)\hat{B} &= \left(\sum_{k=0}^{\infty}\frac{(-\mathrm{i}\theta\hat{\hat{A}})^k}{k!}\right)\hat{B} \\ &= \hat{B}\left(\sum_{k=0}^{\infty}\frac{(\mathrm{i}\theta)^{2k}}{(2k)!}\right) + \hat{\hat{A}}\hat{B}\left(\sum_{k=0}^{\infty}\frac{(-\mathrm{i}\theta)^{2k+1}}{(2k+1)!}\right) \\ &= \hat{B}\cos\theta - \mathrm{i}\,\hat{\hat{A}}\hat{B}\sin\theta \\ &= \hat{B}\cos\theta + \hat{C}\sin\theta \end{aligned} \tag{2.78}$$

Relationship (2.78) is used during the evaluation of effects of the rf pulses and intervals of free evolution on the spin state represented by the density operator. Its shorthand is an arrow notation in NMR experiments:

$$\hat{B} \xrightarrow{\theta\hat{A}} \hat{B}\cos\theta + \hat{C}\sin\theta \tag{2.79}$$

The Cartesian spin operators obey the cyclic commutation relationships:

$$[\hat{I}_x, \hat{I}_y] = \mathrm{i}\hat{I}_z \iff {}_{z}\overset{x}{\circlearrowleft}{}_{y} \tag{2.80}$$

As an example, the application of a π_x pulse on the equilibrium magnetization $\hat{\rho}(0) \equiv \hat{I}_z$ gives:

$$\hat{\hat{R}}_x(\pi)\,\hat{\rho}(0) \equiv \exp\left(\mathrm{i}\pi\hat{\hat{I}}_x\right)\hat{I}_z = -\hat{I}_z \iff \hat{I}_z \xrightarrow{\pi\,\hat{I}_x} -\hat{I}_z \tag{2.81}$$

$\hat{\hat{R}}_x(\theta)$ is a rotation superoperator generating rotation around the x-axis by an angle θ.

2.2.3.3 Unitary Transformation Superoperators

The rotation superoperator in Eq. (2.81) belongs to a group of unitary transformation superoperators $\hat{\hat{U}}$. Such operators replace the double-sided operator multiplication [10]:

$$\hat{\hat{U}}\hat{A} = \exp\left(-\mathrm{i}\hat{\hat{C}}\right)\hat{A} = \exp\left(-\mathrm{i}\hat{C}\right)\hat{A}\exp\left(\mathrm{i}\hat{C}\right) = \hat{U}\hat{A}\hat{U}^{-1} \tag{2.82}$$

where $\hat{\hat{C}}$ is the commutation superoperator. The matrix representation of $\hat{\hat{U}}$ is constructed from the matrix representations of the operator $\hat{U}$ as follows:

$$\hat{\hat{U}} = \hat{U} \otimes \hat{U}^{-1} \tag{2.83}$$

Unitary transformation operators are used as, e.g., propagator superoperators. Assume that the spin system evolves from its initial state $\hat{\rho}(0)$ under the action of different time-independent Hamiltonians $\hat{H}_1$ and $\hat{H}_2$ for time intervals τ_1 and τ_2, respectively. By using the arrow representation, the set of events is:

$$\hat{\rho}(0) \xrightarrow{\hat{H}_1\tau_1}\xrightarrow{\hat{H}_2\tau_2} \hat{\rho}(\tau_1+\tau_2) \tag{2.84}$$

which is equivalent to:

$$\begin{aligned}
\hat{\rho}(\tau_1+\tau_2) &= \hat{\hat{U}}_2(\tau_1+\tau_2,\tau_1)\,\hat{\hat{U}}_1(\tau_1,0)\,\hat{\rho}(0) \\
&= \exp\left(-\mathrm{i}\hat{\hat{H}}_2\tau_2\right)\exp\left(-\mathrm{i}\hat{\hat{H}}_1\tau_1\right)\,\hat{\rho}(0) \\
&= \exp\left(-\mathrm{i}\hat{H}_2\tau_2\right)\exp\left(-\mathrm{i}\hat{H}_1\tau_1\right)\,\hat{\rho}(0)\exp\left(\mathrm{i}\hat{H}_1\tau_1\right)\exp\left(\mathrm{i}\hat{H}_2\tau_2\right)
\end{aligned} \tag{2.85}$$

Another important example is the transformation between the laboratory and the rotating frames, see Eq. (2.118).

2.2.3.4 Projection and Shift Superoperators

A projection superoperator is related to the density operator, see Eq. (2.53) [10]:

$$\hat{\hat{P}}_B = \frac{|\hat{B})(\hat{B}|}{(\hat{B}|\hat{B})} \iff \hat{\hat{P}}_B\,\hat{A} = \frac{\mathrm{Tr}\{\hat{B}^\dagger\hat{A}\}}{\mathrm{Tr}\{\hat{B}^\dagger\hat{B}\}}\hat{B} = a_B\,\hat{B} \tag{2.86}$$

where the coefficient a_B denotes the amount of $\hat{A}$ in $\hat{B}$. The normalized projection superoperators are idempotent.

A shift superoperator is a generalized version of the projection superoperator [35]:

$$\hat{\hat{P}}_{BA} = \frac{|\hat{B})(\hat{A}|}{(\hat{B}|\hat{B})} \tag{2.87}$$

2.2.4 Two Spin-1/2 System Description

Assume a homonuclear pair ($N = 2$) of coupled spins-1/2 in isotropic phase. Such a spin system occupies $\mathcal{N} = 4$ energy eigenstates, see Eq. (2.46). Each eigenstate is described by:

$$|\psi_i\rangle = \bigotimes_{k=1}^{N} |m_{ki}\rangle = |m_{1i}m_{2i}\rangle \tag{2.88}$$

which is given by the Kronecker product of single spin-1/2 eigenkets:

$$\begin{aligned} |\alpha\rangle &= (1,0)^{\mathsf{T}} \quad \text{for} \quad m_{ki} = +1/2 \\ |\beta\rangle &= (0,1)^{\mathsf{T}} \quad \text{for} \quad m_{ki} = -1/2 \end{aligned} \tag{2.89}$$

Therefore, there exist states with total magnetic quantum number M_i equal to 0 and ±1, where.

$$M_i = \sum_{k=1}^{N} m_{ki} \tag{2.90}$$

The corresponding operator basis consists of $\mathcal{N}^2 = 16$ operators and in total $\mathcal{N}^4 = 256$ linearly independent superoperators. The basis operators $\{\hat{B}_s\}$ are constructed from the Pauli matrices $\hat{\mathcal{I}}_\alpha$, where $\alpha = \{x, y, z\}$, and unity operator $\hat{\mathcal{E}}$, defined in Eq. (D.2), following a general recipe [10]:

$$\hat{B}_s = 2^{(q-1)} \bigotimes_{k=1}^{N} (\hat{\mathcal{I}}_{k\alpha})^{a_{ks}} \tag{2.91}$$

Here $q = \{0, 1, \dots, N\}$ is the number of operators $\hat{\mathcal{I}}_{k\alpha}$ in the product. $a_{ks} = 1$ for q of the operators and $a_{ks} = 0$ for the other $(N - q)$ operators, while $(\hat{\mathcal{I}}_{k\alpha})^0 = \hat{\mathcal{E}}$. Concretely:

$$\begin{aligned} q = 0 :\ & \hat{E}/2 \\ q = 1 :\ & \hat{I}_{1x},\ \hat{I}_{1y},\ \hat{I}_{1z},\ \hat{I}_{2x},\ \hat{I}_{2y},\ \hat{I}_{2z} \\ q = 2 :\ & 2\hat{I}_{1x}\hat{I}_{2x},\ 2\hat{I}_{1x}\hat{I}_{2y},\ 2\hat{I}_{1x}\hat{I}_{2z} \\ & 2\hat{I}_{1y}\hat{I}_{2x},\ 2\hat{I}_{1y}\hat{I}_{2y},\ 2\hat{I}_{1y}\hat{I}_{2z} \\ & 2\hat{I}_{1z}\hat{I}_{2x},\ 2\hat{I}_{1z}\hat{I}_{2y},\ 2\hat{I}_{1z}\hat{I}_{2z} \end{aligned}$$

The basis operators are orthogonal in the following sense [10]:

$$\left(\hat{B}_r \middle| \hat{B}_s\right) = \delta_{r,s}\, 2^{N-2} \tag{2.92}$$

The Cartesian spin operators are convenient, since they provide an insight into the magnetization evolution. Consequently, some of the operators bear special names either due to their relation to the vector model, or due to the spectral appearance, when such operators are included in the spin-system density operator, see Appendix D.3.

The basic form of the two spins-1/2 Hamiltonian in the rotating frame is:

$$\hat{H} = \Omega_1 \hat{I}_{1z} + \Omega_2 \hat{I}_{2z} + 2\pi J_{12}\, \hat{\mathbf{I}}_1 \cdot \hat{\mathbf{I}}_2 \tag{2.93}$$

where the first two terms belong to the Zeeman Hamiltonian $\hat{H}_\mathrm{Z}$ (2.114), and the third term is called the J-coupling Hamiltonian $\hat{H}_J$ (2.122).

The description of the spin system differs according to the relative contribution of $\hat{H}_\mathrm{Z}$ and $\hat{H}_J$ into the total Hamiltonian $\hat{H}$. The two extreme cases are the weakly and strongly coupled spin systems, for which $|\Omega_1 - \Omega_2| \gg |\pi J_{12}|$ and $|\Omega_1 - \Omega_2| \lesssim |\pi J_{12}|$, respectively. The coupling strength may also be expressed by a mixing angle [36]:

$$\tan\Theta = \frac{\Omega_1 - \Omega_2}{2\pi J_{12}} = \frac{-\gamma B_0 \left(\delta_1 - \delta_2\right)}{2\pi J_{12}} \tag{2.94}$$

For a weakly coupled spin system, $\Theta \approx \pm\pi/2$, while for a strongly coupled spin system, $\Theta \approx 0$. The intermediate case, when $|\Theta| \in (0, \pi/2)$, is treated in detail in Section 7.2.2.

A weakly coupled spin system, including the spin-spin coupling, is conveniently described by the product operator formalism, used above. The eigenstates are described by the Zeeman product states (2.88):

$$\begin{aligned} |\alpha\alpha\rangle &= (1,0,0,0)^\mathsf{T} \\ |\alpha\beta\rangle &= (0,1,0,0)^\mathsf{T} \\ |\beta\alpha\rangle &= (0,0,1,0)^\mathsf{T} \\ |\beta\beta\rangle &= (0,0,0,1)^\mathsf{T} \end{aligned} \tag{2.95}$$

The Hamiltonian $\hat{H}$ (2.93) may be rearranged into:

$$\hat{H}_\mathrm{W} = \underbrace{\Omega_1 \hat{I}_{1z} + \Omega_2 \hat{I}_{2z} + 2\pi J_{12}\, \hat{I}_{1z} \hat{I}_{2z}}_{\hat{H}_\mathrm{A}} + \underbrace{\pi J_{12} (\hat{I}_1^+ \hat{I}_2^- + \hat{I}_1^- \hat{I}_2^+)}_{\hat{H}_\mathrm{B}} \tag{2.96}$$

where $\hat{I}_k^\pm$ are the shift operators defined by Eq. (D.8). The matrix representation of $\hat{H}_\mathrm{W}$ is given by:

$$\hat{H}_\mathrm{W} = \frac{1}{2} \begin{array}{cc} \begin{array}{cccc} |\alpha\alpha\rangle & |\alpha\beta\rangle & |\beta\alpha\rangle & |\beta\beta\rangle \end{array} & \\ \begin{pmatrix} \Omega_\Sigma + \pi J_{12} & 0 & 0 & 0 \\ 0 & \Omega_\Delta - \pi J_{12} & 2\pi J_{12} & 0 \\ 0 & 2\pi J_{12} & -\Omega_\Delta - \pi J_{12} & 0 \\ 0 & 0 & 0 & -\Omega_\Sigma + \pi J_{12} \end{pmatrix} & \begin{array}{c} \langle\alpha\alpha| \\ \langle\alpha\beta| \\ \langle\beta\alpha| \\ \langle\beta\beta| \end{array} \end{array} \tag{2.97}$$

where:

$$\Omega_\Sigma = \Omega_1 + \Omega_2 \tag{2.98}$$

$$\Omega_\Delta = \Omega_1 - \Omega_2 \tag{2.99}$$

The four diagonal elements belong to the Hamiltonian $\hat{H}_\mathrm{A}$. The presence of nonzero off-diagonal elements, arising from the Hamiltonian $\hat{H}_\mathrm{B}$, means that the Zeeman product states are not the exact eigenstates. Nonetheless, under the secular approximation [14]:

$$|\hat{H}_{23}| = |\hat{H}_{32}| \ll |\hat{H}_{22} - \hat{H}_{33}| \iff |\pi J_{12}| \ll |\Omega_\Delta| \tag{2.100}$$

the Hamiltonian $\hat{H}_\mathrm{B}$ may be omitted and $\hat{H}_\mathrm{W} \approx \hat{H}_\mathrm{A}$ becomes diagonal.

A strongly coupled pair may be attained in two different ways. On the one hand, by choosing magnetically (nearly-)equivalent spins, where their chemical shifts are close and the two spins have similar couplings to other nuclei in the molecule [14]. On the other hand, by placing the spin system, which is weakly coupled in the spectrometer high field B_HF, into a very low field $B_\mathrm{LF} \ll B_\mathrm{HF}$. The outcome in both cases is that $|\Omega_\Delta| \lesssim |\pi J_{12}|$.

Assume that the two chemical shifts are the same, so that $\Omega_1 = \Omega_2 \equiv \Omega'$. The Hamiltonian (2.93) then simplifies into [14]:

$$\hat{H}_\mathrm{S} = \Omega' \hat{I}_z + 2\pi J_{12}\, \hat{\mathbf{I}}_1 \cdot \hat{\mathbf{I}}_2 \tag{2.101}$$

where the total spin operator $\hat{I}_z$ is defined by Eq. (D.16). The eigenstates of Hamiltonian (2.101) are the so-called singlet state $|\mathrm{S}_0\rangle$ and three triplet states $|T_{M_i}\rangle$:

$$\begin{aligned} |S_0\rangle &= \frac{|\alpha\beta\rangle - |\beta\alpha\rangle}{\sqrt{2}} \\ |T_{+1}\rangle &= |\alpha\alpha\rangle \\ |T_0\rangle &= \frac{|\alpha\beta\rangle + |\beta\alpha\rangle}{\sqrt{2}} \\ |T_{-1}\rangle &= |\beta\beta\rangle \end{aligned} \tag{2.102}$$

The matrix representation of the Hamiltonian in the singlet-triplet basis equals:

$$\hat{H}_\mathrm{S} = \frac{1}{2} \begin{array}{cc} \begin{array}{cccc} |S_0\rangle & |T_{+1}\rangle & |T_0\rangle & |T_{-1}\rangle \end{array} & \\ \begin{pmatrix} -3\pi J_{12} & 0 & 0 & 0 \\ 0 & 2\Omega' + \pi J_{12} & 0 & 0 \\ 0 & 0 & \pi J_{12} & 0 \\ 0 & 0 & 0 & -2\Omega' + \pi J_{12} \end{pmatrix} & \begin{array}{c} \langle S_0| \\ \langle T_{+1}| \\ \langle T_0| \\ \langle T_{-1}| \end{array} \end{array} \tag{2.103}$$

In the case that $B_0 \approx 0$, the three triplet states become degenerate with an energy separated by $2\pi J_{12}$ from the singlet state, as shown later in Figure 7.1.

Knowledge of the density operator allows determination of the frequency spectrum appearance, i.e., positions and intensities of the peaks. Assume the NMR signal is generated by the (-1)-quantum coherences between the energy levels with frequencies Ω_r and Ω_s, where $r, s = \{\alpha\alpha, \alpha\beta, \beta\alpha, \beta\beta\}$ and $r \neq s$. The NMR signal is given by [14]:

$$s(t) = \sum_{r,s=1}^{4} a_{rs} \exp\left[(\mathrm{i}\Omega_{rs} - \lambda)t\right] \tag{2.104}$$

where a_{rs} are the complex signal amplitudes, to which the intensities of the spectral peaks are proportional. The spectral peaks appear at positions given by the frequency differences between the corresponding pairs of the neighbouring levels:

$$\Omega_{rs} = -\Omega_r + \Omega_s \tag{2.105}$$

The detected magnetization is proportional to the expectation value of the shift operator $\hat{I}^-$, which represents the (-1)-quantum coherence:

$$M^-(t) \propto \langle \hat{I}^- \rangle = \mathrm{Tr}\{\hat{\rho}(t)\hat{I}^-\} = \sum_{r,s} \hat{\rho}_{rs}(t)\langle s|\hat{I}^-|r\rangle \tag{2.106}$$

The terms $\hat{\rho}_{rs}(t)$ arise from the density matrix expansion:

$$\hat{\rho}(t) = \sum_{r,s=1}^{4} \rho_{rs}(t)\, |r\rangle\langle s| \tag{2.107}$$

Therefore, the signal amplitudes a_{rs} at time zero are given by:

$$a_{rs} = 2\mathrm{i}\, \rho_{rs}(0)\langle s|\hat{I}^-|r\rangle\, \mathrm{e}^{-\mathrm{i}\phi_{\mathrm{rec}}} \tag{2.108}$$

where the additional receiver phase ϕ_{rec} results from the spectrometer electronics.

2.2.5 Averaging and Residual Interactions in Solution NMR

A Hamiltonian $\hat{H}_\Lambda$, which describes a specific spin interaction Λ, may in general be written as [2, 10]:

$$\hat{H}_\Lambda = \boldsymbol{u}^\mathsf{T} \boldsymbol{\Lambda} \boldsymbol{v} \tag{2.109}$$

The vector $\boldsymbol{u}$ stands for the Cartesian spin angular momentum operator vector (D.1). The vector $\boldsymbol{v}$ may either be of the same type as $\boldsymbol{u}$, or may denote the magnetic field vector $\boldsymbol{B}$. $\boldsymbol{\Lambda}$ represents a 3×3 Cartesian second-rank tensor:

$$\boldsymbol{\Lambda} = \begin{pmatrix} \Lambda_{xx} & \Lambda_{xy} & \Lambda_{xz} \\ \Lambda_{yx} & \Lambda_{yy} & \Lambda_{yz} \\ \Lambda_{zx} & \Lambda_{zy} & \Lambda_{zz} \end{pmatrix} \tag{2.110}$$

comprising the effect of the interaction under consideration on the given spin. The tensor $\boldsymbol{\Lambda}$ may be decomposed into three irreducible tensors of rank 0, 1 and 2:

$$\boldsymbol{\Lambda} = \boldsymbol{\Lambda}^{(0)} + \boldsymbol{\Lambda}^{(1)} + \boldsymbol{\Lambda}^{(2)} \tag{2.111}$$

where:

$$\begin{aligned} \boldsymbol{\Lambda}^{(0)} &= \frac{1}{3}\mathrm{Tr}\{\boldsymbol{\Lambda}\}\mathbf{E}_3 \equiv \boldsymbol{\Lambda}^{\mathrm{iso}} \\ \boldsymbol{\Lambda}^{(1)} &= \frac{1}{2}(\boldsymbol{\Lambda} - \boldsymbol{\Lambda}^{\mathsf{T}}) \\ \boldsymbol{\Lambda}^{(2)} &= \frac{1}{2}(\boldsymbol{\Lambda} + \boldsymbol{\Lambda}^{\mathsf{T}}) - \boldsymbol{\Lambda}^{(0)} \end{aligned} \tag{2.112}$$

The first term $\boldsymbol{\Lambda}^{(0)}$ is a scalar multiplied by the unit matrix $\mathbf{E}_3$ defined by Eq. (A.11). The second term $\boldsymbol{\Lambda}^{(1)}$ is a traceless antisymmetric tensor, see the definitions in Eqs. (A.6) and (A.15). It leaves unchanged the spin system energy levels and, therefore, the frequency spectrum. The third term $\boldsymbol{\Lambda}^{(2)}$ is a traceless symmetric tensor (A.5). It becomes diagonal in the principal axis coordinate system (PAS) of the interaction Λ. Except for the chemical-shift anisotropy (CSA) interaction [37], $\boldsymbol{\Lambda}^{(1)}$ may be left out and the only tensors, which remain for describing the observed effects, are $\boldsymbol{\Lambda}^{(0)}$ and $\boldsymbol{\Lambda}^{(2)}$.

In isotropic solutions such as a low-concentrated solution of a measured compound, molecules (but not spins) may be found in any possible orientation with respect to the static magnetic field B_0 due to their thermal motion. Nevertheless, Hamiltonian rotational invariance, i.e., $[\hat{R}_\alpha(\theta), \hat{H}] = 0$, limits the types of interactions under consideration.

The dominant Zeeman interaction, linear in the spin operators, is described by the Zeeman Hamiltonian $\hat{H}_{\mathrm{Z}}$ [10]:

$$\hat{H}_{\mathrm{Z}} = -\sum_{k=1}^{N} \gamma_k \hat{\mathbf{I}}_k (\mathbf{E}_3 + \boldsymbol{\delta}_k)\boldsymbol{B}_0 \tag{2.113}$$

where $\hat{\mathbf{I}}_k$ and $\boldsymbol{\delta}_k$ are the spin operator and the chemical shift tensor of the spin k, respectively, and $\boldsymbol{B}_0$ is the static magnetic field. Under assumptions that $\boldsymbol{B}_0$ is aligned along the z-axis and the norm (A.13) of $\boldsymbol{\delta}_k$ is small, i.e., $\|\boldsymbol{\delta}_k\|_F \ll 1$, the Hamiltonian $\hat{H}_{\mathrm{Z}}$ may be approximated by:

$$\hat{H}_{\mathrm{Z}} \approx \sum_{k=1}^{N} \left[-\gamma_k (1 + \delta_k^{\mathrm{iso}}) B_0\right] \hat{I}_{kz} = \sum_{k=1}^{N} \omega_{0k} \hat{I}_{kz} \tag{2.114}$$

where δ_k^{iso} is the motionally averaged isotropic chemical shift, and ω_{0k} is the chemically shifted Larmor frequency.

Similarly with Eq. (2.14), the Hamiltonian $\hat{H}_{\mathrm{rf}}$ represents the interaction of the spins with the radiofrequency field [10]:

$$\begin{aligned} \hat{H}_{\mathrm{rf}} &= -B_1 \sum_{k=1}^{N} \gamma_k [\cos(\omega_{\mathrm{rf}} t + \varphi) \hat{I}_{kx} + \sin(\omega_{\mathrm{rf}} t + \varphi) \hat{I}_{ky}] \\ &= \sum_{k=1}^{N} \omega_{1k} [\cos(\omega_{\mathrm{rf}} t + \varphi) \hat{I}_{kx} + \sin(\omega_{\mathrm{rf}} t + \varphi) \hat{I}_{ky}] \end{aligned} \tag{2.115}$$

The meaning of all frequency- and field-related quantities remains the same as in Section 2.1.

The transformation into the rotating frame changes the laboratory-frame Hamiltonians $\hat{H}_{\mathrm{Z}}$ and $\hat{H}_{\mathrm{rf}}$ correspondingly:

$$\hat{\hat{H}}_{\mathrm{Z}} = \hat{\hat{U}}^{-1}(t)\, \hat{H}_{\mathrm{Z}} = \sum_{k=1}^{N} (\omega_{0k} - \omega_{\mathrm{rf}}) \hat{I}_{kz} = \sum_{k=1}^{N} \Omega_k \hat{I}_{kz} \tag{2.116}$$

$$\hat{\hat{H}}_{\mathrm{rf}} = \hat{\hat{U}}^{-1}(t)\, \hat{H}_{\mathrm{rf}} = \sum_{k=1}^{N} \omega_{1k} \left[\cos\varphi\, \hat{I}_{kx} + \sin\varphi\, \hat{I}_{ky}\right] \tag{2.117}$$

where the unitary transformation superoperator is given by:

$$\hat{\hat{U}}(t) = \exp\left(-\mathrm{i}\omega_{\mathrm{rf}} t \hat{\hat{I}}_z\right) \tag{2.118}$$

The transformation of the density operator and the Liouville-von Neumann equation are performed in Appendix E in detail. The resulting relationships are:

$$\hat{\hat{\rho}}(t) = \hat{\hat{U}}^{-1}(t)\, \hat{\rho}(t) \tag{2.119}$$

$$\frac{\partial}{\partial t} \hat{\hat{\rho}}(t) = -\mathrm{i} \left[\hat{\hat{H}}(t) - \omega_{\mathrm{rf}} \hat{I}_z, \hat{\hat{\rho}}(t)\right] \tag{2.120}$$

The indirect spin-spin coupling, mediated by electrons, bilinear in the spin operators, is described by [10]:

$$\hat{H}_J = 2\pi \sum_{k<l} \hat{\mathbf{I}}_k \mathbf{J}_{kl} \hat{\mathbf{I}}_l \tag{2.121}$$

where only the isotropic part J_{kl} of the spin-spin coupling tensor $\mathbf{J}_{kl}$ is retained:

$$\hat{H}_J \approx 2\pi \sum_{k<l} J_{kl}\, \hat{\mathbf{I}}_k \cdot \hat{\mathbf{I}}_l \approx 2\pi \sum_{k<l} J_{kl}\, \hat{I}_{kz} \hat{I}_{lz} \tag{2.122}$$

The first sum in (2.122) holds generally, while the second approximate expression is valid for weakly coupled spin pairs. The factor 2 belongs to the product of the two spin operators, and the factor π arises due to a convention of expressing J_{kl} in Hz.

The intramolecular direct dipolar (DD) interaction between the nuclear angular moments is given by [10]:

$$\hat{H}_{\mathrm{DD}} = \sum_{k<l} b_{kl} \left(\hat{\mathbf{I}}_k \cdot \hat{\mathbf{I}}_l - \frac{3(\hat{\mathbf{I}}_k \cdot \boldsymbol{r}_{kl})(\hat{\mathbf{I}}_l \cdot \boldsymbol{r}_{kl})}{|r_{kl}|^2} \right), \; b_{kl} = -\frac{\mu_0}{4\pi} \frac{\gamma_k \gamma_l \hbar}{r_{kl}^3} \tag{2.123}$$

where b_{kl} is the dipolar coupling constant in SI units. In solution NMR of isotropic liquids, the dipolar contribution is neglected, except when relaxation is considered.

The quadrupolar interaction is quadratic in the spin operators:

$$\hat{H}_{\mathrm{Q}} = \sum_{k=1}^{N} \hat{\mathbf{I}}_k \boldsymbol{Q}_k \hat{\mathbf{I}}_k \tag{2.124}$$

where $\boldsymbol{Q}_k$ is the quadrupolar coupling tensor:

$$\boldsymbol{Q}_k = \frac{eQ_k}{2I_k(2I_k - 1)\hbar} \boldsymbol{V}_k \tag{2.125}$$

Q_k is the nuclear quadrupolar moment and $\boldsymbol{V}_k$ is the electric field gradient at the site of the nucleus. The quadrupolar interaction exists only for nuclei with spins $I > 1/2$. Nevertheless, it causes scalar relaxation of the second kind, mentioned in Section 5.2.

To summarize, the total rotating-frame Hamiltonian, which is valid for coupled spins-1/2 in solution NMR of isotropic liquids, has the form:

$$\hat{\hat{H}} = \hat{\hat{H}}_{\mathrm{Z}} + \hat{\hat{H}}_{\mathrm{rf}} + \hat{H}_J \tag{2.126}$$

where $\hat{\hat{H}}_{\mathrm{Z}}$, $\hat{\hat{H}}_{\mathrm{rf}}$ and $\hat{H}_J$ are given by Eqs. (2.116), (2.117) and (2.122), respectively.

Chapter 3

Nuclear Singlet States

3.1 Singlet and Triplet States

Compared to well-known electronic singlet states, nuclear singlet states were relatively neglected by NMR spectroscopists from the very beginning of the nuclear physics and quantum mechanics. It appeared in experiments with hydrogen (H_2) gas only during 1980's [38]. When H_2 was used during hydrogenation reaction, an unexpected SNR enhancement was detected by means of NMR with a characteristic anti-phase peak patterns [39, 40]. The signal intensity increased with increasing duration of hydrogenation and decreasing sample temperature. However, since the hydrogenation was catalyzed by transition metal ions, which provide unpaired electrons, the experiments were included in the family of Chemically Induced Dynamic Nuclear Polarization (CIDNP) methods [41–44]. Fortunately, the role of para-H_2 was revealed soon, which led to development of new techniques for the NMR signal enhancement called Parahydrogen Induced Polarization (PHIP) [45], see Section 3.3.

Except for observation, all para-H_2 experiments managed without any NMR intervention. The nuclear singlet state was believed to be an exclusive property of H_2 and other extraordinary symmetric molecules such as H_2O in a fullerene cage, which was proven experimentally much later [46]. In 2004, Professor Levitt and his coworkers Dr. Carravetta and O. G. Johannessen succeeded in generating the nuclear singlet state purely by means of NMR [47, 48]. They demonstrated that the singlet state may be produced in other common molecules, too [49, 50].

3.2 Singlet State Properties

The singlet and triplet states, as introduced in Section 2.2.4, are states with the total spin quantum numbers $I = 0$ and 1 and the total magnetic quantum numbers $M_i = 0$ and ± 1:

$$\begin{array}{r|l} \hat{I}_z \left|S_0\right\rangle = 0 & \hat{I}_z \left|T_{M_i}\right\rangle = M_i\hbar \left|T_{M_i}\right\rangle \\ \hat{\boldsymbol{I}}^2 \left|S_0\right\rangle = 0 & \hat{\boldsymbol{I}}^2 \left|T_{M_i}\right\rangle = 2\hbar^2 \left|T_{M_i}\right\rangle \end{array} \tag{3.1}$$

Due to spin zero, the singlet state is nonmagnetic and generates no NMR signal, see Eq. (2.9). The detectable magnetization belongs exclusively to the triplet manifold.

The singlet state is antisymmetric under the spin exchange operation, whereas the triplet states are symmetric. Assume a generalized idempotent permutation operator $\hat{P}_{ij}$, swapping spins at the ith and jth positions, defined as:

$$\hat{P}_{ij} \left|\ldots r_i s_j \ldots\right\rangle = \left|\ldots s_i r_j \ldots\right\rangle \tag{3.2}$$

where $r, s = \{\alpha, \beta\}$. Using definitions of $\left|S_0\right\rangle$ and $\left|T_{M_i}\right\rangle$ from Eq. (2.102), then:

$$\begin{aligned} \hat{P}_{12} \left|S_0\right\rangle &= -\left|S_0\right\rangle \\ \hat{P}_{12} \left|T_{M_i}\right\rangle &= \left|T_{M_i}\right\rangle \end{aligned} \tag{3.3}$$

Once there exists a difference between the singlet state population and the mean population of the triplet manifold (singlet order), a transition between the antisymmetric and symmetric combinations of spins is only possible through processes, which themselves are antisymmetric with respect to the spin exchange. The dominant relaxation process in solution NMR, the intramolecular direct dipolar (DD) relaxation, is exchange-symmetric. This makes the singlet state immune to DD relaxation and causes it to relax slower. In comparison, the triplet manifold equilibrates with the longitudinal relaxation time constant T_1. The singlet state relaxation time constant T_S may be an order of magnitude longer than T_1. An exceptional example is $T_S/T_1 \approx 37$ [51, 52].

The singlet state may only be maintained in the magnetically nearly-equivalent spin system, when $|\Omega_\Delta| \ll |\pi J_{12}|$. Rewriting the Hamiltonian $\hat{H}$ (2.93) in the matrix representation of the singlet-triplet basis gives:

$$\hat{H} = \frac{1}{2} \begin{array}{cc} \begin{array}{cccc} \left|S_0\right\rangle & \left|T_{+1}\right\rangle & \left|T_0\right\rangle & \left|T_{-1}\right\rangle \end{array} & \\ \begin{pmatrix} -3\pi J_{12} & 0 & \Omega_\Delta & 0 \\ 0 & \Omega_\Sigma + \pi J_{12} & 0 & 0 \\ \Omega_\Delta & 0 & \pi J_{12} & 0 \\ 0 & 0 & 0 & -\Omega_\Sigma + \pi J_{12} \end{pmatrix} & \begin{array}{c} \left\langle S_0\right| \\ \left\langle T_{+1}\right| \\ \left\langle T_0\right| \\ \left\langle T_{-1}\right| \end{array} \end{array} \tag{3.4}$$

The nondiagonal elements between the singlet $|S_0\rangle$ and the central triplet $|T_0\rangle$ states depend on the magnetic field strength and the chemical shift difference. In the case of magnetic (near-)equivalence, they may be neglected. If $|\Omega_\Delta| \gtrsim |\pi J_{12}|$, such elements cause mixing of the populations of these states, and therefore relaxation of the populations. This fast relaxation precludes possible observation of the singlet state.

3.3 Singlet State Experiments

Experiments using singlet states as a probe into the micro-world are based on intentional imposing or breaking of the exchange symmetry of the coupled nuclear sites, i.e., switching magnetic equivalence or inequivalence of the nuclear environments. Feasible techniques for doing this are magnetic field cycling, high-field techniques, and chemical reactions [49, 50].

3.3.1 Field-Cycling

Magnetic-field cycling is a subject of the first submitted paper on the singlet state prepared purely by means of NMR [48]. As an inspiration served the para-H_2 experiment ALTADENA [53], described in Section 3.3.3. Initially the weakly-coupled spin pair is transformed into the strongly-coupled one by moving a sample from high field B_{HF} of several tesla within the spectrometer to low field B_{LF} of order of millitesla (or less) at a certain position outside the magnet. Such a low field is a superposition of a stray field from the spectrometer underneath, which is directionally and temporally constant, and other magnetic fields from surrounding wirings and appliances, which may vary.

The current experimental setup is shown in Figure 3.1. A sample tube is fixed in a sample holder, which is attached to a string. A stepper motor drives a winch and lifts the sample up and down. The whole transport is controlled by a spectrometer console and synchronized with a corresponding pulse sequence.

When the sample is inserted into the spectrometer field, the equilibrium magnetization builds up. Subsequently, a precursor state, denoting a nonequilibrium population of energy levels, may be prepared by using a sequence of rf pulses (PS1). Transport between the two positions proceeds adiabatically. This means that the magnetic field change is slow enough that both the energy levels and their populations follow steadily. The correspondence

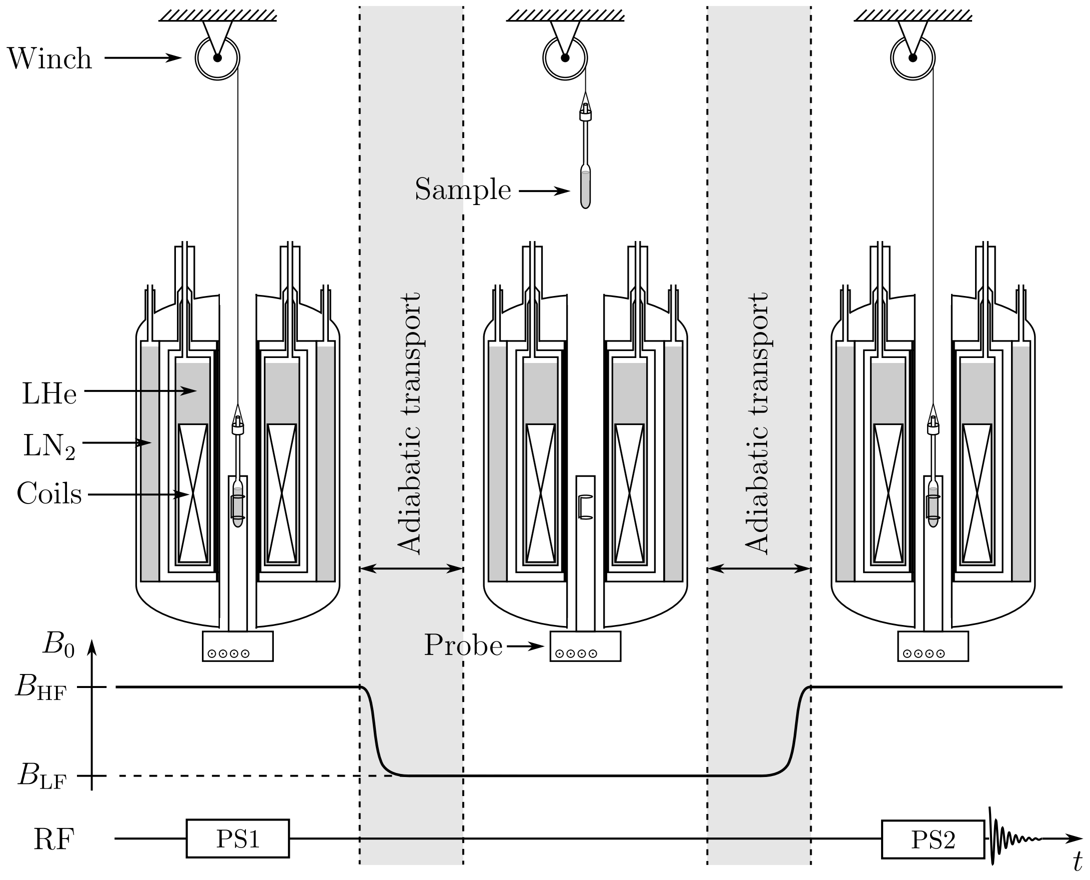

Figure 3.1: The magnetic-field cycling experiment. An initially weakly-coupled spin pair in high field (left) becomes strongly-coupled in low field (centre). The transport between the different magnetic fields is adiabatic. The high-field populations smoothly transform into the low-field populations. After relaxation in the low field, the sample is returned back into the spectrometer for observation (right).

between the high-field and low-field states is given by [53]:

$$\mathrm{sign}J_{12} = \mathrm{sign}(\Omega_1 - \Omega_2): \ |\alpha\alpha\rangle \leftrightarrow |T_{+1}\rangle, \ |\alpha\beta\rangle \leftrightarrow |T_0\rangle, \ |\beta\alpha\rangle \leftrightarrow |S_0\rangle, \ |\beta\beta\rangle \leftrightarrow |T_{-1}\rangle \quad (3.5)$$

$$\mathrm{sign}J_{12} \neq \mathrm{sign}(\Omega_1 - \Omega_2): \ |\alpha\alpha\rangle \leftrightarrow |T_{+1}\rangle, \ |\alpha\beta\rangle \leftrightarrow |S_0\rangle, \ |\beta\alpha\rangle \leftrightarrow |T_0\rangle, \ |\beta\beta\rangle \leftrightarrow |T_{-1}\rangle \quad (3.6)$$

After storing the sample in the low-field for a variable time interval, the sample is adiabatically returned back into the spectrometer. Another series of rf pulses (PS2) is immediately applied to the generated post-cursor state, and the NMR signal is detected.

Field-cycling was successfully used to generate singlet state in pairs of ^{1}H [48, 54], ^{13}C [55, 56] and in ^{15}N pairs in the case of doubly labelled $^{15}N_2O$ [57–61]. The theoretical treatment of field-cycling is summarized in [36, 53, 62]. This technique is the main subject of this work and will be treated in detail in Section 7.2.

3.3.2 High-Field Techniques

The high-field techniques may be divided into three distinct groups according to the strength of the in-pair spin-spin coupling. Spin-locking is used in the case of weakly-coupled spin pairs [47]. For nearly-equivalent spins, pulse sequences called M2S and S2M are used to convert magnetization (M) into singlet order (S) and vice versa [56, 59, 63–67]. Once the singlet order is generated, it lives for extended time intervals in high field without any other pulse sequence. Finally, experiments with more than two spins-1/2 exist, where the singlet state was successfully produced, maintained and observed [68–70].

3.3.2.1 Spin-Locking Technique

The spin-locking experiment, as shown in Figure 3.2, is based on the transformation of the initial longitudinal magnetization $\hat{\rho}_1 \propto \hat{I}_z$ into a zero-quantum coherence, by using a sequence of rf pulses and delays proportional to the spin-spin coupling J_{12}:

$$\hat{\rho}_2 \propto \hat{I}_1^+ \hat{I}_2^- + \hat{I}_1^- \hat{I}_2^+ \iff |T_0\rangle\langle T_0| - |S_0\rangle\langle S_0| \tag{3.7}$$

Adiabatic transport into and storage in the low field is replaced by continuous rf irradiation (spin-locking) with the carrier frequency at the mean of the resonance offsets of the two sites. The case, in which the carrier frequency is different from the mean offset was studied theoretically as well [71].

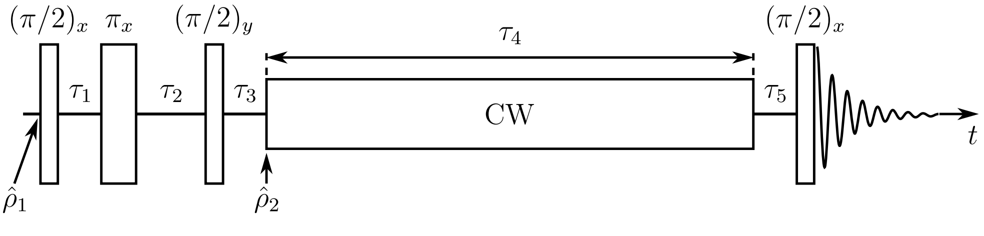

Figure 3.2: The high-field spin-locking singlet experiment. The description is in the text. Adapted from [47].

Spin-locking suppresses chemical shift differences. The Zeeman Hamiltonian in the rotating frame vanishes and $\hat{H} \approx \hat{H}_J$. In the original work [47], the authors used unmodulated (continuous-wave, CW) rf field, for which the amplitude and phase of the rf field are constant. Several other sequences, which are used in broadband decoupling, were exploited later, too [72]. At the end of the storage interval τ_4, the remaining population distribution is converted into an observable signal.

A key point in the spin-locking experiment is that the zero-quantum coherences (3.7) remain intact under the CW irradiation, if relaxation is neglected. In addition, the singlet state is immune to DD relaxation. As long as the nutation frequency $\tilde{\omega}$ of the spin-locking field is much bigger than the difference of the resonance offsets of the two spin sites Ω_Δ, CW irradiation gives similar results as other decoupling sequences. When $\tilde{\omega} \lesssim \Omega_\Delta$, either due to the capabilities or the power-load restrictions of the spectrometer, or due to the large chemical shift difference Ω_Δ of the sites, special decoupling sequences using rf modulation schemes give better results [72]. Otherwise, the field-cycling experiment is a possible alternative.

Advanced experiments, using various decoupling pulse sequences, were studied by Sarkar [51, 73] in order to maintain the singlet state in more complex molecules such as proteins. These methods extended several existing experiments, as discussed in Section 3.4, and became the basis for follow-up works in the Levitt and Bodenhausen groups, some of which are cited below.

3.3.2.2 M2S-S2M Pulse Sequences

The schemes described in the previous sections work well for spin systems, which are rather weakly coupled in the high field. However, strongly coupled or nearly equivalent spins remained almost intact due to their inaccessibility, until the pulse sequences abbreviated as M2S-S2M, appeared [56, 59, 63–66]. M2S and S2M, which is a time-reversed version of M2S, consist of J-synchronized echo trains, see Figure 3.3. Refocusing π-pulses are replaced by composite pulses [74–77] in order to better compensate for possible pulse imperfections.

The principle of the M2S sequence is the following [63]. The first $(\pi/2)_y$ pulse converts

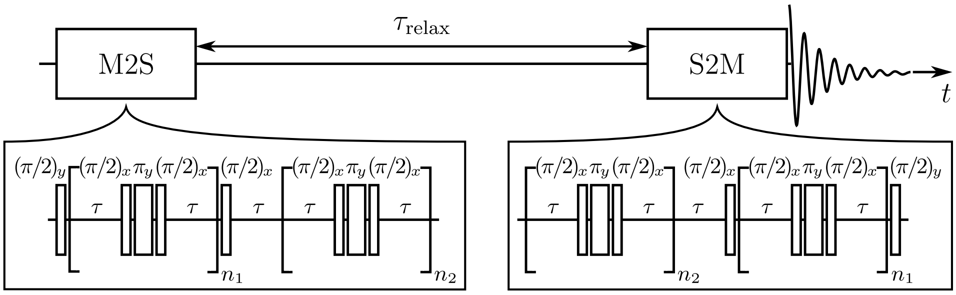

Figure 3.3: The M2S-S2M sequence. The description is in the text. Adapted from [63].

the initial thermal-equilibrium population:

$$\hat{I}_z = |\alpha\alpha\rangle\langle\alpha\alpha| - |\beta\beta\rangle\langle\beta\beta| = |T_{+1}\rangle\langle T_{+1}| - |T_{-1}\rangle\langle T_{-1}| \tag{3.8}$$

into coherences between the triplet states:

$$\hat{I}_x = |T_{+1}\rangle\langle T_0| + |T_0\rangle\langle T_{+1}| + |T_{-1}\rangle\langle T_0| + |T_0\rangle\langle T_{-1}| \tag{3.9}$$

Such coherences are progressively transformed into coherences between the singlet and outer triplet states by the train of n_1 composite π-pulses, which are separated by time intervals τ:

$$\hat{I}_{1y} - \hat{I}_{2y} = \mathrm{i}\left(|T_{+1}\rangle\langle S_0| + |S_0\rangle\langle T_{+1}| - |T_{-1}\rangle\langle S_0| - |S_0\rangle\langle T_{-1}|\right) \tag{3.10}$$

The constants n_1 and τ are defined in the following way:

$$2n_1\Theta \approx \pi \tag{3.11}$$

$$\tau = \frac{\pi}{2}\frac{1}{\sqrt{(2\pi J)^2 + (\Omega_\Delta)^2}} \approx \frac{1}{4J} \tag{3.12}$$

where Θ and Ω_Δ are the mixing angle and the difference of the resonance offsets given by Eqs. (2.94) and (2.99), respectively.

The $(\pi/2)_x$ pulse results in another coherence between the singlet and central triplet states:

$$\hat{I}_{1z} - \hat{I}_{2z} = \mathrm{i}\left(|T_0\rangle\langle S_0| + |S_0\rangle\langle T_0|\right) \tag{3.13}$$

Finally, the the second train of $n_2 = n_1/2$ composite π-pulses converts the coherence (3.13) into the singlet and central triplet population difference:

$$\mathrm{i}\left(|S_0\rangle\langle S_0| - |T_0\rangle\langle T_0|\right) \tag{3.14}$$

After a storage time τ_{relax}, during which the spin order relaxes, the S2M sequence is applied to transform the remaining population distribution into observable magnetization.

Originally, the M2S-S2M sequence was tested in combination with the field-cycling experiment, during the low-field storage interval [59]. Later, the sequence was shown to be useful also in high field, which is the case in Figure 3.3. Application in MRI followed afterwards [64]. Especially with respect to modern MRI methods, the M2S-S2M sequence together with molecular engineering, which may design and supply a water-soluble bio-compatible molecule, containing the nearly-equivalent spin-1/2 pairs, offers superior possibilities over the field cycling method with $^{15}N_2O$.

Finally, magnetic field gradients and an extra $(\pi/2)_y$ pulse were inserted between the M2S and S2M blocks in order to filter out possible single-quantum coherences after the non-ideal M2S sequence, and partially recovered longitudinal magnetization after the storage interval [66].

3.3.2.3 Singlet State in Multinuclear Systems

Several experiments were performed, in which the singlet state was prepared in the vicinity of other coupled spin-1/2 nuclei [68–70]. Due to slightly different chemical shifts and nonnegligible spin-spin couplings, the extra nuclei served as a means for breaking the magnetic equivalence of the nuclear pair environments.

Theoretical study together with experimental results suggested that the nuclear singlet state is not a “collective” state of several nuclei. It is rather localized at a certain pair of nuclei [70, 78–80]. Also a role of spin-spin coupling between the paired nuclei was revealed to be a mechanism stabilizing the singlet state against the action of other out-of-pair coupled nuclei [81].

3.3.3 Symmetry Switching by Chemical Reaction

The main representatives of this group are para-H_2 experiments. Naturally occurring hydrogen consists of three nuclear isotopes with the mass number $A = \{1, 2, 3\}$: light ^{1}H, heavy ^{2}D (deuterium) and super-heavy ^{3}T (tritium) hydrogens. All three isotopes create diatomic molecules, where both atoms may be the same or different. Experimentally, para-H_2 itself is known only in cases of $^1H_2$ and $^2D_2$. The mixed molecules do not create states with spin zero either due to large differences in magnetogyric ratios or due to the spin-1 of deuterium. ^{3}T has, in addition, a very low natural abundance ($A_N = 0.115(7)$ ‰) and is radioactive (β^-, $T_{1/2} = 12.32(2)$ yr) [4]. Despite all the drawbacks, if ^{3}T is used for NMR investigation, it provides high SNR spectra with sharp lines, which are free of the natural background [82, 83].

^{1}H atoms in the naturally most abundant H_2 molecule may combine to the states with nuclear spin $I = 0$ (para-H_2) and $I = 1$ (ortho-H_2). Due to the $(2I + 1)$-fold energy level degeneracy, the ratio of para-H_2 vs. ortho-H_2 equals 1:3 at high temperatures. The state with the lowest energy, and the most abundant one at temperatures below 77 K, is para-H_2. On the contrary, in the case of ^{2}D, ortho-D_2 includes states with spin $I = \{0, 2\}$, while para-D_2 is the spin-1 state. The state with the lowest energy is ortho-D_2. In the absence of any relaxation centre, both para- and ortho-states coexist in the gas phase as two distinct species for months [84]. The interconversion is mediated by molecular collisions, or by contact with paramagnetic solids such as transition metals or activated charcoal [62].

As mentioned in Section 3.1, PHIP methods include several important experiments. Namely "Parahydrogen And Synthesis Allow Dramatically Enhanced Nuclear Alignment" (PASADENA) and "Adiabatic Longitudinal Transport After Dissociation Engenders Net Alignment" (ALTADENA) [38, 85]. 20 years later, "Signal Amplification by Reversible-Exchange" (SABRE) joined the two [86].

PASADENA was first predicted theoretically [87]. Soon, it was proved experimentally by two independent groups. In the true PASADENA experiment [88], a sample containing unsaturated bonds was bubbled with the para-H_2 enriched H_2 gas within the spectrometer field and subsequently observed. In the para-H_2 CIDNP experiment [89], the sample, initially stored at the liquid nitrogen temperature, was then melted and shaken with the introduced para-H_2 rich H_2 gas in the laboratory magnetic field, and quickly inserted into the spectrometer. The two para-H_2 protons are transferred pairwise into magnetically inequivalent sites, still maintaining a resolved scalar coupling J_{HH}. Hydrogenation has to proceed faster than the T_1 of the product molecule.

PASADENA was used, e.g., for a detailed investigation of kinetics and mechanisms of several hydrogenation reactions, where para-H_2 served as a spin label. Extensions for probing chemical exchange processes and mapping of coupling connectivities exist [62]. Using either the INEPT sequence [90] or para-H_2 labeling [91], hyperpolarization resulting from para-H_2 may be transferred to other hetero-nuclei with a lower magnetogyric ratio, and further increase their SNR.

Although a sort of field-cycling had already been used during the para-H_2 CIDNP experiments [45, 89], it remained overlooked. However, the transport between the low and high magnetic fields, with emphasis on the transfer adiabaticity, became the basis for the ALTADENA method [53]. The energy eigenstates and the population distribution of the spin-system in the laboratory field right after hydrogenation differ from the final states, when hydrogenation takes place entirely in high field. Adiabatic transport into the spectrometer field assures nearly lossless transformation of the low-field populations into the high field nonequilibrium population distribution, which can readily be detected. The acronym of the method comes from the net aligned FT spectra containing no anti-phase peaks compared to PASADENA.

The SABRE method is based on hyperpolarization transfer from para-H_2, mediated through a labile complex formed from the substrate molecule, transition-metal carrier and para-H_2. Para-H_2 is introduced and the polarization transfer proceeds in low magnetic field. The complex lives long enough, so that the substrate may be polarized, but decomposes again to its initial components. The whole process may be regenerated by just adding fresh para-H_2 enriched gas. The signal enhancement may be transferred to other NMR isotopes [86].

One important non-para-H_2 case is worth noting, where a chemical reaction is used for breaking the exchange-symmetry. Warren reported reversible generation of singlet states in ^{13}C doubly-labelled diacetyl by dehydration (singlet state) and rehydration (triplet state) [92].

3.4 Singlet State Applications

The singlet state has mostly been exploited in NMR experiments, which study processes over extended time scales, but which are limited by fast T_1 relaxation. However, the search for a molecule, which displays high T_S/T_1 ratio, and ideally has other promising characteristics, is itself a topic.

Singlet NMR methods were successfully used to measure various molecular properties. The original Diffusion Ordered Spectroscopy (DOSY) [93], which observes spin echoes stimulated by pulsed field gradients in order to determine diffusion coefficients of individual components of a sample, was improved by combining with the spin-locking sequence [94–97]. In a similar way was upgraded the EXchange SpectroscopY (EXSY) [98], which is a two-dimensional method for monitoring chemical exchange processes [51, 73].

Tayler used singlets to get insight into the geometry of small molecules [52]. He used an example of a phenylalanine isotopologue to demonstrate that a torsional angle around a C−C bond influences the singlet relaxation rate of two diastereotopic protons in a CH_2 group. In a similar manner, the dynamics of protein unfolding was observed by measuring the singlet state relaxation of different conformers, otherwise hardly sensed by routine T_1/T_2 relaxation measurements [99]. Recently, singlet states were also used for the exploration of ligand-protein interactions [100].

Low sensitivity is an inherent feature of NMR. Therefore many methods were developed to increase it as much as possible. Especially in medical applications, common techniques as, e.g., Dynamic Nuclear Polarization (DNP) [101], see also Section 4.3.1, are inapplicable due to the sensitivity of living tissues to temperatures and the use of microwaves. Only in 2003, a method called dissolution-DNP overcame such obstacles [102]. Nonetheless, despite of the enormous levels of enhancement by four orders of magnitude, hyperpolarized spin order decays quickly due to the radical content of the sample, which is essential for the successful hyperpolarization, or due to a short T_1 value and field-dependent relaxation. The singlet state is capable of storing the hyperpolarized spin order and therefore maintain the very strong signal for prolonged time intervals [54, 55, 103, 104].

Concretely, the singlet state has already been exploited during the veterinary [64], as well as medical [105] MRI examination. An exceptional example represents the singlet state in dissolved, ^{15}N doubly-labelled $^{15}\mathrm{N}_2\mathrm{O}$. Its $T_\mathrm{S} \approx 26$ min and $T_\mathrm{S}/T_1 \approx 8$ ($\underline{^{15}\mathrm{N}}{}^{15}\mathrm{NO}$) or 14 ($^{15}\mathrm{N}\underline{^{15}\mathrm{N}}\mathrm{O}$), when dissolved in degassed and perdeuterated DMSO, and $T_\mathrm{S} \approx 7$ min and $T_\mathrm{S}/T_1 \approx 20$ ($^{15}\mathrm{N}\underline{^{15}\mathrm{N}}\mathrm{O}$), when dissolved in blood, makes it a fairly realistic candidate for use as a MRI tracer [57, 60, 106].

In material sciences, the singlet state has allowed measurement of restricted diffusion during investigations of macroscopic pores in different materials [107]. Last but not least is the application of singlet states in quantum computing [108–113].

A special family of singlet-state related experiments includes methods exploiting the long-lived singlet-triplet coherent superposition (long-lived coherence, LLC) [114–116]:

$$Q_\mathrm{LLC} = \hat{I}_{kx} - \hat{I}_{lx} = |S_0\rangle\langle T_0| + |T_0\rangle\langle S_0| \tag{3.15}$$

The Q_LLC coherence NMR signal intensity evolves according to [114]:

$$\frac{\mathrm{d}}{\mathrm{d}t} Q_\mathrm{LLC} = -\left(\mathrm{i}2\pi J_{kl} + R_\mathrm{LLC}\right) Q_\mathrm{LLC} \tag{3.16}$$

where R_LLC is the relaxation rate constant. On the one hand, the FT spectrum displays very sharp peaks, since their FWHM is proportional to R_LLC. On the other hand, the positions of the spectral peaks are determined by J_{kl} values, which can be determined with very high precision.

LLCs were used in combination with signal-enhancing dissolution-DNP [117], or for refinement of COrrelation SpectroscopY (COSY) [118]. The LLC-COSY boosts ordinary COSY performance since LLCs overcome both the homogeneous and the inhomogeneous broadenings of the peaks. This results in ultrahigh resolution spectra with sub-Hz linewidths [119]. The LLC experiments, mentioned so far, took place in the spectrometer magnetic field of several tesla. An example exists, preceding these mentioned above, which was performed in extremely low magnetic field around 1 mT, as well [58].

Chapter 4

Fourier Transform Spectroscopy

Since its invention, NMR spectroscopy was practised as the so-called continuous wave (CW) spectroscopy. Absorption of electromagnetic radiation was recorded as a function of magnetic field, and the whole spectrum range was gradually scanned through. Besides its unique resolution power and accuracy, the main drawbacks were (and often still are) the high time cost of experiments and data evaluation, and limited sensitivity. In 1966, Fourier transform (FT) NMR was introduced [120], which alleviated the time expenditure and further increased the resolution. In parallel with NMR, FT spectroscopy became very popular as a means for electron paramagnetic resonance (EPR), and since 1969, also in optical infrared spectroscopy (FT-IR) [121].

In FT-NMR, the whole spin system is excited at once by rf pulses, which may last from a fraction of microsecond up to hundreds of milliseconds, depending on the specific purpose. Subsequently, de-excitation (relaxation) towards equilibrium is observed. The time-varying signal generated by the macroscopic nuclear magnetization is acquired and digitized. Spectral information is subsequently extracted either from the time-domain signal or from the frequency-domain spectrum after FT. Compared to sweeping for minutes through the whole spectrum, an experiment may be repeated after several T_1 intervals. This allows a sensitivity increase by, e.g., signal averaging described in Section 4.3.2, if T_1 is sufficiently short. FT-NMR becomes less advantageous, compared to high-resolution CW-NMR, for high values of the T_1/T_2^* ratio [120, 122].

4.1 Fourier Transformation

Fourier transformation (FT) is used for interconversion of the time-domain, $s(t)$, and frequency-domain, $S(f)$, signals. Both domains provide the same information, only in a different form. The time domain is preferably used for the signal acquisition and manipulations. The frequency domain serves for reading the spectroscopic information.

Forward FT, $\mathcal{F}$, maps from the time to the frequency domain [2]:

$$\begin{aligned} \mathcal{F}\{s(t)\} &= \int_{-\infty}^{\infty} \mathrm{d}t\, s(t)\, \mathrm{e}^{-\mathrm{i}\omega t} \equiv S(\omega) \\ &= \int_{-\infty}^{\infty} \mathrm{d}t\, s(t)\, \mathrm{e}^{-\mathrm{i}2\pi f t} \equiv S(f) \end{aligned} \tag{4.1}$$

where $\omega = 2\pi f$. The inverse or backward FT, $\mathcal{F}^{-1}$, is defined as:

$$\begin{aligned} s(t) &= \frac{1}{2\pi} \int_{-\infty}^{\infty} \mathrm{d}\omega\, S(\omega)\, \mathrm{e}^{\mathrm{i}\omega t} \equiv \mathcal{F}^{-1}\{S(\omega)\} \\ &= \int_{-\infty}^{\infty} \mathrm{d}f\, S(f)\, \mathrm{e}^{\mathrm{i}2\pi f t} \equiv \mathcal{F}^{-1}\{S(f)\} \end{aligned} \tag{4.2}$$

FT is the linear mapping. As such, it obeys several important properties, which result from its definition [2, 10]:

Similarity theorem: $$\mathcal{F}\{s(at)\} = \frac{1}{|a|} S\left(\frac{f}{a}\right) \tag{4.3}$$

Time shift theorem: $$\mathcal{F}\{s(t-t_0)\} = \mathrm{e}^{-\mathrm{i}2\pi f t_0}\, S(f) \tag{4.4}$$

Frequency shift theorem: $$\mathcal{F}^{-1}\{S(f-f_0)\} = \mathrm{e}^{\mathrm{i}2\pi f_0 t}\, s(t) \tag{4.5}$$

Derivative theorem: $$\mathcal{F}\left\{\frac{\mathrm{d}^k}{\mathrm{d}t^k} s(t)\right\} = (\mathrm{i}2\pi f)^k\, S(f) \tag{4.6}$$

Convolution theorem: $$\mathcal{F}\{s_1(t) * s_2(t)\} = S_1(f)\, S_2(f) \tag{4.7}$$

$$\mathcal{F}^{-1}\{S_1(f) * S_2(f)\} = s_1(t)\, s_2(t) \tag{4.8}$$

Parseval's theorem: $$\int_{-\infty}^{\infty} \mathrm{d}t\, |s(t)|^2 = \int_{-\infty}^{\infty} \mathrm{d}f\, |S(f)|^2 \tag{4.9}$$

The asterisk denotes the convolution of two functions:

$$r(t) * s(t) = \int_{-\infty}^{\infty} \mathrm{d}\tau\, r(\tau)\, s(t-\tau) = \int_{-\infty}^{\infty} \mathrm{d}\tau\, r(t-\tau)\, s(\tau) \tag{4.10}$$

All digital signals are discrete, for which the discrete FT, $\mathcal{F}_\mathrm{d}$, is suited [2]:

$$S_k = \mathcal{F}_\mathrm{d}\{s_j\} = \sum_{j=0}^{N-1} s_j\, \mathrm{e}^{-\mathrm{i}2\pi jk/N} \tag{4.11}$$

where:

$$\begin{aligned} s_j &\equiv s(j\Delta t) &\iff& \quad s(t) \\ S_k &\equiv S\left(\frac{k}{N\Delta t}\right) &\iff& \quad S(f) \end{aligned} \tag{4.12}$$

N is the number of complex points (acquisition length), Δt is the sampling interval (dwell time), and $k = \{-N/2, \ldots, 0, \ldots, N/2\}$. The inverse discrete FT, $\mathcal{F}_{\mathrm{d}}^{-1}$, is given by:

$$s_j = \mathcal{F}_{\mathrm{d}}^{-1}\{S_k\} = \frac{1}{N} \sum_{k=0}^{N-1} S_k \mathrm{e}^{\mathrm{i}2\pi jk/N} \tag{4.13}$$

The frequency spectrum spans between $-1/(2\Delta t)$ and $1/(2\Delta t)$. The frequency steps are given by $\Delta f = 1/(N\Delta t)$.

In the case that $N = 2^n$, where n is an integer, the so-called fast Fourier transform (FFT) is conveniently used. Its basis was laid by Gauss [123] and rediscovered by Cooley and Tukey 160 years later [124, 125]. Compared to the discrete FT, which scales as N^2, the FFT scales as $N \log_2 N$, which is much faster for large N [126].

4.2 Signal versus Noise

NMR spectroscopy may be described by linear time-invariant (LTI) system theory [10, 127], see the scheme in Figure 4.1. Linearity means that the output is a linear function of the input, and time invariance denotes that the system acts on a given input signal in exactly the same way at any time. The relationship between the time-domain, $x(t)$, and frequency-domain, $X(f)$, input signals and the corresponding output signals $s(t)$ and $S(f)$ in the case of LTI system is given by a convolution (4.10) with the system impulse response, $h(t)$, or frequency transfer function, $H(f)$, respectively:

$$s(t) = x(t) * h(t) = kx(t - t_0) \tag{4.14}$$

$$S(f) = X(f) * H(f) = kX(f)\mathrm{e}^{-\mathrm{i}2\pi f t_0} \tag{4.15}$$

where k and t_0 are constants.

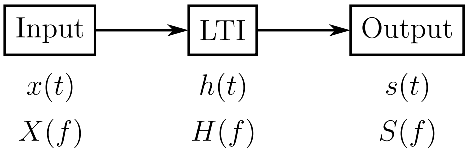

Figure 4.1: Scheme of the linear time-invariant system. Adapted from [127].

Real experimental signals, $r(t)$, are always accompanied by noise, $n(t)$:

$$r(t) = s(t) + n(t) \tag{4.16}$$

While the pure signal $s(t)$ is deterministic, the noise $n(t)$ is usually considered as stochastic.

Assume a free-induction NMR signal generated by a single (−1)-quantum coherence in a general form [2]:

$$s(t) = \begin{cases} s_0 \exp[(\mathrm{i}\Omega - \lambda)(t + t_0) + \mathrm{i}\phi_0] & \text{for } 0 \leq t \leq t_{\mathrm{acq}} \\ 0 & \text{otherwise} \end{cases} \tag{4.17}$$

where s_0 is the signal amplitude, $\Omega\,(\mathrm{rad\,s^{-1}}) = 2\pi \times f\,(\mathrm{Hz})$ is the resonance offset, $\lambda = 1/T_2^*$ is the decay rate constant, t_0 is the acquisition delay, and ϕ_0 is the initial instrumental phase. Limiting the signal to times $t \geq 0$ makes it causal. The corresponding form of a digitized discrete NMR signal for $t \geq 0$ is:

$$s_j = s_0 \exp[(\mathrm{i}\Omega - \lambda)(j\Delta t + t_0) + \mathrm{i}\phi_0] \tag{4.18}$$

comprising N complex points evenly spaced by Δt time intervals. The spacing of the points in the time domain determines the bandwidth W of the frequency-domain spectrum after discrete FT. The bandwidth equals $W = 1/\Delta t$. The total acquisition time of the time-domain signal gives the spacing of the points in the frequency-domain spectrum (spectral resolution) $\Delta f = 1/(N\Delta t)$.

The forward FT of the time-domain signal (4.17) leads to:

$$S(\omega) = s_0 \exp[(\mathrm{i}\Omega - \lambda)t_0 + \mathrm{i}\phi_0]\,\mathcal{L}(\omega; \Omega, \lambda) \tag{4.19}$$

where:

$$\mathcal{L}(\omega; \Omega, \lambda) = \frac{1}{\lambda + \mathrm{i}(\omega - \Omega)} \tag{4.20}$$

$\mathcal{L}(\omega; \Omega, \lambda)$ is the complex Lorentzian function, centered at Ω with FWHM proportional to λ. Its real part, $\mathcal{A}(\omega; \Omega, \lambda)$, is an absorption Lorentzian, and the imaginary part, $\mathcal{D}(\omega; \Omega, \lambda)$, is a dispersion Lorentzian:

$$\mathcal{A}(\omega; \Omega, \lambda) = \mathrm{Re}[\mathcal{L}(\omega; \Omega, \lambda)] = \frac{\lambda}{\lambda^2 + (\omega - \Omega)^2} \tag{4.21}$$

$$\mathcal{D}(\omega; \Omega, \lambda) = \mathrm{Im}[\mathcal{L}(\omega; \Omega, \lambda)] = \frac{(\Omega - \omega)}{\lambda^2 + (\Omega - \omega)^2} \tag{4.22}$$

The symmetric absorption Lorentzian (4.21) is the conventional NMR lineshape. Its FWHM is equal to:

$$2\lambda = \frac{2}{T_2^*}\ (\text{in rad\,s}^{-1}) \quad \text{or} \quad \frac{2\lambda}{2\pi} = \frac{1}{\pi T_2^*}\ (\text{in Hz}) \tag{4.23}$$

The dispersion Lorentzian (4.22) is used as the primary lineshape in EPR, and 2λ corresponds to the distance between the maximum and minimum of $\mathcal{D}(\omega; \Omega, \lambda)$.

The noise arises mainly from the thermal motion of electrons in the NMR probe circuits. It is represented by a so-called additive white Gaussian noise (AWGN). AWGN is described by a random function n with the values characterized by the Gaussian probability density function $p(n)$ with zero mean and a given variance σ^2 at an arbitrary time t [127]:

$$p(n) = \frac{1}{\sigma\sqrt{2\pi}} \exp\left(-\frac{n^2}{2\sigma^2}\right) \tag{4.24}$$

The power spectral density of the noise $G_n(f)$ is the same for all frequencies f in the interval of interest $f_l < f < f_u$, where $W = f_u - f_l$:

$$G_n(f) = \begin{cases} n_0/2 & \text{for } |f| < f_u \\ 0 & \text{otherwise} \end{cases} \tag{4.25}$$

f_l and f_u (often $f_l = -f_u$) are the lower and upper cutoff frequencies, respectively. n_0 is a constant. Since two-sided $G_n(f)$ is uniform, such noise is called white by analogy with white light, where all frequencies in the continuous visible range are equally abundant. The LTI system output, which corresponds to the input $G_n(f)$, is given by:

$$G_N(f) = G_n(f)\,|H(f)|^2 \tag{4.26}$$

The signal-to-noise ratio (SNR) is used as a measure of the signal quality. In terms of NMR, it is defined as the spectral peak amplitude divided by the root-mean-square (RMS) noise amplitude [10]. More generally, it is given by the square root of the ratio of the signal power $P_s(t)$ and the average noise power $\langle P_n \rangle$ at the beginning of the signal acquisition ($t = 0$) [2, 127]:

$$\mathrm{SNR} = \sqrt{\frac{P_s(t)}{\langle P_n \rangle}}\Bigg|_{t=0} = \sqrt{\frac{a^2(t)}{\sigma_0^2}}\Bigg|_{t=0} \tag{4.27}$$

The signal, corresponding to the LTI system output, is given by:

$$a(t) = \int_{-\infty}^{\infty} \mathrm{d}f\, H(f) S(f)\, \mathrm{e}^{\mathrm{i}2\pi f t} \tag{4.28}$$

Using Eq. (4.26), the average noise power equals to:

$$\sigma_0^2 = \int_{-\infty}^{\infty} \mathrm{d}f\, G_N(f) = \frac{n_0}{2} \int_{-\infty}^{\infty} \mathrm{d}f\, |H(f)|^2 \tag{4.29}$$

Therefore, the full expression for the SNR is as follows:

$$\mathrm{SNR} = \sqrt{\left|\int_{-\infty}^{\infty} \mathrm{d}f\, H(f) S(f)\right|^2 \Bigg/ \left(\frac{n_0}{2} \int_{-\infty}^{\infty} \mathrm{d}f\, |H(f)|^2\right)} \tag{4.30}$$

In NMR, the SNR is proportional to the ratio of the induced signal current and the noise current in the detection coil. In terms of the NMR probe and the sample parameters, the SNR is proportional to [128]:

$$\mathrm{SNR} \propto \frac{m^{1/2}\, N\, \gamma_e\, \gamma_d^{3/2}\, B_0^{3/2}\, (B_1/I_\mathrm{c})}{\sqrt{W_\mathrm{r}\left[R_c(T_c + T_a) - R_s(T_s + T_a)\right]}} \tag{4.31}$$

where m is the number of accumulated scans, N is the number of spins, γ_e and γ_d are the magnetogyric ratios of the excited and detected nuclei (often $\gamma_e = \gamma_d$), B_0 and B_1 are the strengths of the static and rf magnetic fields, I_c is the current generated by the rf coil, W_r is the receiver bandwidth, R_c and T_c are the resistance and temperature of the detection coil, R_s is the resistance induced by the sample in the coil, T_s is the sample temperature, and T_a is the noise temperature of the preamplifier.

The sensitivity of the NMR experiment is defined as SNR per square-root unit time [10]. Assume the total time needed to acquire m FID signals:

$$t_\mathrm{tot} = m(t_\mathrm{acq} + t_\mathrm{pd}) \tag{4.32}$$

where the single scan acquisition time is t_acq, and the next scan is repeated only after a pulse delay $t_\mathrm{pd} \geq 3T_1$ in order to restore the thermal-equilibrium longitudinal magnetization. Then the sensitivity $\mathcal{S}$ is given by [10]:

$$\mathcal{S} = \mathrm{SNR} \big/ \sqrt{t_\mathrm{tot}} \tag{4.33}$$

4.3 Methods of Sensitivity Enhancement

4.3.1 Overview of Technical Solutions

Most methods for enhancing the SNR and the sensitivity in NMR are nicely summarized by Eq. (4.31). NMR instrument manufacturers reflect this and push the technology to its edges in the respective directions.

Mainly due to advances in material sciences, spectrometers exploiting still higher static magnetic fields B_0 are produced. The first 23.5 T commercial NMR, operating at 1 GHz ^{1}H frequency built by Bruker, was installed at the Centre de Resonance Magnétique Nucléaire à Très Hauts Champs (CRMN) in Lyon in 2009 [129]. However, with the increasing magnetic field, numerous serious factors need to be considered such as the critical parameters of the innermost coil wire material related to its superconducting state, the total stored energy, size and mass of the system, magnetic shielding, or liquid He consumption

[130–132]. Especially in the case of organic and biological applications, the sample power load and the exposure to strong magnetic fields may have damaging effects [133].

A decrease in the operating temperature of the spectrometer electronics represents another pathway. Cooling down the probe coil (T_c) and the preamplifier (T_a) to the temperature of liquid He substantially reduces electronic noise generated by thermal agitation of charge carriers [128, 134].

A whole group of methods is based on the polarization transfer within a coupled heteronuclear pair. Polarization is transferred from more abundant nuclei S with higher magnetogyric ratio γ_S and large Boltzmann population differences (often ^{1}H) to less abundant nuclei I with a lower magnetogyric ratio γ_I (^{13}C or ^{15}N). An example is a method called "Insensitive Nuclei Enhanced by Polarization Transfer" (INEPT) [135] or its improved version, the "Distortionless Enhancement by Polarization Transfer" (DEPT) [136]. Polarization is transferred by using spin echoes and time delays proportional to the inverse of the scalar coupling J_{IS}. The signal enhancement is given by γ_S/γ_I independent of any relaxation mechanism, except for the longitudinal relaxation of the two nuclei.

Finally, the oldest technique of the SNR enhancement, originally developed for polarized target production in nuclear and particle physics, is Dynamic Nuclear Polarization (DNP) [137, 138]. DNP, including Overhauser effect [101, 139, 140], solid effect [141–143], thermal mixing [144–146], and cross effect [147–150], exploits polarization transfer from electrons. To this family of methods belong CIDNP and PHIP, mentioned in Sections 3.1 and 3.3.3, as well as the Spin-Exchange Optical Pumping (SEOP) [151] of noble-gas nuclei such as ^{3}He [152] or ^{129}Xe [153, 154], in a mixture with alkali metal vapours.

4.3.2 Signal Averaging

The principle of the signal averaging [155] is already contained in Eq. (4.31). In the case of the LTI system and AWGN noise, the addition of m scans improves the SNR by a factor of $\sqrt{m}$. The total time needed is given by Eq. (4.32). Such a method is convenient in the case that T_1 is reasonably short ($\lesssim 1$ min).

In the case of nonlinear systems and nonadditive noise, the SNR enhancement may be less than $\sqrt{m}$ [156].

4.3.3 Matched Filter

The matched filter (MF), initially called the North filter [157], was designed to provide the maximum SNR at the LTI system output for a noisy input signal of a form (4.16). As is apparent from Eq. (4.30), either the frequency transfer function $H(f)$ or the corresponding impulse response $h(t)$, are the candidates for optimization. Application of Schwartz's inequality [127]:

$$\left|\int_{-\infty}^{\infty} \mathrm{d}x\, f(x)g(x)\right|^2 \leq \int_{-\infty}^{\infty} \mathrm{d}x\, |f(x)|^2 \int_{-\infty}^{\infty} \mathrm{d}x\, |g(x)|^2 \tag{4.34}$$

on the numerator of the fraction in Eq. (4.30) gives:

$$\left|\int_{-\infty}^{\infty} \mathrm{d}f\, H(f)S(f)\right|^2 \leq \int_{-\infty}^{\infty} \mathrm{d}f\, |H(f)|^2 \int_{-\infty}^{\infty} \mathrm{d}f\, |S(f)|^2 \tag{4.35}$$

The expression (4.30) for the SNR simplifies to:

$$\mathrm{SNR} \leq \sqrt{\frac{2}{n_0} \int_{-\infty}^{\infty} \mathrm{d}f\, |S(f)|^2} \tag{4.36}$$

The integral in (4.36) represents, according to Eq. (4.9), the energy E of either the time-domain or the frequency-domain input signal. In fact, from:

$$\max(\mathrm{SNR}) = \sqrt{2E/n_0} \tag{4.37}$$

arises that the maximum SNR is given only by the energy of the input signal and the power spectral density of the noise, but not by the particular shape of the input signal.

Taking into account Eqs. (4.4) and (4.28), the optimized transfer function for the input signal at a general time $t = T$, equals to:

$$H_{\mathrm{opt}}(f) = kS^*(f)\,\mathrm{e}^{-\mathrm{i}2\pi fT} \iff h_{\mathrm{opt}}(t) = \begin{cases} ks(T-t) & \text{for } 0 \leq t \leq T \\ 0 & \text{otherwise} \end{cases} \tag{4.38}$$

where k is the proportionality constant. In practice, MF in NMR is taken as a real function, by which the time-domain signal is apodized before FT. It is, therefore, sufficient to take:

$$|H_{\mathrm{opt}}(f)| = kS(f) \iff h_{\mathrm{opt}}(t) = \begin{cases} ks(t) & \text{for } 0 \leq t \leq t_{\mathrm{acq}} \\ 0 & \text{elsewhere} \end{cases} \tag{4.39}$$

The proper MF is given by the scaled version of the output time-domain signal $s(t)$. Further simplification is made by identifying MF with the envelope of $s(t)$. Reference [158] provides an alternative derivation and discussion of the two distinct approaches to

MF used in signal processing on the one hand, Eq. (4.38), and in NMR on the other hand, Eq. (4.39).

Matched filtering is exact for a single resonance but not for a signal comprising multiple resonances. The complex signal is then routinely multiplied by a single exponential filter function derived from the global decay of the signal. Such an exponential apodization increases the SNR of the spectrum, but is no longer equivalent to MF in general.

4.3.4 Noise Reduction by Singular Value Decomposition

Singular Value Decomposition (SVD) is a well established method in Linear algebra [159]. Due to the efforts of Golub [160, 161] and Chan [162], there exist computationally stable and efficient numerical algorithms. SVD is most often used for computing the pseudo-inverse even in ill-conditioned problems, and for solving the majority of least-squares related tasks. It is also widely applied in processing and analysis of diverse acoustic, visual, radar, telecommunication, and bio-electrical signals.

The SVD method has been used in NMR and MRI for the suppression of spectral artefacts or solvent peaks, speeding up the signal acquisition, or the SNR enhancement by reducing the noise contribution [163–169]. Compared to the linear methods used for ordinary NMR signal processing, SVD noise reduction is a nonlinear procedure and is, therefore, accepted less willingly by the NMR community.

Assume a set of n experimental signals $r_i(t)$ of the form (4.16) such as determination of T_1 by inversion recovery. Assume further that each individual signal consists of m discrete, real or complex values, i.e., it is represented by a $m \times 1$ vector $\boldsymbol{r}_i$. The whole set of $\boldsymbol{r}_i$ may be arranged column-wise into a $m \times n$ measurement matrix $\mathbf{A}$:

$$\mathbf{A} = [\boldsymbol{r}_1, \boldsymbol{r}_2, \ldots, \boldsymbol{r}_n] \tag{4.40}$$

An important property of the useful signals $s_i(t)$, represented by $m \times 1$ vectors $\boldsymbol{s}_i$, is that they maintain a certain pattern through all measurements, which at most scales by a real (relaxation) or complex (phase) constant, but which remains unchanged otherwise. The noise n_i, introduced either before the signal digitization (probe or electrical circuits) or afterwards (discretization, truncation errors), is assumed to be AWGN. It is, therefore, possible to approximate the measurement matrix $\mathbf{A}$, which is the noisy version of a signal matrix $\mathbf{S}$:

$$\mathbf{S} = [\boldsymbol{s}_1, \boldsymbol{s}_2, \ldots, \boldsymbol{s}_n] \tag{4.41}$$

by a matrix $\mathbf{A}(k)$ of a lower rank $k < \min(m,n)$. Such a matrix $\mathbf{A}(k)$, conveniently found by SVD, may approximate the signal matrix $\mathbf{S}$ better than the original measurement matrix $\mathbf{A}$. SVD further allows one to split the span of $\mathbf{A}$ into an equivalent orthogonal span, and to identify from it the dominant (persisting patterns) and the sub-dominant (varying noise) sub-spaces [170].

Generally, any $m \times n$ matrix $\mathbf{A}$, where $m,n \geq 2$, may be factorized in the following way [126]:

$$\mathbf{A} = \mathbf{U}\mathbf{\Sigma}\mathbf{V}^{\dagger} \iff \mathbf{U}^{\dagger}\mathbf{A}\mathbf{V} = \operatorname{diag}(\sigma_1, \sigma_2, \ldots, \sigma_p) \tag{4.42}$$

$\mathbf{U} = [\boldsymbol{u}_1, \ldots, \boldsymbol{u}_m]$ is a $m \times m$ unitary orthogonal matrix. Its columns, $\boldsymbol{u}_i$, are the left singular vectors of $\mathbf{A}$, i.e., eigenvectors of $\mathbf{A}\mathbf{A}^{\dagger}$. $\mathbf{V} = [\boldsymbol{v}_1, \ldots, \boldsymbol{v}_n]$ is a $n \times n$ unitary orthogonal matrix. It consists of the right singular vectors $\boldsymbol{v}_i$, which are eigenvectors of $\mathbf{A}^{\dagger}\mathbf{A}$. $\mathbf{\Sigma}$ is a $m \times n$ diagonal matrix, for which:

$$\Sigma_{ij} = \begin{cases} \sigma_i & \text{for } i = j = \{1, \ldots, p\} \\ 0 & \text{for } i \neq j \text{ or } i,j > p \end{cases} \tag{4.43}$$

where $p = \min(m,n)$. The leading diagonal elements, σ_i, are the singular values of $\mathbf{A}$, ordered in the way that $\sigma_1 \geq \ldots \geq \sigma_p \geq 0$. The squares of the singular values σ_i^2 are equal to the eigenvalues of both $\mathbf{A}\mathbf{A}^{\dagger}$ and $\mathbf{A}^{\dagger}\mathbf{A}$ [126, 171].

SVD of $\mathbf{A}$, given by Eq. (4.42), provides a series of approximations of $\mathbf{A}$:

$$\mathbf{A}(k) = \mathbf{U}\mathbf{\Sigma}(k)\mathbf{V}^{\dagger} = \left[\begin{array}{c|c} \mathbf{U}(k) & \mathbf{U}(m-k) \end{array}\right] \times \left[\begin{array}{c|c} \mathbf{\Sigma}(k) & \mathbf{0} \\ \hline \mathbf{0} & \mathbf{\Sigma}(n-k) \end{array}\right] \times \left[\begin{array}{c} \mathbf{V}^{\mathsf{T}}(k) \\ \hline \mathbf{V}^{\mathsf{T}}(n-k) \end{array}\right] \tag{4.44}$$

$\mathbf{\Sigma}(k)$ is the rank-k version of $\mathbf{\Sigma}$ with the remaining singular values $\{\sigma_{k+1}, \ldots, \sigma_p\}$ in the $\mathbf{\Sigma}(n-k)$ block replaced by zeros. The matrix $\mathbf{A}(k)$ best approximates the original measurement matrix $\mathbf{A}$ in the sense of the F-norm (A.13), i.e., in the least squares sense.

As found empirically, the largest singular values correspond to persisting signal components with a non-varying pattern. On the contrary, the smallest singular values, which are set to zero, are related to the less significant signal components [172]. Inevitably, the pattern of the signal changes to some extent after recalculating the matrix $\mathbf{A}(k)$. This distortion is the price for the noise reduction [170].

Assume a case, when one of the dimensions of $\mathbf{A}$ is much bigger than the other one, and $\max(m,n) \gtrsim 10^4$. The full SVD then becomes very demanding with respect to the memory and processor time, if not utterly incalculable. In the case that, e.g., $m \gg n$, the bigger matrix $\mathbf{U}$ may be truncated from originally $m \times m$ to $m \times n$ matrix $\mathbf{U}_{\mathsf{tr}}$, see Eq. (4.44).

In parallel, $\mathbf{\Sigma}$ is truncated from $m \times n$ to $n \times n$ matrix $\mathbf{\Sigma}_{\mathrm{tr}}$, and the matrix $\mathbf{V}$ remains unchanged. Then:

$$\mathbf{A} \approx \mathbf{A}_{\mathrm{tr}} = \mathbf{U}_{\mathrm{tr}}\mathbf{\Sigma}_{\mathrm{tr}}\mathbf{V}^{\dagger} \tag{4.45}$$

Immediately, the whole task simplifies substantially, providing almost identical results to the full SVD (4.42). This technique is called the thin SVD [126].

SVD is applicable without a need of any prior knowledge about $\mathbf{A}$. Due to "commutation" with FT, identical results are obtained regardless of whether SVD is applied to the time-domain signals or the frequency-domain spectra [172]. Assume that the measurement matrices $\mathbf{A}^{(t)}$ and $\mathbf{A}^{(f)}$ contain time-domain and frequency-domain signals respectively. Two-dimensional FT may be represented by a matrix $\mathbf{F}$, which connects the two measurement matrices as follows:

$$\mathbf{A}^{(f)} = \mathbf{F}\mathbf{A}^{(t)} \tag{4.46}$$

Individual signal patterns after the decomposition are contained within the columns of $\mathbf{U}$. It may therefore be written:

$$\mathcal{F}\left\{\mathrm{SVD}\left[\mathbf{A}^{(t)}\right]\right\} = \mathbf{F}\mathbf{U}\mathbf{\Sigma}\mathbf{V}^{\dagger} \tag{4.47}$$

$$\mathrm{SVD}\left[\mathcal{F}\left\{\mathbf{A}^{(f)}\right\}\right] = \mathbf{X}\mathbf{\Psi}\mathbf{Y}^{\dagger} \tag{4.48}$$

Due to the linearity of FT and the existence of a unique SVD decomposition for any matrix, $\mathbf{X} \equiv \mathbf{F}\mathbf{U}$, $\mathbf{\Psi} \equiv \mathbf{\Sigma}$ and $\mathbf{Y} \equiv \mathbf{V}$.

Regarding the effectiveness of SVD, if the initial SNR of the signals $\boldsymbol{r}_i$ is much higher than 1, only a small number of measurements needs to be collected for the signal pattern recognition and a possible significant noise suppression. In such a case, the signal patterns remain almost undistorted. The difference between the biggest and the small singular values is large enough that the threshold for singular values to be zeroed is clear-cut.

To be able to distinguish between the useful signal and noise, when $\mathrm{SNR} \lesssim 1$ for the majority of $\boldsymbol{r}_i$, a much higher number of measurements needs to be accumulated. SVD is otherwise ineffective, since all the singular values are too close one to another, and the value of the threshold for zeroing cannot be satisfactorily set. Nevertheless, the obtained noise reduction may be better than after using the signal averaging, where the SNR increases as the square root of the number of measurements. The signal patterns are, however, likely to be severely distorted.

More advanced signal processing techniques, which are either derived from or directly exploit SVD, are Principal Component Analysis (PCA) [171] and Independent Component

Analysis (ICA) [173]. In contrast to SVD, they can even handle cases, where the useful signals are much weaker than the noise. Such methods are used for higher-dimensional datasets as, e.g., functional MRI maps or various bio-electrical signals (EEG, EMG).

4.4 Data Manipulation

It is rather unlikely that the NMR signal or the corresponding frequency spectrum is suitable for analysis immediately after acquisition. A basic set of corrections has to be applied first in order to remove specific instrumental distortions, FT artifacts, and to additionally enhance either the sensitivity or the resolution in the frequency domain [2, 174]. The basic principle of linear filtering, as described in Section 4.2, is represented by Eq. (4.8).

Though these techniques are an integral part of various data-analysis software packages, such programs may not always either be available or fit to the needs of an experimentalist. Corresponding routines may, nonetheless, easily be coded by hand in a preferred programming language or environment, which is also the case here.

4.4.1 Dc Offset

Due to instrumental offsets in the signal-processing circuitry, the whole time-domain signal $s(t)$, given by Eq. (4.17), may become displaced by a constant voltage value s_{dc}. The FT of such a signal gives:

$$\mathcal{F}\left\{s_{\mathrm{dc}} + s(t)\right\} = -\mathrm{i}s_{\mathrm{dc}}/\omega + S(\omega) \tag{4.49}$$

According to (4.22):

$$-\mathrm{i}s_{\mathrm{dc}}/\omega \equiv s_{\mathrm{dc}}\,\mathcal{D}(\omega; 0, 0) \tag{4.50}$$

is a narrow dispersion Lorentzian at the zero resonance offset. This peak adds to the regular spectrum and may cause significant distortions.

The dc offset is removed by subtracting a mean value, computed from the last 10 – 20 % of samples, from the whole time-domain signal [175]. After FT, the unwanted peak is completely or to a great extent suppressed. If multiple scans are accumulated, phase cycling of the receiver phase may be used to correct for the offset during the pulse sequence.

4.4.2 Apodization

Apodization of the time-domain signal has a twofold use: either sensitivity or resolution enhancement [10]. The NMR signal is always acquired during a finite time interval

$0 \le t \le t_{\mathrm{acq}}$, see Eq. (4.17). An incompletely decayed (truncated) signal may be represented by the Heaviside Π-function [176]:

$$\Pi(t) = \begin{cases} 1 & \text{for } |t| \le 1/2 \\ 0 & \text{for } |t| > 1/2 \end{cases} \tag{4.51}$$

FT of such a signal results in:

$$\mathcal{F}\left\{\Pi\left(\frac{t}{2t_{\mathrm{acq}}}\right) s(t)\right\} = t_{\mathrm{acq}}\sqrt{2/\pi}\,\mathrm{sinc}(\omega t_{\mathrm{acq}}) * S(\omega) \tag{4.52}$$

where the sinc function is defined by [176]:

$$\mathrm{sinc}\, x = \begin{cases} \dfrac{\sin x}{x} & \text{for } x \ne 0 \\ 1 & \text{for } x = 0 \end{cases} \tag{4.53}$$

The sinc function modifies peak tails by a typical oscillatory pattern also called sinc wiggles, see Figure 6.26. Application of a properly chosen filter function, which attenuates the end part of the signal to a certain degree, e.g., $\lesssim 0.01\, s_0$, successfully suppresses this artifact [2, 10].

Assume the noisy NMR signal (4.16). FT of the time-domain noise results in the frequency-domain noise. A filter function, which is selected according to the envelope of the observed signal (4.17), may enhance the initial part of the signal $r(t)$, where $s(t) \gtrsim n(t)$, and suppress the the end part, where $s(t) \lesssim n(t)$. The SNR of the spectrum is enhanced as the noise is reduced. However, the sensitivity is traded off for the resolution as the peaks become broader. Assume the case of an exponentially decaying filter function with a decay rate constant $\lambda' > 0$:

$$h(t) = \mathrm{e}^{-\lambda' t} \tag{4.54}$$

The frequency spectrum is given by:

$$\mathcal{F}\{h(t)s(t)\} = s_0 \exp[(\mathrm{i}\Omega - \lambda)t_0 + \mathrm{i}\phi_0]\,\mathcal{L}(\omega; \Omega, \lambda + \lambda') \tag{4.55}$$

A special case of apodization is the matched filter, which is discussed in detail in Section 4.3.3. The resolution may be enhanced by using the filter function (4.54) with a negative decay rate constant $\lambda' < 0$ and/or some other function [2, 10].

4.4.3 Zero Filling

Assume a discrete NMR signal s_j composed of N complex points, i.e., $2N$ real plus imaginary points in total. After the discrete FT, the real part represents the frequency spectrum:

$$S_k = \frac{1}{N}\,\mathrm{Re}\left(\sum_{j=0}^{N-1} s_j\, \mathrm{e}^{-\mathrm{i}2\pi jk/N}\right) \tag{4.56}$$

The remaining N imaginary points, together with any information contained in them, are discarded. In order to include the full information available, the data may be filled (padded) with extra N zeros:

$$S_k^{\mathrm{ZF}} = \frac{1}{2N}\,\mathrm{Re}\left(\sum_{j=0}^{2N-1} s_j\,\mathrm{e}^{-\mathrm{i}\pi jk/N}\right) = \frac{1}{2N}\,\mathrm{Re}\left(\sum_{j=0}^{N-1} s_j\,\mathrm{e}^{-\mathrm{i}\pi jk/N}\right) \tag{4.57}$$

Despite the halving of the spectral amplitude, the number of points in the spectrum is doubled, which increases the resolution and makes the quantification of the spectrum more accurate [30]. Further zero-filling beyond $2N$ points may also be used. The consequent interpolation of the frequency spectrum, however, brings no extra information.

As mentioned in Section 4.1, the FFT algorithm is efficient only for the number of points $N = 2^n$, where n is an integer. In the case that $2^{n-1} < N < 2^n$, zero-filling to the nearest power of two, 2^{n+1}, may be beneficial [2].

4.4.4 Phase Corrections

FT of the general time-domain signal (4.19), which corresponds to a single resonance, already contains a phase distortion. It may be rewritten in the following way:

$$S(\omega) = s_0'\,\mathrm{e}^{\mathrm{i}(\Omega t_0+\phi_0)}\,\mathcal{L}(\omega;\Omega,\lambda) = s_0'\,[S_{\mathrm{Re}}(\omega) + \mathrm{i}S_{\mathrm{Im}}(\omega)] \tag{4.58}$$

where $s_0' = s_0\,\mathrm{e}^{-\lambda t_0}$ and:

$$S_{\mathrm{Re}}(\omega) = \cos(\Omega t_0 + \phi_0)\,\mathcal{A}(\omega;\Omega,\lambda) - \sin(\Omega t_0 + \phi_0)\,\mathcal{D}(\omega;\Omega,\lambda) \tag{4.59}$$

$$S_{\mathrm{Im}}(\omega) = \cos(\Omega t_0 + \phi_0)\,\mathcal{D}(\omega;\Omega,\lambda) + \sin(\Omega t_0 + \phi_0)\,\mathcal{A}(\omega;\Omega,\lambda) \tag{4.60}$$

The frequency spectrum (4.59) contains an admixture of the dispersion Lorentzian. In such a case, the phase distortion may be corrected by a so-called zero-order phase correction. Multiplication of Eq. (4.58) by a factor $\mathrm{e}^{\mathrm{i}\varphi_0}$, where:

$$\varphi_0 = -(\Omega t_0 + \phi_0) \tag{4.61}$$

restores the absorption mode of the frequency spectrum (4.59).

The zero-order phase distortion occurs because the time-domain signal acquisition never starts immediately after the rf pulse ends. It is delayed by a certain time interval t_0 in order to protect the amplifier circuitry against the high rf power during the “ring-down” interval. The phase shift Ωt_0 is a consequence of the time-shift theorem (4.4). An additional constant phase ϕ_0 in Eq. (4.58) results from the spectrometer electronics settings.

Assume the case of a frequency spectrum containing several resonances at different offsets Ω_i:

$$S_\Sigma(\omega) = \mathrm{e}^{\mathrm{i}\phi_0} \sum_i s'_{0i}\, \mathrm{e}^{\mathrm{i}\Omega_i t_0}\, \mathcal{L}(\omega; \Omega_i, \lambda_i) \tag{4.62}$$

where $s'_{0i} = s_0\, \mathrm{e}^{-\lambda_i t_0}$. The phase distortion now becomes resonance-offset dependent. In order to correct it, $S_\Sigma(\omega)$ has to be multiplied point-by-point by a factor $\mathrm{e}^{-\mathrm{i}\varphi(\Omega)}$, where $\varphi(\Omega)$ is given by [30]:

$$\varphi(\Omega) = \sum_{k=0}^{m} \varphi_k \Omega^k \tag{4.63}$$

In most cases, correction up to the linear term is enough. One of the peaks at the position Ω_p, a pivot peak, is phased by using the zero-order phase correction. The total phase φ_0 corresponding to the pivot peak offset equals to:

$$\varphi_0 = \Omega_\mathrm{p} t_0 + \phi_0\,, \;\; \varphi_0 \in [-\pi, \pi] \tag{4.64}$$

Keeping the phase correction φ_0 fixed, a constant φ_1 is set such that the remaining peak lineshapes resemble absorption Lorentzians. The overall correction is then given by:

$$\varphi(\Omega) = \varphi_0 + \frac{\Omega - \Omega_\mathrm{p}}{2\pi W} \varphi_1 \tag{4.65}$$

The phase factors φ_0 and φ_1 are given in radians, the resonance offsets Ω and Ω_p are given in radians per second. The bandwidth W, as introduced in Section 4.2, is in Hz. The value of the dimensionless fraction in (4.65) remains between −1 and 1 for any resonance offset Ω within the bandwidth.

The whole phasing procedure is often interactive. Various techniques of automatic phasing have also been proposed [177–179]. When the spectrum contains only a limited number of resonances, a simple technique is based on the fact that the pure absorption Lorentzian (4.21) has a finite integral:

$$\int_{-\infty}^{\infty} \mathrm{d}\omega\, \mathcal{A}(\omega; \Omega, \lambda) = \pi \tag{4.66}$$

whereas the integral of the pure dispersion Lorentzian (4.22) is equal to zero:

$$\int_{-\infty}^{\infty} \mathrm{d}\omega\, \mathcal{D}(\omega; \Omega, \lambda) = 0 \tag{4.67}$$

A properly phased spectrum, therefore, has the maximum integral.

Chapter 5

^{15}N NMR

5.1 Nitrogen NMR

All experiments presented in Chapters 5 to 7 are based on NMR of nitrogen ^{15}N. Solutions of ^{15}N doubly-labelled compounds were used, namely ammonium nitrate ($^{15}NH_4{}^{15}NO_3$) and nitrous oxide ($^{15}N_2O$).

Nitrogen with its both naturally occurring isotopes ^{14}N and ^{15}N, listed in Table 5.1, plays a vital role from the early days of NMR. In the form of $^{15}NH_4{}^{15}NO_3$, it allowed observation of the chemical shift [182], determination of the nitrogen magnetogyric ratios [183], or the first liquid state ^{15}N-NMR [184].

Nowadays, ^{15}N is often exploited in NMR of proteins. The characteristic features of ^{15}N-NMR spectroscopy are usually very narrow spectral lines, a wide chemical shift range, and a high sensitivity of ^{15}N chemical shifts to the solvent environment [185].

Nucleus	$I/\hbar$	$\gamma\,/\,\mathrm{rad\,s^{-1}\,T^{-1}}$	μ/μ_N	$A_N\,/\,\%$
^{14}N	1	$+1.9338 \times 10^7$	+0.4038	99.6337(4)
^{15}N	1/2	-2.7126×10^7	−0.2832	0.3663(4)

Table 5.1: NMR properties of the naturally occurring nitrogen isotopes. I is the nuclear spin in units of the reduced Planck constant, and γ is the magnetogyric ratio. μ is the nuclear magnetic moment in units of the nuclear magneton $\mu_\mathrm{N} = e\hbar/2m_p \approx 5.0508 \times 10^{-27}\,\mathrm{J\,T^{-1}}$, where $e \approx 1.6022 \times 10^{-19}\,\mathrm{C}$ is the elementary charge and $m_p \approx 1.6726 \times 10^{-27}$ kg is the proton rest mass [180]. A_N is the isotopic natural abundance [181].

5.2 $^{15}NH_4{}^{15}NO_3$

The $^{15}NH_4{}^{15}NO_3$ sample consisted of 37.3 mg of ^{15}N doubly-labelled salt of 98 % enrichment (Sigma-Aldrich), dissolved in 1 ml of D_2O. The sample was used as prepared, without any additional modification or degassing.

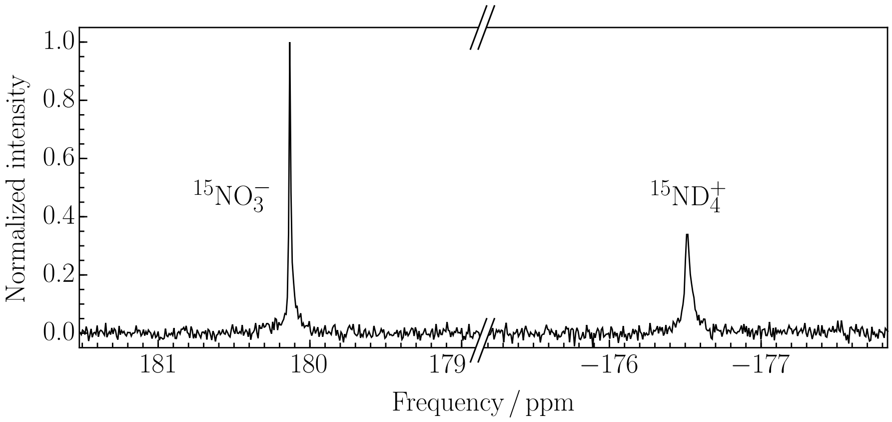

Figure 5.1: Spectrum of $^{15}NH_4{}^{15}NO_3$ dissolved in D_2O as measured on the 300 MHz NMR instrument

The spectrum of $^{15}NH_4{}^{15}NO_3$ in D_2O is shown in Figure 5.1. It consists of a $^{15}NO_3^-$ singlet ($\delta^{\text{iso}} \approx -4$ ppm w.r.t. CH_3NO_2 [186, 187]) and a $^{15}ND_4^+$ multiplet ($\delta^{\text{iso}} \approx -360$ ppm w.r.t. CH_3NO_2 [186, 187]). The multiplet merged into a single peak either due to the undergoing chemical exchange between ^1H and ^2D, or more likely due to the relaxation of ^{15}N by the attached quadrupolar ^2D nuclei, i.e., the scalar relaxation of the first and second kind, respectively [2, 26]. Due to the dissociation of $^{15}NH_4{}^{15}NO_3$ in solution, the ^{15}N-^{15}N J-coupling may be neglected.

5.3 $^{15}N_2O$

The $^{15}N_2O$ sample contained ^{15}N doubly-labelled $^{15}N_2O$ of 98 % enrichment (CK-Gas, U.K.), dissolved under the pressure of 3.5 bar in perdeuterated DMSO. In order to avoid paramagnetic singlet-state relaxation due to the dissolved oxygen, the DMSO was degassed prior to $^{15}N_2O$ filling. The whole procedure of sample preparation is described in full detail in [60].

The $^{15}N_2O$ frequency spectrum is shown in Figure 5.2. It consists of two doublets, one corresponding to the terminal ^{15}N site ($\underline{^{15}N}{}^{15}NO$, $\delta^{\text{iso}} \approx -219$ ppm $\equiv \delta_1$ w.r.t. $H^{15}NO_3$ [188]) and the other corresponding to the central ^{15}N site ($^{15}N\underline{^{15}N}O$, $\delta^{\text{iso}} \approx -135$ ppm $\equiv \delta_2$

w.r.t. $H^{15}NO_3$ [188]). The experimental J-coupling constant is -8.20 ± 0.06 Hz, see also [188].

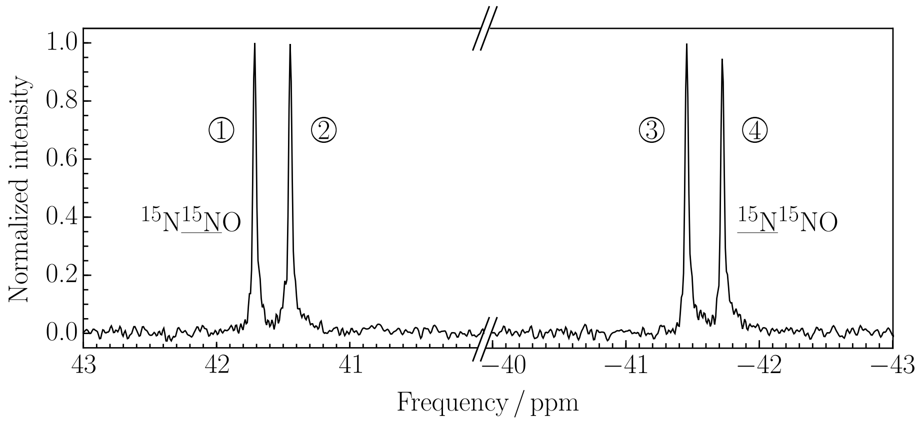

Figure 5.2: Spectrum of $^{15}N_2O$ dissolved in DMSO as measured on the 300 MHz NMR instrument

5.4 Measurement of Relaxation Times

Experimental time constants for the $^{15}NH_4{}^{15}NO_3$ and $^{15}N_2O$ samples are summarized in Table 5.2. Individual procedures used for their determination are described in the following subsections.

Nucleus	T_1 / s	T_2 / s	T_2^* / ms	T_2' / ms	T_2'/T_2 ($\times 10^{-3}$)
$^{15}ND_4^+$	256.5 ± 8.0	0.336 ± 0.013	81.9 ± 8.4	108 ± 15	323 ± 46
$^{15}NO_3^-$	131.1 ± 2.3	51.3 ± 1.6	223 ± 40	224 ± 40	4.37 ± 0.80
$^{15}N^{15}\underline{N}O$	114.8 ± 5.1	48.2 ± 2.5	218 ± 17	219 ± 17	4.53 ± 0.42
$^{15}\underline{N}^{15}NO$	207.7 ± 11.0	45.3 ± 2.1	221 ± 20	222 ± 21	4.91 ± 0.51

Table 5.2: Summary of experimental time constants for $^{15}NH_4{}^{15}NO_3$ in D_2O and $^{15}N_2O$ in DMSO. The longitudinal relaxation time constant T_1 was determined by inversion recovery. The transverse relaxation time constant T_2 was determined by the CPMG spin-echo sequence (π-pulse spacing: $\tau = 0.01$ s for $^{15}ND_4^+$, $\tau = 1$ s for $^{15}NO_3^-$ and $^{15}N_2O$). T_2^* was determined from the FWHM of the spectral peaks. T_2' was determined by using Eq. (2.34). The errors in T_1, T_2 and T_2^* are standard deviations of the ensemble of experimental values. The errors of the derived quantities T_2' and T_2'/T_2 are computed by using Eq. (F.11).

5.4.1 Determination of T_1

The value of the longitudinal relaxation time constant T_1 was determined by means of the inversion recovery pulse sequence shown in Figure 2.1, using nonselective rf pulses.

The integrals $\mathfrak{I}(\tau)$ of the spectral peaks were plotted against the relaxation interval τ, and fitted by a modified version of Eq. (2.32):

$$\mathfrak{I}(\tau) = \mathfrak{I}_0 \left(1 - 2\epsilon\, \mathrm{e}^{-\tau/T_1}\right) \tag{5.1}$$

where $\mathfrak{I}_0$ is the initial amplitude, and the constant ϵ denotes the magnetization inversion effectiveness. Typically, $0.95 \leq \epsilon \leq 1$.

The plots of the peak integrals and the best fits are shown in Figure 5.3 for $^{15}\mathrm{NH}_4{}^{15}\mathrm{NO}_3$ and in Figure 5.4 for $^{15}\mathrm{N}_2\mathrm{O}$. The results of fitting are summarized in Table 5.2. All values were evaluated from a large ensemble of repeated measurements. Some values differ slightly from those given in [61].

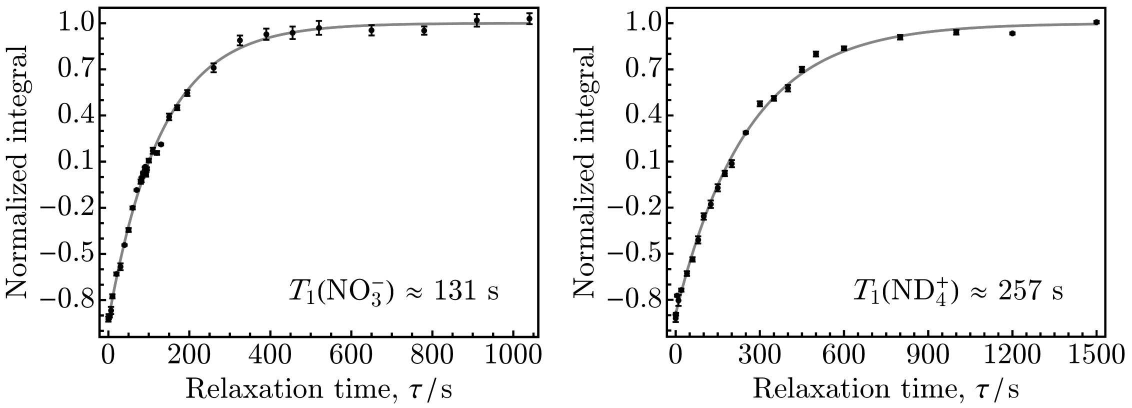

Figure 5.3: T_1 determination for $^{15}\mathrm{NO}_3^-$ (left) and $^{15}\mathrm{ND}_4^+$ (right) by inversion recovery

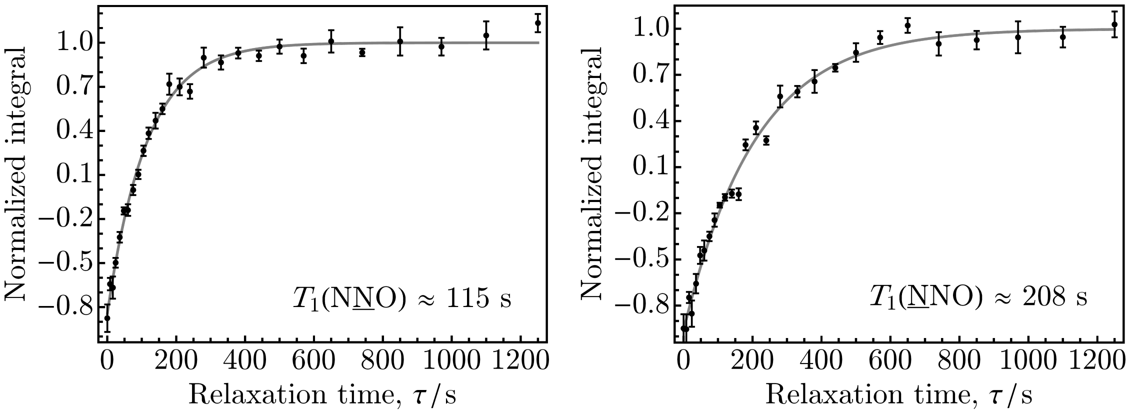

Figure 5.4: T_1 determination for $^{15}\mathrm{N}\underline{^{15}\mathrm{N}}\mathrm{O}$ (left) and $\underline{^{15}\mathrm{N}}{}^{15}\mathrm{NO}$ (right) by inversion recovery

5.4.2 Determination of T_2

The T_2 constant was determined by means of the CPMG spin-echo pulse sequence with semi-selective rf pulses, described in detail in Chapter 6 (see particularly Figure 6.5). A train of a varying number of π pulses was applied in order to refocus the magnetization. The spacing τ of the π pulses was chosen carefully with respect to both the expected T_2 value and the efficient removal of B_0 inhomogeneity effects (τ = 0.01 s for $^{15}\mathrm{ND}_4^+$, τ = 1 s for $^{15}\mathrm{NO}_3^-$ and $^{15}\mathrm{N}_2\mathrm{O}$). The number of pulses was kept as low as possible to avoid accumulation of errors.

The FID signal was acquired after the $\tau/2$ delay following the last π pulse. The peak integrals were plotted against the total time between the end of the first ($\pi/2$) pulse and the time point, when the signal acquisition started. Assuming n_π pulses of length τ_p, then the total refocusing time τ_r is given by:

$$\tau_\mathrm{r} = n_\pi(\tau + \tau_\mathrm{p}) \tag{5.2}$$

The corresponding fitting function is a simple decaying exponential:

$$\mathfrak{I}(\tau_\mathrm{r}) = \mathfrak{I}_0\, \mathrm{e}^{-\tau_\mathrm{r}/T_1} \tag{5.3}$$

The peak integrals and the best fits are shown in Figure 5.5 for $^{15}\mathrm{NH}_4{}^{15}\mathrm{NO}_3$ and in Figure 5.6 for $^{15}\mathrm{N}_2\mathrm{O}$. The resulting values are summarized in Table 5.2.

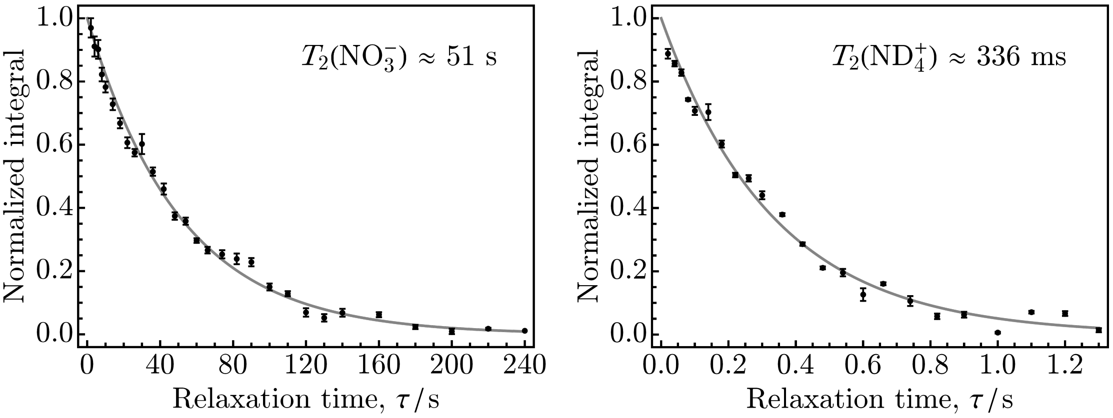

Figure 5.5: T_2 determination for $^{15}\mathrm{NO}_3^-$ (left) and $^{15}\mathrm{ND}_4^+$ (right) by a CPMG spin-echo sequence with the π-pulse spacing τ = 1 s for $^{15}\mathrm{NO}_3^-$ and τ = 0.01 s for $^{15}\mathrm{ND}_4^+$

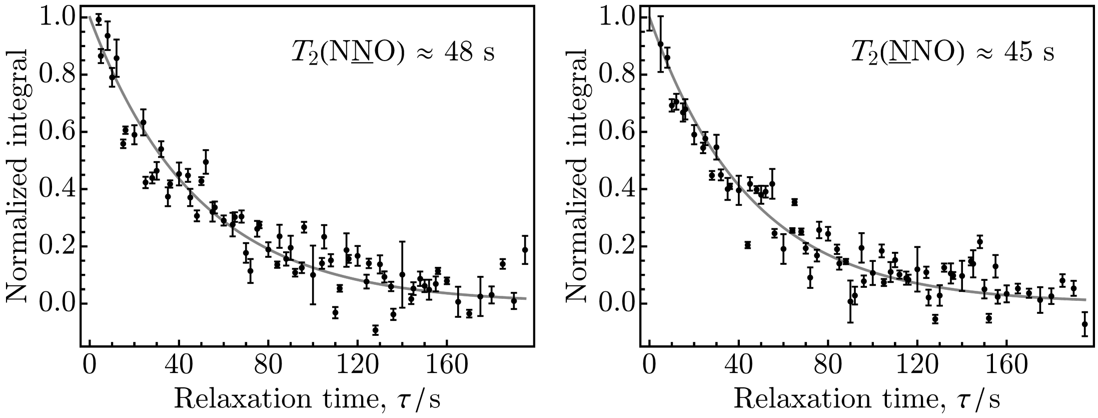

Figure 5.6: T_2 determination for $^{15}N\underline{^{15}N}O$ (left) and $\underline{^{15}N}{}^{15}NO$ (right) by a CPMG spin-echo sequence with the π-pulse spacing $\tau = 1$ s

5.4.3 Determination of T_2^* and T_2'

The T_2^* value was determined from FWHM of the spectral peaks by using Eq. (4.23). The T_2' mean value was computed by using (2.34):

$$\mu\left(T_2'\right) = \frac{\mu(T_2)\ \mu(T_2^*)}{\mu(T_2) - \mu\left(T_2^*\right)} \tag{5.4}$$

The standard deviation of T_2' was determined by using Eq. (F.11), assuming that T_2 and T_2^* are uncorrelated:

$$\sigma\left(T_2'\right) = \frac{\sqrt{\left[\mu\left(T_2^*\right)\right]^4 \sigma^2(T_2) + \left[\mu(T_2)\right]^4 \sigma^2\left(T_2^*\right)}}{\left[\mu(T_2) - \mu\left(T_2^*\right)\right]^2} \tag{5.5}$$

The resulting values of T_2^* and T_2' are provided in Table 5.2.

Chapter 6

Multiple Spin-Echo Sensitivity Enhancement

6.1 Spin Echoes

Transverse relaxation has been introduced in Section 2.1.4. Although the true homogeneous decay rate is given by $1/T_2$, the signal in solution NMR often fades away much faster. This is predominantly caused by B_0 inhomogeneity, which combines with the homogeneous decay in the overall apparent relaxation rate $1/T_2^* \gg 1/T_2$. Fortunately, the effect of B_0 inhomogeneity can be reversed by spin echoes.

6.1.1 Overview

Besides the inventors of NMR [189–191], Erwin Hahn may surely be ranked among the co-founders of the method. By using strong rf fields for excitation for the first time [192], and introducing the spin echo sequence [193], see Figure 6.1, he paved the way for the modern multi-pulse NMR methods, where the spin echo plays an essential role.

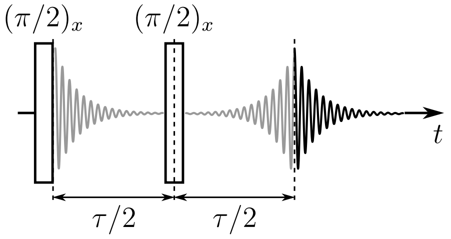

Figure 6.1: The Hahn spin echo pulse sequence. The oscillating gray curve denotes the time evolution of the NMR signal. Only the black signal is usually acquired.

The Hahn echo consists of an initial excitation $(\pi/2)_x$ pulse, which is followed by another $(\pi/2)_x$ pulse after a time interval $\tau/2$. Although the signal has almost disappeared before the second pulse is applied ($T_2^* \lesssim \tau/2$), it reappears again, peaking at time $t = \tau$. This resembles well known acoustic echoes, hence the name of the sequence.

The principle of the Hahn echo is shown in Figure 6.2 [193, 194]. The first $(\pi/2)_x$ pulse flips the longitudinal magnetization into the transverse plane (1) , and individual magnetization isochromats start unwinding (2). After the second $(\pi/2)_x$ pulse at time $t = \tau/2$, the x-component of the transverse magnetization remains unaffected (3), but the y-component becomes aligned along the z-axis (4). The isochromats, which are close to the x-axis continue in precession during the second $\tau/2$ interval to form the echo (5). If the third $(\pi/2)_x$ pulse is applied at time $\tau < T < T_2$, the magnetization z-component is rotated back into the transverse plane (6), and a stimulated echo occurs at time $T + \tau$ (7).

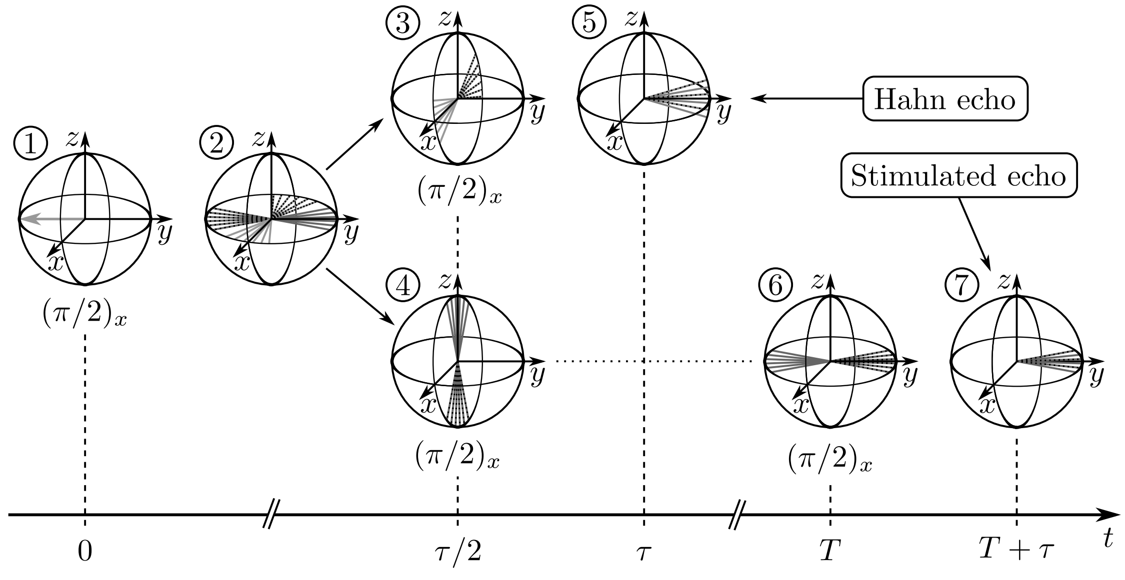

Figure 6.2: Origin of the Hahn and stimulated spin echoes. The description is in the text. Adapted from [194].

Despite the phenomenal success, the compensatory capabilities of the Hahn echo are weak, regarding the B_0 inhomogeneity. Besides, only a fraction of the magnetization is responsible for either of the echo signals. As a result, the NMR signal fades away quickly. A partial improvement came with the Carr-Purcell (CP) modification [195]. Two versions of the CP echoes were published, as shown in Figure 6.3.

“Method A” was just a simple extension of the original Hahn echo. The replacement of the second $(\pi/2)_x$ pulse by a π_x pulse, however, allowed a complete refocussing of the

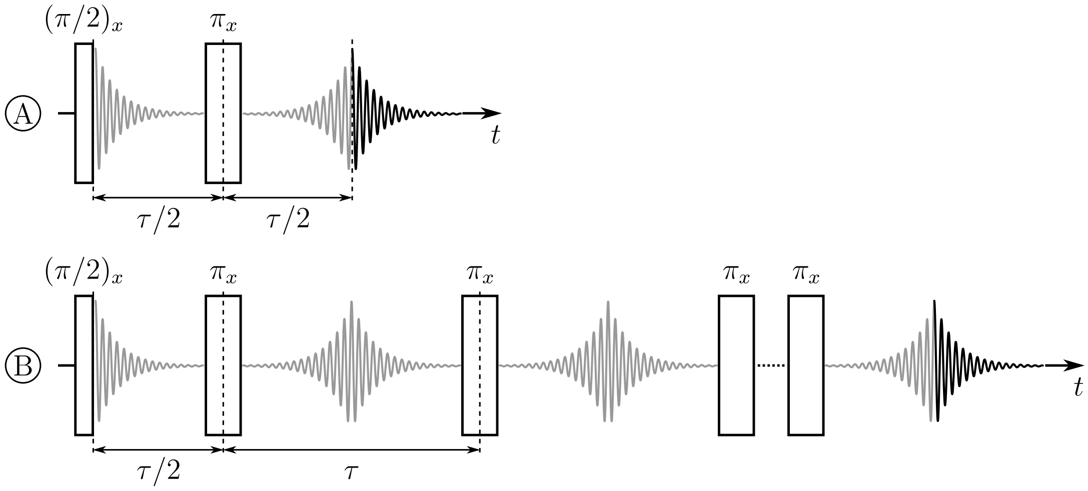

Figure 6.3: The CP spin echo pulse sequences

magnetization. In order to measure the T_2 value, the sequence was repeated for different values of τ. Nevertheless, if the B_0 inhomogeneity and diffusion are significant, and T_1 is too long, Method A becomes inefficient. It was shown that instead of the single π_x pulse, a train of many π pulses may be applied consecutively. The so-called "Method B" allows repeated refocussing and observation of multiple spin-echo signals for extended time intervals in just one scan.

In comparison to Method A, the refocussing performance of Method B strongly depends on the accuracy of the π pulse. When the π pulse length is inaccurate, the flip angle is different from 180° and the magnetization ends up above the xy-plane. Every other π pulse rotates the magnetization still farther away from the transverse plane, see Figure 6.4.

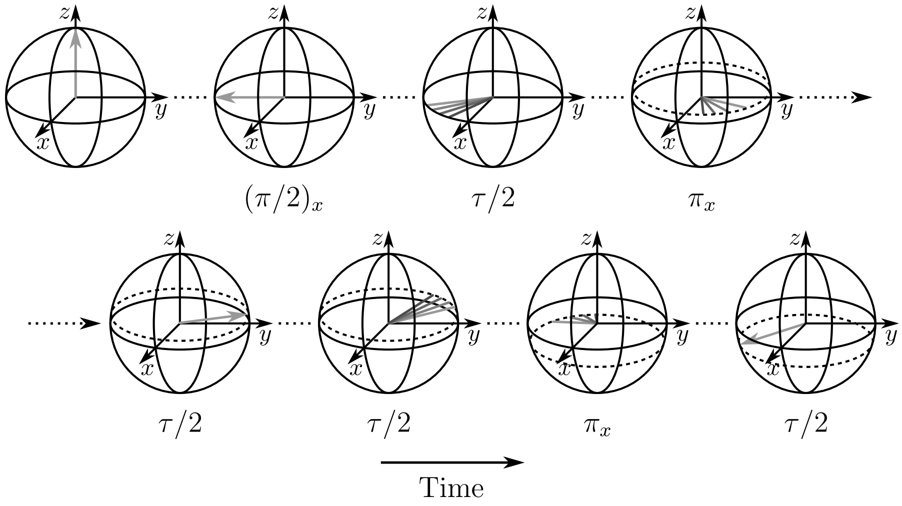

Figure 6.4: The CP spin echo refocusing capabilities. The description is in the text. Adapted from [194].

Possible B_1 inhomogeneity during the rf pulse across the sample needs to be included as well [196]. Refocussing then becomes ineffective, which again results in a speeding-up of the signal decay.

A remedy for the obstacles listed above was devised by Meiboom and Gill [197], see Figure 6.5. In their CPMG spin echo, the phase of the π pulses is shifted by 90° with respect to the first excitation pulse. If the magnetization ends above the xy-plane after the odd π pulse, it is returned back to the transverse plane by the following even π pulse, see Figure 6.6. As a result, the change in the pulse phase causes self-compensation in every even echo.

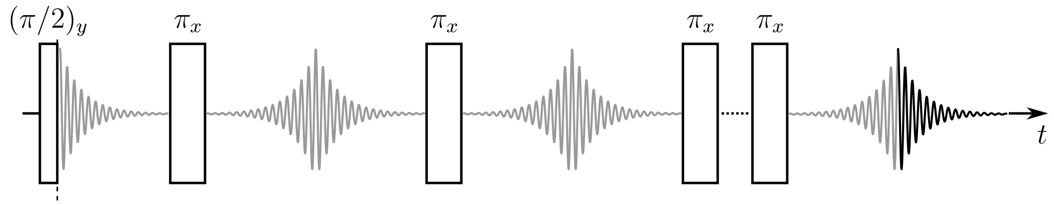

Figure 6.5: The CPMG spin echo pulse sequence

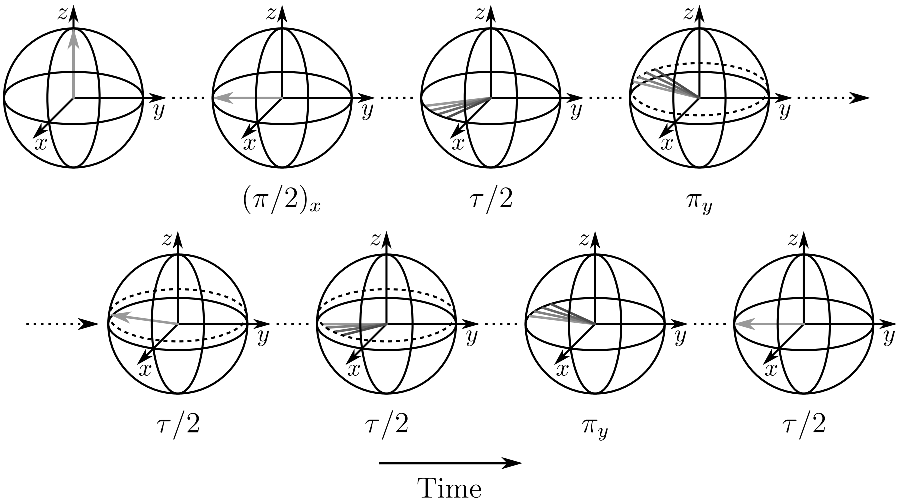

Figure 6.6: The CPMG spin echo refocusing capabilities. The description is in the text. Adapted from [194].

The use of the spin echoes spans over all fields of MRS. They may be used for removal of unwanted features in order to enhance spectral information. On the one hand, they allow refocusing of the B_0 inhomogeneity, so that NMR signal is repeatedly resurrected. On the other hand, spin echoes provide a means for quantification of diffusion (DOSY) or chemical exchange processes (EXSY). Chemical shift effects and heteronuclear couplings may be refocussed, too, except for homonuclear couplings [196], see Section 6.1.2.

Spin echoes are used in J-spectroscopy [198] or for polarization transfer between coupled nuclear partners (INEPT) [194]. Repeatedly refocused NMR signal may be further exploited for the SNR enhancement, see Section 6.5. In solid-state NMR, where the dipolar and quadrupolar interactions need to be taken into account, an alternative of the Hahn echo, a solid echo, is used [199]. In MRI, pulse sequences incorporating many different types of echoes exist for obtaining images of the human body in a noninvasive way.

6.1.2 CPMG Spin Echo Sequence

The principles of the CPMG spin echo may be visualized by using the vector model, see Figure 6.7. The equilibrium z-magnetization is rotated by the $(\pi/2)_y$ pulse towards the x-axis. During an interval $\tau/2$, transverse magnetization freely evolves and individual magnetization isochromats unwind, each of a slightly different precession frequency. This is either due to different chemical shifts or due to an inhomogeneous B_0 field.

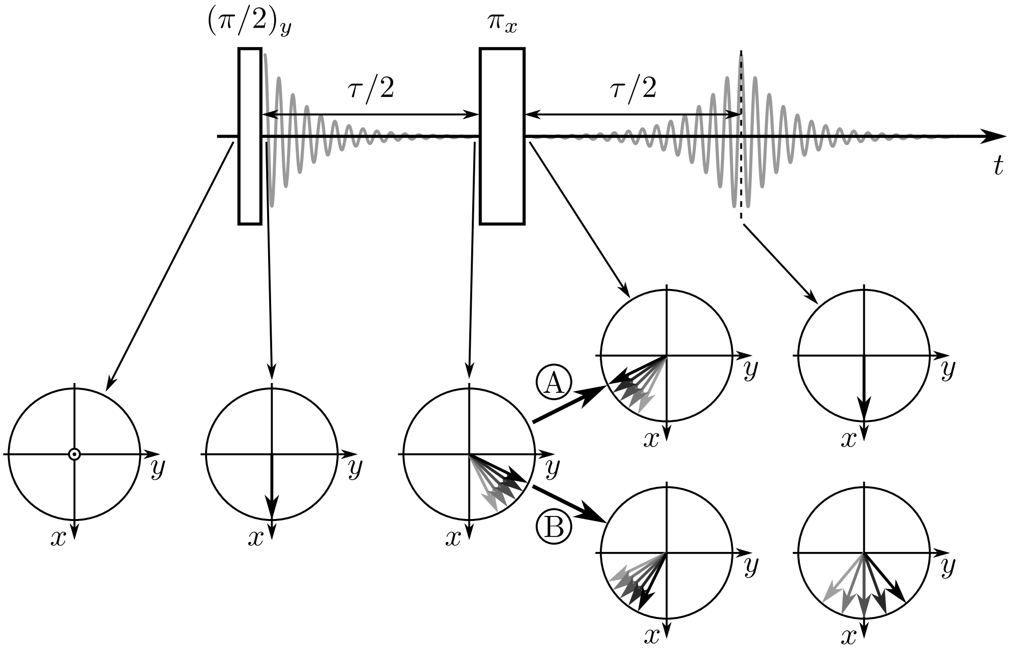

Figure 6.7: The CPMG spin-echo sequence visualized by means of the vector model. (A) The time evolution of magnetization common to either isolated spins or coupled spins, where the rf pulses are applied to a single spin species. (B) The time evolution of magnetization in the case that the rf pulses are applied to all spins.

The time evolution of the magnetization differs after the π_x pulse. In the case (A), which is common for either the isolated or coupled spins, where the π pulse is applied to only one spin species, magnetization is mirrored through the xz-plane, and refocused after another $\tau/2$ interval again. In the case (B), which corresponds to magnetization evolution of a coupled spins, where the π pulse is applied to all spins at the same time, the spin-spin coupling causes further divergence of the isochromats during the other free-evolution interval.

In order to describe such effects in a more rigorous way, assume a pair of weakly coupled spins-1/2, described by Hamiltonian $\hat{H}_\mathrm{A}$ (2.96). In such a case, the product operator formalism may be used. The thermal-equilibrium magnetization is given by [14]:

$$\hat{\rho}(0-) \approx \frac{1}{4}\left(\hat{E} + \frac{\hbar\gamma B_0}{k_\mathrm{B}T}\hat{I}_z\right) \tag{6.1}$$

where $\hat{\rho}(0-)$ denotes the state of the spin system shortly before the $(\pi/2)_y$ pulse, which is applied at time zero. For the sake of simplicity, all rf pulses are assumed to be negligibly short with respect to the evolution intervals. Therefore, magnetization relaxation during the pulses may be ignored. Simultaneously, only relevant terms containing spin operators $\hat{I}$ will be retained, while the unity operator $\hat{E}$ and the Boltzmann factor in front of $\hat{I}_z$ will be left out.

Assume first the case, in which the semi-selective rf pulses are applied exclusively to the spin $\hat{I}_1$ and the other spin remains unaffected. The initial $(\pi/2)_{1y}$ pulse transforms $\hat{\rho}(0-)$ into:

$$\hat{\rho}(0-) \xrightarrow{\frac{\pi}{2}\hat{I}_{1y}} \hat{\rho}(0) \propto \hat{I}_{1x} + \hat{I}_{2z} \tag{6.2}$$

Free evolution under the Hamiltonian $\hat{H}_\mathrm{A}$ during the time interval $\tau/2$ results in:

$$\begin{aligned}\hat{\rho}(0) &\xrightarrow{\frac{\tau}{2}\Omega_1\hat{I}_{1z}} \xrightarrow{\frac{\tau}{2}\pi J_{12}\,2\hat{I}_{1z}\hat{I}_{2z}} \\ &\hat{\rho}(\tau/2-) \propto \hat{I}_{1x}\cos(\Omega_1\tau/2)\cos(\pi J_{12}\tau/2) + 2\hat{I}_{1y}\hat{I}_{2z}\cos(\Omega_1\tau/2)\sin(\pi J_{12}\tau/2) \\ &\qquad +\hat{I}_{1y}\sin(\Omega_1\tau/2)\cos(\pi J_{12}\tau/2) - 2\hat{I}_{1x}\hat{I}_{2z}\sin(\Omega_1\tau/2)\sin(\pi J_{12}\tau/2) + \hat{I}_{2z}\end{aligned} \tag{6.3}$$

The π_{1x} pulse acts on the spin operators in the following way:

$$\begin{aligned}\hat{\rho}(\tau/2-) &\xrightarrow{\pi\hat{I}_{1x}} \\ &\hat{\rho}(\tau/2) \propto \hat{I}_{1x}\cos(\Omega_1\tau/2)\cos(\pi J_{12}\tau/2) - 2\hat{I}_{1y}\hat{I}_{2z}\cos(\Omega_1\tau/2)\sin(\pi J_{12}\tau/2) \\ &\qquad -\hat{I}_{1y}\sin(\Omega_1\tau/2)\cos(\pi J_{12}\tau/2) - 2\hat{I}_{1x}\hat{I}_{2z}\sin(\Omega_1\tau/2)\sin(\pi J_{12}\tau/2) + \hat{I}_{2z}\end{aligned} \tag{6.4}$$

Free evolution under $\hat{H}_\mathrm{A}$ during the second evolution interval $\tau/2$ results in 16 terms, which simplify into:

$$\hat{\rho}(\tau/2) \xrightarrow{\frac{\tau}{2}\Omega_1\hat{I}_{1z}} \xrightarrow{\frac{\tau}{2}\pi J_{12}\,2\hat{I}_{1z}\hat{I}_{2z}} \hat{\rho}(\tau) \propto \hat{I}_{1x} + \hat{I}_{2z} \tag{6.5}$$

This is the same expression as in Eq. (6.2). Both the chemical shift and B_0 inhomogeneity effects are refocused. This result corresponds to the case (A) in Figure 6.7.

Excluding relaxation, the refocused component $\hat{\rho}_1(t)$ of $\hat{\rho}(t)$ displays a following periodic behaviour during the CPMG spin echo:

$$\hat{\rho}_1(0) = \hat{\rho}_1(k\tau)\,,\; k = \{1, 2, \ldots\} \tag{6.6}$$

In the case of the CP spin-echo sequence, a different result is obtained:

$$\hat{\rho}_1(2k\tau) = -\hat{\rho}_1[(2k+1)\tau]\,,\; k = \{0, 1, \ldots\} \tag{6.7}$$

Assume now that the nonselective rf pulses are applied to both spins. The first $(\pi/2)_y$ pulse transforms the equilibrium magnetization (6.1) as follows:

$$\hat{\rho}(0-) \xrightarrow{\frac{\pi}{2}\hat{I}_y} \hat{\rho}(0) = \hat{I}_x \tag{6.8}$$

Application of the sequence $\tau/2 - \pi_x - \tau/2$, also called a spin-echo "sandwich" [14], to $\hat{\rho}(0)$ results in 32 terms. These fortunately simplify as follows:

$$\hat{\rho}(0) \xrightarrow{\frac{\tau}{2}\hat{H}_\mathrm{A}} \xrightarrow{\pi\hat{I}_x} \xrightarrow{\frac{\tau}{2}\hat{H}_\mathrm{A}} \hat{\rho}(\tau) \propto \hat{I}_x\cos(\tau\pi J_{12}) + (2\hat{I}_{1y}\hat{I}_{2z} + 2\hat{I}_{1z}\hat{I}_{2y})\sin(\tau\pi J_{12}) \tag{6.9}$$

This divergence of isochromats, rather than their refocussing, corresponds to the case (B) in Figure 6.7, and is further treated in Section 6.2.1.

6.2 Interference Effects in Multi-Pulse Experiments

6.2.1 J-Modulation

The result of the application of the nonselective rf pulses to the coupled homonuclear spin pair, or simultaneous application of rf pulses to each of the two spins in the heteronuclear pair, given by Eq. (6.9), is called J-modulation [193, 200]. J-modulation causes complex oscillations of the multiple spin-echo signal. This reflects in varying phases of peaks in the frequency spectrum [201].

Several different remedies exist. One has already been exposed in Section 6.1.2. Application of (semi-)selective rf pulses to only one of the coupled spins or to individual resonances avoids evolution under the J-coupling Hamiltonian $\hat{H}_J$, and the observed magnetization is refocused by the π pulse.

Another solution is to use spin-locking, in which π pulses are spaced by $\tau < 1/J_{12}$ [194]. Individual magnetization isochromats evolve only slightly during the inter-pulse intervals and are immediately refocused. They are literally "locked" to the rotation axis.

The effects of J-modulation in various spin-1/2 systems were successfully suppressed by modified spin-echo pulse sequences such as "perfect spin echo" [202, 203], "Stabilization by Interconversion within a Triad of COherences under Multiple refocusing pulses" (SITCOM) [204, 205], and "Periodic Refocusing of J Evolution by Coherence Transfer" (PROJECT) [206].

Finally, several methods exist for eliminating the dispersion contribution from the frequency spectra. Although such methods were primarily intended for the correction of two-dimensional NMR spectra, they may also be applied to the one-dimensional spectra. It was recognized that when the signal envelope is symmetric, which is also the case of the spin-echo signal, a proper treatment of the signal as a whole [207] or of its halves [208] leads to a cancellation of the dispersion contribution to the spectral lineshapes. One peculiar example of these techniques uses so-called pseudo-echoes [209]. The pseudo-echoes arise after artificial symmetrization of the ordinary FID signal, which also leads to the desired result.

6.2.2 Non-Ideal Rf Pulses

Three main sources of a non-ideal performance of the rf pulses may be discerned. These are: off-resonance effects, static field (B_0) inhomogeneity, and rf field (B_1) inhomogeneity. The B_0 inhomogeneity may be overcome by using the spin-echo sequence. The remaining two cases will now be treated in more detail. An impact of these effects on the spin-echo signal has been studied both theoretically and experimentally [210, 211].

6.2.2.1 Off-Resonance Effects

Assume the frequency spectrum containing multiple resonances. Since only one value of the carrier frequency ω_{rf} can be used at a time, some of the peaks may be located on-resonance or very close to it ($0 \approx |\Omega_i| \ll \omega_1$), or also significantly off-resonance ($|\Omega_i| \gtrsim \omega_1$). When the ideal $(\pi/2)_y$ pulse is applied, a magnetization isochromat vector, which corresponds to the on-resonance peak, will end up in the xy-plane, parallel to the x-axis. As the resonance offset increases, the equivalent magnetization isochromat rotates at the nutation frequency $\omega_{\mathrm{nut}} > \omega_1$ around the effective field $\tilde{\boldsymbol{B}}$ through the angle $\beta_{\mathrm{eff}} \neq \pi/2$. After the pulse ends, the transverse magnetization phase is shifted by $\Delta\varphi$, see Figures 6.8.

Assume application of a general rf pulse β_φ, which is represented by the composite rotation (B.6), to the thermal-equilibrium magnetization $\boldsymbol{M}(0) \equiv \boldsymbol{M}_0$, including nonzero resonance offset Ω. Assume further that $\varphi = \pi/2$, $\beta = \omega_{\text{nut}}\,\tau_{\text{p}} = \tau_{\text{p}}\sqrt{\Omega^2 + \omega_1^2}$ and $\tan\theta = \omega_1/\Omega$. The final orientation of the magnetization vector $\boldsymbol{M}$ after the pulse is given as follows:

$$\begin{pmatrix} M_x(0) \\ M_y(0) \\ M_z(0) \end{pmatrix} = \mathbf{R}(\beta,\varphi,\theta) \begin{pmatrix} 0 \\ 0 \\ M_0 \end{pmatrix} = \frac{M_0}{\Omega^2 + \omega_1^2} \begin{pmatrix} \omega_1\sqrt{\Omega^2+\omega_1^2}\sin\left(\tau_{\text{p}}\sqrt{\Omega^2+\omega_1^2}\right) \\ \Omega\,\omega_1\left[1 - \cos\left(\tau_{\text{p}}\sqrt{\Omega^2+\omega_1^2}\right)\right] \\ \Omega^2 + \omega_1^2\cos\left(\tau_{\text{p}}\sqrt{\Omega^2+\omega_1^2}\right) \end{pmatrix} \tag{6.10}$$

The dependence of the magnetization components (6.10) on the Ω/ω_1 ratio is shown in Figure 6.9. A semi-selective $(\pi/2)_y$ pulse, which was applied during experiments described later in the text, is taken as an example.

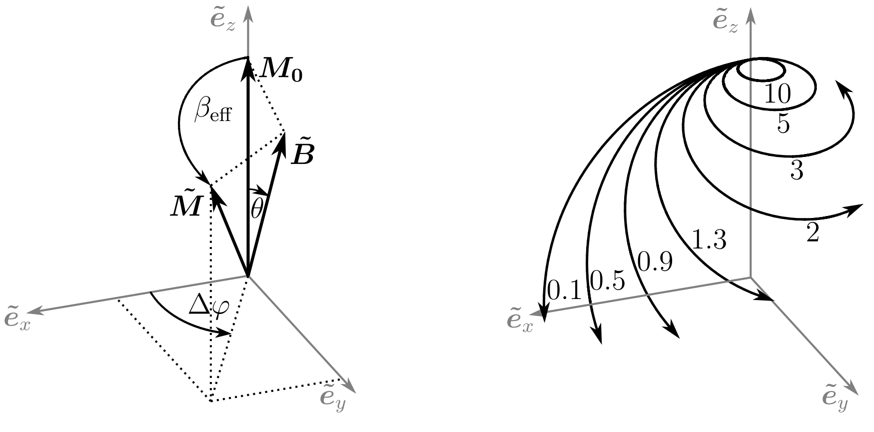

a) b)

Figure 6.8: Off-resonance effects on the longitudinal magnetization vector trajectory after application of the nominal $(\pi/2)_y$ pulse. a) The magnetization vector $\tilde{\boldsymbol{M}}$ is rotated through the angle β_{eff} from the initial orientation along the z-axis around the effective magnetic field $\tilde{\boldsymbol{B}}$, tilted by the angle θ. The transverse magnetization phase is shifted by $\Delta\varphi$. b) Trajectories of the longitudinal magnetization vector as a function of the resonance offset Ω relative to the rf field strength ω_1. The numbers next to the trajectories are equal to Ω/ω_1.

Expressions for the effective tilt angle β_{eff} and the phase shift $\Delta\varphi$ are given by [10]:

$$\beta_{\text{eff}} = \tau_{\text{p}}\sqrt{\Omega^2 + \omega_1^2} \tag{6.11}$$

$$\tan\Delta\varphi = M_y(0)/M_x(0) \tag{6.12}$$

The dependence of β_{eff} and $\Delta\varphi$ on the size of Ω/ω_1 ratio is shown in Figure 6.10.

The angle χ_β between the magnetization vector $\boldsymbol{M}$ and the z-axis, as a result of the action of the rf pulse β_φ, is called the excitation profile [2]. Assuming that $|\boldsymbol{M}| \equiv M_0$, χ_β is defined by [31]:

$$\cos\chi_\beta = M_z(0)/M_0 \tag{6.13}$$

This dependence is plotted in Figure 6.11. The excitation profile of a π pulse is twice as narrow as that of a $\pi/2$ pulse. The π pulse is more frequency selective.

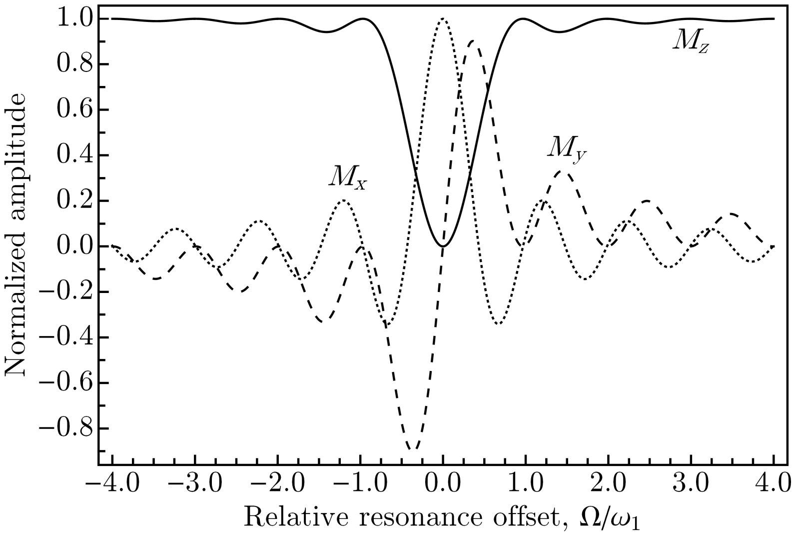

Figure 6.9: The dependence of the magnetization components M_x (dotted line), M_y (dashed line) and M_z (solid line) on the resonance offset relative to the rf field strength after the semi-selective rectangular $(\pi/2)_y$ pulse ($\omega_1/2\pi = 250$ Hz, $\tau_\mathrm{p} = 1.0$ ms).

6.2.2.2 B_1 Inhomogeneity

B_1 inhomogeneity manifests only during rf pulses. In the case that the pulse sequence consists of a small number of pulses, its effect is negligible compared to multi-pulse sequences. B_1 inhomogeneity may be approximated by [2]:

$$B_1(\boldsymbol{r}) = B_1(\boldsymbol{0}) + \Delta B_1(\boldsymbol{r}) \tag{6.14}$$

where $B_1(\boldsymbol{0})$ is the nominal B_1 field in the centre of the rf coil, and $\Delta B_1(\boldsymbol{r})$ is the position dependent B_1 inhomogeneity.

An example of a B_1 inhomogeneity during a $(\pi/2)_y$ pulse on the equilibrium magnetization $\boldsymbol{M}_0$, averaged over the sample volume V, leads to [2]:

$$\hat{I}_z \xrightarrow{|\gamma B_1(\boldsymbol{r})\tau_\mathrm{p}|\hat{I}_y} \frac{1}{V}\left[\hat{I}_z \int_V \mathrm{d}\boldsymbol{r}\cos(|\gamma B_1(\boldsymbol{r})\tau_\mathrm{p}|) + \hat{I}_x \int_V \mathrm{d}\boldsymbol{r}\sin(|\gamma B_1(\boldsymbol{r})\tau_\mathrm{p}|)\right] \tag{6.15}$$

The values of the integrals depend on the distribution of $\Delta B_1(\boldsymbol{r})$.

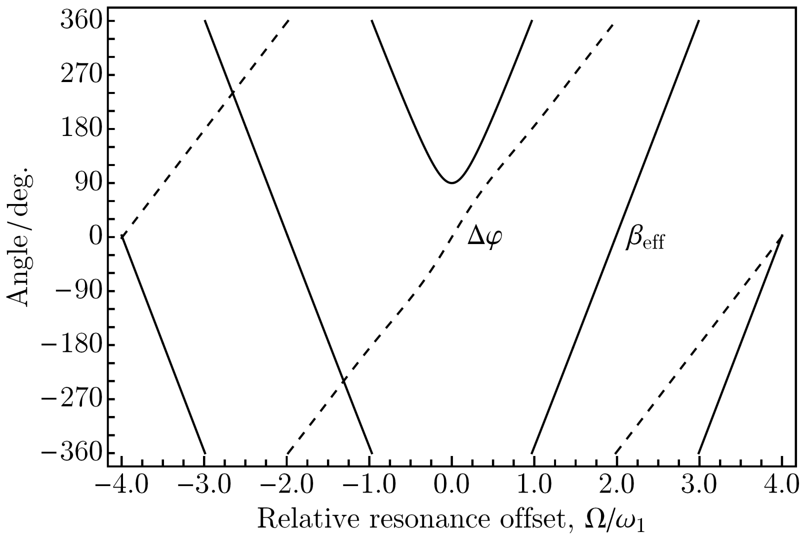

Figure 6.10: The dependence of the effective flip angle β_{eff} (solid line) and the transverse magnetization phase shift $\Delta\varphi$ (dashed line) on the resonance offset relative to the rf field strength after the semi-selective rectangular $(\pi/2)_y$ pulse ($\omega_1/2\pi$ = 250 Hz, τ_p = 1.0 ms). Discontinuities are caused by limiting the angle size to the interval $[-360°, +360°]$.

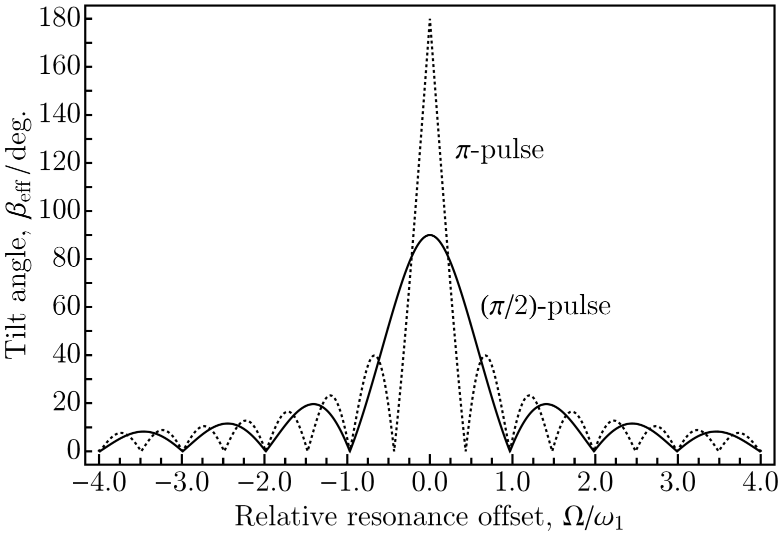

Figure 6.11: The dependence of the excitation profile of the semi-selective $\pi/2$ (solid line) and π (dotted line) rf pulses on the resonance offset relative to the rf field strength ($\omega_1/2\pi$ = 250 Hz, $\tau_\text{p}(\pi) = 2\tau_\text{p}(\pi/2)$ = 2.0 ms).

6.3 MSE Signal

The multiple spin-echo (MSE) signal is acquired by using a modified version of the CPMG spin-echo sequence in Figure 6.5. Assume that semi-selective rf pulses are used in order to avoid J-modulation. The MSE signal $s_{\mathrm{MSE}}(t)$ is recorded between the pulses during the whole sequence for a time interval of several multiples of T_2. In accordance with [61], $s_{\mathrm{MSE}}(t)$ may be described by:

$$s_{\mathrm{MSE}}(t) = h_{\mathrm{MSE}}(t)\, s^0_{\mathrm{MSE}}(t)\,,\ t \geq 0 \tag{6.16}$$

where $h_{\mathrm{MSE}}(t)$ is the signal envelope function and $s^0_{\mathrm{MSE}}(t)$ is the undecaying periodic NMR signal.

The signal envelope incorporates both the irreversible decay due to homogeneous transverse relaxation (T_2) and the reversible effect of B_0 inhomogeneity (T_2'), see Figure 6.12. A general and compact form of $h_{\mathrm{MSE}}(t)$ is given by:

$$h_{\mathrm{MSE}}(t) = \mathrm{e}^{-t/T_2}\, g(|t - n_e(t)\tau|) \tag{6.17}$$

The monotonically decaying function $g(t)$ obeys:

$$g(t) = \begin{cases} 1 & \text{for } t = 0 \\ 0 & \text{for } t \to +\infty \end{cases} \tag{6.18}$$

The expression $|t - n_e(t)\tau|$ describes individual whole-echo signals centered at times $t = n_e(t)\tau$, where $n_e(t)$ is an echo index:

$$n_e(t) = \left\lfloor \frac{t}{\tau} + \frac{1}{2} \right\rfloor \tag{6.19}$$

The brackets $\lfloor\cdot\rfloor$ denote the "floor" function, which rounds any real number to its nearest smaller integer. The echo index introduces MSE signal periodicity due to the reversible refocusing. Assume that B_0 field inhomogeneity causes exponential decay and rise of the signal, excluding T_2 relaxation. An explicit form of $g(t)$ is then:

$$g(t) = \mathrm{e}^{-t/T_2'} \tag{6.20}$$

When Eqs. (6.17) to (6.20) are combined, a compact and computationally effective form of the envelope function arises:

$$h_{\mathrm{MSE}}(t;\tau,T_2,T_2') = \exp\left\{ -\left| \frac{t}{\tau} - \left\lfloor \frac{t}{\tau} + \frac{1}{2} \right\rfloor \right| \frac{\tau}{T_2'} - \frac{t}{T_2} \right\},\ t \geq 0 \tag{6.21}$$

An equivalent form, which is more illustrative, but computationally inefficient for large numbers of echoes N_{e}, is given by:

$$h_{\mathrm{MSE}}(t;\tau,N_{\mathrm{e}},T_2,T_2') = \sum_{k=0}^{N_{\mathrm{e}}} \Pi\left(\frac{t - k\tau}{\tau}\right) \exp\left\{ -\frac{|t - k\tau|}{T_2'} - \frac{t}{T_2} \right\},\ t \geq 0 \tag{6.22}$$

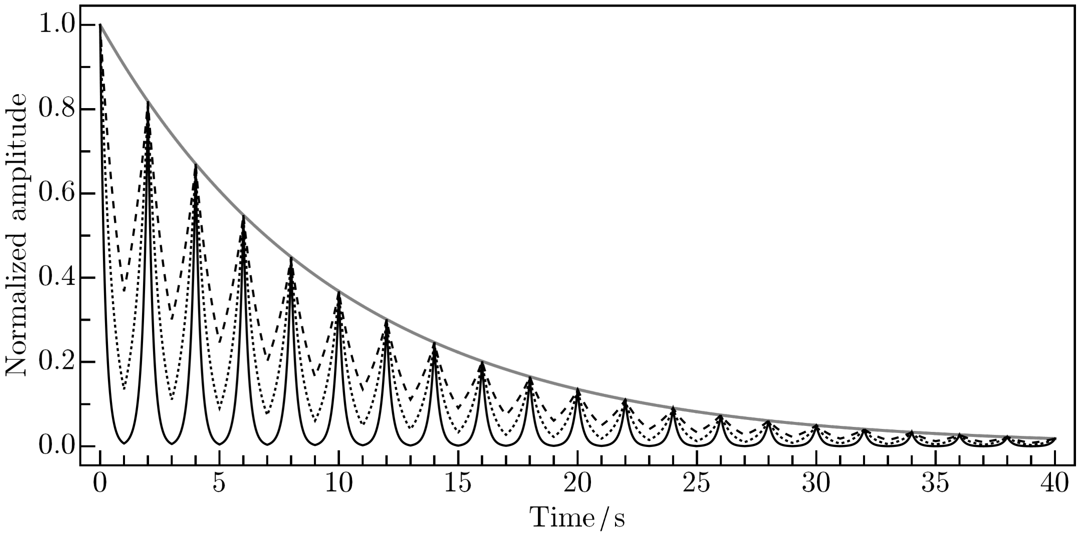

Figure 6.12: Examples of the MSE signal envelope function $h_{\mathrm{MSE}}(t)$. Parameters: $T_2 = 10$ s, $\tau = 2$ s, $T_2^* = 0.2$ s (black solid line, $T_2' \approx 0.2$ s), $T_2^* = 0.5$ s (dotted line, $T_2' \approx 0.53$ s), $T_2^* = 1$ s (dashed line, $T_2' \approx 1.11$ s), $T_2^* = T_2$ (gray solid line, $T_2' = \infty$). The values of T_2' are computed by using Eq. (2.34).

where the Heaviside Π-function is defined by Eq. (4.51).

Finally, an idealized form of the undecaying signal, generated by a single resonance, which oscillates at the resonance offset frequency Ω, may be written as follows:

$$s^0_{\mathrm{MSE}}(t) = |a(0)| \exp\left\{ \mathrm{i} \left[\Omega(t - n_e(t)\tau) + (-1)^{n_e(t)}\phi_0 + \phi_{\mathrm{inst}} \right] \right\} \tag{6.23}$$

Here $a(0)$ is the signal amplitude at time zero, ϕ_0 is the initial signal phase alternated by the π pulses, and ϕ_{inst} is a constant instrumental phase shift.

6.4 MSE Matched Filter

Based on the discussion in Section 4.3.3, the matched filter suited for the MSE signal is given by the envelope function $h_{\mathrm{MSE}}(t)$ in Eq. (6.21). The maximum achievable SNR enhancement after processing the MSE signal described in Section 6.5.3.1, relative to the SNR of a single FID, may be simply estimated. Considering Parseval's theorem (4.9) and Eqs. (4.36) and (4.37), the enhancement $\varepsilon_{\mathrm{MSE}}$ is defined by:

$$\varepsilon_{\mathrm{MSE}} = \frac{\max(\mathrm{SNR}_{\mathrm{MSE}})}{\max(\mathrm{SNR}_{\mathrm{FID}})} = \sqrt{\int_0^\infty \mathrm{d}t\, |h_{\mathrm{MSE}}(t)|^2 \Big/ \int_0^\infty \mathrm{d}t\, |h_{\mathrm{FID}}(t)|^2} \tag{6.24}$$

Assume that the FID signal decays exponentially with the time constant T_2^*. Its envelope function $h_{\mathrm{FID}}(t)$ is given by:

$$h_{\mathrm{FID}}(t) = \mathrm{e}^{-t/T_2^*} \tag{6.25}$$

and the resulting expression for $\varepsilon_{\mathrm{MSE}}$ is the following, using Eq. (6.22):

$$\varepsilon_{\mathrm{MSE}} = \sqrt{1 + \frac{2\left[\exp\left(\frac{\tau}{T_2} - \frac{\tau}{T_2'}\right) - 1\right]}{\left[\exp\left(\frac{2\tau}{T_2}\right) - 1\right]\left[\frac{T_2'}{T_2} - 1\right]}} = \sqrt{1 + \frac{2(\mathrm{e}^{\alpha-\alpha/\beta} - 1)}{(\mathrm{e}^{2\alpha} - 1)(\beta - 1)}} \tag{6.26}$$

Constants $\alpha = \tau/T_2$ and $\beta = T_2'/T_2$ are the π-pulse spacing and the inhomogeneous decay time constant in units of T_2, respectively. The dependence of the enhancement $\varepsilon_{\mathrm{MSE}}$ on the parameters α and β is shown in Figure 6.13.

Small values of the ratio α correspond to a closely spaced π pulses, whereas small values of the ratio β imply a large influence of B_0 inhomogeneity. As both α and β approach zero, the SNR enhancement increases. This regime is, nevertheless, inconvenient. On the one hand, the frequency spectrum resolution is heavily compromised as a consequence of either the small number of points per half-echo, or of truncation artifacts. On the other hand, errors may accumulate with a large number of π pulses. On the contrary, when both α and β approach unity, the signal is not refocused at all.

Therefore, an optimal number of echoes N_{e} and the π-pulse spacing τ has to be found with respect to the desired frequency spectrum properties such as the SNR enhancement and the frequency resolution. In the case of a single resonance, there exists practically no limitation. In the case of multiplets, the maximum resulting FWHM of the peaks should be less than the value of J-coupling.

6.5 Experimental Procedures

6.5.1 Initial Considerations

In our experiments, the main purpose of the MSE pulse sequence is to enable SNR-enhanced singlet NMR. During its devising, information from Section 6.2 was taken into account together with details of the field-cycling experiments in Section 7.2.

The carrier frequency is preferably set either close to a singlet or to the mean frequency of a multiplet. Peaks are located near zero frequency, which minimizes off-resonance effects. Full advantage may, therefore, be taken of the use of semi-selective rf excitation and refocusing pulses. J-modulation is avoided. Based on the excitation profiles of typical rf pulses (Figure 6.11), the other coupled spins are affected only minimally.

The CPMG spin-echo sequence itself compensates sufficiently well for both B_0 and B_1 inhomogeneities and alleviates possible diffusion effects. If the pulse lengths are properly determined, pulse imperfections are minimized. In addition, the CPMG sequence with single π pulses is the least demanding with respect to both the power load of the spectrometer electronics (transmitter) and the heat load of the sample, when compared to the composite or shaped π pulses.

Precise timing during the whole MSE sequence is of the utmost priority in order to ensure optimal performance of the MSE method. The occurrence of each element within

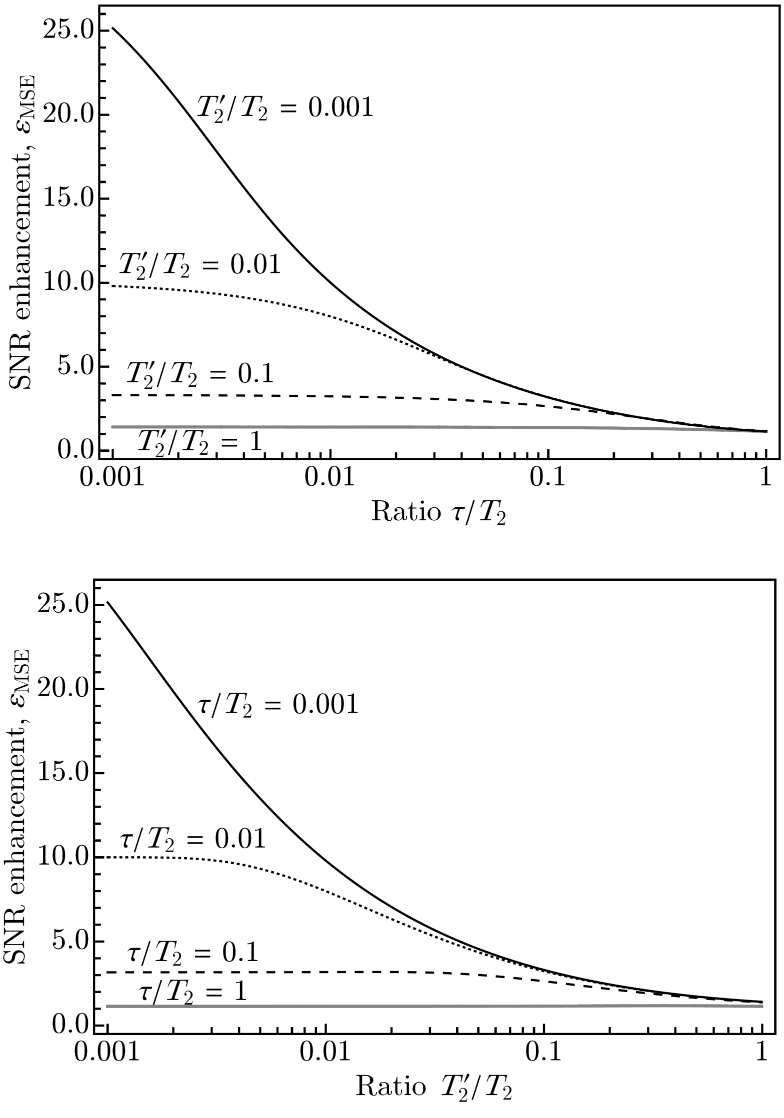

Figure 6.13: The dependence of the $\varepsilon_{\mathrm{MSE}}$ enhancement on the ratios τ/T_2 (top) and T_2'/T_2 (bottom)

the sequence, as well as each sample within the resulting MSE signal, is orchestrated with respect to the dwell time Δt, see Figures 6.14 and 6.15.

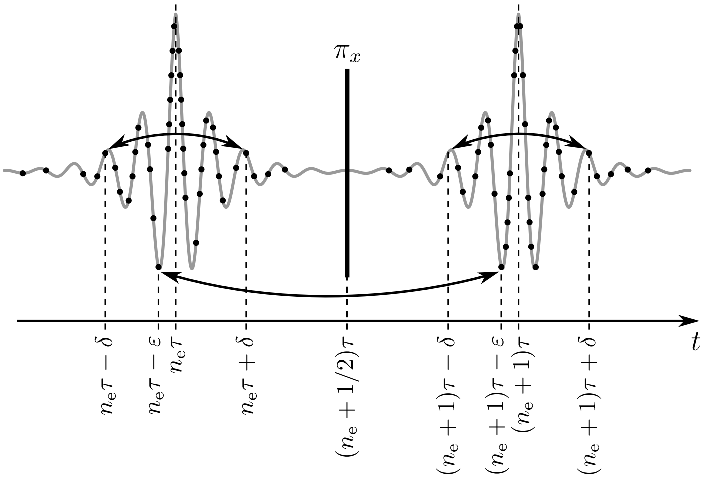

Figure 6.14: The MSE pulse sequence timing. Every element of the MSE sequence and the MSE signal occurs at a time given by an integer multiple of the dwell time. This ensures that all points (dots) in the MSE signal occur periodically, and every point in one half-echo signal has its counterpart in the other half-echo signal. n_e denotes the echo index, τ is the π-pulse spacing, the time shifts δ and ε are multiples of the dwell time.

6.5.2 MSE Pulse Sequence

A scheme of the MSE pulse sequence is shown in 6.15. The first $(\pi/2)_y$ pulse excites the spin system. Since the resonance offset is small, the flip angle is close to 90°. The end of the $(\pi/2)_y$ pulse is the time zero reference point.

A delay Δ_1 follows:

$$\Delta_1 = m \times \Delta t\,,\ m = \left\lceil \frac{\tau_{\mathrm{ad}} + \tau_{\mathrm{rd}}}{\Delta t} \right\rceil \tag{6.27}$$

where m is an integer and the brackets $\lceil\cdot\rceil$ denote the "ceiling" function, which rounds any real number to its nearest greater integer. Δ_1 is made longer than an acquisition delay τ_{ad}, during which the strong rf pulse "rings-down", plus a receiver delay τ_{rd}, needed for preparing the receiver for signal acquisition so that the first point of the signal is recorded properly.

During the acquisition interval of length τ_1, ν_1 samples of the first decreasing half-echo are acquired:

$$\tau_1 = \nu_1\,\Delta t \tag{6.28}$$

The delay Δ_2 is placed symmetrically around the refocusing π_x pulses. It takes into account the duration of the π pulse, a time interval $\tau_{\mathrm{prep}} < \{\tau_{\mathrm{ad}}, \tau_{\mathrm{rd}}\}$ needed for the rf pulse preparation (amplitude and phase setting), as well as τ_{ad} and τ_{rd} intervals. Therefore:

$$\Delta_2 = n \times \Delta t - \tau_{\mathrm{p}}(\pi_x)/2\,,\ n = \left\lceil \frac{\tau_{\mathrm{ad}} + \tau_{\mathrm{rd}} + \tau_{\mathrm{p}}(\pi_x)/2}{\Delta t} \right\rceil \tag{6.29}$$

where n is integer and $\tau_{\mathrm{p}}(\pi_x)$ is the π_x pulse length.

After the sequence $\Delta_2 - \pi_x - \Delta_2$, the whole-echo signal of ν_2 samples is recorded during an interval τ_2:

$$\tau_2 = \nu_2\,\Delta t \tag{6.30}$$

The bracketed part of the sequence is repeated N_{e}-times in total, where N_{e} is the number of echoes. After the pulse sequence ends, the accumulated signal is sent to the spectrometer, and the next experiment is repeated after the pulse delay $t_{\mathrm{pd}} \geq 3\,T_1$ (not shown).

As apparent from Figure 6.15, the π-pulse spacing obeys:

$$\tau \equiv 2[\Delta_1 + \tau_1 + \Delta_2 + \tau_{\mathrm{p}}(\pi_x)/2] = \tau_{\mathrm{p}}(\pi_x) + 2\Delta_2 + \tau_2 \tag{6.31}$$

which simplifies as follows:

$$m + \nu_1 = \nu_2/2 \tag{6.32}$$

The total number of acquired samples within the MSE signal is given by:

$$\nu_{\mathrm{acq}} = \nu_1 + N_{\mathrm{e}}\,\nu_2 \tag{6.33}$$

Taking into account Eq. (6.31), the total duration of the sequence is equal to:

$$T_{\mathrm{MSE}} = \tau_{\mathrm{p}}[(\pi/2)_y] + (N_{\mathrm{e}} + 1/2)\tau \tag{6.34}$$

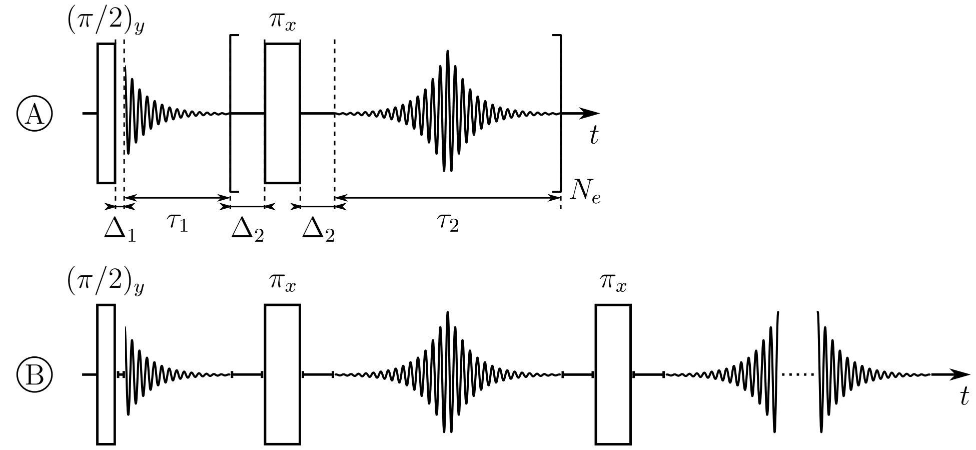

Figure 6.15: The MSE pulse sequence. (A) A compact and detailed scheme. (B) An expanded form of the pulse sequence.

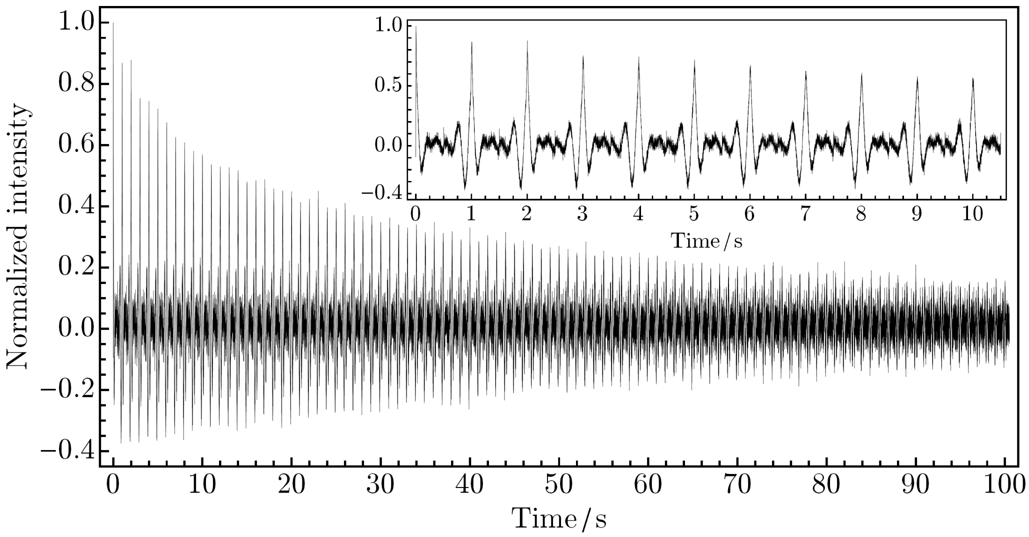

Figure 6.16: Example of the $^{15}\text{N}\underline{^{15}\text{N}}\text{O}$ MSE signal (64 scans). Experimental parameters: $N_\text{e} = 100$, $\tau = 1$ s, $\tau_\text{p}(\pi_x)/2 = \tau_\text{p}[(\pi/2)_y] = 1.066$ ms, $\tau_\text{ad} = \tau_\text{rd} = 30$ μs, $\Delta t = 0.8$ ms, $m = 1$, $n = 2$, $t_\text{pd} = 450$ s, $t_\text{acq} = 100.5$ s, $\nu_2 = 1250$, $\nu_\text{acq} = 125\,624$.

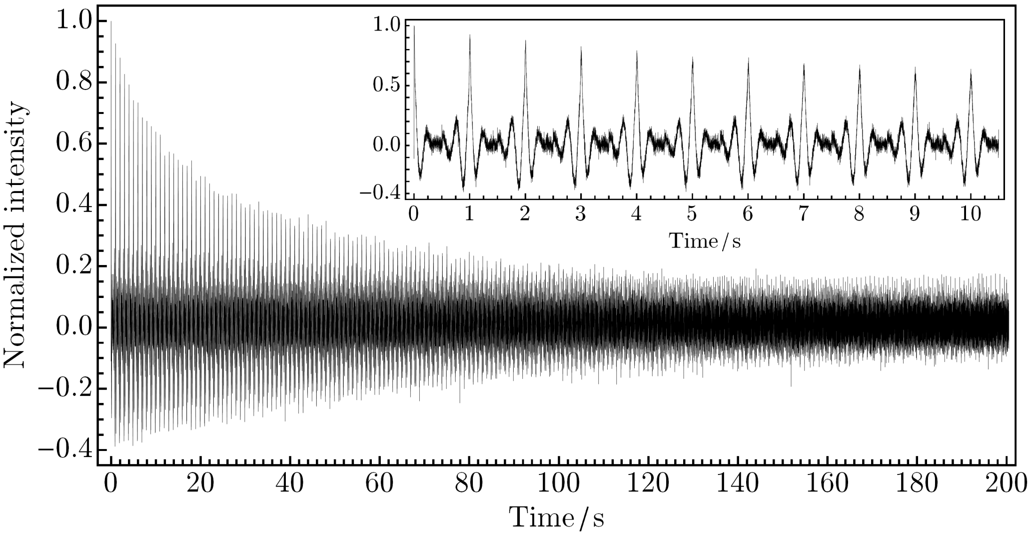

Figure 6.17: Example of the $\underline{^{15}\text{N}}^{15}\text{NO}$ MSE signal (49 scans). Experimental parameters: $N_\text{e} = 200$, $\tau = 1$ s, $\tau_\text{p}(\pi_x)/2 = \tau_\text{p}[(\pi/2)_y] = 1.066$ ms, $\tau_\text{ad} = \tau_\text{rd} = 30$ μs, $\Delta t = 0.8$ ms, $m = 1$, $n = 2$, $t_\text{pd} = 800$ s, $t_\text{acq} = 200.5$ s, $\nu_2 = 1250$, $\nu_\text{acq} = 250\,624$.

The frequency resolution of the processed MSE signal without zero-filling is given by $1/\tau_2$. The spectral bandwidth is equal to $1/\Delta t$. Both may be set independently of each other.

Examples of MSE signals are shown in Figures 6.16 and 6.17. The sample was ^{15}N doubly-labelled $^{15}\text{N}_2\text{O}$ dissolved in perdeuterated DMSO.

6.5.3 MSE Signal Processing

The MSE signal acquisition and processing in order to enhance SNR or sensitivity is not an entirely new topic. It has already been approached in different ways. In solid-state NMR, the whole MSE signal is directly Fourier transform [212–219]. A broad continuous spectrum of a low SNR is transformed into a set of sidebands (spikelets), the SNR of which is substantially enhanced. The lineshape of the spikelets is affected by homogeneous interactions. Inhomogeneous interactions give rise to a specific shape of the spikelet envelope, which is equivalent to the original solid-state spectrum [212].

Another possibility is the splitting of the MSE signal either into the individual half-echoes [122, 220] or into the whole-echoes [207], which are then added together. The combined half-echo signal resembles the FID. The combined whole-echoes may be processed into the absorption spectrum without any need of phase correction, as described in Section 6.2.1.

The two techniques examined in the current work are based on splitting the MSE signal into half-echoes. This is followed by either matched filtering [220, 221] or singular value decomposition [167].

6.5.3.1 Matched-Filter Technique

The matched-filter technique (MF-MSE) is a modified version of the "superposition method" [220]. In accordance with the block diagram in Figure 6.18, the main steps are as follows:

1. raw time-domain signal import and conversion;
2. dc offset correction;
3. signal multiplication by MF;
4. signal splitting into individual half-echoes;
5. separate summation of decreasing and increasing half-echoes;
6. phase correction to maximize frequency spectrum SNR;
7. time reversal and complex conjugation of combined increasing half-echoes;
8. addition of both half-echo signals together;
9. signal zero-filling and FT;
10. phase correction to obtain absorption lineshapes.

The raw MSE signal is stored in the binary format as two separate arrays of real and imaginary amplitudes. It is necessary to merge the two datasets into an array of complex amplitudes first (1). Such a complex n-tuple is corrected for the dc offset. The mean of the last 20 % of the samples is computed and subtracted from the whole signal (2). The MSE signal multiplication by the matched filter follows (3).

The MSE signal is split into the individual half-echoes (4). The decreasing and increasing half-echoes are co-added separately, so that only two half-echo datasets of the length $\tau_2/2$ remain (5). Each dataset is then multiplied by a constant phase correction $\mathrm{e}^{\mathrm{i}\varphi_{\text{proc}}}$ (6), where:

$$\varphi_{\text{proc}} = -\phi_0 - \phi_{\text{inst}} \tag{6.35}$$

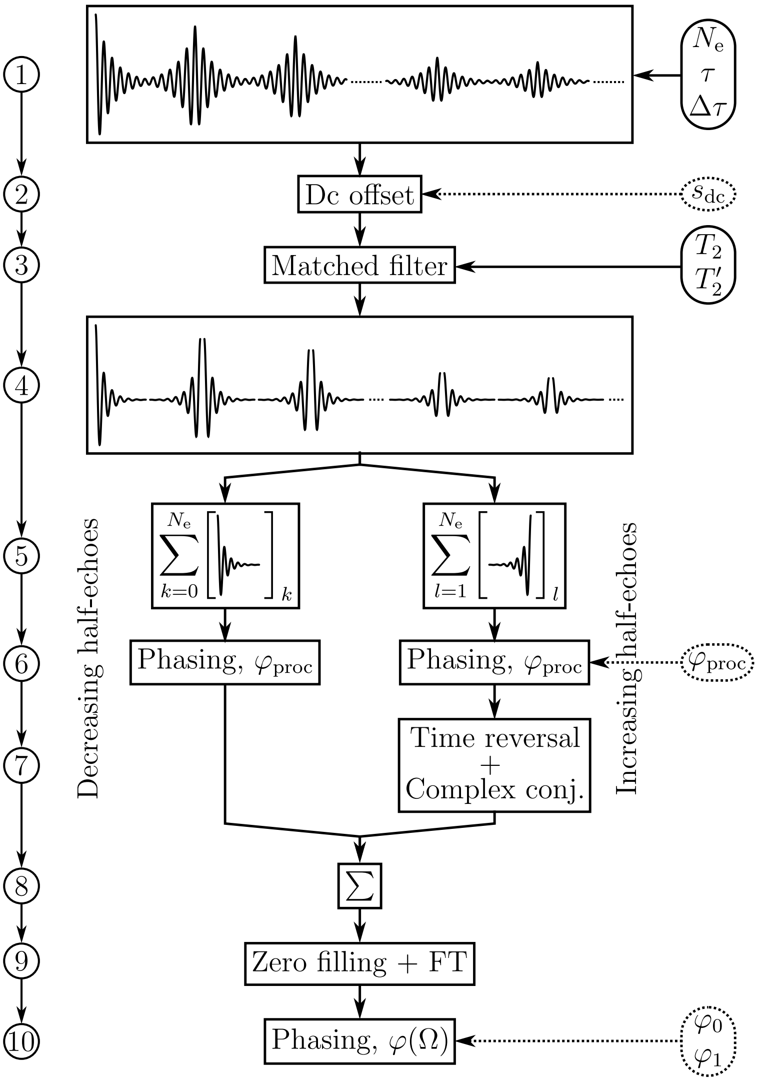

Figure 6.18: Block diagram of the MF-MSE technique for MSE signal processing. The detailed description of the individual steps is provided in the text.

which corrects for the initial and instrumental signal phases, see Eq. (6.23). In addition, the increasing half-echo dataset is time-reversed and complex conjugate, so that it becomes equivalent to the decreasing half-echo signal (7).

The value of the phase φ_{proc} is found iteratively by maximizing the SNR of the final frequency spectrum. Variation of φ_{proc} leaves the peak lineshapes almost unaffected, since the imaginary parts of the two signals nearly cancel, but influences their amplitudes. Assume that the combined decreasing and increasing half-echoes are denoted $\boldsymbol{s}_{\mathrm{dec}}$ and $\boldsymbol{s}_{\mathrm{inc}}$, respectively. Then:

$$\boldsymbol{s}_{\mathrm{dec}}\,\mathrm{e}^{\mathrm{i}\varphi_{\mathrm{proc}}} + \boldsymbol{s}_{\mathrm{inc}}\,\mathrm{e}^{-\mathrm{i}\varphi_{\mathrm{proc}}} = (\boldsymbol{s}_{\mathrm{dec}} + \boldsymbol{s}_{\mathrm{inc}})\cos\varphi_{\mathrm{proc}} + \mathrm{i}\,(\boldsymbol{s}_{\mathrm{dec}} - \boldsymbol{s}_{\mathrm{inc}})\sin\varphi_{\mathrm{proc}} \tag{6.36}$$

If $\boldsymbol{s}_{\mathrm{dec}} \approx \boldsymbol{s}_{\mathrm{inc}}$, only the first term survives and its amplitude is modulated by $\cos\varphi_{\mathrm{proc}}$.

Finally, $\boldsymbol{s}_{\mathrm{dec}}$ and $\boldsymbol{s}_{\mathrm{inc}}$ are summed together. A proper time coordinate is added to each complex amplitude, so that the full time-domain signal $s_{\mathrm{proc}}(t)$ is obtained (8):

$$s_{\mathrm{proc}}(t) = \sum_{j=0}^{N_{\mathrm{e}}} s_{\mathrm{MSE}}(j\tau + t)\,h_{\mathrm{MSE}}(j\tau + t)\,\mathrm{e}^{\mathrm{i}\varphi_{\mathrm{proc}}} + \sum_{j=1}^{N_{\mathrm{e}}} \{s_{\mathrm{MSE}}(j\tau - t)\}^{*}\,h_{\mathrm{MSE}}(j\tau - t)\,\mathrm{e}^{-\mathrm{i}\varphi_{\mathrm{proc}}} \tag{6.37}$$

The two sums represent the decreasing and increasing half-echo signals, respectively. After zero-filling and FT (9), phase correction is applied to get the absorption lineshapes for all peaks (10).

In order to perform the whole procedure, several input constants need to be provided in advance, since they cannot be deduced from the data. Some constants are the parameters of the pulse sequence, directly available in the log files of a given measurement. Such constants are the number of echoes N_{e}, the π-pulse spacing τ, and the dwell time Δt. The number of samples per half-echo $\nu_2/2$ can be determined from the data-length ν_{acq}. The dwell time Δt also serves for computing of the time coordinates. Evaluation of the matched filter is impossible without a prior knowledge of the relaxation time constants T_2 and T_2'. Their determination is described in detail in Section 5.4.

The dc offset correction, as well as the phase corrections may be performed fully automatically. Otherwise, the values of the complex signal offset (s_{dc}) and the two (φ_{proc} and φ_0) or three (also φ_1) phases need to be provided. In the simple case of one singlet or doublet, a zero-order phase correction φ_0 is usually sufficient.

6.5.3.2 Singular Value Decomposition Technique

The fundamental motivation behind the use of the singular value decomposition technique (SVD-MSE) instead of matched filtering was to avoid measurement of the T_2 value, which is often very precarious. A similar approach has already been successfully used in MRI [167]. The scheme of the SVD-MSE technique is shown in Figure 6.19, and the main steps are as follows:

1. raw time-domain signal import and conversion;

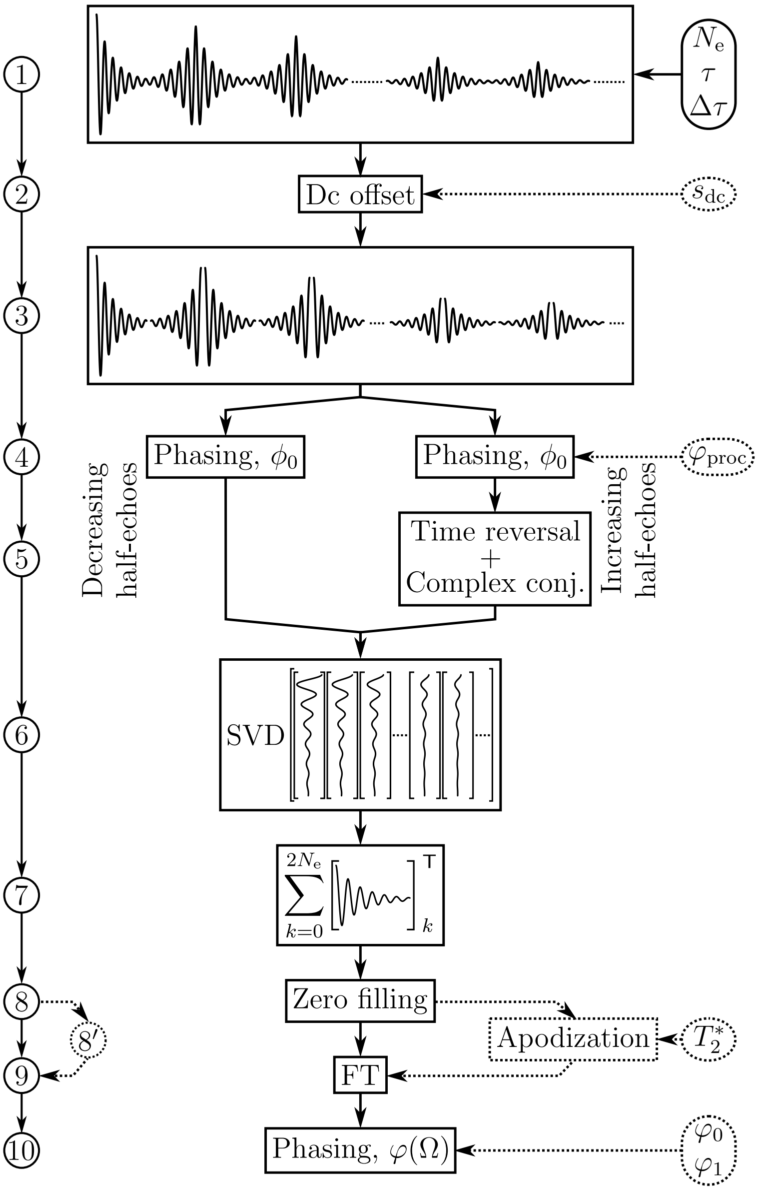

Figure 6.19: Block diagram of the SVD-MSE technique for the MSE signal processing. The detailed description of the individual steps is provided in the text.

2. dc offset correction;
3. signal splitting into individual half-echoes;
4. phase correction to maximize frequency spectrum SNR;
5. time reversal and complex conjugation of increasing half-echoes;
6. column-wise arrangement of half-echoes into matrix and SVD noise reduction;
7. summation of recomputed matrix columns;
8. signal zero-filling;

$8'$. signal apodization;

9. FT;
10. phase correction to obtain absorption lineshapes.

Steps (1) to (5) are the same as in the MF-MSE technique, except for MF application, which is not required in the SVD-MSE technique. After correcting all individual half-echoes, these are arranged column-wise into the measurement matrix (4.40). Due to its dimensions, the thin SVD method (4.45) is preferably used. The smallest singular values are zeroed and the modified measurement matrix (4.44) is recomputed (6). The matrix columns are summed up into one dataset (7). The time coordinates are added in order to obtain the full time-domain signal, which is then zero-filled (8). The signal may be apodized for example by a decaying exponential with time constant T_2^* ($8'$), see Eq. (6.25). After FT (9), the frequency spectrum is phase-corrected, if necessary (10).

SVD-MSE technique uses the same set of input parameters as the MF-MSE technique, except for T_2 and possibly also T_2^*. In the case that the MSE signal SNR is greater than 1, or in the case that it comprises $\gtrsim 100$ half-echo signals, the discrepancy between the biggest singular value(s) and the rest is usually big enough to set the threshold for zeroing safely. In step (6), it makes no difference whether the half-echoes are arranged column-wise or row-wise. SVD gives the same results for both cases. Attention has to be paid to step (7). If the half-echo signals are treated as columns in step (6), they have to be added together column-wise.

The technique of SVD noise reduction in the time domain may also be adapted for the frequency domain. Although this approach gives the same results, as elucidated in Section 4.3.4, the FT of all individual half-echoes requires extra computational time.

6.6 Sensitivity Enhancement Observation

The MSE pulse sequence was performed on the 300 MHz Varian Infinity+ NMR instrument. The spectrometer control and pulse programing was accomplished by using the SpinSight software. Neither gradient coils, nor deuterium lock were available, which significantly limited the spectrometer performance and also the potential possibilities regarding the spin-echo pulse sequence. A 10 mm liquid state probe was employed.

6.6.1 $^{15}NH_4{}^{15}NO_3$

6.6.1.1 Experimental Realization

The MSE sequence was tested on $^{15}NH_4{}^{15}NO_3$ dissolved in D_2O. MSE signals were recorded for various values of the pulse sequence parameters: the number of echoes N_e, the half of the π-pulse spacing $\tau_{1/2} \equiv \tau/2$, and the total number of acquired samples ν_{acq}, as introduced in Section 6.5.2.

The maximum number of samples, which the spectrometer was able to acquire, was limited to $\nu_{max} = 2^{18} = 262\,144$ (or 256k) samples. This specific limitation is likely to be irrelevant on some other spectrometers. ν_{max} may also be given any other value, if a different maximum length of the MSE signal is desired, see Figure 6.16.

In order to avoid problems related to the machine precision of real numbers and to acquire exactly the intended number of samples within the MSE signal, pairs of the parameters $\{N_e, \tau_{1/2}\}$ were computed according to:

$$N_e = \left\lfloor \frac{(\nu_{max} - m)\,\Delta t}{\tau} - \frac{1}{2} \right\rfloor \tag{6.38}$$

$$\tau_{1/2} = \left\lfloor \frac{\nu_{max} - m}{2N_e + 1} \frac{\Delta t}{(1\,\mathrm{ms})} \right\rfloor \times (1\,\mathrm{ms}) \tag{6.39}$$

$\tau_{1/2}$ was provided with a millisecond accuracy. The number of unused points $(\nu_{max} - \nu_{acq})$ was kept minimal.

As apparent from Table 5.2, the T_2'/T_2 ratio is very large for the $^{15}ND_4^+$ site. Therefore, the corresponding SNR enhancement for the given values of T_2 and T_2' would be at best:

$$\lim_{\tau \to 0} \varepsilon_{MSE} \approx 2.03 \text{ for } T_2'/T_2 \approx 0.323 \tag{6.40}$$

Other inconvenient properties of $^{15}ND_4^+$ are the very long T_1 and quite short time constants T_2 and T_2^*. The time constants of the $^{15}NO_3^-$ site are similar to those of $^{15}N_2O$. Therefore, the $^{15}NO_3^-$ site was chosen for the trials.

6.6.1.2 MF-MSE Technique

The SNR enhancement was studied for different strengths of the $^{15}NO_3^-$ signal, see Figure 6.20. To achieve less intense signals, the MSE pulse sequence in Figure 6.15 was tentatively used with deliberately short duration of the initial $(\pi/2)_y$ pulse. The relative transverse magnetization intensity is then given by:

$$M_{xy}/M_0 = \sin(\omega_{\mathrm{nut}}\tau_{\mathrm{p}}) \tag{6.41}$$

However, it became clear that the remaining longitudinal magnetization has a destructive effect on the MSE signal. An alternative solution was proposed. The inversion recovery sequence was combined with the MSE sequence in such a way that the second $(\pi/2)$ pulse of the inversion recovery sequence became the first pulse of the MSE sequence:

$$\overbrace{\pi_x - \tau_{\mathrm{ir}} - (\pi/2)_y}^{\text{Inversion recovery}}\!\!\!\!\!\!\!\!\!\underbrace{\!\!\!\! - \tau/2 - [\pi_x - \tau\,]_{N_{\mathrm{e}}}}_{\text{MSE sequence}} \tag{6.42}$$

Any transverse magnetization generated due to the initial π_x pulse imperfections decays during the time interval τ_{ir} before the $(\pi/2)_y$ pulse. The recovering longitudinal magnetization is converted into transverse magnetization and the train of π_x pulses follows. In all cases, a SNR enhancement up to a factor of 10 was achieved, see Figure 6.20.

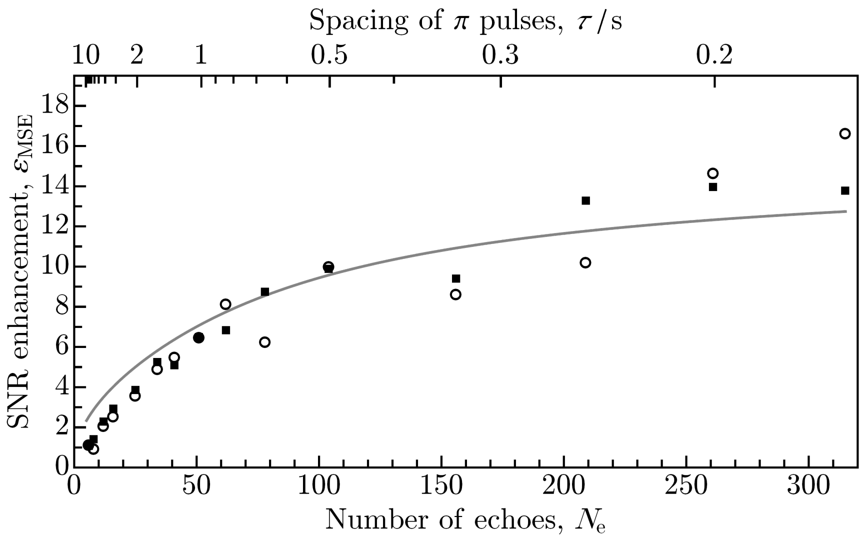

Figure 6.20: The enhancement $\varepsilon_{\mathrm{MSE}}$ for different $^{15}NO_3^-$ signal strengths, when using the MF-MSE technique for processing the MSE signal. The plot markers denote the following signal strengths: 100 % M_0 (▪) and 11.06 % M_0 (○).

6.6.1.3 SVD-MSE Technique

Recalling the block diagram from Figure 6.19, two different approaches were considered. The SNR enhancement after the SVD noise reduction without and with exponential apodization are shown in Figures 6.21 and 6.22, respectively.

Performance of the SVD-MSE technique relative to the MF-MSE technique is compared by means of a ratio $\varepsilon_{\mathrm{rel}}$:

$$\varepsilon_{\mathrm{rel}} = \frac{\varepsilon_{\mathrm{MSE}}(\mathrm{SVD})}{\varepsilon_{\mathrm{MSE}}(\mathrm{MF})} = \left(\frac{\mathrm{SNR}_{\mathrm{MSE}}(\mathrm{SVD})}{\mathrm{SNR}_{\mathrm{FID}}(\mathrm{MF})}\right)\left(\frac{\mathrm{SNR}_{\mathrm{MSE}}(\mathrm{MF})}{\mathrm{SNR}_{\mathrm{FID}}(\mathrm{MF})}\right)^{-1} = \frac{\mathrm{SNR}_{\mathrm{MSE}}(\mathrm{SVD})}{\mathrm{SNR}_{\mathrm{MSE}}(\mathrm{MF})} \tag{6.43}$$

Here $\varepsilon_{\mathrm{MSE}}(\mathrm{SVD})$ is the ratio of the frequency spectrum SNR, $\mathrm{SNR}_{\mathrm{MSE}}(\mathrm{SVD})$, of the MSE signal processed by the SVD-MSE technique, and the frequency spectrum SNR, $\mathrm{SNR}_{\mathrm{FID}}(\mathrm{MF})$, of a single FID treated by the matched filter (6.25) in the same way as in the case of the MF-MSE technique. The quantities $\varepsilon_{\mathrm{MSE}}(\mathrm{MF}) \equiv \varepsilon_{\mathrm{MSE}}$, $\mathrm{SNR}_{\mathrm{MSE}}(\mathrm{MF}) \equiv \mathrm{SNR}_{\mathrm{MSE}}$ and $\mathrm{SNR}_{\mathrm{FID}}(\mathrm{MF}) \equiv \mathrm{SNR}_{\mathrm{FID}}$ are introduced in Eq. (6.24).

The dependence of $\varepsilon_{\mathrm{rel}}$ for the SVD-MSE technique without and with exponential apodization is shown in Figures 6.23 and 6.24, respectively. Whenever $\varepsilon_{\mathrm{rel}} > 1$, the SVD-MSE technique gives a better SNR enhancement compared to the MF-MSE technique and vice versa.

The useful signal was represented by only one dominant singular value, see the plot d) in Figures 6.25 and 6.26 for illustration, depicting a similar situation for $^{15}\mathrm{N}_2\mathrm{O}$. The remaining singular values, which were much smaller than the largest singular value, were zeroed. Without exponential apodization, $\varepsilon_{\mathrm{rel}}$ ranges between 0.7 and 0.9, and the MF-MSE technique gives better performance. With exponential apodization, the $\varepsilon_{\mathrm{rel}}$ is between 0.9 and 1.1, therefore the SVD-MSE technique works similarly well as the MF-MSE technique.

The initial points in Figures 6.20 to 6.24 result from the MSE signals with small numbers of echoes N_{e}. Due to less efficient refocusing, corresponding frequency spectra contain a significant portion of the noise. Consequently, all singular values are too close together, which makes a proper setting of the threshold for zeroing impossible. Compared to the theoretical prediction, the MF-MSE technique is less effective in this case, too.

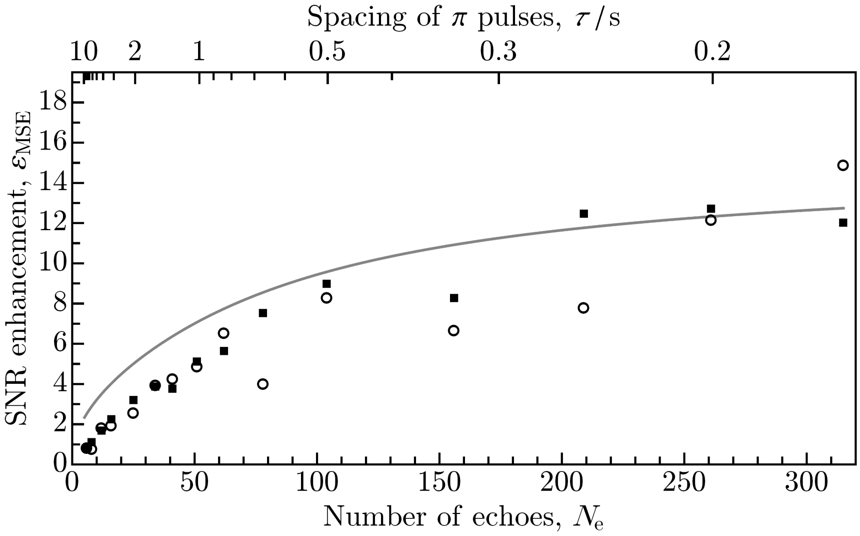

Figure 6.21: The enhancement $\varepsilon_{\mathrm{MSE}}$ for different $^{15}\mathrm{NO}_3^-$ signal strengths, when using the SVD-MSE technique without apodization for processing the MSE signal. The plot markers denote the following signal strengths: 100 % M_0 (▪) and 11.06 % M_0 (∘).

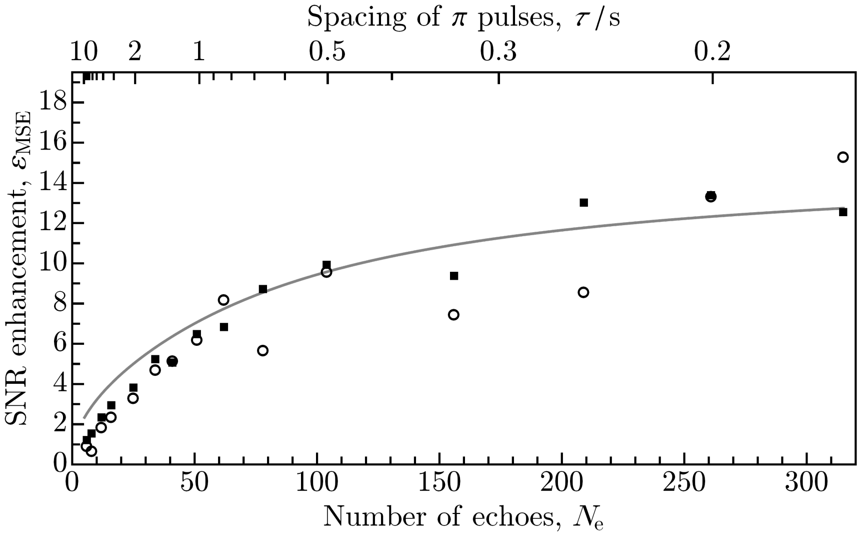

Figure 6.22: The enhancement $\varepsilon_{\mathrm{MSE}}$ for different $^{15}\mathrm{NO}_3^-$ signal strengths, when using the SVD-MSE technique with exponential apodization for processing the MSE signal. The plot markers denote the following signal strengths: 100 % M_0 (▪) and 11.06 % M_0 (∘).

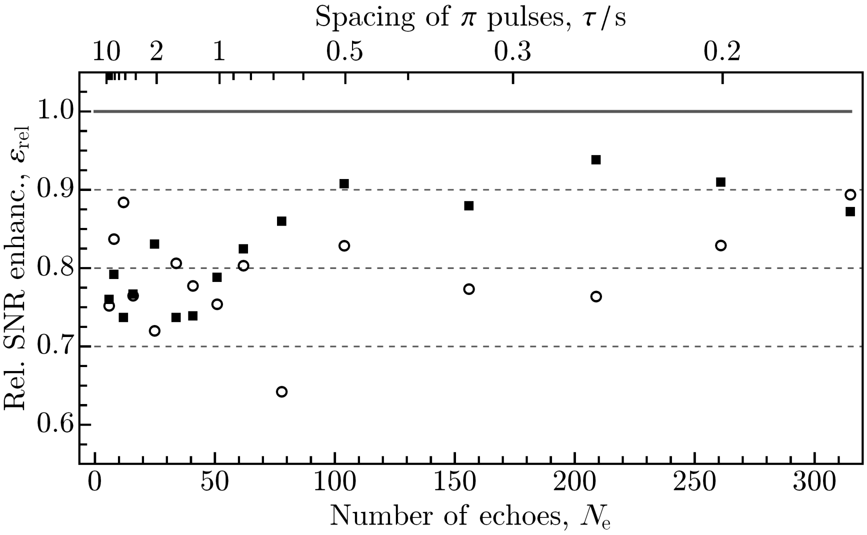

Figure 6.23: The enhancement $\varepsilon_{\mathrm{rel}}$ for different $^{15}\mathrm{NO}_3^-$ signal strengths achieved by using the SVD-MSE technique without apodization, relative to the MF-MSE technique. The plot markers denote the following signal strengths: 100 % M_0 (▪) and 11.06 % M_0 (∘).

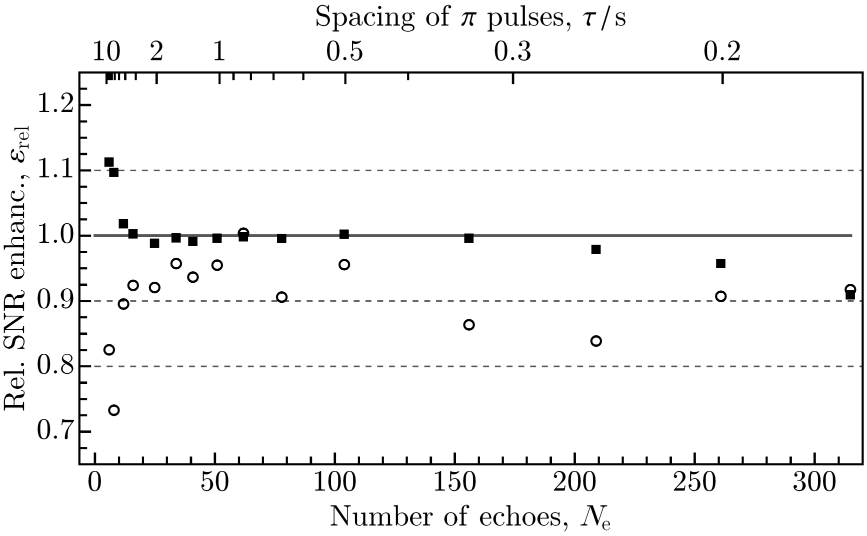

Figure 6.24: The enhancement $\varepsilon_{\mathrm{rel}}$ for different $^{15}\mathrm{NO}_3^-$ signal strengths achieved by using the SVD-MSE technique with exponential apodization, relative to the MF-MSE technique. The plot markers denote the following signal strengths: 100 % M_0 (▪) and 11.06 % M_0 (∘).

6.6.2 $^{15}N_2O$

In the case of $^{15}NH_4{}^{15}NO_3$, both the MF-MSE and SVD-MSE techniques provided the SNR enhancement of up to an order of magnitude, when applied during the MSE signal processing. The next step was to examine their performance in the case of $^{15}N_2O$. Examples from the $^{15}N_2O$ MSE signal processing are shown in Figures 6.25 and 6.26.

6.6.2.1 MF-MSE Technique

Pairs of values $\{N_\mathrm{e}, \tau_{1/2}\}$ were computed by using Eqs. (6.38) and (6.39), and the MSE signals were acquired. Following the same practice as in the case of $^{15}NH_4{}^{15}NO_3$, the achieved SNR enhancement after application of the MF-MSE technique for each doublet separately, and also the average values from both doublets, are shown in Figure 6.27. All error bars are computed as standard deviation of the experimental data.

The experimental values of the SNR enhancement ε_MSE deviate slightly from the theoretically predicted dependence given by Eq. (6.26). Due to a much higher number of points, the effect is much better visible in Figure 6.27 than for the similar plot for $^{15}NH_4{}^{15}NO_3$ in Figure 6.20.

The points on the left-hand side were acquired by using large values of the π-pulse spacing τ. In this case, the refocusing of the MSE signal was inefficient, NMR signal decayed faster and the corresponding frequency spectra contained more noise. The deviation of the points on the right-hand side arises from a heavily compromised resolution in the frequency-domain spectrum due to a small number of samples per half-echo signal and truncation artifacts. Another reason is a changed phasing of the frequency spectra, since only one set of phase corrections was used for all datasets, which were recorded randomly during a measurement series lasting many hours. A minor contribution to this kind of deviation comes from the cumulative pulse-length imperfections as N_e approaches 1000 π pulses.

6.6.2.2 SVD-MSE Technique

The SNR enhancement provided by the SVD-MSE technique without and with exponential apodization are shown in Figures 6.28 and 6.29, respectively. The comparison of the SVD-MSE and the MF-MSE techniques is shown in Figures 6.30 and 6.31.

Similarly with $^{15}NH_4{}^{15}NO_3$, the SVD-MSE technique without apodization gives slightly worse results than MF-MSE. When exponential apodization is used, the SNR enhancement is about the same or slightly better than that obtained with the MF-MSE technique.

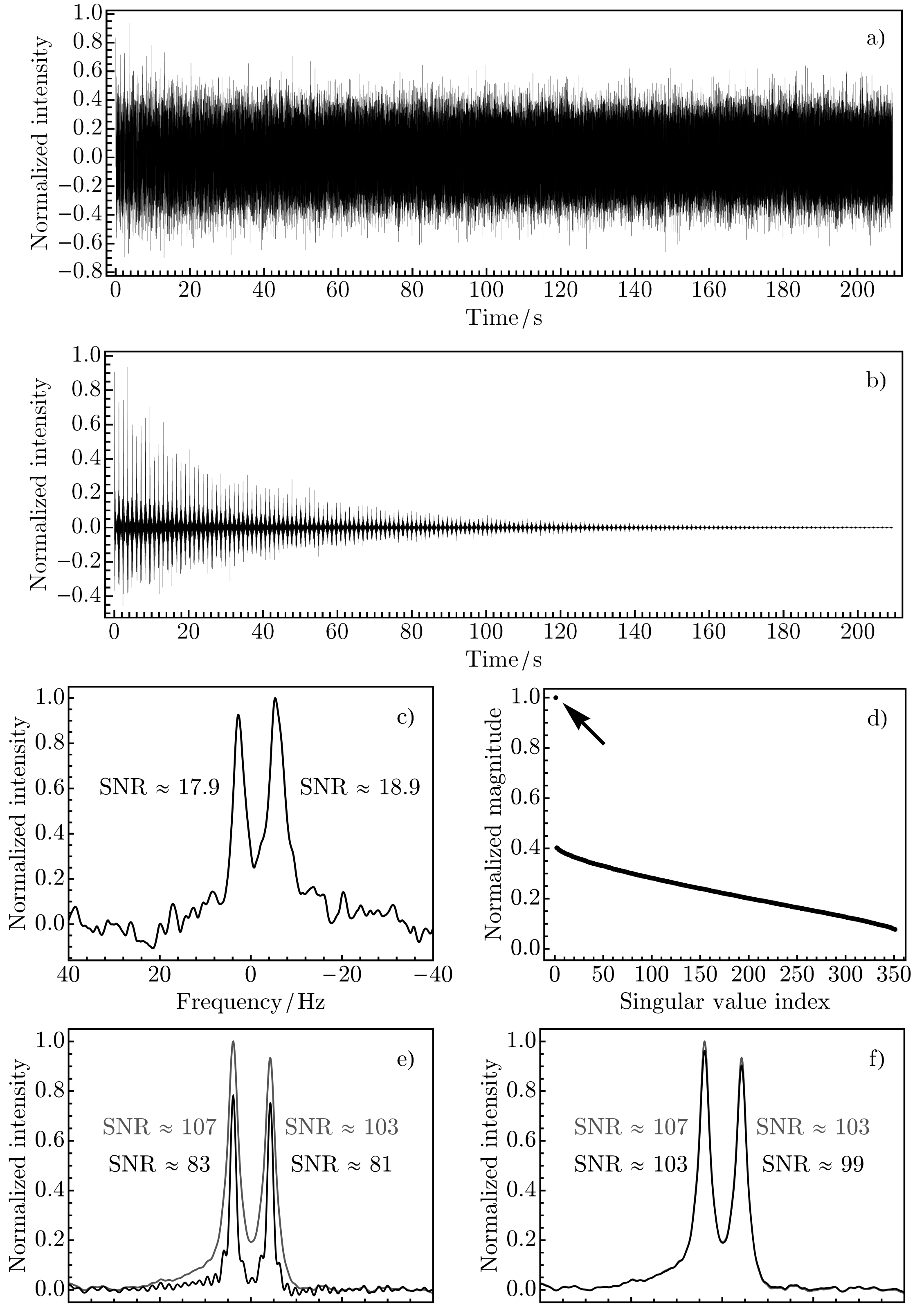

Figure 6.25: Example of $^{15}\mathrm{N}\underline{^{15}\mathrm{N}}\mathrm{O}$ MSE signal processing (N_e = 175, τ = 1194 ms). a) The MSE signal as recorded. b) The MSE signal after matched weighting. c) FT of a single FID after matched weighting. d) Normalized singular values. There is only one dominant singular value emphasized by the arrow. e) SVD-MSE without apodization (black) compared to MF-MSE technique (gray). f) SVD-MSE with exponential apodization (black) compared to MF-MSE technique (gray).

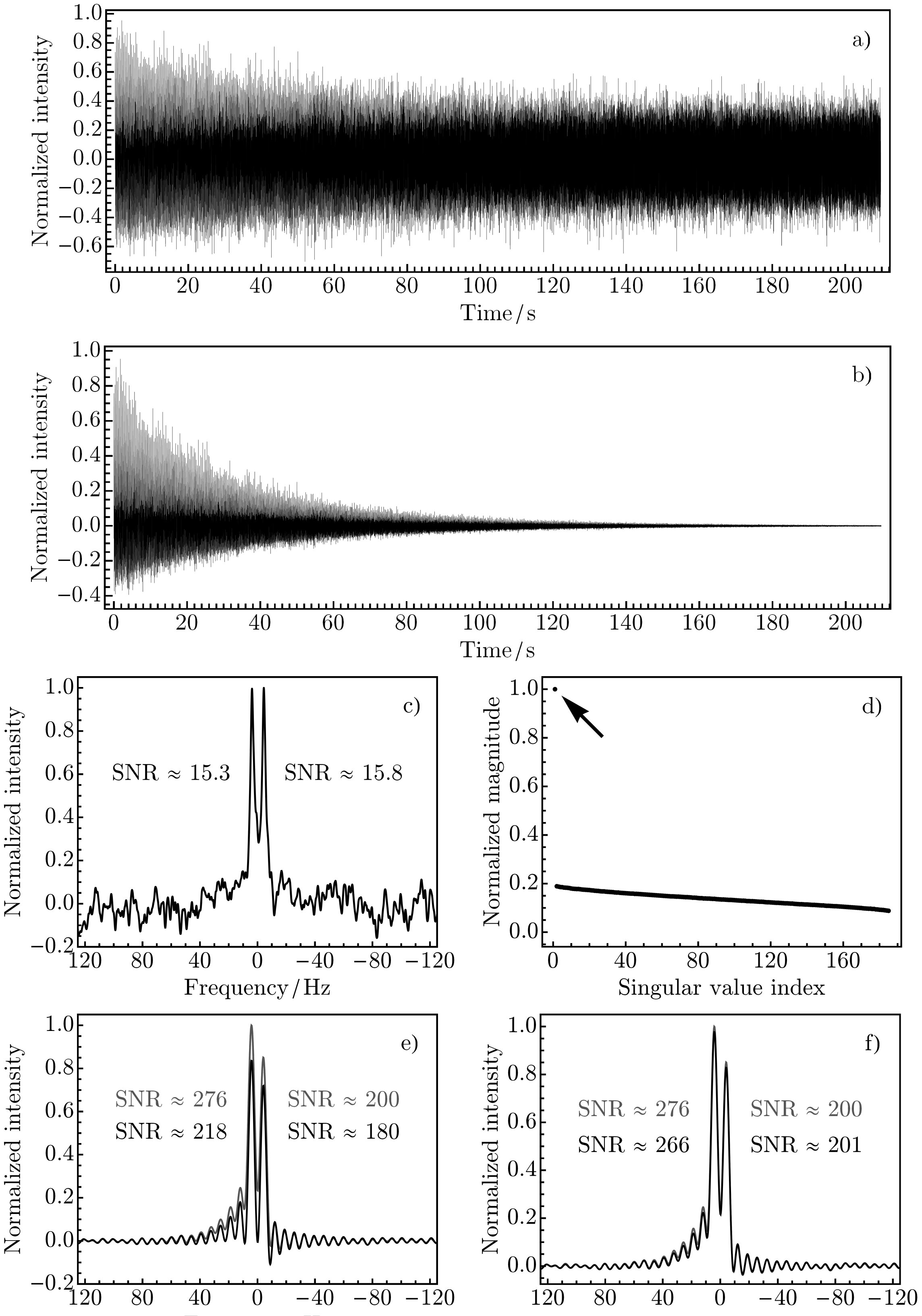

Figure 6.26: Example of $\underline{^{15}\mathrm{N}}{}^{15}\mathrm{NO}$ MSE signal processing (N_e = 708, τ = 296 ms). a) The MSE signal as recorded. b) The MSE signal after matched weighting. c) FT of a single FID after matched weighting. d) Normalized singular values. There is only one dominant singular value emphasized by the arrow. e) SVD-MSE without apodization (black) compared to MF-MSE technique (gray). f) SVD-MSE with exponential apodization (black) compared to MF-MSE technique (gray).

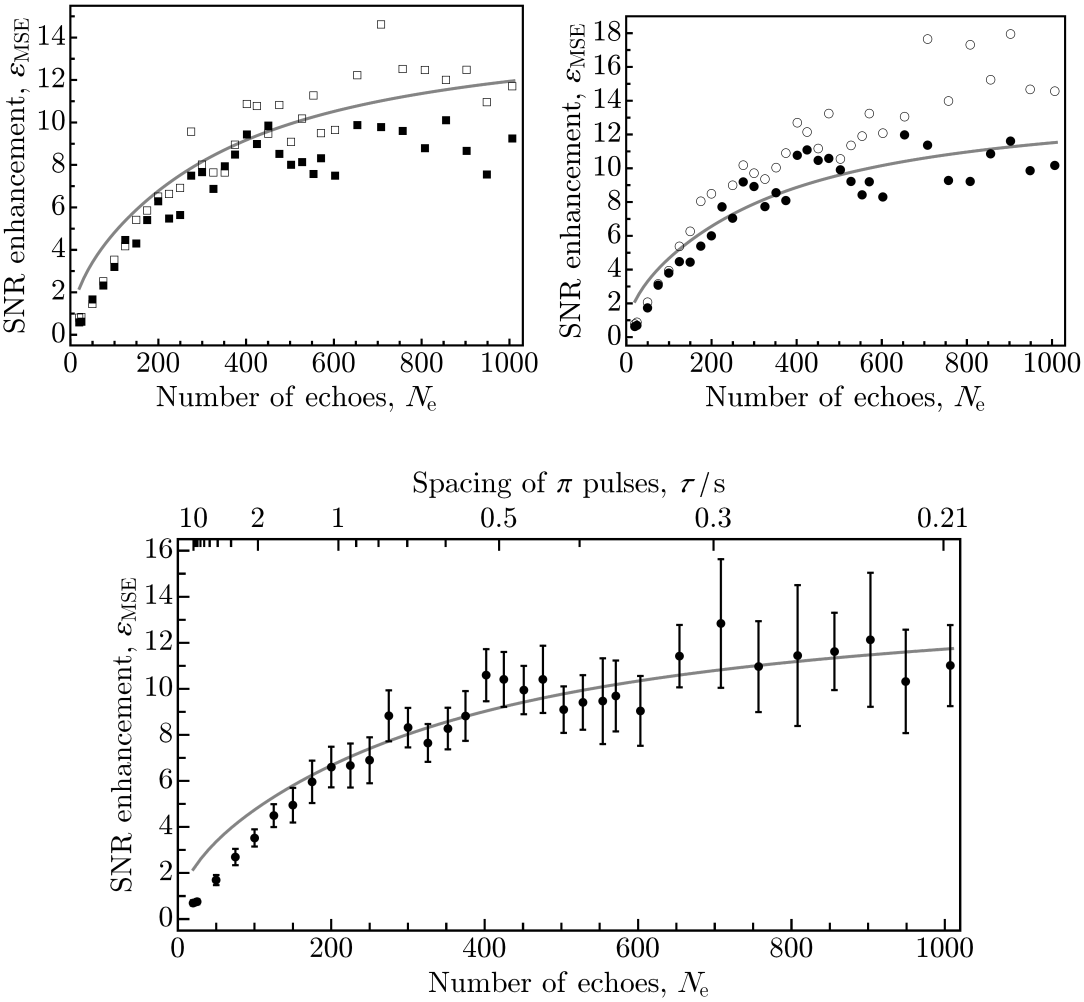

Figure 6.27: The enhancement ε_{MSE} for $^{15}\text{N}_2\text{O}$ in DMSO, when using the MF-MSE technique for the MSE signal processing. Top left: The enhancement ε_{MSE} for peak 1 (■) and peak 2 (□) in the $^{15}\text{N}\underline{^{15}\text{N}}\text{O}$ doublet. Top right: The enhancement ε_{MSE} for peak 3 (●) and peak 4 (○) in the $\underline{^{15}\text{N}}{}^{15}\text{NO}$ doublet. Bottom: The average enhancement ε_{MSE} for both doublets. Gray lines denote the maximum theoretical SNR enhancement as given by Eq. (6.26) for the values of time constants from Table 5.2.

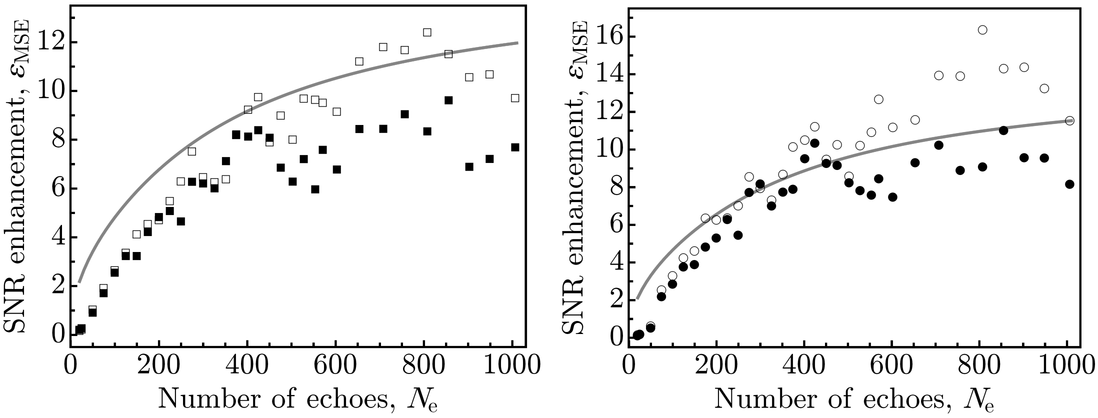

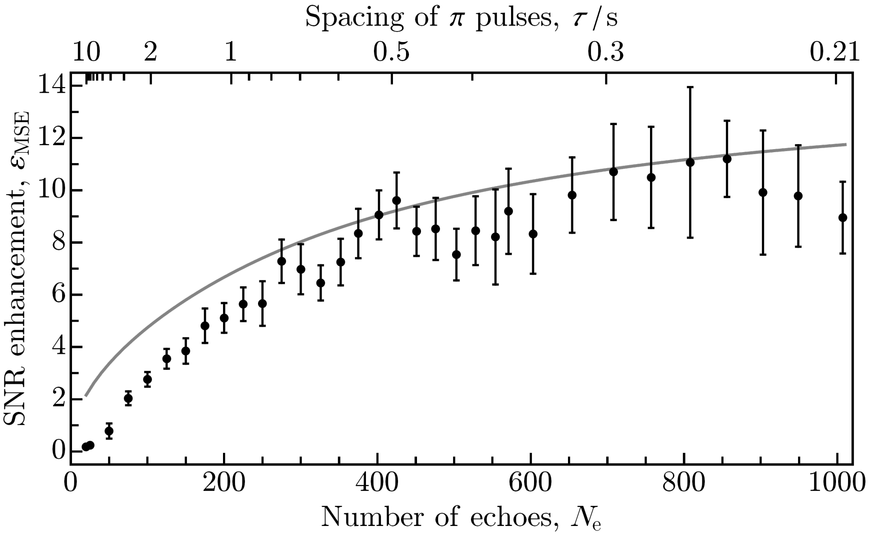

Figure 6.28: The enhancement $\varepsilon_{\mathrm{MSE}}$ for $^{15}N_2O$ in DMSO, when using the SVD-MSE technique without apodization for the MSE signal processing. Top left: The enhancement $\varepsilon_{\mathrm{MSE}}$ for peak 1 (▪) and peak 2 (▫) in the $^{15}N\underline{^{15}N}O$ doublet. Top right: The enhancement $\varepsilon_{\mathrm{MSE}}$ for peak 3 (•) and peak 4 (◦) in the $\underline{^{15}N}{}^{15}NO$ doublet. Bottom: The average enhancement $\varepsilon_{\mathrm{MSE}}$ for both doublets. Gray lines denote the maximum theoretical SNR enhancement as given by Eq. (6.26) for the values of time constants from Table 5.2.

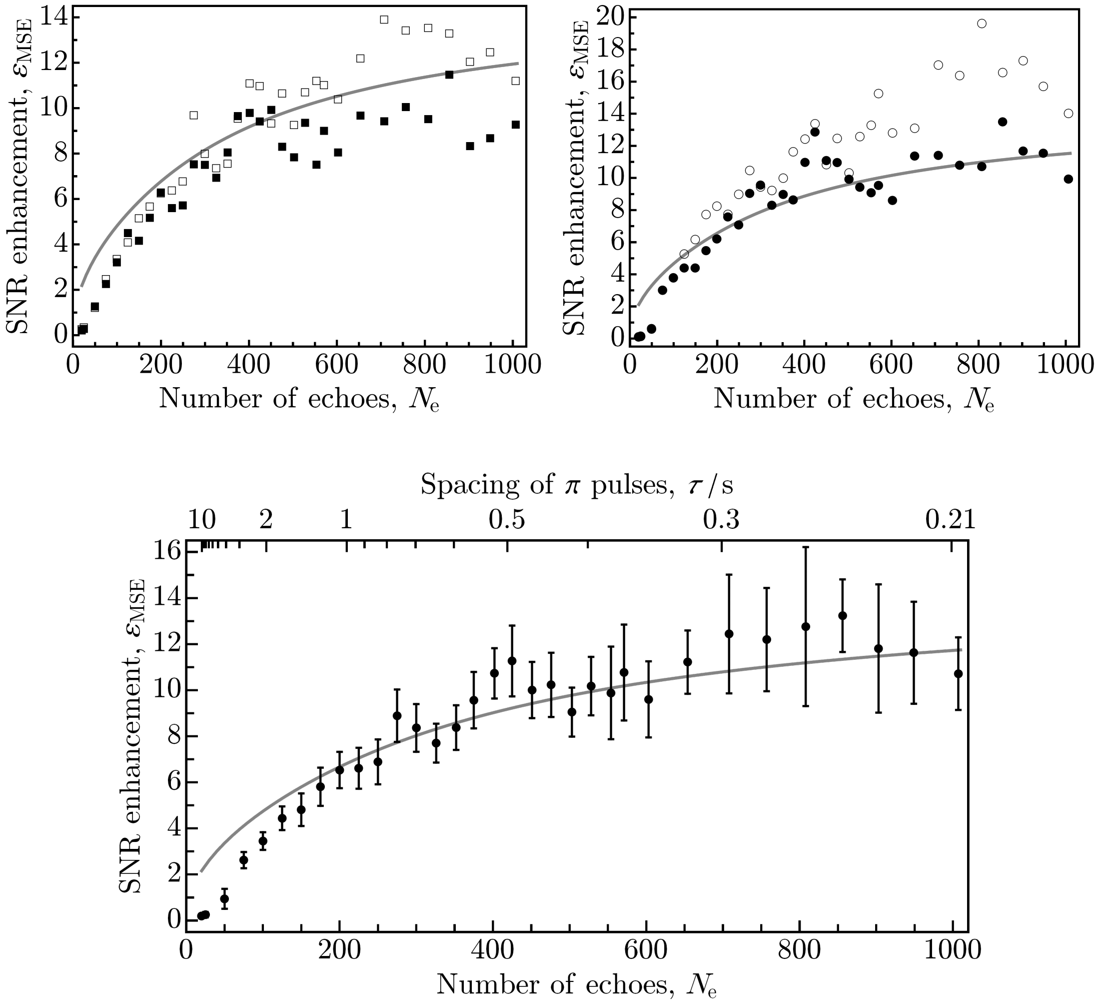

Figure 6.29: The enhancement $\varepsilon_{\mathrm{MSE}}$ for $^{15}\mathrm{N}_2\mathrm{O}$ in DMSO, when using the SVD-MSE technique with exponential apodization for the MSE signal processing. Top left: The enhancement $\varepsilon_{\mathrm{MSE}}$ for peak 1 (■) and peak 2 (□) in the $^{15}\mathrm{N}\underline{^{15}\mathrm{N}}\mathrm{O}$ doublet. Top right: The enhancement $\varepsilon_{\mathrm{MSE}}$ for peak 3 (●) and peak 4 (○) in the $\underline{^{15}\mathrm{N}}{}^{15}\mathrm{NO}$ doublet. Bottom: The average enhancement $\varepsilon_{\mathrm{MSE}}$ for both doublets. Gray lines denote the maximum theoretical SNR enhancement as given by Eq. (6.26) for the values of time constants from Table 5.2.

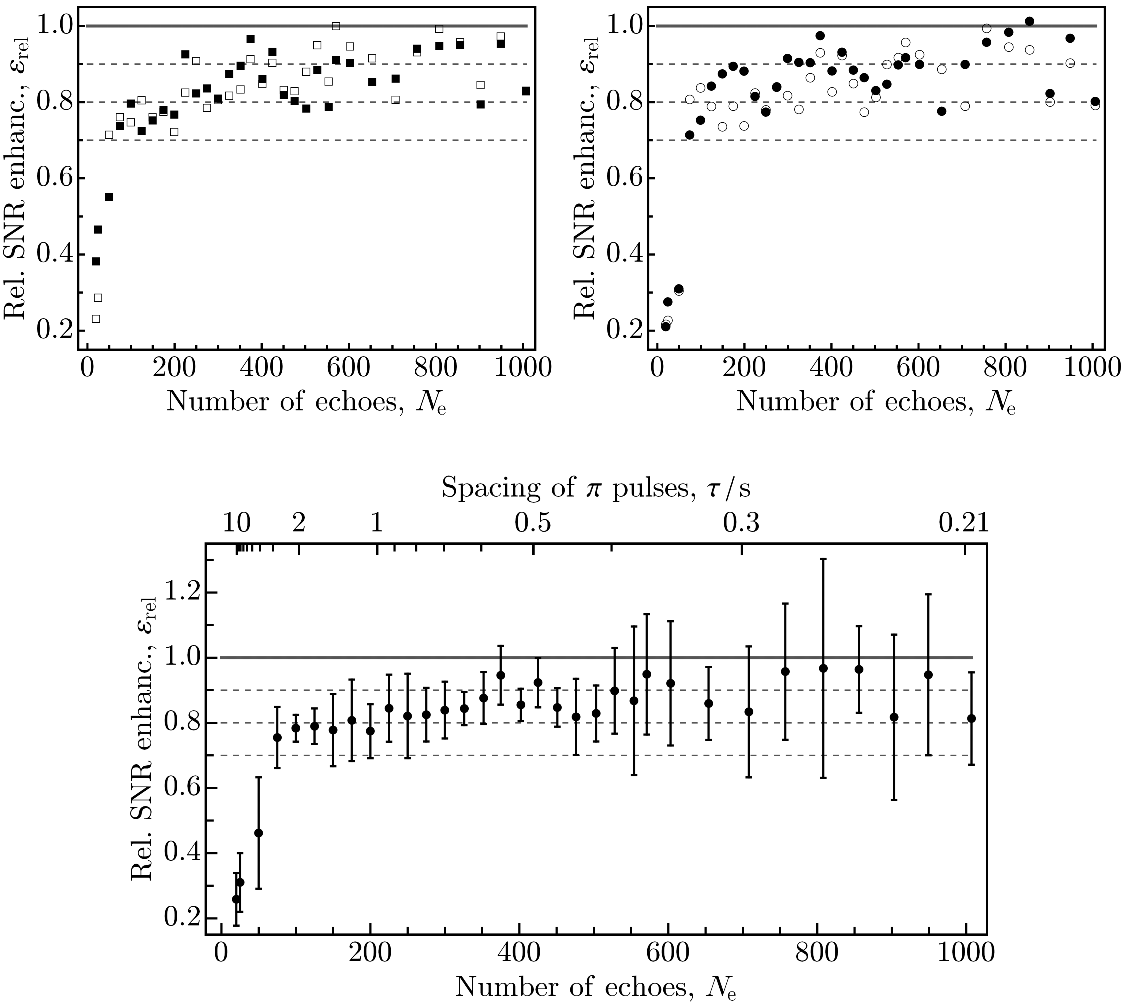

Figure 6.30: The enhancement $\varepsilon_{\mathrm{rel}}$ for $^{15}\mathrm{N}_2\mathrm{O}$ in DMSO, when using the SVD-MSE technique without apodization for the MSE signal processing, relative to the matched filter technique, as defined in Eq. (6.43). Top left: The enhancement $\varepsilon_{\mathrm{rel}}$ for peak 1 (■) and peak 2 (□) in the $^{15}\mathrm{N}\underline{^{15}\mathrm{N}}\mathrm{O}$ doublet. Top right: The enhancement $\varepsilon_{\mathrm{rel}}$ for peak 3 (●) and peak 4 (○) in the $\underline{^{15}\mathrm{N}}{}^{15}\mathrm{NO}$ doublet. Bottom: The average enhancement $\varepsilon_{\mathrm{rel}}$ for both doublets.

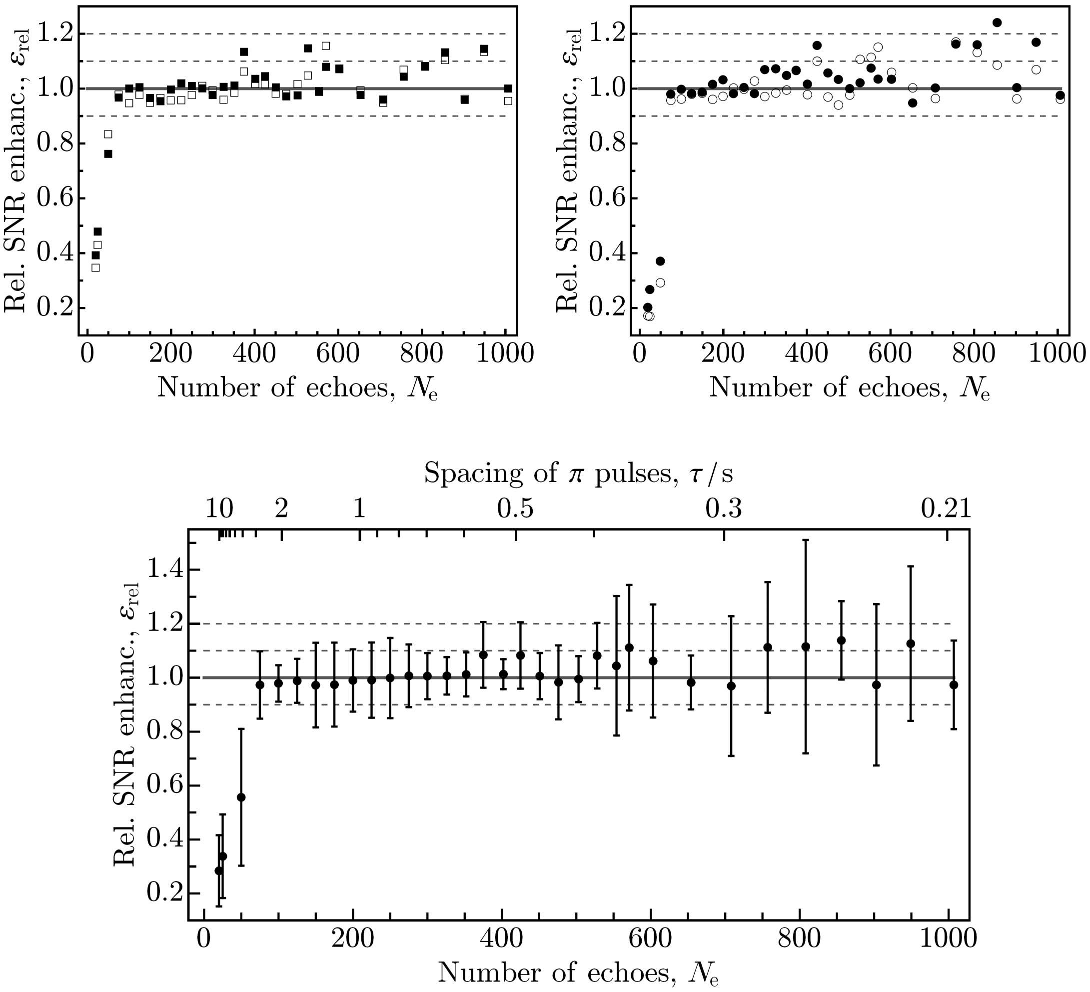

Figure 6.31: The enhancement $\varepsilon_{\mathrm{rel}}$ for $^{15}\mathrm{N}_2\mathrm{O}$ in DMSO, when using the SVD-MSE technique with exponential apodization for the MSE signal processing, relative to the MF-MSE technique, as defined in Eq. (6.43). Top left: The enhancement $\varepsilon_{\mathrm{rel}}$ for peak 1 (■) and peak 2 (□) in the $^{15}\mathrm{N}\underline{^{15}\mathrm{N}}\mathrm{O}$ doublet. Top right: The enhancement $\varepsilon_{\mathrm{rel}}$ for peak 3 (●) and peak 4 (○) in the $\underline{^{15}\mathrm{N}}^{15}\mathrm{NO}$ doublet. Bottom: The average enhancement $\varepsilon_{\mathrm{rel}}$ for both doublets.

Chapter 7

Field-Dependent $^{15}N_2O$ Relaxation

Several important works on relaxation in NMR appeared so far [10, 24, 26, 37, 222–224], but none of them treated singlet states. After 2004, core works on singlet state relaxation were published alongside with new experimental observations [36, 56, 72, 78, 79, 81, 225]. They treated individual aspects of the singlet relaxation by using various approaches. The first attempt towards unified description of basic, well understood relaxation processes may be found in work of Dr. Pileio [226].

7.1 Formal Relaxation Theory

7.1.1 Master Equation

Assume the spin system under consideration is described by the wavefunction. The most general solution of the Schrödinger equation (2.36) is provided by Eq. (2.42). In the case of a general time-dependent Hamiltonian, an exact solution does not exist. The expansion hidden behind the Dyson time-ordering superoperator (C.9) may, however, be truncated at a desired accuracy of approximation, integrated and evaluated.

A similar derivation holds in the case of the density operator, which fully characterizes any spin system. After introducing several simplifications, which separate the evolution of the spin system from the evolution of the lattice, which evolves stochastically at much smaller time scales than the nuclear spins, the Bloch-Redfield-Wangsness theory arises [223].

Assume the Liouville-von Neumann equation (2.73) written in the following form [227]:

$$\frac{\partial}{\partial t}\hat{\rho}(t) = -\mathrm{i}\left(\hat{\hat{H}}_0 + \hat{\hat{H}}_1(t)\right)\hat{\rho}(t) \tag{7.1}$$

$\hat{\hat{H}}_0$ is the commutation superoperator, which includes the time-independent terms of the Liouvillian (2.73). $\hat{\hat{H}}_1(t)$ is the commutation superoperator, which comprises time-dependent terms modulated by the lattice stochastic evolution. Without loss of generality, the ensemble average (denoted by the overbar) of $\hat{\hat{H}}_1(t)$ is assumed to be equal to zero:

$$\overline{\hat{\hat{H}}_1(t)} = 0 \tag{7.2}$$

Eq. (7.1) may be further simplified by transforming into the interaction frame (denoted by a tilde), which is equivalent to transformation from the laboratory to the rotating frame derived in Appendix E:

$$\frac{\partial}{\partial t}\tilde{\hat{\rho}}(t) = -\mathrm{i}\tilde{\hat{\hat{H}}}_1(t)\tilde{\hat{\rho}}(t) \tag{7.3}$$

$\hat{\hat{H}}_1(t)$ and $\hat{\rho}(t)$ are transformed according to:

$$\tilde{\hat{\hat{H}}}_1(t) = \hat{\hat{U}}^{-1}(t)\,\hat{\hat{H}}_1(t) \tag{7.4}$$

$$\tilde{\hat{\rho}}(t) = \hat{\hat{U}}^{-1}(t)\,\hat{\rho}(t) \tag{7.5}$$

where the propagator is given by:

$$\hat{\hat{U}}(t) = \exp\left(-\mathrm{i}\hat{\hat{H}}_0 t\right) \tag{7.6}$$

Formal integration of (7.3) leads to a series similar to that in Eq. (C.7), where the operators $\hat{H}(t)$ are replaced by $\tilde{\hat{\hat{H}}}_1(t)$. Keeping only terms up to the second order and substituting back gives:

$$\frac{\partial}{\partial t}\tilde{\hat{\rho}}(t) = -\mathrm{i}\tilde{\hat{\hat{H}}}_1(t)\tilde{\hat{\rho}}(0) - \int_0^t \mathrm{d}t_2\,\tilde{\hat{\hat{H}}}_1(t)\tilde{\hat{\hat{H}}}_1(t_2)\tilde{\hat{\rho}}(0) \tag{7.7}$$

An important property of the stochastic evolution is that the state of the system at a given time $t = T$ is independent of the previous states at times $0 \leq t < T$. This assumption simplifies ensemble average of (7.7) in the following way:

$$\begin{aligned}\frac{\partial}{\partial t}\overline{\tilde{\hat{\rho}}(t)} &= -\mathrm{i}\overline{\tilde{\hat{\hat{H}}}_1(t)\tilde{\hat{\rho}}(0)} - \int_0^t \mathrm{d}t_2\,\overline{\tilde{\hat{\hat{H}}}_1(t)\tilde{\hat{\hat{H}}}_1(t_2)\tilde{\hat{\rho}}(0)} \\ &\longrightarrow -\mathrm{i}\overline{\tilde{\hat{\hat{H}}}_1(t)}\,\overline{\tilde{\hat{\rho}}(0)} - \int_0^t \mathrm{d}t_2\,\overline{\tilde{\hat{\hat{H}}}_1(t)\tilde{\hat{\hat{H}}}_1(t_2)}\,\overline{\tilde{\hat{\rho}}(0)}\end{aligned} \tag{7.8}$$

The first term vanishes due to (7.2). Both Hamiltonians in the argument of the integral are evaluated at different time points $t \neq t_2$. But neither of them depends on the form of the other; they are uncorrelated. Therefore, absolute time coordinates may be replaced by a relative time interval [226]:

$$\frac{\partial}{\partial t}\overline{\tilde{\hat{\rho}}(t)} = -\int_0^t \mathrm{d}\tau\,\overline{\tilde{\hat{\hat{H}}}_1(t)\tilde{\hat{\hat{H}}}_1(t+\tau)}\,\overline{\tilde{\hat{\rho}}(0)} \tag{7.9}$$

If the density operator $\hat{\tilde{\rho}}(0)$ changes much slower than the Hamiltonians $\hat{\hat{\tilde{H}}}_1(t)$ during the time interval, over which the integral is evaluated, then approximately $\hat{\tilde{\rho}}(0) \approx \hat{\tilde{\rho}}(t)$. The stochastic evolution also allows setting the integration upper limit to infinity. Eq. (7.9) may, therefore, be rewritten as:

$$\frac{\partial}{\partial t}\overline{\hat{\tilde{\rho}}(t)} = -\int_0^\infty \mathrm{d}\tau\, \overline{\hat{\hat{\tilde{H}}}_1(t)\hat{\hat{\tilde{H}}}_1(t+\tau)}\,\overline{\hat{\tilde{\rho}}(t)} \equiv \hat{\hat{\tilde{\Gamma}}}\,\overline{\hat{\tilde{\rho}}(t)} \tag{7.10}$$

where $\hat{\hat{\tilde{\Gamma}}}$ is the relaxation superoperator. Finally, since the integral and the density operator are separate, transformation back to the laboratory frame results in the so-called master equation:

$$\frac{\partial}{\partial t}\hat{\rho}(t) = \left(-\mathrm{i}\hat{\hat{H}}_0 + \hat{\hat{\Gamma}}\right)\hat{\rho}(t) \tag{7.11}$$

7.1.2 Relaxation Superoperator

The relaxation superoperator $\hat{\hat{\Gamma}}$ introduced by Eq. (7.10) describes various relaxation mechanisms, denoted by Λ in general, see Section 2.2.5. These are represented by the double commutator of Hamiltonians $\hat{\hat{\tilde{H}}}_1(t)$. Such Hamiltonians are often expressed in terms of the spherical tensor operators $\hat{T}$ [226, 228]:

$$\hat{\hat{H}}_1^\Lambda(t) = c^\Lambda \sum_{m=-l}^{l} (-1)^m \left[A_{lm}^\Lambda(t)\right]^L \left[\hat{T}_{l-m}^\Lambda\right]^L \tag{7.12}$$

where c^Λ is an interaction specific constant, $\left[A_{lm}^\Lambda(t)\right]^L$ and $\left[\hat{T}_{l-m}^\Lambda\right]^L$ are the spatial and spin parts of the considered interaction Λ. The indices l and $m = \{-l, \ldots, l\}$ in the subscripts denote the rank and component of the tensor, and the superscript L denotes the laboratory reference frame.

While the spin part may be represented in the laboratory frame, the spatial part is often expressed in the principal axis system (P), in which the interaction tensor is diagonal. Between the L and P frames, there is a molecular frame (M) connected with the molecular geometry. Transformation between individual frames is carried out by Wigner rotation matrices. These depend on the mutual angles Ω_{IJ} of the frames, and are tabulated, e.g., in [229]:

$$\left[A_{lm}^\Lambda(t)\right]^L = \sum_{p,q=-l}^{l} \left[A_{lq}^\Lambda(t)\right]^P D_{qp}^l(\Omega_{PM}^\Lambda) D_{pm}^l(\Omega_{ML}) \tag{7.13}$$

After substituting Eq. (7.13) into (7.12), and the resulting form of the Hamiltonian $\hat{\hat{H}}_1^\Lambda(t)$

into (7.10), a complicated formula arises:

$$\begin{aligned}\hat{\hat{\tilde{\Gamma}}}^{\Lambda,jk} = -c^{\Lambda,j}c^{\Lambda,k} \sum_{m,p,q=-l}^{l} \sum_{m',p',q'=-l'}^{l'} \Bigg(\int_0^{\infty} \mathrm{d}\tau\, \overline{\left[A_{lq}^{\Lambda,j}(t)\right]^P \left[A_{l'q'}^{*\Lambda,k}(t+\tau)\right]^P} \\ \overline{\times D_{qp}^{l}(\Omega_{PM}^{\Lambda,j}) D_{q'p'}^{*l'}(\Omega_{PM}^{\Lambda,k}) D_{pm}^{l}(\Omega_{ML}(t)) D_{p'm'}^{*l'}(\Omega_{ML}(t+\tau))}\Bigg) \\ \times(-1)^{m+m'}\left[\hat{\tilde{T}}_{l-m}^{\Lambda,j}\right]^L \left[\hat{\tilde{T}}_{l'-m'}^{\dagger\Lambda,k}\right]^L\end{aligned} \tag{7.14}$$

where j and k are the spin indices.

The whole expression (7.14) may, after further assumptions and modifications, be simplified into a convenient form [226]:

$$\hat{\hat{\Gamma}}^{\Lambda,jk} = -\frac{1}{2}c^{\Lambda,j}c^{\Lambda,k} \sum_{m=-l}^{l} (-1)^m \mathcal{J}_{lm}^{\Lambda}(\omega) \left[\hat{T}_{l-m}^{\Lambda,j}\right]^L \left[\hat{T}_{lm}^{\Lambda,k}\right]^L \tag{7.15}$$

which applies for small molecules dissolved in an isotropic nonviscous solvent. $\mathcal{J}_{lm}^{\Lambda}(\omega)$ is the spectral density given by [14]:

$$\mathcal{J}_{lm}^{\Lambda}(\omega) = 2\int_0^{\infty} \mathrm{d}\tau\, G_{llmm}^{\Lambda}(\tau)\,\mathrm{e}^{-\mathrm{i}\omega\tau} = 2G_{llmm}^{\Lambda}(0)\frac{\tau_c^{\Lambda}}{1+(\omega\tau_c^{\Lambda})^2} \tag{7.16}$$

where $G_{llmm}^{\Lambda}(\tau)$ is the autocorrelation function and τ_c^{Λ} is the correlation time constant.

The autocorrelation function quantifies how rapidly the molecular orientation or local magnetic field fluctuates. It is dependent on the size τ of the time interval between the determination of the two orientations, and is connected with the correlation time τ_c, due to stochastic character of the fluctuations, through:

$$G_{llmm}^{\Lambda}(\tau) = G_{llmm}^{\Lambda}(0)\mathrm{e}^{-|\tau|/\tau_c} \tag{7.17}$$

The amplitude $G_{llmm}^{\Lambda}(0)$ denotes the mean square value of the fluctuations averaged over the spin ensemble or over time; both lead to the same mean value for all spins. $G_{llmm}^{\Lambda}(0)$ includes changes in both the spatial tensors A and the Wigner matrices D. The two-sided spectral density (7.16) is the Fourier transform of $G_{llmm}^{\Lambda}(\tau)$. The case with $\omega\tau_c^{\Lambda} \ll 1$, is called the extreme-narrowing [14] or fast-motion [226] limit regime. All the formulae which follow will be evaluated in this regime.

7.1.3 Relaxation Mechanisms

The master equation (7.11) contains two superoperators, which act upon the density operator. The time-independent Hamiltonian $\hat{\hat{H}}_0$ includes all coherent interactions, whereas the relaxation superoperator $\hat{\hat{\Gamma}}$ comprises all incoherent relaxation mechanisms. The coherent processes include the chemical shift and the J-coupling. The incoherent processes comprise the dominant intramolecular direct dipolar (DD), chemical-shift anisotropy (CSA), spin-rotation (SR), and other (Ξ) relaxation processes such as the scalar relaxation of the second kind [225] or the paramagnetic relaxation [230]. Though the coherent processes are time independent, they may mix and redistribute populations of the states and, therefore, influence the relaxation [226, 231]. The resulting form of the relaxation superoperator, which describes relaxation of two coupled spins j and k, may be written as follows:

$$\hat{\hat{\Gamma}}^{jk} = \hat{\hat{\Gamma}}^{\mathrm{DD},jk} + \hat{\hat{\Gamma}}^{\mathrm{CSA},jk} + \hat{\hat{\Gamma}}^{\mathrm{SR},jk} + \hat{\hat{\Gamma}}^{\Xi,jk} \tag{7.18}$$

In the following text, the explicit form of the relaxation superoperators $\hat{\hat{\Gamma}}^{\Lambda,jk}$ are provided for the most important singlet relaxation processes.

7.1.3.1 Direct Dipolar Relaxation

Any nucleus with a nonzero spin is a source of the magnetic dipolar field. This field fluctuates due to the motion of the molecule or its parts. If there exists another nucleus with a nonzero spin in proximity (in either the same or another molecule), the fluctuating field causes its relaxation.

A simplified form of the intramolecular DD relaxation superoperator is given by [226]:

$$\hat{\hat{\Gamma}}^{\mathrm{DD},jk} = -\frac{6\tau_c^{\mathrm{DD}} b_{jk}^2}{5} \sum_{m=-2}^{2} (-1)^m \left[\hat{T}_{2-m}^{\mathrm{DD},jk}\right]^L \left[\hat{T}_{2m}^{\mathrm{DD},jk}\right]^L \tag{7.19}$$

where the values of the corresponding terms in Eq. (7.13) are:

$$\begin{array}{l|l} c^{\mathrm{DD}} = 1 & \left[\hat{T}_{20}^{\mathrm{DD}}\right]^L = (3\hat{I}_{jz}\hat{I}_{kz} - \hat{I}_1 \cdot \hat{I}_2)/\sqrt{6} \\ \left[A_{20}^{\mathrm{DD}}(t)\right]^P = \sqrt{6}\, b_{jk} & \left[\hat{T}_{2\pm1}^{\mathrm{DD}}\right]^L = \mp\hat{I}_j^{\pm}\hat{I}_{kz} + \hat{I}_{jz}\hat{I}_k^{\pm}/2 \\ b_{jk} = -\dfrac{\mu_0}{4\pi}\dfrac{\gamma_j\gamma_k\hbar}{r_{jk}^3} & \left[\hat{T}_{2\pm2}^{\mathrm{DD}}\right]^L = \hat{I}_j^{\pm}\hat{I}_k^{\pm}/2 \end{array} \tag{7.20}$$

b_{jk} is the dipolar coupling constant, μ_0 is the magnetic permeability, and r_{jk} is the internuclear distance.

7.1.3.2 Chemical-Shift Anisotropy Relaxation

Chemical shift anisotropy is an indirect relaxation process, mediated by molecular electrons. Electronic motion in the external field, which itself is dependent on the field strength, induces local magnetic fields on the site of the nuclei. These fields vary in direction, with respect to the nucleus, according to the molecular geometry, see Eq. (2.113). The resulting field at the nuclear site causes nuclear relaxation.

Assume the principal axis system is the same for both nuclei. Then the relaxation superoperator is given by [226]:

$$\hat{\hat{\Gamma}}^{\mathrm{CSA},jk} = -\frac{\gamma_j \gamma_k \tau_c^{\mathrm{CSA}}}{5} \sum_{m,q=-2}^{2} (-1)^m \left[A_{2q}^{\mathrm{CSA},j}\right]^P \left[A_{2q}^{*\mathrm{CSA},k}\right]^P \left[\hat{T}_{2-m}^{\mathrm{CSA},j}\right]^L \left[\hat{T}_{2m}^{\mathrm{CSA},k}\right]^L \tag{7.21}$$

where:

$$\begin{array}{l|l|l} c_j^{\mathrm{CSA}} = \gamma_j & \left[A_{20}^{\mathrm{CSA},j}(t)\right]^P = \sqrt{3/2}\,\Delta\delta_j & \left[\hat{T}_{20}^{\mathrm{CSA}}\right]^L = \sqrt{2/3}\,B_0 \hat{I}_z \\ \Delta\delta_j = \delta_{zz,j} - \mathrm{Tr}\{\boldsymbol{\delta}\}/3 & \left[A_{2\pm1}^{\mathrm{CSA},j}(t)\right]^P = 0 & \left[\hat{T}_{2\pm1}^{\mathrm{CSA}}\right]^L = \mp B_0 \hat{I}_j^{\pm}/2 \\ \eta_j = (\delta_{yy,j} - \delta_{xx,j})/\Delta\delta_j & \left[A_{2\pm2}^{\mathrm{CSA},j}(t)\right]^P = \eta_j \Delta\delta_j/2 & \left[\hat{T}_{2\pm2}^{\mathrm{CSA}}\right]^L = 0 \end{array} \tag{7.22}$$

$\Delta\delta_j$ is the chemical shift anisotropy, $\delta_{j,\mathrm{iso}} \equiv \mathrm{Tr}\{\boldsymbol{\delta}_j\}/3$ is the isotropic chemical shift, and η_j is the asymmetry parameter or biaxiality of the chemical shift tensor of the jth spin.

7.1.3.3 Spin-Rotation Relaxation

Spin-rotation relaxation is the significant mechanism for gases and for small, freely-rotating molecules in other phases. Two different motions, molecular tumbling and intramolecular rotations or reorientations, combine into the time-dependent space part of $\hat{\hat{\tilde{H}}}_1(t)$.

The form of the superoperator $\hat{\hat{\Gamma}}$, valid for spins in the liquid phase, is given by [226]:

$$\hat{\hat{\Gamma}}^{\mathrm{SR},jk} = -\frac{k_{\mathrm{B}}T}{3\hbar^2} \sum_{m,p,q,q',\nu,\nu'=-1}^{1} (-1)^m C_{p,q,j} C_{p,q',k} I_{\nu\nu'} D_{q\nu}^{1}(\Omega_{PM}^{\mathrm{SR},j}) D_{q'\nu'}^{*1}(\Omega_{PM}^{\mathrm{SR},k}) \left[\hat{T}_{1-m}^{\mathrm{SR},j}\right]^L \left[\hat{T}_{1m}^{\mathrm{SR},k}\right]^L \tag{7.23}$$

where:

$$\begin{array}{l|l} c^{\mathrm{SR}} = 1 & \left[\hat{T}_{10}^{\mathrm{SR}}\right]^L = \hat{I}_{jz} \\ \left[A_{10}^{\mathrm{SR},j}(t)\right]^P = C_{zz,j} J_z(t) & \left[\hat{T}_{1\pm1}^{\mathrm{SR}}\right]^L = \mp \hat{I}_j^{\pm}/\sqrt{2} \\ \left[A_{1\pm1}^{\mathrm{SR},j}(t)\right]^P = \mp[C_{xx,j} J_x(t) \pm \mathrm{i} C_{yy,j} J_y(t)]/\sqrt{2} & \end{array} \tag{7.24}$$

Here $\boldsymbol{J} = (J_x, J_y, J_z)$ is the molecular angular momentum vector, $\boldsymbol{C} = (C)_{p,q,j}$ is the spin-rotation coupling tensor. Its elements in the Cartesian representation are denoted by $C_{\alpha\alpha,j}$, where $\alpha = \{x, y, z\}$. $I_{\nu\nu'}$ denotes the $\nu\nu'$-th element of the molecular moment of inertia with ν, $\nu' = \{1, 0, -1\}$. $I_{\nu\nu'}$ is related to the correlation function of the molecular angular momentum $J_\nu(t)$. Its form in the spherical coordinate system is given by [226]:

$$\overline{J_\nu(t) J_{\nu'}^{*}(t+\tau)} = \delta_{\nu|\nu'|} \frac{k_{\mathrm{B}} T}{\hbar^2} I_{\nu\nu'} \tag{7.25}$$

Explicitly:

$$I_{\nu\nu'} = \frac{1}{2} \begin{pmatrix} I_x\,\mathrm{e}_x + I_y\,\mathrm{e}_y & 0 & -I_x\,\mathrm{e}_x + I_y\,\mathrm{e}_y \\ 0 & I_z\,\mathrm{e}_z & 0 \\ -I_x\,\mathrm{e}_x + I_y\,\mathrm{e}_y & 0 & I_x\,\mathrm{e}_x + I_y\,\mathrm{e}_y \end{pmatrix} \tag{7.26}$$

where $\mathrm{e}_\alpha = \mathrm{e}^{-\tau/\tau^{\mathrm{SR}}_{\mathrm{c},\alpha}}$, and $\tau^{\mathrm{SR}}_{\mathrm{c},\alpha}$ is the correlation time for the Cartesian component α.

7.2 Field-Cycling Experiments

7.2.1 Field-Dependent Energy Eigenstates

The field cycling experiments described below are based on the transport of the spin system under consideration between magnetic fields of different strengths. As given in Sections 5.1 and 5.3, $^{15}\mathrm{N}_2\mathrm{O}$ is characterized by:

$$\gamma(^{15}\mathrm{N}) < 0\,,\ \delta_1 < \delta_2\,,\ J_{12} < 0 \tag{7.27}$$

where the spin indices "1" and "2" refer to the $\underline{^{15}\mathrm{N}}{}^{15}\mathrm{NO}$ and $^{15}\mathrm{N}\underline{^{15}\mathrm{N}}\mathrm{O}$ site, respectively. Therefore:

$$\operatorname{sign} J_{12} = \operatorname{sign}(\Omega_1 - \Omega_2) \tag{7.28}$$

The correspondence between the high-field eigenstates of the weakly-coupled spin system ($\Theta \approx \pi/2$) and the low-field eigenstates of the strongly-coupled spin system ($\Theta \approx 0$) is, according to Eq. (3.5), the following:

$$|\alpha\alpha\rangle \leftrightarrow |T_{+1}\rangle,\ |\alpha\beta\rangle \leftrightarrow |T_0\rangle,\ |\beta\alpha\rangle \leftrightarrow |S_0\rangle,\ |\beta\beta\rangle \leftrightarrow |T_{-1}\rangle \tag{7.29}$$

The field-dependent eigenstates $|\xi_i\rangle$, where $i = \{1,2,3,4\}$, may then be expressed as linear combination of the singlet and triplet states, defined in Eq. (2.102):

$$\begin{pmatrix} |\xi_1\rangle \\ |\xi_2\rangle \\ |\xi_3\rangle \\ |\xi_4\rangle \end{pmatrix} = \begin{pmatrix} 1 & 0 & 0 & 0 \\ 0 & \cos(\Theta/2) & -\sin(\Theta/2) & 0 \\ 0 & \sin(\Theta/2) & \cos(\Theta/2) & 0 \\ 0 & 0 & 0 & 1 \end{pmatrix} \begin{pmatrix} |T_{+1}\rangle \\ |S_0\rangle \\ |T_0\rangle \\ |T_{-1}\rangle \end{pmatrix} \tag{7.30}$$

where Θ is the mixing angle given by Eq. (2.94).

The matrix representation of the two spins-1/2 Hamiltonian (2.93) in the basis of the field-dependent states (7.30) is given by:

$$\hat{H}(\Theta) = \frac{1}{2} \begin{array}{c} \begin{array}{cccc} |\xi_1\rangle & |\xi_2\rangle & |\xi_3\rangle & |\xi_4\rangle \end{array} \\ \left(\begin{array}{cccc} \Omega_\Sigma + \pi J_{12} & 0 & 0 & 0 \\ 0 & -\Omega_\Delta s_\Theta - \pi J_{12}(2c_\Theta + 1) & \Omega_\Delta c_\Theta - 2\pi J_{12} s_\Theta & 0 \\ 0 & \Omega_\Delta c_\Theta - 2\pi J_{12} s_\Theta & \Omega_\Delta s_\Theta + \pi J_{12}(2c_\Theta - 1) & 0 \\ 0 & 0 & 0 & -\Omega_\Sigma + \pi J_{12} \end{array}\right) \end{array} \begin{array}{c} \\ \langle\xi_1| \\ \langle\xi_2| \\ \langle\xi_3| \\ \langle\xi_4| \end{array} \tag{7.31}$$

where $s_\Theta = \sin\Theta$ and $c_\Theta = \cos\Theta$. The energies of the states $|\xi_i\rangle$ are equal to:

$$\begin{aligned}
E(\xi_1) &= \frac{\Omega_\Sigma + \pi J_{12}}{2} \\
E(\xi_2) &= -\frac{\sqrt{(\Omega_\Delta)^2 + (2\pi J_{12})^2} + \pi J_{12}}{2} \\
E(\xi_3) &= \frac{\sqrt{(\Omega_\Delta)^2 + (2\pi J_{12})^2} - \pi J_{12}}{2} \\
E(\xi_4) &= \frac{-\Omega_\Sigma + \pi J_{12}}{2}
\end{aligned} \tag{7.32}$$

In the case of $^{15}N_2O$, ordering of the high-field and low-field eigenstates with respect to energy leads to:

$$\begin{aligned}
&E(\alpha\alpha) > E(\beta\alpha) > E(\alpha\beta) > E(\beta\beta) \\
&E(S_0) > E(T_{+1}) \geq E(T_0) \geq E(T_{-1})
\end{aligned} \tag{7.33}$$

7.2.2 Adiabatic Transport

The preferred way of the transport between the different magnetic fields is the adiabatic transport, see Figure 7.1. During such kind of a transport, the energy levels follow the changing magnetic field immediately. At the same time, the populations re-equilibrate in the actual field with the field-dependent T_1 time constant. Adiabaticity further ensures a low-loss transformation of the populations of the high-field states into the populations of the low-field states and vice versa, as the transitions between the energy states are minimized [26].

All the above mentioned characteristics of the adiabatic transport, however, constrain the transport speed. The adiabaticity condition is usually expressed either in terms of the

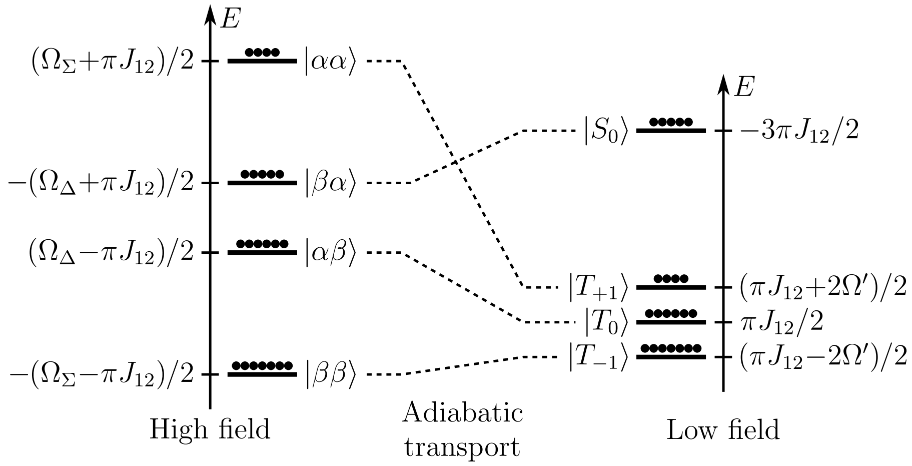

Figure 7.1: $^{15}N_2O$ energy levels in high and low magnetic fields

B_0 field strength [2, 232]:

$$\left|\frac{1}{B_0}\frac{\mathrm{d}B_0}{\mathrm{d}t}\right| \ll |2\pi J_{12}| \tag{7.34}$$

or by using the mixing angle Θ [2]:

$$\left|\frac{\mathrm{d}\Theta}{\mathrm{d}t}\right| \ll |2\pi J_{12}| \tag{7.35}$$

The time-derivative of B_0 and Θ in the left-hand side of the inequalities (7.34) and (7.35) are shown in Figures 7.2 and 7.3, respectively, for the realistic experimental magnetic field profile, also shown in Figure 7.2. The expression on the right-hand side arises from the condition that the rate of change of the Hamiltonian eigenstates has to be slower than the smallest difference of the eigenstate energies. Eqs. (7.32) in the low-field limit, when

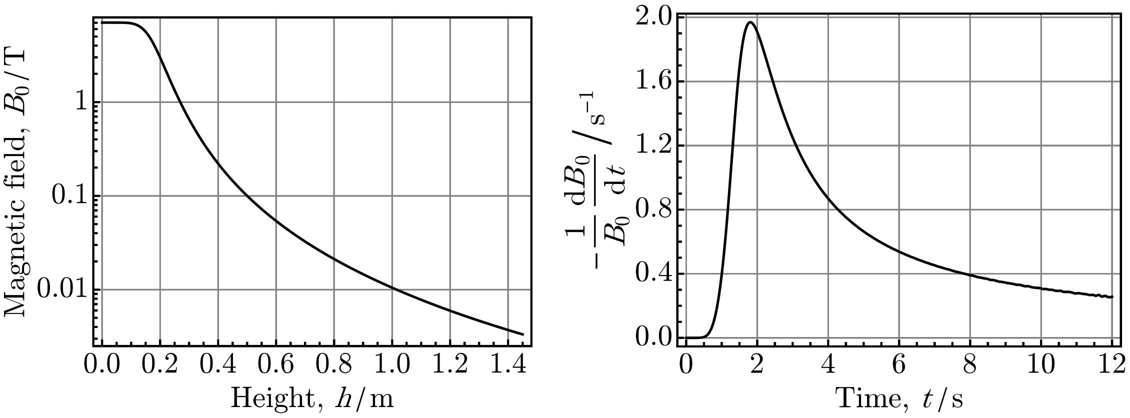

Figure 7.2: Left: The realistic dependence of the B_0 field strength on the vertical position relative to the usual detection position (provided by Oxford Instruments, U.K.). Right: The rate of change of the magnetic field strength during the field-cycling experiment.

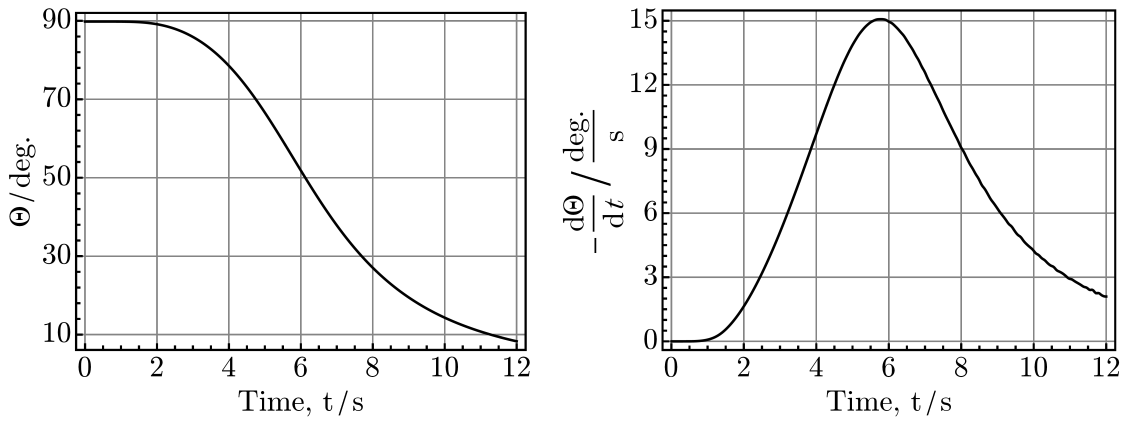

Figure 7.3: Left: The realistic time evolution of the mixing angle Θ during the field-cycling experiment. Right: The rate of change of the mixing angle Θ during the field-cycling experiment.

$\Omega_\Delta \ll 2\pi J_{12}$, give:

$$|E(\xi_2) - E(\xi_3)| = \sqrt{(\Omega_\Delta)^2 + (2\pi J_{12})^2} \approx |2\pi J_{12}| \tag{7.36}$$

Alternatively, according to [48], the transport has to be slower than $1/J_{12}$ in order to minimize transitions between the Hamiltonian eigenstates, but faster than T_1 to maintain distribution of the populations during and after the transport. The transport time τ_{tr}, therefore, obeys:

$$1/|J_{12}| < \tau_{\text{tr}} < T_1 \tag{7.37}$$

During the field-cycling experiments shown in Figures 7.4 and 7.7, the default high magnetic field was $B_{\text{HF}} = 7046$ mT at the zero reference height $h_0 = 0$ cm inside the spectrometer. The lowest field was $B_{\text{LF}} \approx 3.3$ mT at the height $h_1 = 145$ cm above the reference zero level. The transport time for reaching h_1 was $\tau_{\text{tr}} = 12$ s. The transport speed of $v_{\text{tr}} \approx 12.1\ \text{cm}\,\text{s}^{-1}$ was kept fixed during all experiments. From the plots 7.2(b) and 7.3(b) follows that:

$$\max\left|\frac{1}{B_0}\frac{\mathrm{d}B_0}{\mathrm{d}t}\right| \approx 1.97\ \text{s}^{-1} \tag{7.38}$$

$$\max\left|\frac{\mathrm{d}\Theta}{\mathrm{d}t}\right| \approx 0.263\ \text{s}^{-1} \tag{7.39}$$

which is much less than the value of the $^{15}\text{N}_2\text{O}$ J-coupling constant:

$$|2\pi J_{12}| \approx 51.5\ \text{s}^{-1} \tag{7.40}$$

The comparison of Eqs. (7.38), (7.39) and (7.40) leads to conclusion that the transport was adiabatic.

7.2.3 Singlet Experiment

The singlet experiment shown in Figure 7.4 serves for preparation, storage and observation of the singlet state in coupled pairs of spin-1/2 nuclei, which are weakly coupled in the high field. It is based on a modified version of the field-cycling singlet experiment from [57], the rf pulse sequence of which is provided in Figure 7.5, combined with the MSE pulse sequence in order to observe SNR-enhanced singlet signals.

The initial high-field equilibrium magnetization $\hat{I}_z$ is converted by the semi-selective π_y pulse into a so-called singlet precursor state [61]. A selective inversion of, e.g., the $\underline{^{15}\text{N}}{}^{15}\text{NO}$ site gives:

$$\hat{I}_z = |\alpha\alpha\rangle\langle\alpha\alpha| - |\beta\beta\rangle\langle\beta\beta| \xrightarrow{\pi \hat{I}_{1y}} -\hat{I}_{1z} + \hat{I}_{2z} = |\beta\alpha\rangle\langle\beta\alpha| - |\alpha\beta\rangle\langle\alpha\beta| \tag{7.41}$$

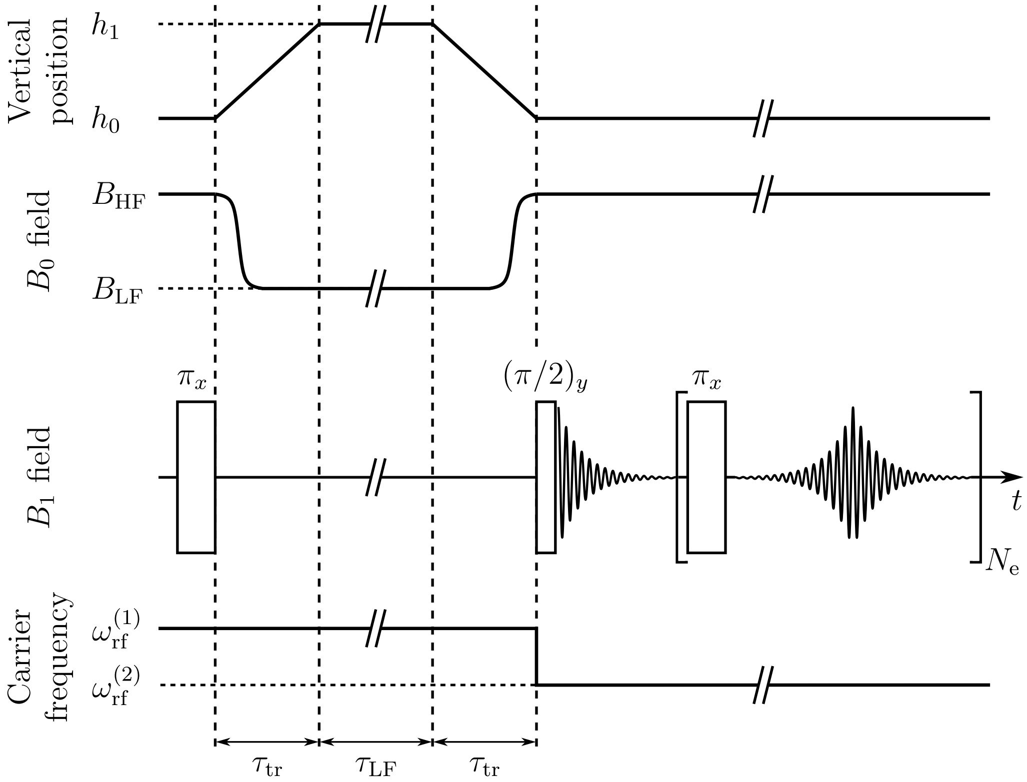

Figure 7.4: Scheme of the field-cycling singlet experiment. Shown are the vertical position of the sample (1st line), the B_0 field strength (2nd line), the rf pulse sequence (3rd line), and the carrier frequency (4th line) during the experiment. Time intervals τ_{tr} and τ_{LF} denote the adiabatic transport time and the time spent in the low-field. The carrier frequency may be switched between the centres of $\underline{^{15}\mathrm{N}}{}^{15}\mathrm{NO}$ and $^{15}\mathrm{N}\underline{^{15}\mathrm{N}}\mathrm{O}$ doublets either before the first π_x pulse or the $(\pi/2)_y$ pulse.

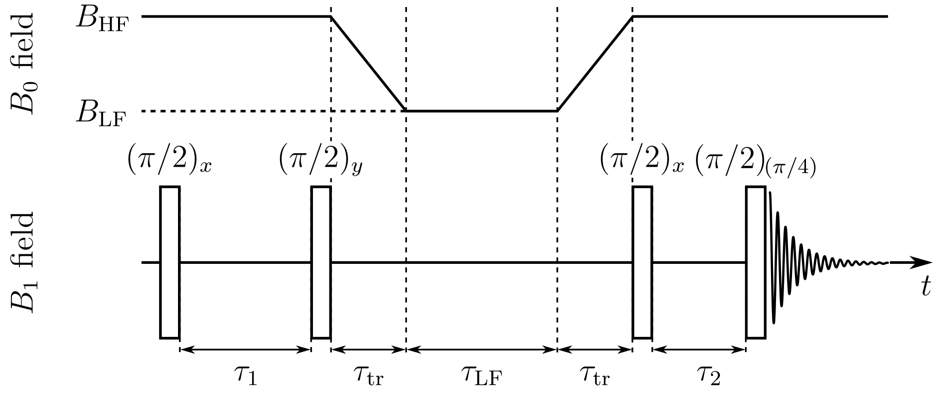

Figure 7.5: Scheme of the original field-cycling singlet NMR experiment [48, 57]. The carrier frequency of the nonselective rf pulses is set to the mean of the nuclear spin precession frequencies. Adapted from [57].

As shown in Figure 7.4, the carrier frequency may be set either to $\omega_{\mathrm{rf}}^{(1)}$ or $\omega_{\mathrm{rf}}^{(2)}$, which corresponds to the frequency of the $\underline{^{15}\mathrm{N}}{}^{15}\mathrm{NO}$ or $^{15}\mathrm{N}\underline{^{15}\mathrm{N}}\mathrm{O}$ doublet centre, respectively. This semi-selective π_y pulse replaces the first pair of nonselective $(\pi/2)$ pulses with the carrier at the mean of the nuclear spin precession frequencies, and a delay $\tau_1 = \pi/|-\gamma B_{\mathrm{HF}}(\delta_1 - \delta_2)|$ between the pulses, as used in the original pulse sequence for the semi-selective inversion of the either nuclear site, see Figure 7.5 [48, 57].

The sample is then adiabatically transported into the low field region. According to Eq. (7.29), the population difference between the high-field states $|\alpha\beta\rangle$ and $|\beta\alpha\rangle$ transforms into the difference between populations of the low-field states $|T_0\rangle$ and $|S_0\rangle$:

$$|\beta\alpha\rangle\langle\beta\alpha| - |\alpha\beta\rangle\langle\alpha\beta| \xrightarrow{B_{\mathrm{HF}} \xrightarrow{\text{adiab.}} B_{\mathrm{LF}}} |S_0\rangle\langle S_0| - |T_0\rangle\langle T_0| \tag{7.42}$$

During the relaxation interval τ_{LF}, the singlet population decays with the T_S time constant, whereas the populations of the triplet states equilibrate with the time constant $T_1 \ll T_S$. After $\tau_{\mathrm{LF}} > T_1$, the spin state (singlet order) evolves in accordance with [36]:

$$\hat{\rho} \propto \left(|S_0\rangle\langle S_0| - \frac{|T_{+1}\rangle\langle T_{+1}| + |T_0\rangle\langle T_0| + |T_{-1}\rangle\langle T_{-1}|}{3} \right) \mathrm{e}^{-\tau_{\mathrm{LF}}/T_S} \tag{7.43}$$

The sample is transported back into the high-field during the transport interval τ_{tr}, which is of the same duration as the interval of high-to-low field transport.

Finally, the carrier frequency is set to the appropriate value and the semi-selective $(\pi/2)_y$ pulse triggers the subsequent acquisition of the MSE signal. The $(\pi/2)_y$ pulse replaces the second pair of nonselective pulses and the inter-pulse delay $\tau_2 = \tau_1/2$ in the original pulse sequence, which act as the semi-selective excitation, too.

Examples of the observed singlet relaxation of the $^{15}\mathrm{N}\underline{^{15}\mathrm{N}}\mathrm{O}$ doublet in the field of $B_0 \approx 4.7$ mT ($\tau_{\mathrm{tr}} \approx 10.81$ s) are shown in Figure 7.6. The carrier frequency was set to the mean frequency of the $^{15}\mathrm{N}\underline{^{15}\mathrm{N}}\mathrm{O}$ doublet during the whole pulse sequence.

7.2.4 T_1 Experiment

The field-cycling T_1 experiment is used for the determination of the field-dependent T_1 time constant. Its scheme is shown in Figure 7.7. The thermal equilibrium magnetization of the sample is established in high field. The sample is then adiabatically transported into low field. The resulting population distribution is different from that corresponding to a new value of the magnetic field strength, see Eq. (6.1). Therefore, the equilibrium population distribution is reestablished during the relaxation interval τ_{LF}. Finally, the

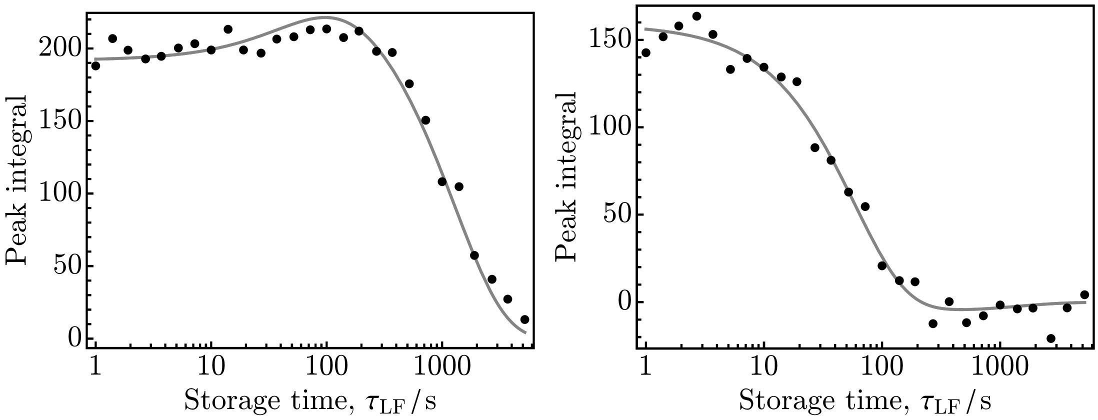

Figure 7.6: Singlet relaxation in the magnetic field of 4.7 mT ($\tau_{\mathrm{tr}} \approx 10.81$ s) observed in $^{15}\mathrm{N}\underline{^{15}\mathrm{N}}\mathrm{O}$ doublet. The points represent experimental integrals of the peak 1 (left) and the peak 2 (right). The gray lines are the best fits of the relaxation model described in Section 7.3.3.

sample is adiabatically returned back into the spectrometer. A single nonselective $(\pi/2)_y$ pulse is followed by the acquisition of the FID signal.

Examples of the observed $^{15}\mathrm{N}_2\mathrm{O}$ T_1 relaxation in the field of $B_0 \approx 4.7$ mT ($\tau_{\mathrm{tr}} \approx 10.81$ s) are shown in Figure 7.8.

7.3 Field-Dependent Relaxation Description

The field-cycling singlet and T_1 experiments introduced in Sections 7.2.3 and 7.2.4 were performed for magnetic fields of the strength between the spectrometer field (7046 mT) and the lowest available field (3.3 mT), as stated at the end of Section 7.2.2. It is clear from Figures 7.6 and 7.8 that four different dependencies may in principal be obtained, using the two experiments.

Assume no prior knowledge about the individual relaxation mechanisms, which are responsible for the observed relaxation. A phenomenological model may be constructed, taking into account the theory introduced in Section 7.1, in order to describe the observations. The overall relaxation of the spin system will be represented by a time-dependent exchange of populations of the individual energy levels.

7.3.1 Generalized Relaxation Model

As seen in Section 7.1.2, the relaxation superoperator $\hat{\hat{\Gamma}}$ is conveniently represented by means of spherical tensor operators. The considered spin system consists of two coupled

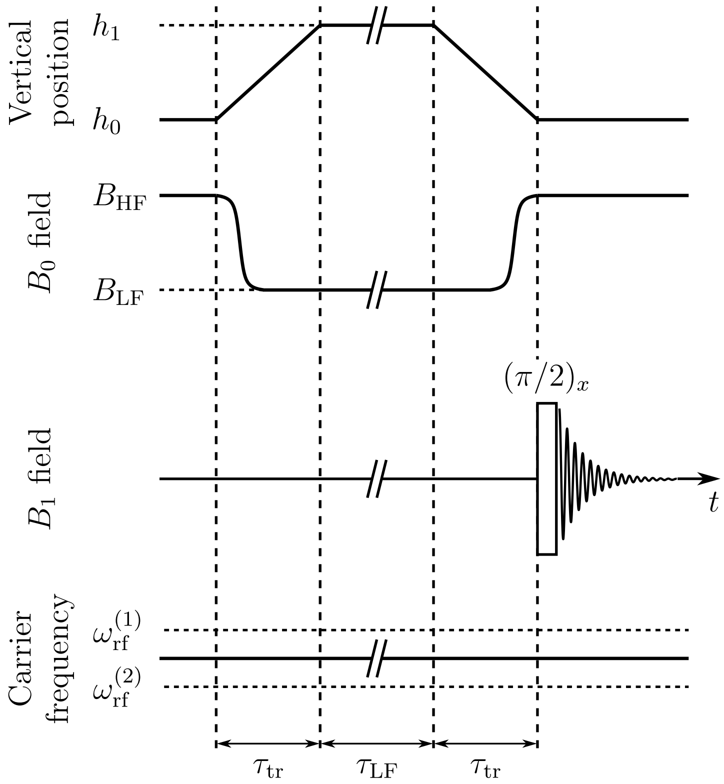

Figure 7.7: Scheme of the field-cycling T_1 experiment. Shown are the vertical position of the sample (1st line), the B_0 field strength (2nd line), the rf pulse sequence (3rd line), and the carrier frequency (4th line) during the experiment. Time intervals τ_{tr} and τ_{LF} denote the transport time and the time spent in the low-field. The carrier frequency is set to the mean frequency of the $^{15}\underline{\mathrm{N}}{}^{15}\mathrm{NO}$ and $^{15}\mathrm{N}{}^{15}\underline{\mathrm{N}}\mathrm{O}$ doublets during the whole experiment.

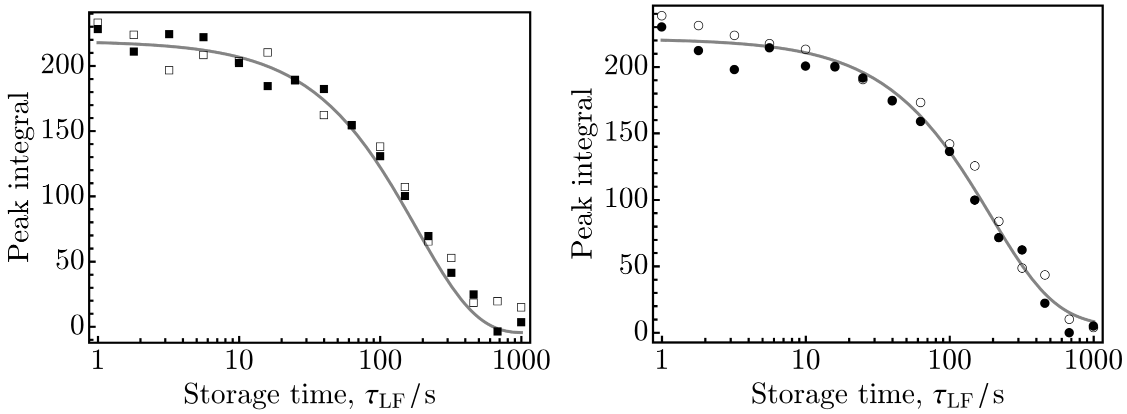

Figure 7.8: $^{15}\mathrm{N}_2\mathrm{O}$ T_1 relaxation observed in the magnetic field of 4.7 mT ($\tau_{\mathrm{tr}} \approx 10.81$ s). The points represent experimental integrals for peak 1 (■) and peak 2 (□) of the $^{15}\mathrm{N}{}^{15}\underline{\mathrm{N}}\mathrm{O}$ doublet (left), and for peak 3 (●) and peak 4 (○) of the $^{15}\underline{\mathrm{N}}{}^{15}\mathrm{NO}$ doublet (right). The gray lines are the best fits of the relaxation model described in Section 7.3.3.

spins-1/2. The relaxation mechanisms may cause relaxation of both spins simultaneously or of each spin separately. Therefore, one-spin and two-spins spherical tensor operators have to be included. Their complete basis $\left\{\hat{\hat{B}}_i\right\}$ is listed in Table 7.1 [35].

One-spin operators	Two-spins operators
$\hat{B}_1 = -\hat{I}_1^+ / \sqrt{2} \equiv \hat{T}_{11}^{(1)}$	$\hat{B}_8 = \hat{I}_1^+ \hat{I}_2^+ \equiv 2\hat{T}_{22}^{(1,2)}$
$\hat{B}_2 = \hat{I}_{1z} \equiv \hat{T}_{10}^{(1)}$	$\hat{B}_9 = -\hat{I}_1^+ \hat{I}_{2z} - \hat{I}_{1z} \hat{I}_2^+ \equiv 2\hat{T}_{21}^{(1,2)}$
$\hat{B}_3 = \hat{I}_1^- / \sqrt{2} \equiv \hat{T}_{1-1}^{(1)}$	$\hat{B}_{10} = -\left(\hat{I}_1^- \hat{I}_2^+ + \hat{I}_1^+ \hat{I}_2^- - 4\hat{I}_{1z} \hat{I}_{2z}\right) / \sqrt{6} \equiv 2\hat{T}_{20}^{(1,2)}$
$\hat{B}_4 = -\hat{I}_2^+ / \sqrt{2} \equiv \hat{T}_{11}^{(2)}$	$\hat{B}_{11} = \hat{I}_1^- \hat{I}_{2z} + \hat{I}_{1z} \hat{I}_2^- \equiv 2\hat{T}_{2-1}^{(1,2)}$
$\hat{B}_5 = \hat{I}_{2z} \equiv \hat{T}_{10}^{(2)}$	$\hat{B}_{12} = \hat{I}_1^- \hat{I}_2^- \equiv 2\hat{T}_{2-2}^{(1,2)}$
$\hat{B}_6 = \hat{I}_2^- / \sqrt{2} \equiv \hat{T}_{1-1}^{(2)}$	$\hat{B}_{13} = -\hat{I}_1^+ \hat{I}_{2z} + \hat{I}_{1z} \hat{I}_2^+ \equiv 2\hat{T}_{11}^{(1,2)}$
$\hat{B}_7 = \hat{E}/2 \equiv \hat{T}_{00}^{(1)} \equiv \hat{T}_{00}^{(2)}$	$\hat{B}_{14} = \left(\hat{I}_1^- \hat{I}_2^+ - \hat{I}_1^+ \hat{I}_2^-\right) / \sqrt{2} \equiv 2\hat{T}_{10}^{(1,2)}$
	$\hat{B}_{15} = -\hat{I}_1^- \hat{I}_{2z} + \hat{I}_{1z} \hat{I}_2^- \equiv 2\hat{T}_{1-1}^{(1,2)}$
	$\hat{B}_{16} = -\left(\hat{I}_1^- \hat{I}_2^+ + \hat{I}_1^+ \hat{I}_2^- + 2\hat{I}_{1z} \hat{I}_{2z}\right) / \sqrt{3} \equiv 2\hat{T}_{00}^{(1,2)}$

Table 7.1: Spherical tensor operator basis for two spins-1/2

The conventional nomenclature of the spherical tensor operators, using the symbol $\hat{T}_{km}^{(s)}$, is on the right-hand side of each expression in Table 7.1. The subscripts k and $m = \{-k, \ldots, k\}$ denote the rank and the component of the operator, and the superscript s denotes the related spin(s).

The relaxation superoperator $\hat{\hat{\Gamma}}$ is constructed as the sum of the projection superoperators from the basis operators $\hat{B}_i$ in Table 7.1 as follows:

$$\hat{\hat{\Gamma}} = -\sum_{i=1}^{16} a_i \frac{|\hat{B}_i)(\hat{B}_i|}{(\hat{B}_i|\hat{B}_i)} \tag{7.44}$$

The constants a_i represent transition probabilities per unit time and denote a contribution of the ith projection superoperator to $\hat{\hat{\Gamma}}$. A correct and full form of the $\hat{\hat{\Gamma}}$ expansion would have to include all 256 shift superoperators. However, due to the fact that only populations are used for relaxation description and that only four different relaxation dependencies are available, only a tiny fraction of the superoperators is relevant, whose contribution may be determined unambiguously.

Assume the energy level scheme for $^{15}N_2O$ in Figure 7.1. The population exchange between different pairs of the levels may be described by a master equation for populations [10]. The time evolution of the populations after the adiabatic transport into the magnetic field of a given strength obeys the first-order homogeneous differential equations:

$$\frac{\mathrm{d}}{\mathrm{d}t}\boldsymbol{P}(t,\chi) = \mathbf{W}(\chi)\cdot[\boldsymbol{P}(t,\chi) - \boldsymbol{P}_{\mathrm{eq}}(\chi)] \tag{7.45}$$

The parameter $\chi = B_0/B_{\mathrm{HF}}$ describes the magnetic field strength relative to the spectrometer field B_{HF}. $\boldsymbol{P}(t,\chi)$ is the time and magnetic-field dependent population vector defined by:

$$\boldsymbol{P}(t,\chi) = \begin{pmatrix} \langle\xi_1(\chi)|\hat{\rho}(t,\chi)|\xi_1(\chi)\rangle \\ \langle\xi_2(\chi)|\hat{\rho}(t,\chi)|\xi_2(\chi)\rangle \\ \langle\xi_3(\chi)|\hat{\rho}(t,\chi)|\xi_3(\chi)\rangle \\ \langle\xi_4(\chi)|\hat{\rho}(t,\chi)|\xi_4(\chi)\rangle \end{pmatrix} \tag{7.46}$$

The field-dependent states $|\xi_i(\chi)\rangle$ are defined by Eq. (7.30). $\hat{\rho}(t,\chi)$ denotes the density operator of the spin system. The field-strength dependence of the mixing angle (2.94) is the following:

$$\Theta(\chi) = \arctan\left[\frac{\Omega_1(\chi) - \Omega_2(\chi)}{2\pi J_{12}}\right] = \arctan\left[\frac{-\gamma B_{\mathrm{HF}}\,(\delta_1 - \delta_2)}{2\pi J_{12}}\chi\right] \tag{7.47}$$

The symbol $\mathbf{W}(\chi)$ in Eq. (7.45) represents a relaxation matrix:

$$\mathbf{W}(\chi) = \begin{array}{c} \begin{array}{cccc} |\xi_1\rangle & |\xi_2\rangle & |\xi_3\rangle & |\xi_4\rangle \end{array} \\ \begin{pmatrix} \Delta_1(\chi) & W_{12}(\chi) & W_{13}(\chi) & W_{14}(\chi) \\ W_{21}(\chi) & \Delta_2(\chi) & W_{23}(\chi) & W_{24}(\chi) \\ W_{31}(\chi) & W_{32}(\chi) & \Delta_3(\chi) & W_{34}(\chi) \\ W_{41}(\chi) & W_{42}(\chi) & W_{43}(\chi) & \Delta_4(\chi) \end{pmatrix} \begin{array}{c} \langle\xi_1| \\ \langle\xi_2| \\ \langle\xi_3| \\ \langle\xi_4| \end{array} \end{array} \tag{7.48}$$

The individual matrix elements $W_{ij}(\chi)$ denote the transition probabilities per unit time, which characterize the population exchange between the ith and jth energy level, see Figure 7.9. They are given by:

$$W_{ij}(\chi) = \Big(|\xi_i(\chi)\rangle\langle\xi_i(\chi)|\,\Big|\hat{\hat{\Gamma}}\Big|\,|\xi_j(\chi)\rangle\langle\xi_j(\chi)|\Big) \tag{7.49}$$

Using Eqs. (7.30), (7.44) and (7.47), the transition probabilities $W_{ij}(\chi)$ are explicitly equal to the following expressions:

$$\begin{aligned} W_{12}(\chi) = W_{21}(\chi) &= [3s_\Theta(a_2 - a_5) + 2(1 - c_\Theta)a_{10} + (1 + 2c_\Theta)a_{16}]/12 \\ W_{13}(\chi) = W_{31}(\chi) &= [-3s_\Theta(a_2 - a_5) + 2(1 + c_\Theta)a_{10} + (1 - 2c_\Theta)a_{16}]/12 \\ W_{14}(\chi) = W_{41}(\chi) &= [3(a_2 + a_5) - 2a_{10} - a_{16}]/12 \\ W_{23}(\chi) = W_{32}(\chi) &= [3s_\Theta^2(a_2 + a_5) - 2(1 - c_\Theta^2)a_{10} - (1 - 4c_\Theta^2)a_{16}]/12 \\ W_{24}(\chi) = W_{42}(\chi) &= [-3s_\Theta(a_2 - a_5) + 2(1 - c_\Theta)a_{10} + (1 + 2c_\Theta)a_{16}]/12 \\ W_{34}(\chi) = W_{43}(\chi) &= [3s_\Theta(a_2 - a_5) + 2(1 + c_\Theta)a_{10} + (1 - 2c_\Theta)a_{16}]/12 \end{aligned} \tag{7.50}$$

where $s_\Theta = \sin\Theta(\chi)$ and $c_\Theta = \cos\Theta(\chi)$. The negative diagonal elements $\Delta_i(\chi)$, which ensure conservation of the populations, are given by:

$$\Delta_i(\chi) = -\sum_{\substack{j=1 \\ j\neq i}}^{4} W_{ij}(\chi) \tag{7.51}$$

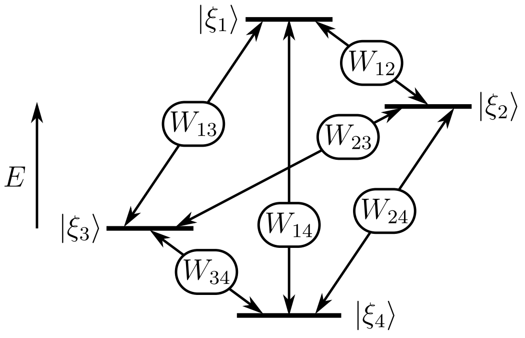

Figure 7.9: $^{15}N_2O$ energy-level scheme in a general magnetic field

The solution of Eq. (7.45) is of the form:

$$\boldsymbol{P}(t,\chi) = \boldsymbol{P}_{\text{eq}}(\chi) + \mathrm{e}^{\mathsf{W}(\chi)\,t} \cdot [\boldsymbol{P}(0,1) - \boldsymbol{P}_{\text{eq}}(\chi)] \tag{7.52}$$

where $\boldsymbol{P}(0,1)$ is the population vector immediately after the transport into the region of the field strength χB_{HF}. The equilibrium population vector $\boldsymbol{P}_{\text{eq}}(\chi)$ in the field χB_{HF} is defined by:

$$\boldsymbol{P}_{\text{eq}}(\chi) = \boldsymbol{P}(t,\chi)\big|_{t\to\infty} = \chi(-1,0,0,1)^{\mathsf{T}} \tag{7.53}$$

After the low-field relaxation interval τ_{LF} and the adiabatic transport back into the spectrometer, either MSE or FID signal is acquired during the singlet or T_1 experiment, respectively. The observed spectral peak amplitudes correspond to the population difference across pairs of the energy levels in high field. The difference pattern $\boldsymbol{Q}_p$, which gives rise to the peak $p = \{1,2,3,4\}$, if read in the traditional way from left-to-right, using labeling according to Figure 5.2, is given by vectors:

$$\begin{aligned}
\boldsymbol{Q}_1 &= (0,1,0,-1)^{\mathsf{T}} \\
\boldsymbol{Q}_2 &= (1,0,-1,0)^{\mathsf{T}} \\
\boldsymbol{Q}_3 &= (0,0,1,-1)^{\mathsf{T}} \\
\boldsymbol{Q}_4 &= (1,-1,0,0)^{\mathsf{T}}
\end{aligned} \tag{7.54}$$

The peaks 1 and 2 belong to the $^{15}\text{N}\underline{^{15}\text{N}}\text{O}$ doublet, whereas the $\underline{^{15}\text{N}}{}^{15}\text{NO}$ doublet comprises the peaks 3 and 4. Combining Eqs. (7.52) and (7.54) together, the amplitudes of the individual peaks are equal to:

$$A_p(\tau_{\mathrm{LF}},\chi) = \boldsymbol{Q}_p^{\mathsf{T}} \cdot \boldsymbol{P}(\tau_{\mathrm{LF}},\chi) \tag{7.55}$$

Due to the evaluation of the relaxation matrix exponential $\mathrm{e}^{\mathbf{W}(\chi)\,t}$, the explicit form of the solution (7.52) and the peak amplitudes (7.55) for the two field-cycling experiments may be found numerically for a general magnetic field strength χB_{HF}.

7.3.2 Low-Field Relaxation

7.3.2.1 Zero-Field Approximation

The relaxation in zero to low magnetic field may be described to a sufficient accuracy by equations from Section 7.3.1 for $\chi = 0$. The elements $W_{ij}(\chi)$ of the relaxation matrix $\mathbf{W}(\chi)$ given by Eq. (7.50) simplify to:

$$\begin{aligned}
W_{12}(0) = W_{21}(0) &= a_{16}/4 \\
W_{13}(0) = W_{31}(0) &= (4a_{10} - a_{16})/12 \\
W_{14}(0) = W_{41}(0) &= [3(a_2 + a_5) - 2a_{10} - a_{16}]/12 \\
W_{23}(0) = W_{32}(0) &= a_{16}/4 \\
W_{24}(0) = W_{42}(0) &= a_{16}/4 \\
W_{34}(0) = W_{43}(0) &= (4a_{10} - a_{16})/12
\end{aligned} \tag{7.56}$$

Assuming that the zero-field eigenstates (7.30) are equal to:

$$\big(|\xi_1(0)\rangle, |\xi_2(0)\rangle, |\xi_3(0)\rangle, |\xi_4(0)\rangle\big)^{\mathsf{T}} = \big(|T_{+1}\rangle, |S_0\rangle, |T_0\rangle, |T_{-1}\rangle\big)^{\mathsf{T}} \tag{7.57}$$

the three unique values of the transition probabilities per unit time in (7.56) may be relabelled in the following way:

$$\begin{aligned}
W_{12}(0), W_{21}(0), W_{23}(0), W_{24}(0), W_{32}(0), W_{42}(0) &\Longrightarrow W^{\mathrm{ST}} \\
W_{13}(0), W_{31}(0), W_{34}(0), W_{43}(0) &\Longrightarrow W_1^{\mathrm{TT}} \\
W_{14}(0), W_{41}(0) &\Longrightarrow W_2^{\mathrm{TT}}
\end{aligned} \tag{7.58}$$

The three newly defined transition probabilities per unit time are depicted in Figure 7.10. W^{ST} characterizes transitions between the singlet state and the three triplet states. W_1^{TT} describes transitions between the central triplet state and the two outer triplet states. Finally, W_2^{TT} represents the rank-2 transition between the outer triplet states.

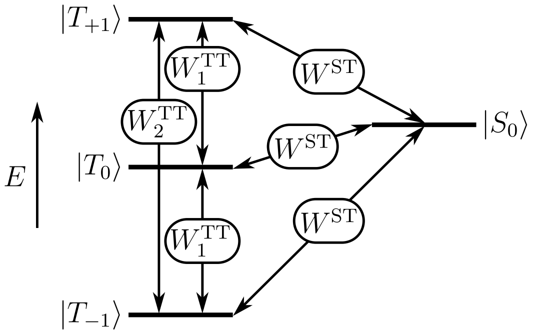

Figure 7.10: $^{15}N_2O$ energy-level scheme in low magnetic field

The relaxation matrix $\mathbf{W}_0 \equiv \mathbf{W}(0)$ is then:

$$\mathbf{W}_0 = \begin{array}{c} \begin{array}{cccc} |T_{+1}\rangle & |S_0\rangle & |T_0\rangle & |T_{-1}\rangle \end{array} \\ \left(\begin{array}{cccc} \Delta_{+1}^{\mathrm{T}} & W^{\mathrm{ST}} & W_1^{\mathrm{TT}} & W_2^{\mathrm{TT}} \\ W^{\mathrm{ST}} & \Delta_0^{\mathrm{S}} & W^{\mathrm{ST}} & W^{\mathrm{ST}} \\ W_1^{\mathrm{TT}} & W^{\mathrm{ST}} & \Delta_0^{\mathrm{T}} & W_1^{\mathrm{TT}} \\ W_2^{\mathrm{TT}} & W^{\mathrm{ST}} & W_1^{\mathrm{TT}} & \Delta_{-1}^{\mathrm{T}} \end{array}\right) \end{array} \begin{array}{c} \\ \langle T_{+1}| \\ \langle S_0| \\ \langle T_0| \\ \langle T_{-1}| \end{array} \tag{7.59}$$

where:

$$\begin{aligned} \Delta_{\pm1}^{\mathrm{T}} &= -W^{\mathrm{ST}} - W_1^{\mathrm{TT}} - W_2^{\mathrm{TT}} \\ \Delta_0^{\mathrm{S}} &= -3W^{\mathrm{ST}} \\ \Delta_0^{\mathrm{T}} &= -W^{\mathrm{ST}} - 2W_1^{\mathrm{TT}} \end{aligned} \tag{7.60}$$

The eigenvalues and eigenvectors of the relaxation matrix $\mathbf{W}_0$ are listed in Table 7.2.

Eigenvalue	Eigenvector
0	$(1,1,1,1)^{\mathsf{T}}$
$-4W^{\mathrm{ST}} = -a_{16} \equiv -1/T_S$	$(1,-3,1,1)^{\mathsf{T}} \equiv \boldsymbol{V}_0$
$-W^{\mathrm{ST}} - 3W_1^{\mathrm{TT}} = -a_{10} \equiv -1/T_{\#2}$	$(1,0,-2,1)^{\mathsf{T}} \equiv \boldsymbol{V}_2$
$-W^{\mathrm{ST}} - W_1^{\mathrm{TT}} - 2W_2^{\mathrm{TT}} = -(a_2 + a_5)/2 \equiv -1/T_1$	$(-1,0,0,1)^{\mathsf{T}} \equiv \boldsymbol{V}_1$

Table 7.2: Eigenvalues and eigenvectors of the zero-field relaxation matrix $\mathbf{W}_0$

The zero eigenvalue corresponds to a uniform population distribution, i.e., equilibrium populations in zero field without any relaxation. The eigenvector $\boldsymbol{V}_0$ corresponds to singlet spin order, i.e., the difference between the singlet and the mean triplet populations. The corresponding eigenvalue is the inverse of T_S. The eigenvector $\boldsymbol{V}_2$ represents a rank-2 spin order, i.e., the difference between the populations of the central triplet and the mean of the outer triplet states. The corresponding time constant is denoted $T_{\#2}$. Finally, $\boldsymbol{V}_1$ denotes the population distribution during the low-field T_1 experiment with the corresponding relaxation time constant T_1.

The time evolution of the populations (7.45) for $\chi = 0$ is simply:

$$\boldsymbol{P}(t,0) = \mathrm{e}^{\mathbf{W}_0\, t} \cdot \boldsymbol{P}(0,1) \tag{7.61}$$

7.3.2.2 Singlet Experiment

The description of the singlet experiment follows Figure 7.4. The spin system is initially in the thermal equilibrium. The populations of the energy levels may be described according to Eq. (7.53) by:

$$\boldsymbol{P}_{\text{eq}}(1) = (-1,0,0,1)^{\mathsf{T}} \tag{7.62}$$

After the semi-selective inversion and the adiabatic transport into low field, the initial low-field population vector $\boldsymbol{P}(0,1)$ is given either by:

$$\boldsymbol{P}_{\text{eq}}(1) \xrightarrow{\pi_{1,x}\ +\ \text{adiab.}} \boldsymbol{P}(0,1) = (0,-1,1,0)^{\mathsf{T}} \tag{7.63}$$

if the inversion is applied to the $\underline{^{15}\mathrm{N}}{}^{15}\mathrm{NO}$ site, or by:

$$\boldsymbol{P}_{\text{eq}}(1) \xrightarrow{\pi_{2,x}\ +\ \text{adiab.}} \boldsymbol{P}(0,1) = (0,1,-1,0)^{\mathsf{T}} \tag{7.64}$$

if the $^{15}\mathrm{N}\underline{^{15}\mathrm{N}}\mathrm{O}$ site is selectively inverted. Continuing with, e.g., Eq. (7.63), such a population distribution is the linear combination of the singlet and rank-2 spin orders:

$$(0,-1,1,0)^{\mathsf{T}} = (\boldsymbol{V}_0 - \boldsymbol{V}_2)/3 \tag{7.65}$$

Each of the spin orders relaxes with its own time constant, see Table 7.2. Therefore, the overall time evolution after the relaxation interval τ_{LF} in low field is described by:

$$\boldsymbol{P}(\tau_{\text{LF}},0) = \mathrm{e}^{\mathbf{W}_0\, \tau_{\text{LF}}} \cdot \boldsymbol{P}(0,1) = \frac{1}{3}\left(\boldsymbol{V}_0\, \mathrm{e}^{-\tau_{\text{LF}}/T_S} - \boldsymbol{V}_2\, \mathrm{e}^{-\tau_{\text{LF}}/T_{\#2}}\right) \tag{7.66}$$

After the adiabatic transport back into the spectrometer, the semi-selective $(\pi/2)_{k,y}$ pulse is used to read out the remaining population distribution. The time-dependence of the peak amplitudes in the frequency spectrum is given by, using Eqs. (7.54), (7.55) and (7.66):

$$A_p(\tau_{\text{LF}},\chi) = \boldsymbol{Q}_p^{\mathsf{T}} \cdot \boldsymbol{P}(\tau_{\text{LF}},0) = \boldsymbol{Q}_p^{\mathsf{T}} \cdot \mathrm{e}^{\mathbf{W}_0\, \tau_{\text{LF}}} \cdot \boldsymbol{P}(0,1) \tag{7.67}$$

or explicitly by:

$$\begin{aligned}
A_1(\tau_{\text{LF}}) &= -\frac{4}{3}\mathrm{e}^{-\tau_{\text{LF}}/T_S} + \frac{1}{3}\mathrm{e}^{-\tau_{\text{LF}}/T_{\#2}} \\
A_2(\tau_{\text{LF}}) &= -\mathrm{e}^{-\tau_{\text{LF}}/T_{\#2}} \\
A_3(\tau_{\text{LF}}) &= \mathrm{e}^{-\tau_{\text{LF}}/T_{\#2}} \\
A_4(\tau_{\text{LF}}) &= \frac{4}{3}\mathrm{e}^{-\tau_{\text{LF}}/T_S} - \frac{1}{3}\mathrm{e}^{-\tau_{\text{LF}}/T_{\#2}}
\end{aligned} \tag{7.68}$$

In the other case (7.64) of the initial low-field population vector, peak amplitudes with opposite signs are obtained.

An example of the time evolution of the $^{15}\mathrm{N}\underline{^{15}\mathrm{N}}\mathrm{O}$ doublet in the low field of 3.3 mT is shown in Figure 7.11.

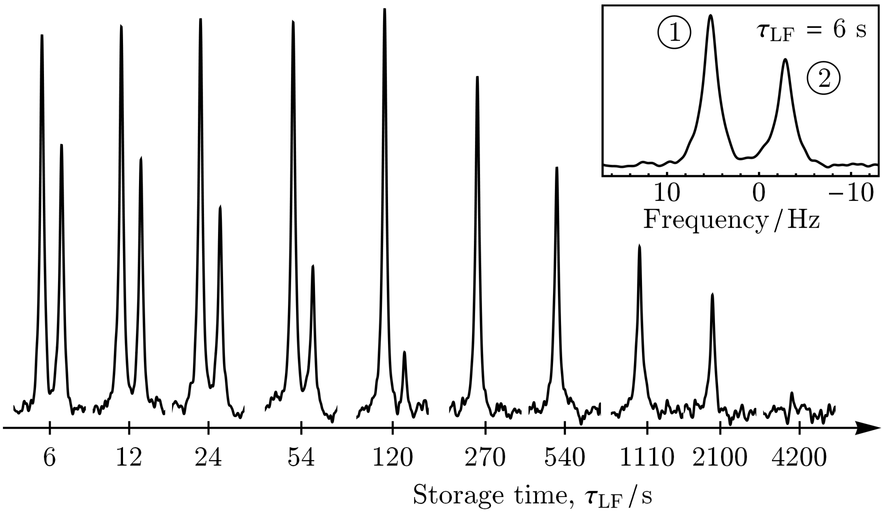

Figure 7.11: The low-field singlet experiment spectra of the $^{15}\mathrm{N}\underline{^{15}\mathrm{N}}\mathrm{O}$ doublet as a function of the low-field interval τ_{LF} ($B_0 \approx 3.3$ mT). The carrier was set to $\omega_{\mathrm{rf}}^{(2)}$ during the whole experiment. The displayed τ_{LF} intervals are approximately equally spaced on a logarithmic scale.

7.3.2.3 T_1 Experiment

The low-field T_1 experiment is described by Figure 7.7. The initial high-field population distribution, given by Eq. (7.62), is adiabatically transported into low field. The initial low-field population vector remains unchanged:

$$\boldsymbol{P}_{\mathrm{eq}}(1) \xrightarrow{\text{adiab.}} \boldsymbol{P}(0,1) = (-1,0,0,1)^{\mathsf{T}} \tag{7.69}$$

Such a population distribution is equivalent to the eigenvector $\boldsymbol{V}_1$ in Table 7.2. It relaxes with the time constant T_1. Therefore, after the low-field relaxation interval τ_{LF}, the populations are given by:

$$\boldsymbol{P}(\tau_{\mathrm{LF}},0) = \mathrm{e}^{\mathbf{W}_0\,\tau_{\mathrm{LF}}} \cdot \boldsymbol{P}(0,1) = \boldsymbol{V}_1\,\mathrm{e}^{-\tau_{\mathrm{LF}}/T_1} \tag{7.70}$$

Using Eqs. (7.54), (7.55) and (7.70), all four peak amplitudes in the frequency spectrum undergo the same time evolution:

$$A_p(\tau_{\mathrm{LF}}) = -\mathrm{e}^{-\tau_{\mathrm{LF}}/T_1} \tag{7.71}$$

for $p = \{1,2,3,4\}$.

7.3.3 Intermediate-Field Relaxation

The description of the case, in which the magnetic field spans between the lowest used field ($B_{\mathrm{LF}} \approx 3.3$ mT) and the spectrometer field ($B_{\mathrm{HF}} \approx 7046$ mT) may be computed numerically by using Eqs. (7.52) and (7.55). The time evolution of the peak amplitudes in the frequency spectrum is given by:

$$A_p(\tau_{\mathrm{LF}}, \chi) = \boldsymbol{Q}_p^{\mathsf{T}} \cdot \left\{ \boldsymbol{P}_{\mathrm{eq}}(\chi) + \mathrm{e}^{\mathbf{W}(\chi)\,\tau_{\mathrm{LF}}} \cdot [\boldsymbol{P}(0,1) - \boldsymbol{P}_{\mathrm{eq}}(\chi)] \right\} \tag{7.72}$$

The equilibrium population vector $\boldsymbol{P}_{\mathrm{eq}}(\chi)$ in the magnetic field of the strength χB_{HF} is given by Eq. (7.53). The high-field population difference patters $\boldsymbol{Q}_p$, which give rise to the spectral peaks are given by Eq. (7.54). Both $\boldsymbol{Q}_p$ and $\boldsymbol{P}_{\mathrm{eq}}(\chi)$ remain the same for the field-dependent "singlet" and T_1 experiments in the field of the strength χB_{HF}.

The population vector $\boldsymbol{P}(0,1)$ immediately after adiabatic transport into low field varies. In the case of the field-dependent "singlet" experiment, $\boldsymbol{P}(0,1)$ is given by Eq. (7.63), if the semi-selective inversion is applied to the $\underline{^{15}\mathrm{N}}{}^{15}\mathrm{NO}$ site, and by Eq. (7.64), if the $^{15}\mathrm{N}\underline{^{15}\mathrm{N}}\mathrm{O}$ site is selectively inverted. In the case of the field-dependent T_1 experiment, $\boldsymbol{P}(0,1)$ is given by Eq. (7.69).

There are two extreme cases of the field-dependent relaxation. The case of zero field ($\chi = 0$, $\Theta = 0$) has already been treated in detail in Section 7.3.2. In the case of the spectrometer field ($\chi = 1$, $\Theta = \pi/2$), for completion, the relaxation matrix elements W_{ij} in Eq. (7.50) simplify into:

$$\begin{aligned} W_{12}(1) = W_{21}(1) = W_{34}(1) = W_{43}(1) &= [3(a_2 - a_5) + 2a_{10} + a_{16}]/12 \\ W_{13}(1) = W_{31}(1) = W_{24}(1) = W_{42}(1) &= [-3(a_2 - a_5) + 2a_{10} + a_{16}]/12 \\ W_{14}(1) = W_{41}(1) = W_{23}(1) = W_{32}(1) &= [3(a_2 + a_5) - 2a_{10} - a_{16}]/12 \end{aligned} \tag{7.73}$$

The eigenvectors and eigenvalues of the relaxation matrix $\mathbf{W}(1)$ are given in Table 7.3.

Eigenvalue	Eigenvector
0	$(1,1,1,1)^{\mathsf{T}}$
$-a_2 \equiv 1/T_1^{(1)}$	$(-1,1,-1,1)^{\mathsf{T}}$
$-a_5 \equiv 1/T_1^{(2)}$	$(-1,-1,1,1)^{\mathsf{T}}$
$-(2a_{10} + a_{16})/3$	$(1,-1,-1,1)^{\mathsf{T}}$

Table 7.3: Eigenvalues and eigenvectors of the high-field relaxation matrix $\mathbf{W}(1)$

The eigenvalue a_2 and the corresponding eigenvector denote the high-field relaxation time constant $T_1^{(1)}$ and the z-magnetization for the $\underline{^{15}\mathrm{N}}{}^{15}\mathrm{NO}$ site. Similarly the eigenvalue

a_5 and the related eigenvector denote the high-field relaxation time constant $T_1^{(2)}$ and the z-magnetization for the $^{15}\mathrm{N}\underline{^{15}\mathrm{N}}\mathrm{O}$ site. The third nontrivial pair of the eigenvalue and eigenvector corresponds to the longitudinal two-spin order of $\underline{^{15}\mathrm{N}}{}^{15}\mathrm{NO}$ and $^{15}\mathrm{N}\underline{^{15}\mathrm{N}}\mathrm{O}$ sites.

In the spectrometer field, the low-field singlet experiment turns into inversion recovery with the peak amplitude trajectories given by Eq. (2.32). The T_1 experiment becomes the one pulse experiment giving constant peak amplitudes.

The constants a_i defined in Eq. (7.44), which appear in the relaxation matrix $\mathbf{W}(\chi)$, are those with indices $i = \{2, 5, 10, 16\}$. They are used as fitting parameters. Comparison of the corresponding spherical tensor operators in the form of projection superoperators with the concrete forms of the relaxation superoperators of individual relaxation mechanisms in Section 7.1.3 reveals that the a_2 and a_5 constants include CSA and SR relaxation mechanisms. Being equal to the longitudinal relaxation rates of the individual ^{15}N nuclear sites, they also include DD relaxation. a_{10} comprises contribution from the DD relaxation, and a_{16} represents other mechanisms.

7.4 Analysis of Results

7.4.1 Low-Field Relaxation

7.4.1.1 Singlet Experiment

The pulse sequence in Figure 7.4 was used for observation of the low-field singlet relaxation. In order to resolve individual peaks of the observed doublet, MSE signals consisting of $N_\mathrm{e} = 104$ echoes with π-pulse spacing of $\tau = 2$ s were acquired. The achieved SNR enhancement was between a factor of 4 and 5.

As derived in Section 7.3.2.2, irrespective of which ^{15}N site was selectively inverted in order to prepare the singlet precursor state, or later selectively excited to observe the population distribution after the low-field relaxation, there are only two distinct dependencies of the peak amplitudes:

$$\begin{aligned} |A_1(\tau_\mathrm{LF})| = |A_4(\tau_\mathrm{LF})| &= \frac{4}{3}\mathrm{e}^{-\tau_\mathrm{LF}/T_S} - \frac{1}{3}\mathrm{e}^{-\tau_\mathrm{LF}/T_{\#2}} \\ |A_2(\tau_\mathrm{LF})| = |A_3(\tau_\mathrm{LF})| &= \mathrm{e}^{-\tau_\mathrm{LF}/T_{\#2}} \end{aligned} \tag{7.74}$$

To confirm this statement, the low-field relaxation of $^{15}\mathrm{N}_2\mathrm{O}$ dissolved in DMSO was measured, while applying the semi-selective inversion and excitation to either of the two ^{15}N sites. The peak integrals from these measurements are shown in Figures 7.12.

Since the time evolution of the peak integrals was similar for all four combinations of the carrier frequency, all four sets of peak integrals were averaged and fitted by the functions in (7.74). Mean values and standard deviations of the peak integrals, together with the best fits are shown in Figure 7.13.

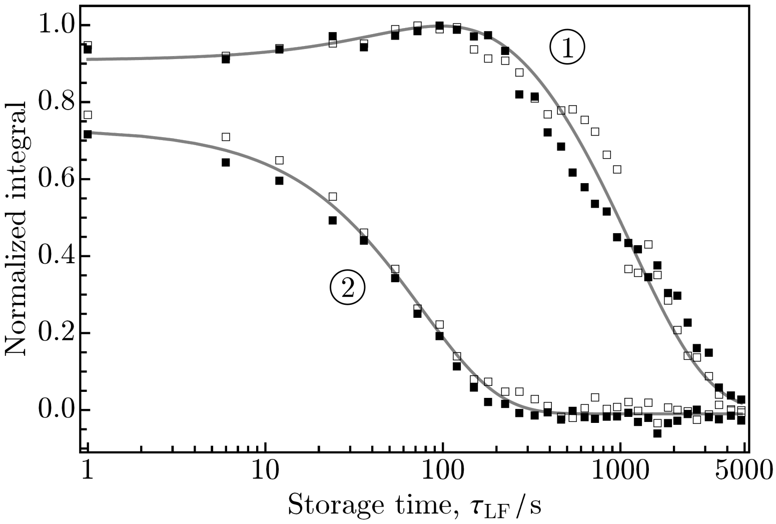

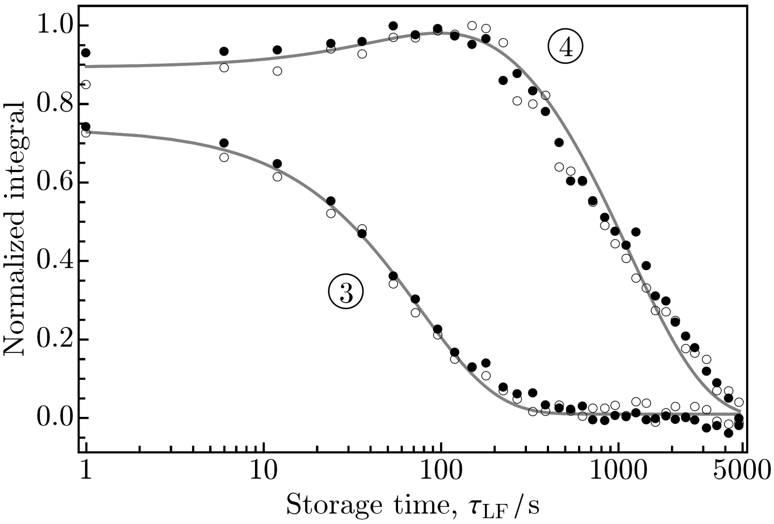

Figure 7.12: $^{15}N_2O$ relaxation observed during the low-field singlet experiment for the different combinations of the selectively inverted and excited ^{15}N sites. The first $\pi_{j,x}$ and the second $(\pi/2)_{k,y}$ rf pulses were applied to the $\{j,k\}$ combination of the ^{15}N sites, where $j,k = \{1,2\}$. Top: Normalized integrals of the $^{15}\mathrm{N}\underline{^{15}\mathrm{N}}\mathrm{O}$ doublet peaks 1 and 2 for the $\{2,2\}$ (▪) and the $\{1,2\}$ (▫) combinations of the ^{15}N sites. Bottom: Normalized integrals of the $\underline{^{15}\mathrm{N}}^{15}\mathrm{NO}$ doublet peaks 3 and 4 for the $\{2,1\}$ (•) and the $\{1,1\}$ (◦) combinations of the ^{15}N sites. The gray curves denotes the best fit of the averaged data by function given in Eq. (7.74).

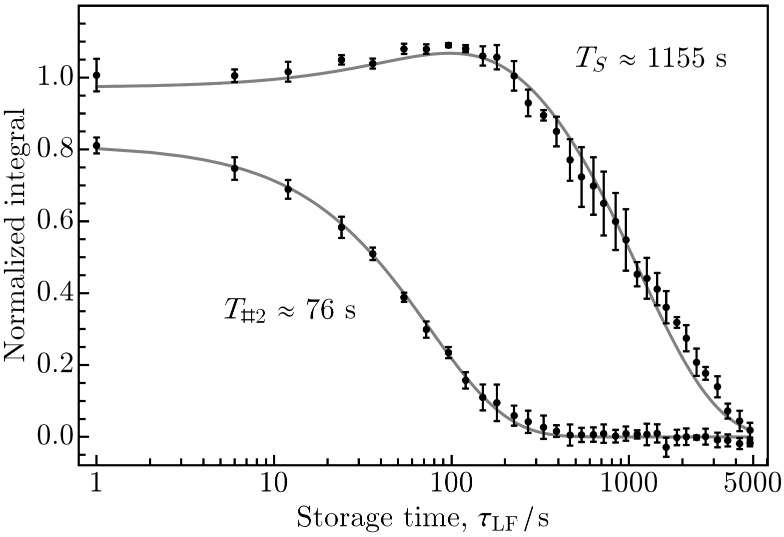

Figure 7.13: $^{15}N_2O$ relaxation observed during the low-field singlet experiment. The averaged data from Figures 7.12 were fitted by the function given in Eq. (7.74). The gray curve denotes the best fit.

All fitting was performed using Mathematica v. 8 [176]. Despite the use of both local and global optimization methods available, it was difficult for the fitting routines to get a better agreement with the data than that shown in Figure 7.13. The numerical values of the transition probabilities per unit time and the corresponding time constants, derived by using relationships in Table 7.2, are [61]:

$$\left.\begin{aligned} W^{\mathrm{ST}} &= (0.216 \pm 0.004) \times 10^{-3}\ \mathrm{s}^{-1} \\ W_2^{\mathrm{TT}} &= (0.140 \pm 0.140) \times 10^{-3}\ \mathrm{s}^{-1} \end{aligned}\right\} \iff \left\{\begin{aligned} T_S &= 1155 \pm 23\ \mathrm{s} \\ T_{\#2} &= 76 \pm 4\ \mathrm{s} \end{aligned}\right. \tag{7.75}$$

When compared to the reference values from [57], measured in the magnetic field of 2 mT ($T_{\#2}$ not determined):

$$\begin{aligned} &\text{Low field:} && T_S = 1583 \pm 57\ \mathrm{s},\ T_1 = 197 \pm 5\ \mathrm{s} \\ &\text{High field:} && T_1^{(1)} \approx 198\ \mathrm{s},\ T_1^{(1)} \approx 114\ \mathrm{s} \end{aligned} \tag{7.76}$$

mainly the singlet relaxation time T_S is substantially lower. Nevertheless, when the expected values (7.76) were tentatively substituted into Eqs. (7.74), the theoretical dependencies were in a significant disagreement with the experimental data. One reason may arise from averaging of the four datasets. Another reason was the discussed difficulties during data fitting as may be seen in Figures 7.12 and 7.13. Less likely, the value reported in [57] might be slightly overestimated, since a single exponential was used for fitting of the singlet relaxation dependence, see Eq. (7.43), which is currently an usual practice.

7.4.1.2 T_1 Experiment

The low-field T_1 relaxation was observed by means of the pulse sequence in Figure 7.7. The SNR enhancement by means of the MSE signal acquisition was avoided. The peak integrals for the $^{15}\text{N}\underline{^{15}\text{N}}\text{O}$ and $\underline{^{15}\text{N}}^{15}\text{NO}$ doublets (not for individual peaks) are shown in Figure 7.14.

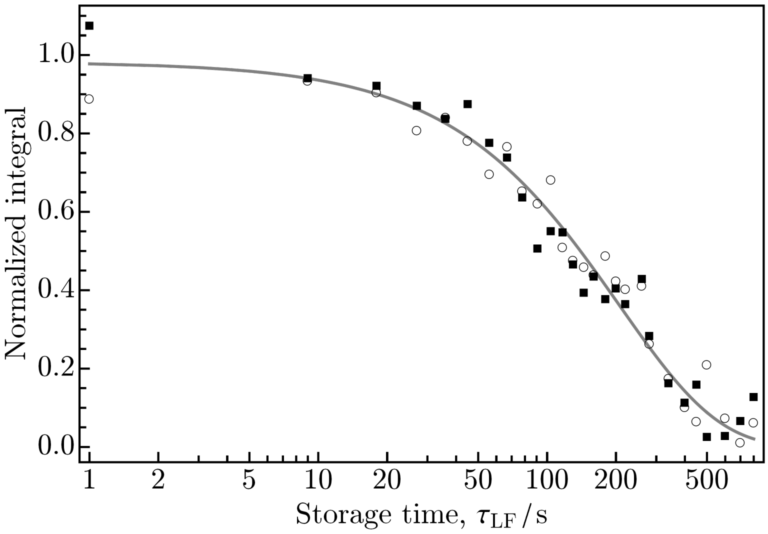

Figure 7.14: The $^{15}\text{N}\underline{^{15}\text{N}}\text{O}$ (▪) and $\underline{^{15}\text{N}}^{15}\text{NO}$ site (∘) relaxation observed during the low-field T_1 experiment. The gray curve denotes the best fit of the averaged data by function given in Eq. (7.77).

In accordance with Eq. (7.71), both ^{15}N sites are expected to relax exponentially with only one time constant:

$$|A(\tau_{\text{LF}})| = \text{e}^{-\tau_{\text{LF}}/T_1} \tag{7.77}$$

Due to similarity of the time evolution of the peak integrals of both doublets, both datasets were averaged and fitted by (7.77), see Figure 7.15. Using the values of the transition probabilities per unit time in (7.75), the remaining relaxation time constant was determined:

$$W_1^{\text{TT}} = (4.32 \pm 0.23) \times 10^{-3}\ \text{s}^{-1} \iff T_1 = 207 \pm 7\ \text{s} \tag{7.78}$$

The T_1 value is in agreement with (7.76).

7.4.1.3 Spin-Rotation Relaxation Effects (Low-Field Relaxation)

The obtained values of the transition probabilities per unit time and the relaxation time constants given in (7.75) and (7.78) were used to resolve the role of the spin-rotation relaxation on the singlet state in $^{15}\text{N}_2\text{O}$ dissolved in DMSO. It is known that spin-rotation relaxation dominates for the gas phase $^{15}\text{N}_2\text{O}$ [233–235].

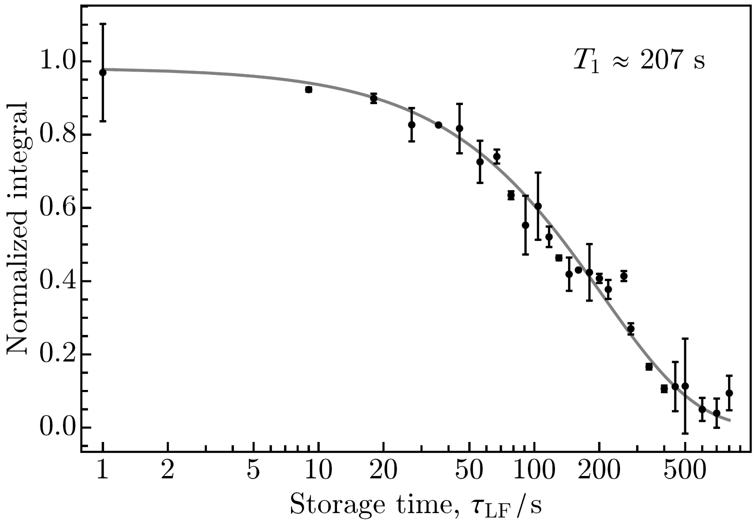

Figure 7.15: $^{15}N_2O$ relaxation observed during the low-field T_1 experiment. The averaged data from Figure 7.14 were fitted by the function given in Eq. (7.77). The gray curve denotes the best fit.

When the double-quantum DD contribution W_2^{TT} to T_1 is subtracted, considering that $W_2^{\mathrm{TT}}(\mathrm{DD}) = 2W_1^{\mathrm{TT}}(\mathrm{DD})$, the modified time constants are obtained:

$$\begin{aligned} W^{\mathrm{ST}}(\text{no DD}) &= (0.216 \pm 0.004) \times 10^{-3}\ \mathrm{s}^{-1} \equiv W^{\mathrm{ST}} \\ W_1^{\mathrm{TT}}(\text{no DD}) &= (4.25 \pm 0.24) \times 10^{-3}\ \mathrm{s}^{-1} \\ W_2^{\mathrm{TT}}(\text{no DD}) &\equiv 0 \end{aligned} \tag{7.79}$$

The ratio of the above transition rates per unit time is equal to:

$$\frac{W_1^{\mathrm{TT}}(\text{no DD})}{W^{\mathrm{ST}}} = 19.7 \pm 1.2 \equiv \mathcal{R}_W^{\mathrm{exp}} \tag{7.80}$$

From [226], the following relationships hold for the largest principal values C_1 and C_2 of the spin-rotation coupling tensors of the $\underline{^{15}\mathrm{N}}{}^{15}\mathrm{NO}$ and $^{15}\mathrm{N}\underline{^{15}\mathrm{N}}\mathrm{O}$ site, respectively:

$$\begin{aligned} W^{\mathrm{ST}}(\mathrm{SR}) &= \frac{1}{2}(C_1 - C_2)^2 J_{\mathrm{RMS}}^2 \tau_{\mathrm{c}}^{\mathrm{SR}} \\ W_1^{\mathrm{TT}}(\mathrm{SR}) &= \frac{1}{2}(C_1 + C_2)^2 J_{\mathrm{RMS}}^2 \tau_{\mathrm{c}}^{\mathrm{SR}} \end{aligned} \tag{7.81}$$

J_{RMS} denotes the RMS value of the fluctuating molecular angular momentum, and $\tau_{\mathrm{c}}^{\mathrm{SR}}$ is the correlation time. Therefore:

$$\frac{W_1^{\mathrm{TT}}(\mathrm{SR})}{W^{\mathrm{ST}}(\mathrm{SR})} = \frac{(C_1 + C_2)^2}{(C_1 - C_2)^2} \equiv \mathcal{R}_W \iff \frac{T_S(\mathrm{SR})}{T_1(\mathrm{SR})} = \frac{C_1^2 + C_2^2}{2(C_1 - C_2)^2} \equiv \mathcal{R}_T \tag{7.82}$$

Two distinct estimates of the C_1 and C_2 values have been published so far. Molecular beam electric resonance experiment carried out by Reinartz and coworkers on the ground vibrational state of $^{14}N^{14}N^{16}O$ gave [236]:

$$\begin{aligned} C_1 &= 1.829 \pm 0.065 \text{ kHz} \\ C_2 &= 3.06 \pm 0.12 \text{ kHz} \end{aligned} \tag{7.83}$$

The corresponding ratios (7.82) are equal to:

$$\begin{aligned} \mathcal{R}_W^{\text{Rei}} &= 15.8 \pm 3.1 \\ \mathcal{R}_T^{\text{Rei}} &= 4.19 \pm 0.78 \end{aligned} \tag{7.84}$$

These values are in good agreement with the current values of $\mathcal{R}_W^{\text{exp}}$ in Eq. (7.80) and with:

$$\mathcal{R}_T^{\text{exp}} = 5.14 \pm 0.30 \tag{7.85}$$

evaluated from values in (7.75) and (7.78).

Based on nuclear spin-lattice relaxation data, Jameson and coworkers provided a different set of values [233–235]:

$$\begin{aligned} C_1 &= 2.48 \text{ kHz} \\ C_2 &= 3.35 \text{ kHz} \end{aligned} \tag{7.86}$$

These values were published without confidence limits. Values of the corresponding ratios are equal to:

$$\begin{aligned} \mathcal{R}_W^{\text{Jam}} &= 44.9 \\ \mathcal{R}_T^{\text{Jam}} &= 11.5 \end{aligned} \tag{7.87}$$

The values of ratios $\mathcal{R}^{\text{Jam}}$ are almost a factor of 2 bigger than the experimental values $\mathcal{R}^{\text{exp}}$ and a factor of 3 bigger compared to $\mathcal{R}^{\text{Rei}}$. If Jameson was right, then the spin-rotation relaxation would proceed two- to three-times faster than what is observed experimentally. Further detailed study is needed to resolve this contradiction.

7.4.2 Intermediate-Field Relaxation

7.4.2.1 Field-Dependent Experiments

Data for the field-dependent relaxation study were acquired in a similar way to the low-field experiments. The carrier frequency was set to $\omega_{\text{rf}}^{(2)}$, i.e., the centre of the $^{15}N\underline{^{15}N}O$ doublet, during all experiments. The MSE sequence was not use. Acquired time-domain signals were treated by a decaying exponential matched filter (6.25), and the spectral peak areas were integrated. Examples of the experimental data for different magnetic field strengths are shown in Figures 7.16, 7.17 and 7.18.

All the datasets from both the field-dependent "singlet" and T_1 experiments were fitted simultaneously using the peak amplitude dependencies derived in Section 7.3.3. The best fit values of the constants a_i and the corresponding relaxation time constants are the following, using relationships in Tables 7.2 and 7.3:

$$\left.\begin{aligned} a_2 &= 3.66\times10^{-3}\ \mathrm{s}^{-1} \\ a_5 &= 7.04\times10^{-3}\ \mathrm{s}^{-1} \\ a_{10} &= 1.74\times10^{-2}\ \mathrm{s}^{-1} \\ a_{16} &= 6.57\times10^{-4}\ \mathrm{s}^{-1} \end{aligned}\right\} \iff \begin{cases} T_1^{(1)} \approx 273\ \mathrm{s}\ \text{(high field)} \\ T_1^{(2)} \approx 142\ \mathrm{s}\ \text{(high field)} \\ T_{\#2} \approx 57\ \mathrm{s} \\ T_S \approx 1522\ \mathrm{s} \\ T_1 \approx 187\ \mathrm{s}\ \text{(low field)} \end{cases} \tag{7.88}$$

Unfortunately, the global optimization routines built in Mathematica do not provide con-

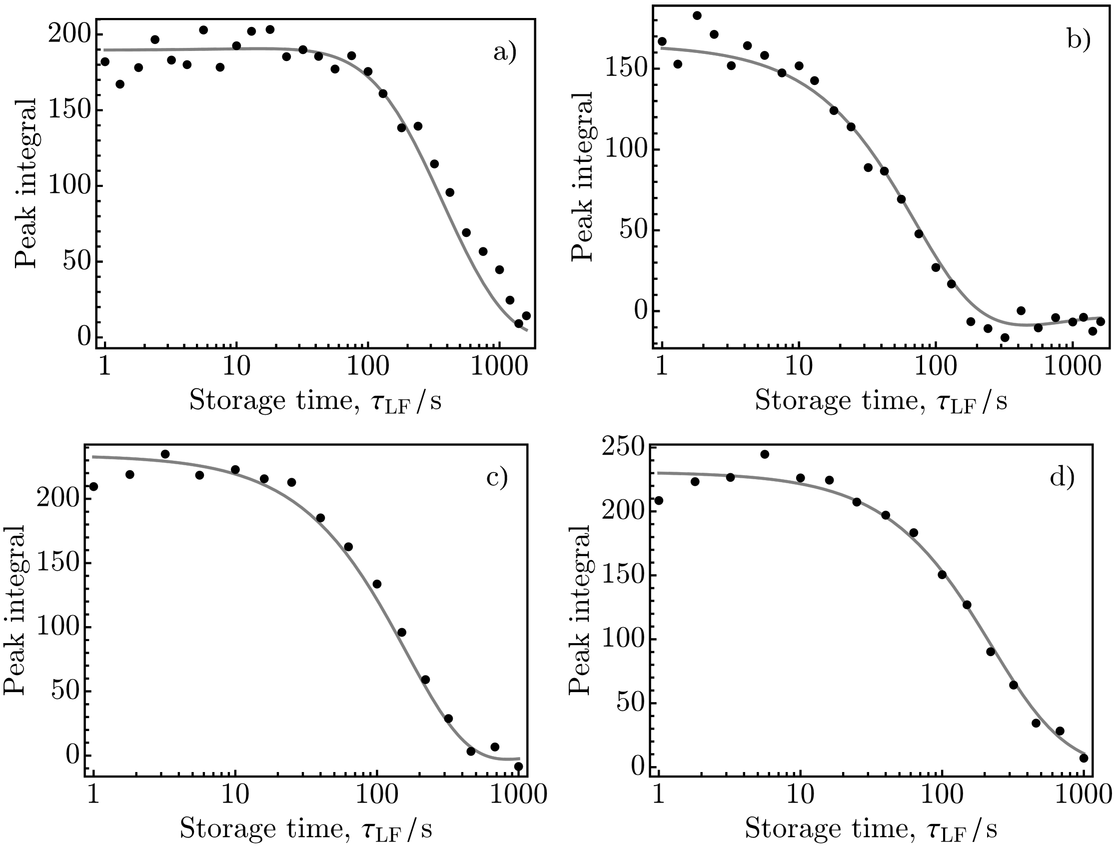

Figure 7.16: $^{15}\mathrm{N}_2\mathrm{O}$ relaxation in the magnetic field of 23.6 mT ($\tau_{\mathrm{tr}} \approx 6.48$ s). The points represent peak integrals. a) The integrals of the peak 1 during the field-dependent "singlet" experiment. b) The integrals of the peak 2 during the field-dependent "singlet" experiment. c) The integrals of the $^{15}\mathrm{N}\underline{^{15}\mathrm{N}}\mathrm{O}$ doublet during the field-dependent T_1 experiment. d) The integrals of the $\underline{^{15}\mathrm{N}}{}^{15}\mathrm{NO}$ doublet during the field-dependent T_1 experiment. The gray lines are the best fits of the relaxation model described in Section 7.3.3.

fidence limits. The T_S value is only 4 % lower than the reference value in (7.76). The low-field T_1 value is lower by 10 % than that in (7.78). The low-field $T_{\#2}$ and the high-field T_1 values deviate by up to 25 % from the values in Eq. (7.75) and Table 5.2.

Besides the global fitting of the full dataset, individual sub-datasets of the peak integrals from the intermediate-field "singlet" and T_1 relaxation experiments were fitted by a single decaying exponential function in order to extract the relaxation time constants. These may be compared to the time constants predicted by the field-dependent relaxation model. Using the intermediate-field "singlet" relaxation experiment datasets, the magnetic-field strength dependence of T_S and $T_{\#2}$ was obtained from the integrals of the peaks 1 and 2, respectively. The values of $T_1^{(1)}$ and $T_1^{(2)}$ were obtained from integrals of the $^{15}\underline{\mathrm{N}}^{15}\mathrm{NO}$ and $^{15}\mathrm{N}^{15}\underline{\mathrm{N}}\mathrm{O}$ doublets from the intermediate-field T_1 relaxation experiment.

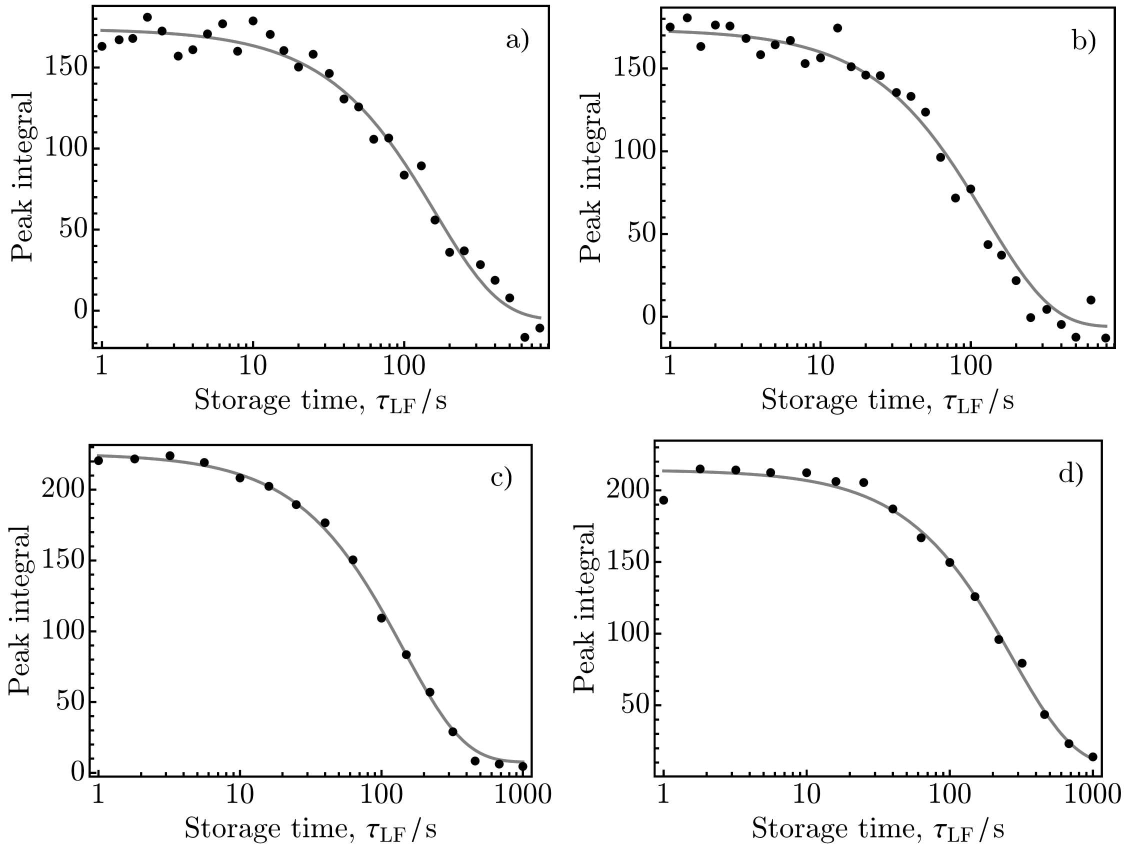

Figure 7.17: $^{15}N_2O$ relaxation in the magnetic field of 235.7 mT ($\tau_{\mathrm{tr}} \approx 3.33$ s). The points represent peak integrals. a) The integrals of the peak 1 during the field-dependent "singlet" experiment. b) The integrals of the peak 2 during the field-dependent "singlet" experiment. c) The integrals of the $^{15}\mathrm{N}^{15}\underline{\mathrm{N}}\mathrm{O}$ doublet during the field-dependent T_1 experiment. d) The integrals of the $^{15}\underline{\mathrm{N}}^{15}\mathrm{NO}$ doublet during the field-dependent T_1 experiment. The gray lines are the best fits of the relaxation model described in Section 7.3.3.

The comparison of the experimental and the model-predicted field-dependent time constants is shown in Figure 7.19 for T_S, in Figure 7.20 for $T_{\#2}$, in Figure 7.21 for $T_1^{(1)}$, and in Figure 7.22 for $T_1^{(2)}$. Despite its simplicity, except for the high-field region above 500 mT of the $T_1^{(1)}$ and possibly also $T_1^{(2)}$ dependencies, the model describes the field-dependence of the relaxation time constants satisfactorily well.

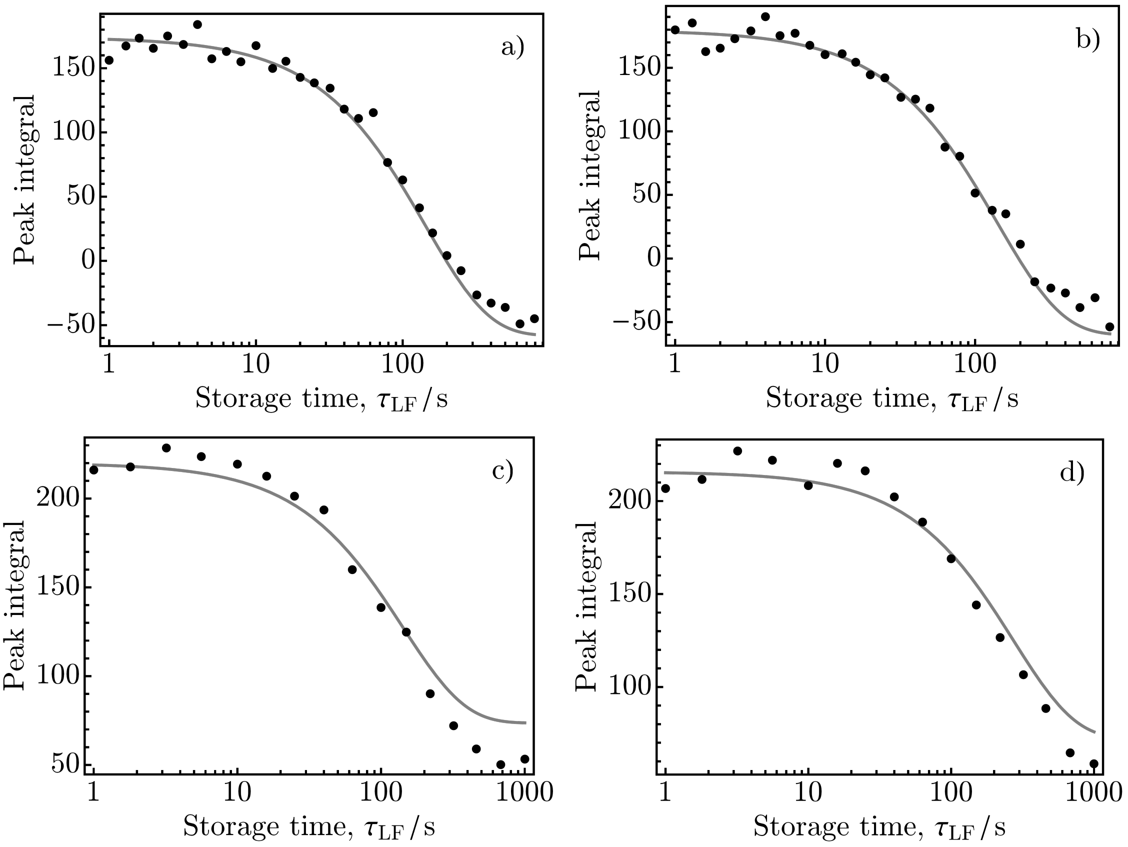

Figure 7.18: $^{15}\mathrm{N}_2\mathrm{O}$ relaxation in the magnetic field of 2357 mT ($\tau_{\mathrm{tr}} \approx 1.85$ s). The points represent peak integrals. a) The integrals of the peak 1 during the field-dependent "singlet" experiment. b) The integrals of the peak 2 during the field-dependent "singlet" experiment. c) The integrals of the $^{15}\mathrm{N}\underline{^{15}\mathrm{N}}\mathrm{O}$ doublet during the field-dependent T_1 experiment. d) The integrals of the $\underline{^{15}\mathrm{N}}{}^{15}\mathrm{NO}$ doublet during the field-dependent T_1 experiment. The gray lines are the best fits of the relaxation model described in Section 7.3.3.

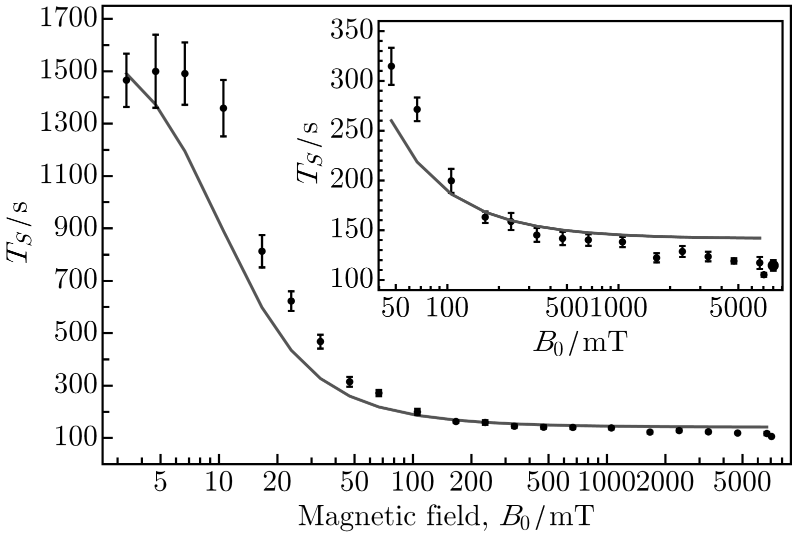

Figure 7.19: The magnetic field strength dependence of the time constant T_S. The experimental integrals (points) are compared to the theoretically predicted dependence using the model described in Section 7.3.3.

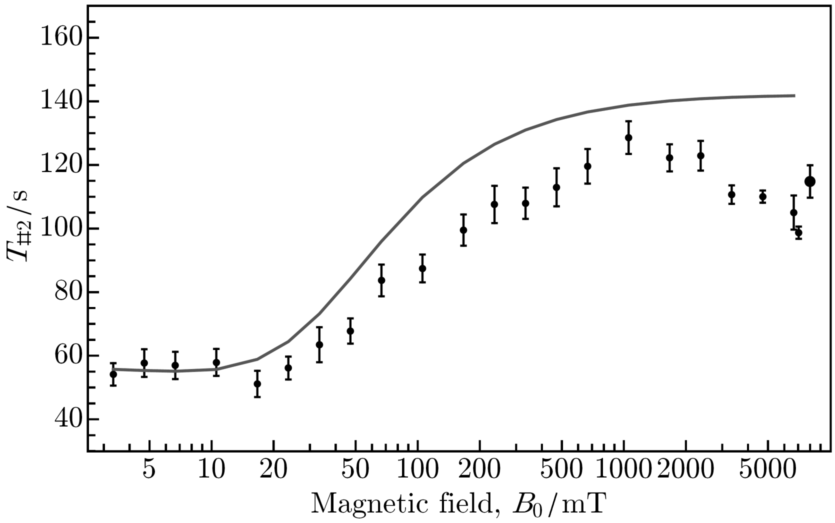

Figure 7.20: The magnetic field strength dependence of the time constant $T_{\#2}$. The experimental integrals (points) are compared to the theoretically predicted dependence using the model described in Section 7.3.3.

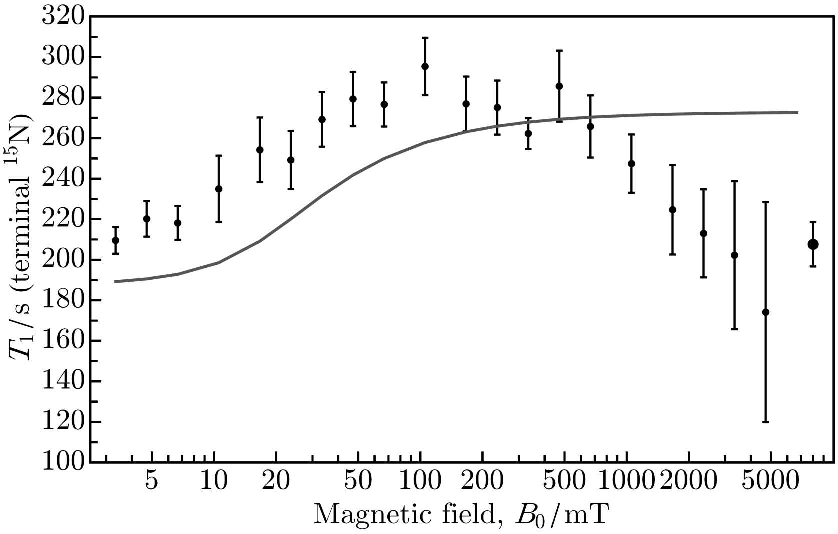

Figure 7.21: The magnetic field strength dependence of the time constant $T_1^{(1)}$. The experimental integrals (points) are compared to the theoretically predicted dependence using the model described in Section 7.3.3.

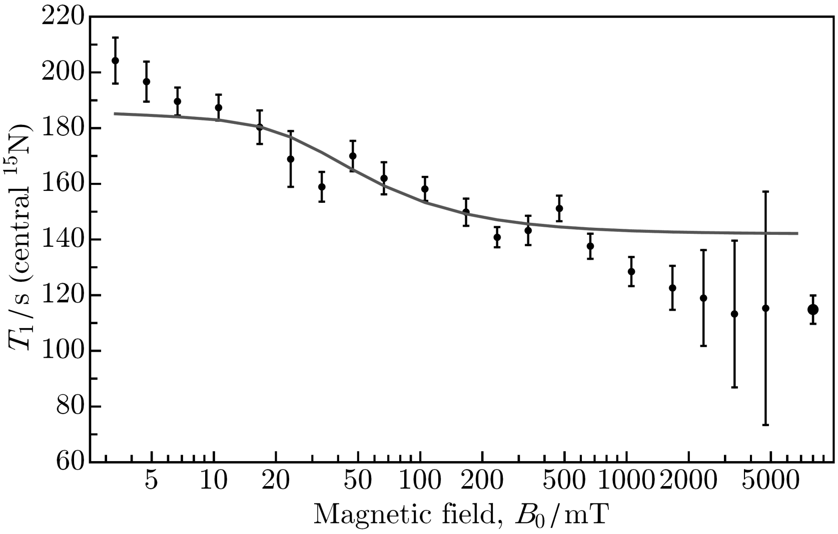

Figure 7.22: The magnetic field strength dependence of the time constant $T_1^{(2)}$. The experimental integrals (points) are compared to the theoretically predicted dependence using the model described in Section 7.3.3.

7.4.2.2 Spin-Rotation Relaxation Effects (Intermediate-Field Relaxation)

The values of ratios $\mathcal{R}_W^{\text{exp}}$ and $\mathcal{R}_T^{\text{exp}}$, computed from the results of fitting in (7.88), may be compared to those in Section 7.4.1.3:

$$\mathcal{R}_W^{\text{exp}} = \frac{-3(a_2 + a_5) + 10a_{10} - a_{16}}{6a_{16}} \approx 35.8 \tag{7.89}$$

$$\mathcal{R}_T^{\text{exp}} = \frac{-3(a_2 + a_5) + 10a_{10} + 5a_{16}}{24a_{16}} \approx 9.2 \tag{7.90}$$

These values are closer to Jameson's rather than Reinartz's findings shown in (7.87) and (7.84), respectively.

Chapter 8

Conclusions

The aim of this research was to extend the scope of singlet NMR of $^{15}N_2O$. The procedure presented in Chapter 6 allows enhancement of the spectral SNR by up to an order of magnitude through the acquisition and proper processing of the multiply refocused spin-echo (MSE) signal. In combination with singlet NMR, this method was used for the detailed study of low-field relaxation of the $^{15}N_2O$ singlet state in Chapter 7. Investigation of $^{15}N_2O$ relaxation was extended to the whole range of field strengths between low field and the spectrometer high field. The observed field-dependent relaxation was described by a general relaxation model.

8.1 SNR Enhancement

The MSE signal was acquired during the CPMG spin-echo train. The use of (semi-)selective rf pulses, which avoided J-modulation of the MSE signal, and minimization of resonance offset effects, allowed up to thousandfold refocusing of the ^{15}N signal and acquisition of $\gtrsim 10^5$ samples during time intervals of several T_2.

Two distinct techniques were used for the MSE signal processing. The linear MF-MSE technique exploited matched weighting. The achievable SNR enhancement depends on the values of the transverse relaxation time constant T_2, time constant T_2' characterizing B_0 inhomogeneity, and spacing τ of the (semi-)selective π pulses. The larger the value of the ratios T_2/T_2' and T_2/τ, the higher the SNR enhancement. While the value of T_2/T_2' is fixed, τ may be varied. Since the spectral resolution of the processed MSE signal is inversely proportional to τ, a balance has to be found between the SNR enhancement and the spectral resolution.

The MF-MSE technique is applicable to signals of any strength. It exploits the full recorded NMR signal, and does not lead to additional spectral distortions. Its weak point is the accuracy of determination of the T_2 value, which the matched filter and the achieved SNR enhancement depend on.

The nonlinear SVD-MSE technique reduces noise by means of singular value decomposition. Its performance is independent of T_2. However, either a certain initial spectral SNR ($\gtrsim 10$) and/or a large number of echo signals ($N_\mathrm{e} \gtrsim 100$) is required for efficient operation of SVD-MSE and minimization of spectral distortions after FT of the processed signal. When combined with signal apodization, the SVD-MSE technique gives a similar SNR enhancement to the MF-MSE technique.

8.2 Field-Dependent $^{15}N_2O$ Relaxation

Field-dependent relaxation of $^{15}N_2O$ was described by a general model, which represented relaxation as a time-dependent exchange of populations of the field-dependent energy eigenstates. Predicted dependencies of the peak amplitudes in the case of low-field and field-dependent relaxation were fitted to the experimental data.

Fitting of the low-field relaxation data gave an unexpectedly low value of the singlet relaxation time constant T_S compared to the previously published one [57]. A possible cause of this discrepancy was discussed. The value of low-field T_1 was in agreement. A new relaxation time constant $T_{\#2}$ of the rank-2 spin order was introduced and determined. Fitting of the field-dependent relaxation gave values of T_S and T_1 differing by less than 10 % from the reference low-field values, while the values of low-field $T_{\#2}$ and high-field T_1 for both ^{15}N sites differed by more than 20 % from the experimentally determined values.

The obtained values of the transition probabilities per unit time and the relaxation time constants were used for an analysis of spin-rotation relaxation of the $^{15}N_2O$ singlet state. Two published estimates of the spin-rotation tensors, which determine the values of the transition probabilities per unit time and the relaxation time constants, were considered. One set, provided by Reinartz, was obtained from molecular beam electric resonance measurements on the ground vibrational state of $^{14}N^{14}N^{16}O$ [236]. The other set, reported by Jameson, was obtained from nuclear spin-lattice relaxation experiments [233–235]. Jameson's results, however, imply that the spin-rotation relaxation proceeds by up to a factor 3 faster compared to Reinartz findings. Fitting of the low-field relaxation agreed best with Reinartz's conclusions, whereas fitting of the field-dependent relaxation gave results closer to Jameson's findings.

Based on the comparison of the field-dependence of the experimental and theoretically predicted relaxation time constants, the relaxation model can describe low- and medium-field relaxation below ~ 1 T. Predictions for higher field strengths agree only partially. With increasing field strength, field-dependent relaxation processes, such as CSA relaxation, become more significant, which is a possible cause of the discrepancy.

8.3 Future Prospects

The proposed MSE pulse sequence may easily be transferred to other NMR experiments, which detect isolated resonances or use (semi-)selective rf pulses. The MSE sequence itself may possibly be enhanced by including magnetic field gradients and phase modulation [237, 238], and its performance improved by means of composite pulses [75] or Optimal Control Theory [239–242].

Processing of the MSE signal may be made fully automatic. In the case of large and/or higher-dimensional datasets, Principal or Independent Component Analysis might be used for further SNR boosting or for obtaining additional information from the data [171, 173].

$^{15}N_2O$ field-dependent relaxation measurements did not provide an unambiguous conclusion about which set of the spin-rotation tensor principal values is closer to reality. More accurate determination of the $^{15}N_2O$ spin-rotation tensors should be performed either experimentally or computationally, if needed.

Appendices

A Basic Algebraic Definitions

A.1 Vectors

Assume a complex column vector $\boldsymbol{a}$ in n-dimensional space. Transpose of $\boldsymbol{a}$ returns a row vector:

$$\boldsymbol{a}^{\mathsf{T}} = \begin{pmatrix} a_1 \\ \vdots \\ a_n \end{pmatrix}^{\mathsf{T}} = (a_1, \ldots, a_n) \tag{A.1}$$

The vector Hölder or 2-norm is defined as [126]:

$$\|\boldsymbol{a}\|_2 = \left(\sum_{i=1}^{n} |a_i|^2 \right)^{1/2} = \left(\sum_{i=1}^{n} a_i^* a_i \right)^{1/2} \tag{A.2}$$

where the asterisk denotes complex conjugate.

The dot product of two vectors $\boldsymbol{a}$ and $\boldsymbol{b}$ of the same length is defined by:

$$\boldsymbol{a} \cdot \boldsymbol{b} = \sum_{i=1}^{n} a_i b_i = \boldsymbol{a}^{\mathsf{T}} \boldsymbol{b} \tag{A.3}$$

The cross product of two vectors $\boldsymbol{a}$ and $\boldsymbol{b}$ in three-dimensional space returns another vector $\boldsymbol{c}$:

$$\boldsymbol{c} = \boldsymbol{a} \times \boldsymbol{b} = \begin{pmatrix} a_2 b_3 - a_3 b_2 \\ a_3 b_1 - a_1 b_3 \\ a_1 b_2 - a_2 b_1 \end{pmatrix} = \begin{vmatrix} \boldsymbol{e}_x & \boldsymbol{e}_y & \boldsymbol{e}_z \\ a_1 & a_2 & a_3 \\ b_1 & b_2 & b_3 \end{vmatrix} \tag{A.4}$$

where the rightmost expression denotes the determinant, and $\boldsymbol{e}_x$, $\boldsymbol{e}_y$, and $\boldsymbol{e}_z$ are the unit vectors pointing along the corresponding Cartesian axes.

A.2 Matrices

Consider an $m \times n$ complex matrix $\mathbf{A}$ with elements A_{ij}. The matrix is symmetric, when:

$$A_{ij} = A_{ji} \tag{A.5}$$

and antisymmetric, when:

$$A_{ij} = -A_{ji} \tag{A.6}$$

Transpose of the matrix gives:

$$\mathbf{A}^{\mathsf{T}} = (A^{\mathsf{T}})_{ij} = A_{ji} \tag{A.7}$$

Adjoint of the matrix returns:

$$\mathbf{A}^{\dagger} = (A^{\dagger})_{ij} = A^{*}_{ji} \tag{A.8}$$

An $n \times n$ matrix $\mathbf{A}$ is Hermitian, if:

$$\mathbf{A} = \mathbf{A}^{\dagger} \iff A_{ij} = A^{*}_{ji} \tag{A.9}$$

and unitary, if:

$$\mathbf{A}^{\dagger}\mathbf{A} = \mathbf{A}\mathbf{A}^{\dagger} = \mathbf{E}_n \tag{A.10}$$

$\mathbf{E}_n$ denotes $n \times n$ diagonal unit matrix:

$$\mathbf{E}_n = \operatorname{diag}(1, \ldots, 1) \tag{A.11}$$

A general $m \times n$ matrix $\mathbf{B}$ is diagonal, if only matrix elements B_{ij}, where $i = j$, are nonzero. The simplified notation is:

$$\mathbf{B} = \operatorname{diag}(B_{11}, \ldots, B_{pp}) \tag{A.12}$$

where $p = \min(m, n)$.

The Frobenius or F-norm of $m \times n$ matrix $\mathbf{B}$ is defined as [126]:

$$\|\mathbf{B}\|_F = \left(\sum_{i=1}^{m}\sum_{j=1}^{n} B^{*}_{ij} B_{ij}\right)^{1/2} = \left(\sum_{i=1}^{m}\sum_{j=1}^{n} |B_{ij}|^2\right)^{1/2} \tag{A.13}$$

The trace of $n \times n$ matrix $\mathbf{A}$ denotes:

$$\operatorname{Tr}\{\mathbf{A}\} = \sum_{i=1}^{n} A_{ii} \tag{A.14}$$

The matrix $\mathbf{A}$ is called traceless, when:

$$\operatorname{Tr}\{\mathbf{A}\} = 0 \tag{A.15}$$

The following equality holds for the trace of product of several square matrices of the same dimensions:

$$\operatorname{Tr}\{\mathbf{ABC}\} = \operatorname{Tr}\{\mathbf{BCA}\} = \operatorname{Tr}\{\mathbf{CAB}\} \tag{A.16}$$

The commutator of two $n \times n$ matrices $\mathbf{A}$ and $\mathbf{B}$ is defined as:

$$[\mathbf{A}, \mathbf{B}] = \mathbf{AB} - \mathbf{BA} \tag{A.17}$$

The Kronecker product of $i \times j$ matrix $\mathbf{A}$ and $r \times s$ matrix $\mathbf{B}$ leads to a $ir \times js$ matrix $\mathbf{A} \otimes \mathbf{B}$ given by:

$$\begin{aligned} \mathbf{A} \otimes \mathbf{B} &= \begin{pmatrix} A_{11}\mathbf{B} & \cdots & A_{1j}\mathbf{B} \\ \vdots & \ddots & \vdots \\ A_{i1}\mathbf{B} & \cdots & A_{ij}\mathbf{B} \end{pmatrix} \\ &= \begin{pmatrix} A_{11}B_{11} & \cdots & A_{1j}B_{1s} \\ \vdots & \ddots & \vdots \\ A_{i1}B_{r1} & \cdots & A_{ij}B_{rs} \end{pmatrix} \\ &= \begin{pmatrix} (\mathbf{A} \otimes \mathbf{B})_{11;11} & \cdots & (\mathbf{A} \otimes \mathbf{B})_{11;js} \\ \vdots & \ddots & \vdots \\ (\mathbf{A} \otimes \mathbf{B})_{ir;11} & \cdots & (\mathbf{A} \otimes \mathbf{B})_{ir;js} \end{pmatrix} \end{aligned} \tag{A.18}$$

The matrix representation of the Kronecker product is described by [243]:

$$(\mathbf{A} \otimes \mathbf{B} \otimes \mathbf{C} \otimes \ldots)_{ijk\ldots;rst\ldots} = A_{ir}B_{js}C_{kt}\ldots \tag{A.19}$$

The ordinary product, adjoint, inverse, and trace of the Kronecker products are defined as follows:

$$(\mathbf{A} \otimes \mathbf{B} \otimes \mathbf{C} \otimes \ldots)(\mathbf{A}' \otimes \mathbf{B}' \otimes \mathbf{C}' \otimes \ldots) = \mathbf{AA}' \otimes \mathbf{BB}' \otimes \mathbf{CC}' \otimes \ldots \tag{A.20}$$

$$(\mathbf{A} \otimes \mathbf{B} \otimes \mathbf{C} \otimes \ldots)^\dagger = \mathbf{A}^\dagger \otimes \mathbf{B}^\dagger \otimes \mathbf{C}^\dagger \otimes \ldots \tag{A.21}$$

$$(\mathbf{A} \otimes \mathbf{B} \otimes \mathbf{C} \otimes \ldots)^{-1} = \mathbf{A}^{-1} \otimes \mathbf{B}^{-1} \otimes \mathbf{C}^{-1} \otimes \ldots \tag{A.22}$$

$$\mathrm{Tr}\{\mathbf{A} \otimes \mathbf{B} \otimes \mathbf{C} \otimes \ldots\} = \mathrm{Tr}\{\mathbf{A}\}\,\mathrm{Tr}\{\mathbf{B}\}\,\mathrm{Tr}\{\mathbf{C}\}\,\ldots \tag{A.23}$$

As an example, the Kronecker product of two 2×2 matrices $\mathbf{A} = \begin{pmatrix} A_{11} & A_{12} \\ A_{21} & A_{22} \end{pmatrix}$ and

$\mathbf{B} = \begin{pmatrix} B_{11} & B_{12} \\ B_{21} & B_{22} \end{pmatrix}$ equals:

$$\begin{aligned}
\mathbf{A} \otimes \mathbf{B} &= \begin{pmatrix} A_{11}\begin{pmatrix} B_{11} & B_{12} \\ B_{21} & B_{22} \end{pmatrix} & A_{12}\begin{pmatrix} B_{11} & B_{12} \\ B_{21} & B_{22} \end{pmatrix} \\ A_{21}\begin{pmatrix} B_{11} & B_{12} \\ B_{21} & B_{22} \end{pmatrix} & A_{22}\begin{pmatrix} B_{11} & B_{12} \\ B_{21} & B_{22} \end{pmatrix} \end{pmatrix} \\
&= \begin{pmatrix} A_{11}B_{11} & A_{11}B_{12} & A_{12}B_{11} & A_{12}B_{12} \\ A_{11}B_{21} & A_{11}B_{22} & A_{12}B_{21} & A_{12}B_{22} \\ A_{21}B_{11} & A_{21}B_{12} & A_{22}B_{11} & A_{22}B_{12} \\ A_{21}B_{21} & A_{21}B_{22} & A_{22}B_{21} & A_{22}B_{22} \end{pmatrix} \qquad (A.24) \\
&= \begin{pmatrix} (\mathbf{A}\otimes\mathbf{B})_{11;11} & (\mathbf{A}\otimes\mathbf{B})_{11;12} & (\mathbf{A}\otimes\mathbf{B})_{11;21} & (\mathbf{A}\otimes\mathbf{B})_{11;22} \\ (\mathbf{A}\otimes\mathbf{B})_{12;11} & (\mathbf{A}\otimes\mathbf{B})_{12;12} & (\mathbf{A}\otimes\mathbf{B})_{12;21} & (\mathbf{A}\otimes\mathbf{B})_{12;22} \\ (\mathbf{A}\otimes\mathbf{B})_{21;11} & (\mathbf{A}\otimes\mathbf{B})_{21;12} & (\mathbf{A}\otimes\mathbf{B})_{21;21} & (\mathbf{A}\otimes\mathbf{B})_{21;22} \\ (\mathbf{A}\otimes\mathbf{B})_{22;11} & (\mathbf{A}\otimes\mathbf{B})_{22;12} & (\mathbf{A}\otimes\mathbf{B})_{22;21} & (\mathbf{A}\otimes\mathbf{B})_{22;22} \end{pmatrix}
\end{aligned}$$

B Rotation Matrices

The rotation matrices, which generate rotations around x-, y- and z-axes by an angle ϕ in the three-dimensional Euclidean space are defined as follows [31]:

$$\mathbf{R}_x(\phi) = \begin{pmatrix} 1 & 0 & 0 \\ 0 & \cos\phi & -\sin\phi \\ 0 & \sin\phi & \cos\phi \end{pmatrix} \qquad (B.1)$$

$$\mathbf{R}_y(\phi) = \begin{pmatrix} \cos\phi & 0 & \sin\phi \\ 0 & 1 & 0 \\ -\sin\phi & 0 & \cos\phi \end{pmatrix} \qquad (B.2)$$

$$\mathbf{R}_z(\phi) = \begin{pmatrix} \cos\phi & -\sin\phi & 0 \\ \sin\phi & \cos\phi & 0 \\ 0 & 0 & 1 \end{pmatrix} \qquad (B.3)$$

The three matrices are unitary:

$$\mathbf{R}_\alpha^* \mathbf{R}_\alpha = \mathbf{R}_\alpha \mathbf{R}_\alpha^* = \mathbf{E}_3 \text{ for } \alpha = \{x, y, z\} \qquad (B.4)$$

The inverse is defined as:

$$\mathbf{R}_\alpha^{-1}(\phi) = \mathbf{R}_\alpha(-\phi) \qquad (B.5)$$

The explicit form of the general composite rotation, given by Eq. (2.26) equals:

$$\begin{aligned}
&\mathbf{R}(\beta,\varphi,\theta)\\
&\equiv \; \mathbf{R}_z(\varphi)\,\mathbf{R}_y(\theta)\,\mathbf{R}_z(\beta)\,\mathbf{R}_y(-\theta)\,\mathbf{R}_z(-\varphi)\\
&= \begin{pmatrix} c_\phi^2(c_\beta c_\theta^2 + s_\theta^2) + c_\beta s_\phi^2 & -c_\theta s_\beta + s_{\beta/2}^2 s_\theta^2 s_{2\phi} & s_\theta[s_\beta s_\phi - (c_\beta - 1)c_\theta c_\phi] \\ c_\theta s_\beta + s_{\beta/2}^2 s_\theta^2 s_{2\phi} & c_\beta c_\phi^2 + (c_\beta c_\theta^2 + s_\theta^2)s_\phi^2 & -s_\theta[c_\phi s_\beta + (c_\beta - 1)c_\theta s_\phi] \\ -s_\theta[(c_\beta - 1)c_\theta c_\phi + s_\beta s_\phi] & s_\theta[c_\phi s_\beta - (c_\beta - 1)c_\theta s_\phi] & c_\theta^2 + c_\beta s_\theta^2 \end{pmatrix}
\end{aligned} \tag{B.6}$$

where $s_\alpha = \sin\alpha$ and $c_\alpha = \cos\alpha$.

C Schrödinger Equation

Solution of the Schrödinger equation (2.36) with the time-independent Hamiltonian $\hat{H}$ may be derived as follows [30]. The Taylor series expansion of the wavefunction $|\Psi(t)\rangle$ about a point $t_0 \leq t$ is:

$$|\Psi(t)\rangle = \sum_{k=0}^{\infty} \frac{1}{k!} \left.\frac{\partial^k}{\partial t^k}|\Psi(t)\rangle\right|_{t=t_0} (t - t_0)^k \tag{C.1}$$

The kth derivative of Eq. (2.36) with respect to time leads to:

$$\left.\frac{\partial^k}{\partial t^k}|\Psi(t)\rangle\right|_{t=t_0} = (-\mathrm{i}\hat{H})^k |\Psi(t_0)\rangle \tag{C.2}$$

Inserting (C.2) into (C.1) results in:

$$|\Psi(t)\rangle = \left[\sum_{k=0}^{\infty} \frac{[-\mathrm{i}\hat{H}(t-t_0)]^k}{k!}\right] |\Psi(t_0)\rangle = \exp[-\mathrm{i}\hat{H}(t-t_0)]\,|\Psi(t_0)\rangle \tag{C.3}$$

The Schrödinger equation with the time-dependent Hamiltonian $\hat{H}(t)$ is solved in a different way [244]. Derivative of Eq. (2.37) with respect to time equals:

$$\frac{\partial}{\partial t}|\Psi(t)\rangle = \frac{\mathrm{d}}{\mathrm{d}t}\hat{U}(t,t_0)|\Psi(t_0)\rangle = -\mathrm{i}\hat{H}(t)\hat{U}(t,t_0)|\Psi(t_0)\rangle \tag{C.4}$$

This leads to equation for the propagator:

$$\frac{\mathrm{d}}{\mathrm{d}t}\hat{U}(t,t_0) = -\mathrm{i}\hat{H}(t)\hat{U}(t,t_0) \tag{C.5}$$

Integration of (C.5) over a time interval $t \in [t_0, t]$ gives:

$$\hat{U}(t,t_0) = \hat{E} - \mathrm{i}\int_{t_0}^{t} \mathrm{d}t_1\, \hat{H}(t_1)\, \hat{U}(t_1,t_0) \tag{C.6}$$

where $\hat{U}(t_0, t_0) = \hat{E}$ is the unity operator. Eq. (C.6) is formally solved by successive iteration:

$$\begin{aligned} \hat{U}(t,t_0) &= \hat{E} - \mathrm{i}\int_{t_0}^{t} \mathrm{d}t_1\, \hat{H}(t_1) \left(\hat{E} - \mathrm{i}\int_{t_0}^{t_1} \mathrm{d}t_2\, \hat{H}(t_2) \left[\hat{E} - \mathrm{i}\int_{t_0}^{t_2} \mathrm{d}t_3\, \hat{H}(t_3) \ldots\right]\right) \\ &= \hat{E} + \sum_{k=1}^{\infty} (-\mathrm{i})^k \int_{t_0}^{t} \mathrm{d}t_1 \int_{t_0}^{t_1} \mathrm{d}t_2 \ldots \int_{t_0}^{t_{k-1}} \mathrm{d}t_k\, \hat{\hat{T}}[\hat{H}(t_1)\hat{H}(t_2)\ldots\hat{H}(t_k)] \end{aligned} \tag{C.7}$$

where the operator product time-ordering superoperator $\hat{\hat{T}}$ is defined as:

$$\hat{\hat{T}}[\hat{H}(t_1)\hat{H}(t_2)] = \begin{cases} \hat{H}(t_1)\hat{H}(t_2) & \text{for } t_1 \geq t_2 \\ \hat{H}(t_2)\hat{H}(t_1) & \text{for } t_1 < t_2 \end{cases} \tag{C.8}$$

If $t > t_0$, Eq. (C.7) may be simplified:

$$\hat{U}(t,t_0) = \hat{E} + \sum_{k=1}^{\infty} \frac{(-\mathrm{i})^k}{k!} \int_{t_0}^{t} \mathrm{d}t_1 \int_{t_0}^{t} \mathrm{d}t_2 \ldots \int_{t_0}^{t} \mathrm{d}t_k\, \hat{\hat{T}}[\hat{H}(t_1)\hat{H}(t_2)\ldots\hat{H}(t_k)] \tag{C.9}$$

By writing Eq. (C.9) in a formal and compact way, solution of the Schrödinger equation equals:

$$|\Psi(t)\rangle = \hat{\hat{T}} \exp\left[-\mathrm{i}\int_{t_0}^{t} \mathrm{d}t' \hat{H}(t')\right] |\Psi(t_0)\rangle \tag{C.10}$$

D Spin-1/2 Operators

D.1 One Spin-1/2 Cartesian Operators

The nuclear spin angular momentum $\hat{\boldsymbol{\mathcal{I}}}$ is a vector. Using a Cartesian coordinate system, $\hat{\boldsymbol{\mathcal{I}}}$ denotes:

$$\hat{\boldsymbol{\mathcal{I}}} = (\hat{\mathcal{I}}_x, \hat{\mathcal{I}}_y, \hat{\mathcal{I}}_z) \tag{D.1}$$

The individual Cartesian spin operators have the following matrix representations (Pauli matrices), including the unity operator $\hat{\mathcal{E}}$:

$$\hat{\mathcal{I}}_x = \frac{1}{2}\begin{pmatrix} 0 & 1 \\ 1 & 0 \end{pmatrix},\ \hat{\mathcal{I}}_y = \frac{\mathrm{i}}{2}\begin{pmatrix} 0 & -1 \\ 1 & 0 \end{pmatrix},\ \hat{\mathcal{I}}_z = \frac{1}{2}\begin{pmatrix} 1 & 0 \\ 0 & -1 \end{pmatrix},\ \hat{\mathcal{E}} = \begin{pmatrix} 1 & 0 \\ 0 & 1 \end{pmatrix} \tag{D.2}$$

Magnitude of $\hat{\boldsymbol{\mathcal{I}}}$ is expressed as the square root of the square of $\hat{\boldsymbol{\mathcal{I}}}$:

$$\hat{\mathcal{I}}^2 = \hat{\boldsymbol{\mathcal{I}}} \cdot \hat{\boldsymbol{\mathcal{I}}} = \hat{\mathcal{I}}_x^2 + \hat{\mathcal{I}}_y^2 + \hat{\mathcal{I}}_z^2 \tag{D.3}$$

The squares of the operators are equal to:

$$\hat{\mathcal{I}}_x^2 = \hat{\mathcal{I}}_y^2 = \hat{\mathcal{I}}_z^2 = \frac{1}{4}\hat{\mathcal{E}} \tag{D.4}$$

$$\hat{\mathcal{I}}^2 = \frac{3}{4}\hat{\mathcal{E}} \tag{D.5}$$

For convenience, four other spin operators are introduced [14]:

$$\hat{\mathcal{I}}_\alpha = \frac{1}{2}\hat{\mathcal{E}} + \hat{I}_z \tag{D.6}$$

$$\hat{\mathcal{I}}_\beta = \tfrac{1}{2}\hat{\mathcal{E}} - \hat{I}_z \tag{D.7}$$

$$\hat{\mathcal{I}}^\pm = \hat{\mathcal{I}}_x \pm \mathrm{i}\,\hat{\mathcal{I}}_y \tag{D.8}$$

Here $\hat{\mathcal{I}}_\alpha$ and $\hat{\mathcal{I}}_\beta$ are the polarization operators, in other words, projection operators onto states $|\alpha\rangle$ and $|\beta\rangle$ given by (2.89). $\hat{\mathcal{I}}^\pm$ are the shift operators. The corresponding matrix representations are:

$$\hat{\mathcal{I}}_\alpha = \begin{pmatrix} 1 & 0 \\ 0 & 0 \end{pmatrix},\ \hat{\mathcal{I}}_\beta = \begin{pmatrix} 0 & 0 \\ 0 & 1 \end{pmatrix},\ \hat{\mathcal{I}}^+ = \begin{pmatrix} 0 & 1 \\ 0 & 0 \end{pmatrix},\ \hat{\mathcal{I}}^- = \begin{pmatrix} 0 & 0 \\ 1 & 0 \end{pmatrix} \tag{D.9}$$

The individual operators are connected through cyclic commutation relationships. The most important are:

$$[\hat{\mathcal{I}}_x, \hat{\mathcal{I}}_y] = \mathrm{i}\,\hat{\mathcal{I}}_z \iff {}_{z}\overset{x}{\circlearrowright}{}_{y} \tag{D.10}$$

$$[\hat{\mathcal{I}}_z, \hat{\mathcal{I}}^\pm] = \pm\hat{\mathcal{I}}^\pm \tag{D.11}$$

$$[\hat{\mathcal{I}}^+, \hat{\mathcal{I}}^-] = 2\hat{\mathcal{I}}_z \tag{D.12}$$

$$[\hat{\mathcal{I}}^2, \hat{\mathcal{I}}_\kappa] = 0 \tag{D.13}$$

where the symbol ${}_{z}\overset{x}{\circlearrowright}{}_{y}$ denotes cyclic permutation of indices $x \to y \to z \to x$, and $\kappa = \{x, y, z, +, -\}$.

D.2 Two Spins-1/2 Cartesian Operators

Two spins-1/2 operators are constructed from the one spin-1/2 operators according to Eq. (2.91). All relationships from Section D.1 are similarly valid for the two spins-1/2 operators. In addition, the scalar product of two vector operators is given by:

$$\hat{I}_1 \cdot \hat{I}_2 = \hat{I}_{1x}\hat{I}_{2x} + \hat{I}_{1y}\hat{I}_{2y} + \hat{I}_{1z}\hat{I}_{2z} \tag{D.14}$$

where:

$$\hat{I}_{1x}\hat{I}_{2x} + \hat{I}_{1y}\hat{I}_{2y} = \frac{1}{2}(\hat{I}_1^+\hat{I}_2^- + \hat{I}_1^-\hat{I}_2^+) \tag{D.15}$$

The total spin operators are defined as follows:

$$\hat{I}_\kappa = \hat{I}_{1\kappa} + \hat{I}_{2\kappa} \tag{D.16}$$

D.3 Two Spins-1/2 Operators Nomenclature

As mentioned in Section 2.2.4, the spin operators bear special names related either to their relation to the vector model, or to their spectral appearance, when contained in the spin-system density operator. Taking into account also shift operators (D.8), except for the unity operator $\hat{E}$, the directly observable operators, are [10, 31]:

- $\hat{I}_{kx}$, $\hat{I}_{ky}$: transverse x- and y-magnetization; x- and y-coherence of spin k, in-phase with respect to spin l;
- $\hat{I}_k^{\pm}$: in-phase (±1)-quantum coherence of spin k.

The indirectly observable spin operators are:

- $\hat{I}_{kz}$: longitudinal z-magnetization; equal population difference across all transitions of spin k;
- $2\hat{I}_{kx}\hat{I}_{lz}$, $2\hat{I}_{ky}\hat{I}_{lz}$: x- and y-coherence of spin k, antiphase with respect to spin l;
- $2\hat{I}_k^{\pm}\hat{I}_{lz}$: (±1)-quantum coherence of spin k, antiphase with respect to spins l;
- $2\hat{I}_{kz}\hat{I}_{lz}$: longitudinal two-spin order of spins k and l; nonequilibrium population distribution without net polarization and without observable polarization;
- $2\hat{I}_{kx}\hat{I}_{lx}$, $\hat{I}_{ky}\hat{I}_{ly}$, $2\hat{I}_{kx}\hat{I}_{ly}$, $\hat{I}_{ky}\hat{I}_{lx}$: two-spin coherence of spins k and l containing the unobservable 0- and (±2)-quantum coherences;
- $2\hat{I}_k^{\pm}\hat{I}_l^{\mp}$: in-phase zero-quantum coherence of spins k and l;
- $2\hat{I}_k^{\pm}\hat{I}_l^{\pm}$: in-phase (±2)-quantum coherence of spins k and l.

E Laboratory-to-Rotating Frame Transformation

The laboratory frame Hamiltonian $\hat{H}$ and the density operator $\hat{\rho}$ transform into a rotating-frame quantities according to [2]:

$$\hat{\hat{H}}(t) = \hat{\hat{U}}^{-1}(t)\,\hat{H}(t) = \hat{U}^{-1}(t)\,\hat{H}(t)\,\hat{U}(t) \tag{E.1}$$

$$\hat{\hat{\rho}}(t) = \hat{\hat{U}}^{-1}(t)\,\hat{\rho}(t) = \hat{U}^{-1}(t)\,\hat{\rho}(t)\,\hat{U}(t) \tag{E.2}$$

where $\hat{\hat{U}}$ is given by Eq. (2.118).

The laboratory-frame Liouville-von Neumann equation:

$$\frac{\partial}{\partial t}\hat{\rho}(t) = -\mathrm{i}[\hat{H}(t), \hat{\rho}(t)] \tag{E.3}$$

transforms into the rotating frame in the following way. Consider the time derivative of the identity operator $\hat{E} = \hat{U}^{-1}(t)\,\hat{U}(t)$:

$$\frac{\mathrm{d}}{\mathrm{d}t}\hat{E} = \frac{\mathrm{d}\,\hat{U}^{-1}(t)}{\mathrm{d}t}\,\hat{U}(t) + \hat{U}^{-1}(t)\,\frac{\mathrm{d}\,\hat{U}(t)}{\mathrm{d}t} = \hat{0} \tag{E.4}$$

Then:

$$\begin{aligned}
\frac{\partial}{\partial t}\hat{\hat{\rho}}(t) &= \frac{\partial}{\partial t}\left[\hat{U}^{-1}(t)\hat{\rho}(t)\hat{U}(t)\right] \\
&= \hat{U}^{-1}(t)\,\underbrace{\frac{\partial\hat{\rho}(t)}{\partial t}}_{\text{(E.3)}}\,\hat{U}(t) + \frac{\mathrm{d}\,\hat{U}^{-1}(t)}{\mathrm{d}t}\hat{\rho}(t)\hat{U}(t) + \hat{U}^{-1}(t)\hat{\rho}(t)\frac{\mathrm{d}\,\hat{U}(t)}{\mathrm{d}t} \\
&= -\mathrm{i}\,\underbrace{\hat{U}^{-1}(t)\hat{H}(t)\hat{U}(t)}_{\text{(E.1)}}\,\underbrace{\hat{U}^{-1}(t)\hat{\rho}(t)\hat{U}(t)}_{\text{(E.2)}} + \mathrm{i}\,\underbrace{\hat{U}^{-1}(t)\hat{\rho}(t)\hat{U}(t)}_{\text{(E.2)}}\,\underbrace{\hat{U}^{-1}(t)\hat{H}(t)\hat{U}(t)}_{\text{(E.1)}} \\
&\quad + \frac{\mathrm{d}\,\hat{U}^{-1}(t)}{\mathrm{d}t}\hat{U}(t)\,\underbrace{\hat{U}^{-1}(t)\hat{\rho}(t)\hat{U}(t)}_{\text{(E.2)}} + \underbrace{\hat{U}^{-1}(t)\hat{\rho}(t)\hat{U}(t)}_{\text{(E.2)}}\,\underbrace{\hat{U}^{-1}(t)\frac{\mathrm{d}\,\hat{U}(t)}{\mathrm{d}t}}_{\text{(E.4)}} \\
&= -\mathrm{i}\hat{\hat{H}}(t)\hat{\hat{\rho}}(t) + \mathrm{i}\hat{\hat{\rho}}(t)\hat{\hat{H}}(t) + \frac{\mathrm{d}\,\hat{U}^{-1}(t)}{\mathrm{d}t}\hat{U}(t)\hat{\hat{\rho}}(t) - \hat{\hat{\rho}}(t)\frac{\mathrm{d}\,\hat{U}^{-1}(t)}{\mathrm{d}t}\hat{U}(t) \\
&= -\mathrm{i}\left[\hat{\hat{H}}(t) + \mathrm{i}\frac{\mathrm{d}\,\hat{U}^{-1}(t)}{\mathrm{d}t}\hat{U}(t), \hat{\hat{\rho}}(t)\right]
\end{aligned} \tag{E.5}$$

Finally, assuming Eq. (2.118):

$$\frac{\partial}{\partial t}\hat{\hat{\rho}}(t) = -\mathrm{i}\left[\hat{\hat{H}}(t) - \omega_{\mathrm{rf}}\hat{I}_z, \hat{\hat{\rho}}(t)\right] \tag{E.6}$$

F Law of Error Propagation

Assume that x is a function of u and v:

$$x = u \,\square\, v \tag{F.1}$$

where the symbol "□" denotes an operation combining u and v into x. Each quantity is characterized by a mean value μ and a variance σ^2 or a standard deviation σ, which is the square root of the variance:

$$u = \mu(u) \pm \sigma(u) \tag{F.2}$$

$$v = \mu(v) \pm \sigma(v) \tag{F.3}$$

Assume that the values of the quantities u and v were determined during n independent measurements. The mean values are equal to:

$$\mu(u) = \frac{1}{n}\sum_{i=1}^{n} u_i \tag{F.4}$$

$$\mu(v) = \frac{1}{n}\sum_{i=1}^{n} v_i \tag{F.5}$$

The variances are given by:

$$\sigma^2(u) = \frac{1}{n-1}\sum_{i=1}^{n} [u_i - \mu(u)]^2 \tag{F.6}$$

$$\sigma^2(v) = \frac{1}{n-1}\sum_{i=1}^{n} [v_i - \mu(v)]^2 \tag{F.7}$$

A covariance between the quantities u and v is defined by [245]:

$$\sigma^2(u,v) = \frac{1}{n-1}\sum_{i=1}^{n} [u_i - \mu(u)][v_i - \mu(v)] \tag{F.8}$$

The mean value of x is equal to:

$$\mu(x) = \mu(u) \square \mu(v) \tag{F.9}$$

The variance of x is given by [245]:

$$\sigma^2(x) = \left(\frac{\partial x}{\partial u}\right)^2 \sigma^2(u) + \left(\frac{\partial x}{\partial v}\right)^2 \sigma^2(v) + 2\left(\frac{\partial x}{\partial u}\right)\left(\frac{\partial x}{\partial v}\right)\sigma^2(u,v) \tag{F.10}$$

In the case that u and v are uncorrelated, the value of $\sigma^2(u,v)$ is expected to be equal to zero. Therefore:

$$\sigma^2(x) = \left(\frac{\partial x}{\partial u}\right)^2 \sigma^2(u) + \left(\frac{\partial x}{\partial v}\right)^2 \sigma^2(v) \tag{F.11}$$

List of References

[1] G. E. Uhlenbeck and S. A. Goudsmit. Replacement of the hypothesis of unmechanical force by a claim relating to the internal behavior of each electron. *Naturwissenschaften*, 47(13):953–954, 1925. In German.

[2] J. Cavanagh, W. J. Fairbrother, A. G. Palmer, M. Rance, and N. J. Skelton. *Protein NMR spectroscopy.* Elsevier Academic Press, London, U.K., 2nd edition, 2007.

[3] A. D. McNaught and A. Wilkinson. *IUPAC compendium of chemical terminology (the Gold book).* Blackwell Scientific Publications, Oxford, U.K., 2nd edition, 1997. `http://goldbook.iupac.org/`.

[4] J. K. Tuli. *Nuclear wallet cards.* National Nuclear Data Center, Brookhaven National Laboratory, Upton, New York, U.S.A., 8th edition, 2011. `http://www.nndc.bnl.gov/wallet/`.

[5] P. Zeeman. The effect of magnetisation on the nature of light emitted by a substance. *Nature*, 55:347, 1897.

[6] H. Haken and H. C. Wolf. *The physics of atoms and quanta.* Springer-Verlag, Berlin, Germany, 7th edition, 2005.

[7] J. H. Van Vleck. *The theory of electric and magnetic susceptibilities.* The International series of monographs on physics. Oxford University Press, London, U.K., 1932.

[8] B. G. Lazarev and L. V. Shubnikov. Magnetic moment of the proton. *Phys. Z. Sowjetunion*, 11(4):445–457, 1937. In Russian.

[9] F. Bloch. Nuclear induction. *Phys. Rev.*, 70(7-8):460–474, 1946.

[10] R. R. Ernst, G. Bodenhausen, and A. Wokaun. *Principles of nuclear magnetic resonance in one and two dimensions.* Oxford University Press, Oxford, U.K., 1988.

[11] F. Bloch and A. J. F. Siegert. Magnetic resonance for nonrotating fields. *Phys. Rev.*, 57(6):522–527, 1940.

[12] M. H. Levitt. The signs of frequencies and phases in NMR. *J. Magn. Reson.*, 126(2):164–182, 1997.

[13] J. D. Jackson. *Classical electrodynamics.* John Wiley and Sons, Inc., New York, U.S.A., 3rd edition, 1998.

[14] M. H. Levitt. *Spin dynamics.* John Wiley & Sons Ltd., Chichester, U.K., 2nd edition, 2008.

[15] O. W. Sørensen, G. W. Eich, M. H. Levitt, G. Bodenhausen, and R. R. Ernst. Product operator formalism for the description of NMR pulse experiments. *Prog. Nucl. Magn. Reson. Spectrosc.*, 16:163–192, 1984.

[16] I. Burghardt, J.-M. Böhlen, and G. Bodenhausen. Broadband multiple-quantum nuclear magnetic resonance with frequency-modulated "chirp" pulses: Applications to pairs of scalar-coupled spin $I = 1/2$ nuclei. *J. Chem. Phys.*, 93(11):7687–7697, 1990.

[17] H. Geen and R. Freeman. Band-selective radiofrequency pulses. *J. Magn. Reson.*, 93(1):93–141, 1991.

[18] A. Tannús and M. Garwood. Adiabatic pulses. *NMR Biomed.*, 10(8):423–434, 1997.

[19] R. Freeman. Shaped radiofrequency pulses in high resolution NMR. *Prog. Nucl. Magn. Reson. Spectrosc.*, 32(1):59–106, 1998.

[20] M. Braun and S. J. Glaser. Cooperative pulses. *J. Magn. Reson.*, 207(1):114–123, 2010.

[21] C. D. Ridge and J. D. Walls. Pathway selective pulses. *J. Phys. Chem. Lett.*, 2(19):2478–2482, 2011.

[22] L. Emsley. *Encyclopedia of NMR*, volume 8, chapter Selective pulses, pages 4328–4336. John Wiley and Sons, Ltd., Chichester, U.K., 2nd edition, 2012.

[23] R. Freeman and S. Wittekoek. Selective determination of relaxation times in high resolution NMR. *J. Magn. Reson.*, 1(2):238–276, 1969.

[24] R. Freeman, S. Wittekoek, and R. R. Ernst. High-resolution NMR study of relaxation mechanisms in a two-spin system. *J. Chem. Phys.*, 52(3):1529–1544, 1970.

[25] F. Bloch, W. W. Hansen, and M. E. Packard. The nuclear induction experiment. *Phys. Rev.*, 70(7-8):474–485, 1946.

[26] A. Abragam. *Principles of nuclear magnetism.* The International series of monographs on physics. Oxford University Press, Oxford, U.K., 1983.

[27] E. L. Hahn. An accurate nuclear magnetic resonance method for measuring spin-lattice relaxation times. *Phys. Rev.*, 76(1):145–146, 1949.

[28] R. L. Vold, J. S. Waugh, M. P. Klein, and D. E. Phelps. Measurement of spin relaxation in complex systems. *J. Chem. Phys.*, 48(8):3831–3832, 1968.

[29] J. L. Markley, W. J. Horsley, and M. P. Klein. Spin-lattice relaxation measurements in slowly relaxing complex spectra. *J. Chem. Phys.*, 55(7):3604–3605, 1971.

[30] I. Kuprov. Spin dynamics lecture course. Semester 1, 2012–2013, University of Southampton, U.K. Website. `http://www.spindynamics.org`.

[31] F. J. M. van de Ven. *Multidimensional NMR in liquids.* Wiley-VCH, New York, U.S.A., 1995.

[32] U. Fano. Description of states in quantum mechanics by density matrix and operator techniques. *Rev. Mod. Phys.*, 29(1):74–93, 1957.

[33] D. Ter Haar. Theory and applications of the density matrix. *Rep. Prog. Phys.*, 24(1):304–362, 1961.

[34] J. L. C. Jeener. Superoperators in magnetic resonance. *Adv. Magn. Reson.*, 10:1–51, 1982.

[35] M. H. Levitt, SpinDynamica software package, version 2.4, 2012. Website. `http://www.spindynamica.soton.ac.uk`.

[36] M. Carravetta and M. H. Levitt. Theory of long-lived nuclear spin states in solution nuclear magnetic resonance. I. Singlet states in low magnetic field. *J. Chem. Phys.*, 122(21):214505, 2005.

[37] J. Kowalewski and L. Mäler. *Nuclear spin relaxation in liquids: Theory, experiments, and applications.* Series in Chemical Physics. Taylor & Francis Group, New York, U.S.A, 2006.

[38] J. Natterer and J. Bargon. Parahydrogen induced polarization. *Prog. Nucl. Magn. Reson. Spectrosc.*, 31(4):293–315, 1997.

[39] P. F. Seidler, H. E. Bryndza, J. E. Frommer, L. S. Stuhl, and R. G. Bergman. Synthesis of trinuclear alkylidyne complexes from dinuclear alkyne complexes and metal hydrides. CIDNP evidence for vinyl radical intermediates in the hydrogenolysis of these clusters. *Organometallics*, 2(11):1701–1705, 1983.

[40] S. I. Hommeltoft, D. H. Berry, and R. Eisenberg. Metal-centered radical-pair mechanism for alkyne hydrogenation with a binuclear rhodium hydride complex. CIDNP without organic radicals. *J. Am. Chem. Soc.*, 108(17):5345–5347, 1986.

[41] J. Bargon, H. Fischer, and U. Johnsen. Nuclear magnetic resonance emission lines during rapid radical reactions. I. Admission procedures and examples. *Z. Naturforsch. A*, 22:1551–1555, 1967. In German.

[42] J. Bargon and H. Fischer. Nuclear magnetic resonance emission lines during rapid radical reactions. II. Chemically induced dynamic nuclear polarization. *Z. Naturforsch. A*, 22:1556–1562, 1967. In German.

[43] H. R. Ward and R. G. Lawler. Nuclear magnetic resonance emission and enhanced absorption in rapid organometallic reactions. *J. Am. Chem. Soc.*, 89(21):5518–5519, 1967.

[44] R. G. Lawler. Chemically induced dynamic nuclear polarization. *J. Am. Chem. Soc.*, 89(21):5519–5521, 1967.

[45] R. Eisenberg. Parahydrogen-induced polarization: A new spin on reactions with H_2. *Acc. Chem. Res.*, 24(4):110–116, 1991.

[46] C. Beduz, M. Carravetta, J. Y.-C. Chen, M. Concistre, M. Denning, M. Frunzi, A. J. Horsewill, O. G. Johannessen, R. G. Lawler, X. Lei, M. H. Levitt, Y. Li, S. Mamone, Y. Murata, U. Nagel, T. Nishida, J. Ollivier, S. Rols, T. Room, R. Sarkar, N. J. Turro, and Y. Yang. Quantum rotation of ortho and para-water encapsulated in a fullerene cage. *Proc. Natl. Acad. Sci. U.S.A.*, 109(32):12894–12898, 2012.

[47] M. Carravetta and M. H. Levitt. Long-lived nuclear spin states in high-field solution NMR. *J. Am. Chem. Soc.*, 126(20):6228–6229, 2004.

[48] M. Carravetta, O. Johannessen, and M. H. Levitt. Beyond the T_1 limit: Singlet nuclear spin states in low magnetic fields. *Phys. Rev. Lett.*, 92(15):1–4, 2004.

[49] M. H. Levitt. Singlet nuclear magnetic resonance. *Annu. Rev. Phys. Chem.*, 63:89–105, 2012.

[50] M. H. Levitt. *Encyclopedia of NMR*, volume 8, chapter Singlet and other states with extended lifetimes, pages 4565–4581. John Wiley and Sons, Ltd., Chichester, U.K., 2nd edition, 2012.

[51] R. Sarkar, P. R. Vasos, and G. Bodenhausen. Singlet-state exchange NMR spectroscopy for the study of very slow dynamic processes. *J. Am. Chem. Soc.*, 129(2):328–334, 2007.

[52] M. C. D. Tayler, S. Marie, A. P. Ganesan, and M. H. Levitt. Determination of molecular torsion angles using nuclear singlet relaxation. *J. Am. Chem. Soc.*, 132(24):8225–8227, 2010.

[53] M. G. Pravica and D. P. Weitekamp. Net NMR alignment by adiabatic transport of parahydrogen addition products to high magnetic field. *Chem. Phys. Lett.*, 145(4):255–258, 1988.

[54] A. Bornet, S. Jannin, and G. Bodenhausen. Three-field NMR to preserve hyperpolarized proton magnetization as long-lived states in moderate magnetic fields. *Chem. Phys. Lett.*, 512(4-6):151–154, 2011.

[55] M. C. D. Tayler, I. Marco-Rius, M. I. Kettunen, K. M. Brindle, M. H. Levitt, and G. Pileio. Direct enhancement of nuclear singlet order by dynamic nuclear polarization. *J. Am. Chem. Soc.*, 134(18):7668–7671, 2012.

[56] G. Pileio, J. T. Hill-Cousins, S. Mitchell, I. Kuprov, L. J. Brown, R. C. D. Brown, and M. H. Levitt. Long-lived nuclear singlet order in near-equivalent ^{13}C spin pairs. *J. Am. Chem. Soc.*, 134(42):17494–17497, 2012.

[57] G. Pileio, M. Carravetta, E. Hughes, and M. H. Levitt. The long-lived nuclear singlet state of ^{15}N-nitrous oxide in solution. *J. Am. Chem. Soc.*, 130(38):12582–12583, 2008.

[58] G. Pileio, M. Carravetta, and M. H. Levitt. Extremely low-frequency spectroscopy in low-field nuclear magnetic resonance. *Phys. Rev. Lett.*, 103(8):1–4, 2009.

[59] G. Pileio, M. Carravetta, and M. H. Levitt. Storage of nuclear magnetization as long-lived singlet order in low magnetic field. *Proc. Natl. Acad. Sci. U.S.A.*, 107(40):17135–17139, 2010.

[60] R. K. Ghosh, S. J. Kadlecek, J. H. Ardenkjær-Larsen, B. M. Pullinger, G. Pileio, M. H. Levitt, N. N. Kuzma, and R. R. Rizi. Measurements of the persistent singlet state of N_2O in blood and other solvents–potential as a magnetic tracer. *Magn. Reson. Med.*, 66(4):1177–1180, 2011.

[61] J. Bocan, G. Pileio, and M. H Levitt. Sensitivity enhancement and low-field spin relaxation in singlet NMR. *Phys. Chem. Chem. Phys.*, 14(46):16032–16040, 2012.

[62] C. R. Bowers. *Encyclopedia of NMR*, volume 8, chapter Sensitivity enhancement utilizing parahydrogen, pages 4365–4384. John Wiley and Sons, Ltd., Chichester, U.K., 2nd edition, 2012.

[63] M. C. D. Tayler and M. H. Levitt. Singlet nuclear magnetic resonance of nearly-equivalent spins. *Phys. Chem. Chem. Phys.*, 13(13):5556–5560, 2011.

[64] C. Laustsen, G. Pileio, M. C. D. Tayler, L. J. Brown, R. C. D. Brown, M. H. Levitt, and J. H. Ardenkjær-Larsen. Hyperpolarized singlet NMR on a small animal imaging system. *Magn. Reson. Med.*, 68(4):1262–1265, 2012.

[65] M. C. D. Tayler. *Theory and practice of singlet nuclear magnetic resonance.* PhD thesis, University of Southampton, Southampton, U.K., 2012.

[66] Y. Feng, R. M. Davis, and W. S. Warren. Accessing long-lived nuclear singlet states between chemically equivalent spins without breaking symmetry. *Nat. Phys.*, 8(10):1–4, 2012.

[67] M. C. D. Tayler and M. H. Levitt. Accessing long-lived nuclear spin order by isotope-induced symmetry breaking. *J. Am. Chem. Soc.*, 135(6):2120–2123, 2013.

[68] G. Pileio, M. Concistre, M. Carravetta, and M. H. Levitt. Long-lived nuclear spin states in the solution NMR of four-spin systems. *J. Magn. Reson.*, 182(2):353–357, 2006.

[69] G. Pileio and M. H. Levitt. Long-lived spin-states: Beyond T_1 and deeper into relaxation theory. Conference poster no. RE356, Euromar, Spain, 2007.

[70] P. Ahuja, R. Sarkar, P. R. Vasos, and G. Bodenhausen. Long-lived states in multiple-spin systems. *ChemPhysChem*, 10(13):2217–2220, 2009.

[71] K. Gopalakrishnan and G. Bodenhausen. Lifetimes of the singlet-states under coherent off-resonance irradiation in NMR spectroscopy. *J. Magn. Reson.*, 182(2):254–259, 2006.

[72] G. Pileio and M. H. Levitt. Theory of long-lived nuclear spin states in solution nuclear magnetic resonance. II. Singlet spin locking. *J. Chem. Phys.*, 130(21):214501, 2009.

[73] R. Sarkar, P. Ahuja, D. Moskau, P. R. Vasos, and G. Bodenhausen. Extending the scope of singlet-state spectroscopy. *ChemPhysChem*, 8(18):2652–2656, 2007.

[74] M. H. Levitt and R. Freeman. NMR population inversion using a composite pulse. *J. Magn. Reson.*, 33(2):473–476, 1979.

[75] M. H. Levitt and R. Freeman. Compensation for pulse imperfections in NMR spin-echo experiments. *J. Magn. Reson.*, 43(1):65–80, 1981.

[76] M. H. Levitt. Composite pulses. *Prog. Nucl. Magn. Reson. Spectrosc.*, 18(2):61–122, 1986.

[77] M. H. Levitt. *Encyclopedia of NMR*, volume 2, chapter Composite pulses, pages 648–663. John Wiley and Sons, Ltd., Chichester, U.K., 2nd edition, 2012.

[78] E. Vinogradov and A. K. Grant. Long-lived states in solution NMR: Selection rules for intramolecular dipolar relaxation in low magnetic fields. *J. Magn. Reson.*, 188(1):176–182, 2007.

[79] A. K. Grant and E. Vinogradov. Long-lived states in solution NMR: Theoretical examples in three- and four-spin systems. *J. Magn. Reson.*, 193(2):177–190, 2008.

[80] E. Vinogradov and A. K. Grant. Hyperpolarized long-lived states in solution NMR: Three-spin case study in low field. *J. Magn. Reson.*, 194(1):46–57, 2008.

[81] G. Pileio and M. H. Levitt. J-stabilization of singlet states in the solution NMR of multiple-spin systems. *J. Magn. Reson.*, 187(1):141–145, 2007.

[82] W. Schilf, J. P. Bloxsidge, J. R. Jones, and S.-Y. Lu. Investigations of intramolecular hydrogen bonding in three types of Schiff bases by ^{2}H and ^{3}H NMR isotope effects. *Magn. Reson. Chem.*, 42(6):556–560, 2004.

[83] E. Alexakis, J. P. Bloxsidge, J. R. Jones, and W. J. S. Lockley. Improved analysis of tritiated samples via a ^{3}H-NMR cryo-probe. *J. Labelled. Comp. Rad.*, 50(5-6):300–302, 2007.

[84] D. M. Dennison. A note on the specific heat of the hydrogen molecule. *Proc. R. Soc. Lond. A*, 115(771):483–486, 1927.

[85] S. B. Duckett and C. J. Sleigh. Applications of the parahydrogen phenomenon: A chemical perspective. *Prog. Nucl. Magn. Reson. Spectrosc.*, 34(1):71–92, 1999.

[86] R. W. Adams, J. A. Aguilar, K. D. Atkinson, M. J. Cowley, P. I. P. Elliott, S. B. Duckett, G. G. R. Green, I. G. Khazal, J. Lpez-Serrano, and D. C. Williamson. Reversible interactions with para-hydrogen enhance NMR sensitivity by polarization transfer. *Science*, 323(5922):1708–1711, 2009.

[87] C. R Bowers and D. Weitekamp. Transformation of symmetrization order to nuclear-spin magnetization by chemical reaction and nuclear magnetic resonance. *Phys. Rev. Lett.*, 57(21):2645–2648, 1986.

[88] C. R. Bowers and D. Weitekamp. Parahydrogen and synthesis allow dramatically enhanced nuclear alignment. *J. Am. Chem. Soc.*, 109(18):5541–5542, 1987.

[89] T. C. Eisenschmid, R. U. Kirss, P. P. Deutsch, S. I. Hommeltoft, R. Eisenberg, J. Bargon, R. G. Lawler, and A. L. Balch. Para hydrogen induced polarization in hydrogenation reactions. *J. Am. Chem. Soc.*, 109(26):8089–8091, 1987.

[90] S. B. Duckett, C. L. Newell, and R. Eisenberg. More than INEPT: Parahydrogen and INEPT+ give unprecedented resonance enhancement to ^{13}C by direct ^{1}H polarization transfer. *J. Am. Chem. Soc.*, 115(3):1156–1157, 1993.

[91] J. Barkemeyer, M. Haake, and J. Bargon. Hetero-NMR enhancement via parahydrogen labeling. *J. Am. Chem. Soc.*, 117(10):1156–1157, 1995.

[92] W. S. Warren, E. Jenista, R. T. Branca, and X. Chen. Increasing hyperpolarized spin lifetimes through true singlet eigenstates. *Science*, 323(5922):1711–1714, 2009.

[93] C. S. Johnson. Diffusion ordered nuclear magnetic resonance spectroscopy: Principles and applications. *Prog. Nucl. Magn. Reson. Spectrosc.*, 34(3-4):203–256, 1999.

[94] S. Cavadini, J. Dittmer, S. Antonijevic, and G. Bodenhausen. Slow diffusion by singlet state NMR spectroscopy. *J. Am. Chem. Soc.*, 127(45):15744–15748, 2005.

[95] S. Cavadini and P. R. Vasos. Singlet states open the way to longer time-scales in the measurement of diffusion by NMR spectroscopy. *Conc. Magn. Reson. A*, 32(1):68–78, 2008.

[96] R. Sarkar, P. Ahuja, P. R. Vasos, and G. Bodenhausen. Measurement of slow diffusion coefficients of molecules with arbitrary scalar couplings via long-lived spin states. *ChemPhysChem*, 9(16):2414–2419, 2008.

[97] P. Ahuja, R. Sarkar, P. R. Vasos, and G. Bodenhausen. Diffusion coefficients of biomolecules using long-lived spin states. *J. Am. Chem. Soc.*, 131(22):7498–7499, 2009.

[98] J. Jeener, B. H. Meier, P. Bachmann, and R. R. Ernst. Investigation of exchange processes by two-dimensional NMR spectroscopy. *J. Chem. Phys.*, 71(11):4546–4553, 1979.

[99] A. Bornet, P. Ahuja, R. Sarkar, L. Fernandes, S. Hadji, S. Y. Lee, A. Haririnia, D. Fushman, G. Bodenhausen, and P. R Vasos. Long-lived states to monitor protein unfolding by proton NMR. *ChemPhysChem*, 12(15):2729–2734, 2011.

[100] N. Salvi, R. Buratto, A. Bornet, S. Ulzega, I. R. Rebollo, A. Angelini, C. Heinis, and G. Bodenhausen. Boosting the sensitivity of ligand-protein screening by NMR of long-lived states. *J. Am. Chem. Soc.*, 134(27):11076–11079, 2012.

[101] A. Overhauser. Polarization of nuclei in metals. *Phys. Rev.*, 92(2):411–415, 1953.

[102] J. H. Ardenkjær-Larsen, B. Fridlund, A. Gram, G. Hansson, L. Hansson, M. H. Lerche, R. Servin, M. Thaning, and K. Golman. Increase in signal-to-noise ratio of >10, 000 times in liquid-state NMR. *Proc. Natl. Acad. Sci. U.S.A.*, 100(18):10158–10163, 2003.

[103] P. R. Vasos, A. Comment, R. Sarkar, P. Ahuja, S. Jannin, J.-P. Ansermet, J. A. Konter, P. Hautle, B. van den Brandt, and G. Bodenhausen. Long-lived states to

sustain hyperpolarized magnetization. *Proc. Natl. Acad. Sci. U.S.A.*, 106(44):18469–18473, 2009.

[104] P. Ahuja, R. Sarkar, S. Jannin, P. R. Vasos, and G. Bodenhausen. Proton hyperpolarisation preserved in long-lived states. *Chem. Commun.*, 46(43):8192–8194, 2010.

[105] K. M. Brindle, S. E. Bohndiek, F. A. Gallagher, and M. I. Kettunen. Tumor imaging using hyperpolarized ^{13}C magnetic resonance spectroscopy. *Magn. Reson. Med.*, 66(2):505–519, 2011.

[106] R. K. Ghosh, S. J. Kadlecek, N. N. Kuzma, and R. R. Rizi. Determination of the singlet state lifetime of dissolved nitrous oxide from high field relaxation measurements. *J. Chem. Phys.*, 136(17):174508, 2012.

[107] N. N. Yadav, A. M. Torres, and W. S. Price. NMR q-space imaging of macroscopic pores using singlet spin states. *J. Magn. Reson.*, 204(2):346–348, 2010.

[108] P. Hübler, J. Bargon, and S. J. Glaser. Nuclear magnetic resonance quantum computing exploiting the pure spin state of para hydrogen. *J. Chem. Phys.*, 113(6):2056–2059, 2000.

[109] M. S. Anwar, D. Blazina, H. A. Carteret, S. B. Duckett, T. K. Halstead, J. A. Jones, C. M. Kozak, and R. J. K. Taylor. Preparing high purity initial states for nuclear magnetic resonance quantum computing. *Phys. Rev. Lett.*, 93(4):040501, 2004.

[110] M. S. Anwar, J. A. Jones, D. Blazina, S. B. Duckett, and H. A. Carteret. Implementation of NMR quantum computation with parahydrogen-derived high-purity quantum states. *Phys. Rev. A*, 70(3):032324, 2004.

[111] S. S. Roy and T. S. Mahesh. Density matrix tomography of singlet states. *J. Magn. Reson.*, 206(1):127–133, 2010.

[112] S. S. Roy and T.S. Mahesh. Initialization of NMR quantum registers using long-lived singlet states. *Phys. Rev. A*, 82(5):052302, 2010.

[113] S. S. Roy, T. Mahesh, and G. Agarwal. Storing entanglement of nuclear spins via Uhrig dynamical decoupling. *Phys. Rev. A*, 83(6):062326, 2011.

[114] R. Sarkar, P. Ahuja, P. R. Vasos, and G. Bodenhausen. Long-lived coherences for homogeneous line narrowing in spectroscopy. *Phys. Rev. Lett.*, 104(5):1–4, 2010.

[115] A. Bornet, R. Sarkar, and G. Bodenhausen. Life-times of long-lived coherences under different motional regimes. *J. Magn. Reson.*, 206(1):154–156, 2010.

[116] R. Sarkar, P. Ahuja, P. R. Vasos, A. Bornet, O. Wagnieres, and G. Bodenhausen. Long-lived coherences for line-narrowing in high-field NMR. *Prog. Nucl. Magn. Reson. Spectrosc.*, 59(1):83–90, 2011.

[117] A. Bornet, S. Jannin, J. A. Konter, P. Hautle, B. van den Brandt, and G. Bodenhausen. Ultra high-resolution NMR: Sustained induction decays of long-lived coherences. *J. Am. Chem. Soc.*, 133(39):15644–15649, 2011.

[118] W. P. Aue, E. Bartholdi, and R. R. Ernst. Two-dimensional spectroscopy. Application to nuclear magnetic resonance. *J. Chem. Phys.*, 64(5):2229–2246, 1976.

[119] S. Chinthalapalli, A. Bornet, T. F. Segawa, R. Sarkar, S. Jannin, and G. Bodenhausen. Ultrahigh-resolution magnetic resonance in inhomogeneous magnetic fields: Two-dimensional long-lived-coherence correlation spectroscopy. *Phys. Rev. Lett.*, 109(4):047602, 2012.

[120] R. R. Ernst and W. A. Anderson. Application of Fourier transform spectroscopy to magnetic resonance. *Rev. Sci. Instrum.*, 37(1):93–102, 1966.

[121] P. R. Griffiths and J. A. de Haseth. *Fourier transform infrared spectrometry*. John Wiley & Sons Ltd., Hoboken, U.S.A., 2nd edition, 2007.

[122] A. Allerhand and D. W. Cochran. Carbon-13 Fourier-transform nuclear magnetic resonance. I. Comparison of a simple spin-echo procedure with other methods. *J. Am. Chem. Soc.*, 92(14):4482–4484, 1970.

[123] H. H. Goldstine. *A history of numerical analysis from the 16th through the l9th century*, volume 2 of *Studies in the history of mathematics and physical sciences*. Springer-Verlag, New York, U.S.A., 1977.

[124] J. W. Cooley and J. W. Tukey. An algorithm for the machine calculation of complex Fourier series. *Math. Comp.*, 19(90):297–301, 1965.

[125] P. Duhamel and M. Vetterli. Fast Fourier transforms: A tutorial review and a state of the art. *Signal Processing*, 19(4):259–299, 1990.

[126] G. H. Golub and C. F. Van Loan. *Matrix computations.* Johns Hopkins University Press, Baltimore, Maryland, U.S.A., 3rd edition, 1996.

[127] B. Sklar. *Digital communication: Fundamentals and applications.* Prentice Hall PTR, New Jersey, U.S.A., 2nd edition, 2008.

[128] H. Kovacs, D. Moskau, and M. Spraul. Cryogenically cooled probes – a leap in NMR technology. *Prog. Nucl. Magn. Reson. Spectrosc.*, 46(2-3):131–155, 2005.

[129] Bruker: Press Releases. World's first 1000 MHz NMR spectrometer now offers new research capabilities to European scientists, following its successful installation at CRMN in Lyon, France. Website, Dec. 2 2009. `http://www.bruker.com/`.

[130] G. Roth. Ultra-high-field NMR magnet design. Bruker BioSpin GmbH, Karlsruhe, Germany, 2003.

[131] H. Weijers. *High-temperature superconductors in high-field magnets.* PhD thesis, University of Twente, The Netherlands, 2009.

[132] W. H. Tschopp and D. D. Laukien. *Handbook of applied superconductivity*, volume 2, chapter G2.1 Nuclear magnetic resonance spectroscopy for chemical applicaitons, pages 1191–1212. Institute of Physics Publishing Ltd., Bristol, U.K., 1st edition, 1998.

[133] P.-M. Robitaille and L. Berliner, editors. *Ultra high field magnetic resonance imaging (Biological magnetic resonance)*, volume 26 of *Biological magnetic resonance.* Springer Science, New York, U.S.A., 2006.

[134] P. Styles, N. F. Soffe, C. A. Scott, D. A. Cragg, F. Row, D. J. White, and P. C. J. White. A high-resolution NMR probe in which the coil and preamplifier are cooled with liquid helium. *J. Magn. Reson.*, 213(2):347–354, 2011.

[135] G. A. Morris and R. Freeman. Enhancement of nuclear magnetic resonance signals by polarization transfer. *J. Am. Chem. Soc.*, 101(3):760–762, 1979.

[136] S. W. Sparks and P. D. Ellis. DEPT polarization transfer for the INADEQUATE experiment. *J. Magn. Reson.*, 62(1):1–11, 1985.

[137] A. Abragam and M. Goldman. Principles of dynamic nuclear polarisation. *Rep. Prog. Phys.*, 41(3):395–467, 1978.

[138] U. L. Günther. Dynamic nuclear hyperpolarization in liquids. *Top. Curr. Chem.*, 335:23–69, 2013.

[139] T. Carver and C. Slichter. Polarization of nuclear spins in metals. *Phys. Rev.*, 92(1):212–213, 1953.

[140] T. Carver and C. Slichter. Experimental verification of the Overhauser nuclear polarization effect. *Phys. Rev.*, 102(4):975–980, 1956.

[141] R. V. Pound. Nuclear electric quadrupole interactions in crystals. *Phys. Rev.*, 79(4):685–702, 1950.

[142] A. Abragam. Overhauser effect in nonmetals. *Phys. Rev.*, 98(6):1729–1735, 1955.

[143] C. D. Jeffries. Polarization of nuclei by resonance saturation in paramagnetic crystals. *Phys. Rev.*, 106(1):164–165, 1957.

[144] A. Abragam and W. G. Proctor. Spin temperature. *Phys. Rev.*, 109(5):1441–1458, 1958.

[145] A. Abragam and W. G. Proctor. New method of dynamic polarization of atomic nuclei in solids. *Compt. Rend. Hebd. Seances Acad. Sci.*, 246:2253–2256, 1958. In French.

[146] R. T. Schumacher. Dynamics of interacting spin systems. *Phys. Rev.*, 112(3):837–842, 1958.

[147] A. V. Kessenikh, V. I. Lushchikov, A. A. Manenkov, and Y. V. Taran. Relaxation and dynamic polarization of protons in polyethylenes. *Sov. Phys. – Solid State*, 5:321–329, 1963. In Russian.

[148] A. V. Kessenikh, A. A. Manenkov, and G. I. Pyatnitskii. Towards explanation of experimental data on dynamic nuclear polarization in polyethylenes. *Sov. Phys. – Solid State*, 6:641–643, 1964. In Russian.

[149] C. F. Hwang and D. A. Hill. New effect in dynamic polarization. *Phys. Rev. Lett.*, 18(4):110–112, 1967.

[150] C. F. Hwang and D. A. Hill. Phenomenological model for the new effect in dynamic polarization. *Phys. Rev. Lett.*, 19(18):1011–1014, 1967.

[151] A. Kastler. Some suggestions concerning optical production and optical detection of unequal population of spatially quantized levels of atoms. Application to experiment of Stern and Gerlach and to magnetic resonance. *J. Phys. Radium*, 11(6):255–265, 1950. In French.

[152] M. Bouchiat, T. Carver, and C. Varnum. Nuclear polarization in ^{3}He gas induced by optical pumping and dipolar exchange. *Phys. Rev. Lett.*, 5(8):373–375, 1960.

[153] N. Bhaskar, W. Happer, and T. McClelland. Efficiency of spin exchange between rubidium spins and ^{129}Xe nuclei in a gas. *Phys. Rev. Lett.*, 49(1):25–28, 1982.

[154] M. S. Albert, G. D. Cates, B. Driehuys, W. Happer, B. Saam, C. S. Springer, and A. Wishnia. Biological magnetic resonance imaging using laser-polarized ^{129}Xe. *Nature*, 370(6486):199–201, 1994.

[155] M. P. Klein and G. W. Barton. Enhancement of signal-to-noise ratio by continuous averaging: Application to magnetic resonance. *Rev. Sci. Instrum.*, 34(7):754–759, 1963.

[156] R. R. Ernst. Sensitivity enhancement in magnetic resonance. I. Analysis of the method of time averaging. *Rev. Sci. Instrum.*, 36(12):1689–1695, 1965.

[157] D. O. North. An analysis of the factors which determine signal/noise discrimination in pulsed-carrier systems. *Proc. IEEE*, 51(7):1016–1027, 1963. First published as *Tech. Rept. No. PTR-6C*, RCA Laboratories, Princeton, USA, 1943.

[158] R. G. Spencer. The time-domain matched filter and the spectral-domain matched filter in 1-dimensional NMR spectroscopy. *Conc. Magn. Reson. A*, 36(5):255–264, 2010.

[159] G. W. Stewart. On the early history of the singular value decomposition. *SIAM Rev.*, 35(4):551–566, 1993.

[160] G. H. Golub and W. M. Kahan. Calculating the singular values and pseudo-inverse of a matrix. *J. SIAM Numer. Anal.*, B2(2):205–224, 1965.

[161] G. H. Golub and C. Reinsch. Singular value decomposition and least squares solutions. *Numer. Math.*, 14(5):403–420, 1970.

[162] T. F. Chan. An improved algorithm for computing the singular value decomposition. *ACM Trans. Math. Software*, 8(1):72–83, 1982.

[163] D. W. Tufts, R. Kumaresan, and I. Kirsteins. Data adaptive signal estimation by singular value decomposition of a data matrix. *Proc. IEEE*, 70(6):684–685, 1982.

[164] H. Barkhuijsen and D. van Ormondt R. de Beer. Improved algorithm for noniterative time-domain model fitting to exponentially damped magnetic resonance signals. *J. Magn. Reson.*, 73(3):553–557, 1987.

[165] D. E. Brown and T. W. Campbell. Enhancement of 2D NMR spectra using singular value decomposition. *J. Magn. Reson.*, 89(2):255–264, 1990.

[166] L. P. Panych, R. V. Mulkern, P. Saiviroonporn, G. P. Zientara, and F. A. Jolesz. Non-Fourier encoding with multiple spin echoes. *Magn. Reson. Med.*, 38(6):964–973, 1997.

[167] M. Bydder and J. Du. Noise reduction in multiple-echo data sets using singular value decomposition. *Magn. Reson. Imaging*, 24(7):849–856, 2006.

[168] J.-B. Poullet, D. M. Sima, and S. Van Huffel. MRS signal quantitation: A review of time- and frequency-domain methods. *Magn. Reson. Med.*, 195(2):134–144, 2008.

[169] C. T. Rodgers and M. D. Robson. Receive array magnetic resonance spectroscopy: Whitened singular value decomposition (WSVD) gives optimal Bayesian solution. *Magn. Reson. Med.*, 63(4):881–891, 2010.

[170] L. L. Scharf. The SVD and reduced rank signal processing. *Signal Processing*, 25(2):113–133, 1991.

[171] I. T. Jolliffe. *Principal component analysis.* Springer Series in Statistics. Springer-Verlag, New York, U.S.A., 2nd edition, 2002.

[172] D. Savostyanov. Private communication, 12/03/2013.

[173] A. Hyvärinen, J. Karhunen, and E. Oja. *Independent component analysis*, volume 46 of *Adaptive and learning systems for signal processing, communications and control series.* John Wiley & Sons, New York, U.S.A., 2004.

[174] E. D. Becker, J. A. Ferretti, and P. N. Gambhir. Selection of optimum parameters for pulse Fourier transform nuclear magnetic resonance. *Anal. Chem.*, 51(9):1413–1420, 1979.

[175] G. S. Rule and T. K. Hitchens. Fundamentals of protein NMR spectroscopy. In Bob Kaptein, editor, *Focus on structural biology*, volume 5. Springer, Dordrecht, The Netherlands, 1st edition, 2006.

[176] Wolfram Research Inc., Mathematica 8, 2011. Website. `http://www.wolfram.com/`.

[177] R. R. Ernst. Numerical Hilbert transform and automatic phase correction in magnetic resonance spectroscopy. *J. Magn. Reson.*, 1(1):7–26, 1969.

[178] C. H. Sotak, C. L. Dumoulin, and M. D. Newsham. Automatic phase correction of Fourier transform NMR spectra based on the dispersion versus absorption (DISPA) lineshape analysis. *J. Magn. Reson.*, 57(3):453–462, 1984.

[179] L. Chen, Z. Weng, L. Goh, and M. Garland. An efficient algorithm for automatic phase correction of NMR spectra basaed on entropy minimization. *J. Magn. Reson.*, 158(1-2):164–168, 2002.

[180] D. R. Lide, editor. *Handbook of chemistry and physics.* CRC Press, Taylor & Francis Group, New York, U.S.A, 88th edition, 2007.

[181] T. B. Coplen, J. K. Bohlke, P. De Bievre, T. Ding, N. E. Holden, J. A. Hopple, H. R. Krouse, A. Lamberty, H. S. Peiser, K. Revesz, S. E. Rieder, K. J. R. Rosman, E. Roth, P. D. P. Taylor, R. D. Vocke, Jr., and Y. K. Xiao. Isotope-abundance variations of selected elements (IUPAC technical report). *Pure Appl. Chem.*, 74(10):1987–2017, 2002.

[182] W. G. Proctor and F. C. Yu. The dependence of a nuclear magnetic resonance frequency upon chemical compound. *Phys. Rev.*, 77(5):717, 1950.

[183] J. D. Baldeschwieler. Double resonance spectra of N^{14} and N^{15} ammonium ion. *J. Chem. Phys.*, 36(1):152–158, 1962.

[184] J. D. Ray. Electric quadrupole contribution to chemical shifts in liquids induced by intramolecular hindered rotations. *J. Chem. Phys.*, 40(11):3440–3441, 1964.

[185] G. J. Martin, M. L. Martin, and J.-P. Gouesnad. ^{15}N-NMR spectroscopy. In P. Diehl, E. Fluck, and R. Kosfeld, editors, *NMR basic principles and progress*, volume 18. Springer-Verlag, New York, U.S.A., 1st edition, 1981.

[186] M. Witanowski, L. Stefaniak, S. Szymanski, and H. Januszewski. External neat nitromethane scale for nitrogen chemical shifts. *J. Magn. Reson.*, 28(2):217–226, 1977.

[187] J. Mason. *Encyclopedia of NMR*, volume 5, chapter Nitrogen NMR, pages 2926–2954. John Wiley and Sons, Ltd., Chichester, U.K., 2nd edition, 2012.

[188] P. K. Bhattacharyya. ^{15}N magnetic shielding anisotropies in ^{15}N^{15}NO. *J. Chem. Phys.*, 59(11):5820–5823, 1973.

[189] E. M. Purcell, H. Torrey, and R. Pound. Resonance absorption by nuclear magnetic moments in a solid. *Phys. Rev.*, 69(1-2):37–38, 1946.

[190] F. Bloch, W. Hansen, and M. Packard. Nuclear induction. *Phys. Rev.*, 69(3-4):127, 1946.

[191] Minutes of the spring meeting at Camaridge, April 25-27, 1946, Proceedings of the American Physical Society, *Phys. Rev.*, 69(11-12):674-702,1946.

[192] E. L. Hahn. Nuclear induction due to free Larmor precession. *Phys. Rev.*, 77(2):297–298, 1950.

[193] E. L. Hahn. Spin echoes. *Phys. Rev.*, 80(4):580–594, 1950.

[194] R. Freeman. *Spin choreography.* Spektrum Academic Publishers, Oxford, U.K., 1997.

[195] H. Carr and E. M. Purcell. Effects of diffusion on free precession in nuclear magnetic resonance experiments. *Phys. Rev.*, 94(3):630–638, 1954.

[196] A. G. Avent. *Encyclopedia of NMR*, volume 8, chapter Spin echo spectroscopy of liquid samples, pages 4683–4688. John Wiley and Sons, Ltd., Chichester, U.K., 2nd edition, 2012.

[197] S. Meiboom and D. Gill. Modified spin-echo method for measuring nuclear relaxation times. *Rev. Sci. Instrum.*, 29(8):688–691, 1958.

[198] R. Freeman and H. D. W. Hill. High-resolution study of NMR spin echoes: "J Spectra". *J. Chem. Phys.*, 54(1):301–313, 1971.

[199] I. Solomon. Multiple echoes in solids. *Phys. Rev.*, 110(1):61–65, 1958.

[200] E. L. Hahn and D. E. Maxwell. Chemical shift and field independent frequency modulation of the spin echo envelope. *Phys. Rev.*, 84(6):1246–1247, 1951.

[201] A. Allerhand. Analysis of Carr-Purcell spin-echo NMR experiments on multiple-spin systems. I. The effect of homonuclear coupling. *J. Chem. Phys.*, 44(1):1–9, 1966.

[202] K. Takegoshi, K. Ogura, and K. Hikichi. A perfect spin echo in a weakly homonuclear J-coupled two spin-1/2 system. *J. Magn. Reson.*, 84(3):611–615, 1989.

[203] P. C. M. van Zijl, C. T. W. Moonen, and M. von Kienlin. Homonuclear J refocusing in echo spectroscopy. *J. Magn. Reson.*, 89(1):28–40, 1990.

[204] J. Dittmer and G. Bodenhausen. Multiple refocusing in NMR spectroscopy: Compensation of pulse imperfections by scalar couplings. *ChemPhysChem*, 5(11):1750–1754, 2004.

[205] J. Dittmer and G. Bodenhausen. Quenching echo modulations in NMR spectroscopy. *ChemPhysChem*, 7(4):831–836, 2006.

[206] J. A. Aguilar, M. Nilsson, G. Bodenhausen, and G. A. Morris. Spin echo NMR spectra without J modulation. *Chem. Commun.*, 48(6):811–813, 2012.

[207] A. Bax, A. F. Mehlkopf, and J. Smidt. Absorption spectra from phase-modulated spin echoes. *J. Magn. Reson.*, 35(3):373–377, 1979.

[208] R. Freeman, S. P. Kempsell, and M. H. Levitt. Elimination of dispersion-mode contribuions from two-dimensional NMR spectra. *J. Magn. Reson.*, 34(3):663–667, 1979.

[209] A. Bax, R. Freeman, and G. A. Morris. A simple method for suppressing dispersion-mode contributions in NMR spectra: The "pseudo echo". *J. Magn. Reson.*, 43(2):333–338, 1981.

[210] A. Allerhand. Effect of magnetic field fluctuations in spin-echo NMR experiments. *Rev. Sci. Instrum.*, 41(2):269–274, 1970.

[211] D. M. Korzhnev, E. V. Tischenko, and A. S. Arseniev. Off-resonance effects in ^{15}N T_2 CPMG measurements. *J. Biomol. NMR*, 17(3):231–237, 2000.

[212] F. H. Larsen, H. J. Jakobsen, P. D. Ellis, and N. C. Nielsen. Sensitivity-enhanced quadrupolar-echo NMR of half-integer quadrupolar nuclei. Magnitudes and relative orientation of chemical shielding and quadrupolar coupling tensors. *J. Phys. Chem. A*, 101(46):8597–8606, 1997.

[213] F. H. Larsen, H. J. Jakobsen, P. D. Ellis, and N. C. Nielsen. High-field QCPMG-MAS NMR of half-integer quadrupolar nuclei with large quadrupole couplings. *Mol. Phys.*, 95(6):1185–1195, 1998.

[214] F. H. Larsen and N. C. Nielsen. Effects of finite rf pulses and sample spinning speed in multiple-quantum magic-angle spinning (MQ-MAS) and multiple-quantum quadrupolar Carr-Purcell-Meiboom-Gill magic-angle spinning (MQ-QCPMG-MAS) nuclear magnetic resonance of half-integer quadrupolar nuclei. *J. Phys. Chem. A*, 103(50):10825–10832, 1999.

[215] R. Lefort, J. W. Wiench, M. Pruski, and J.-P. Amoureux. Optimization of data acquisition and processing in Carr-Purcell-Meiboom-Gill multiple quantum magic angle spinning nuclear magnetic resonance. *J. Chem. Phys.*, 116(6):2493–2501, 2002.

[216] I. Hung, A. J. Rossini, and R. W. Schurko. Application of the Carr-Purcell Meiboom-Gill pulse sequence for the acquisition of solid-state NMR spectra of spin-1/2 nuclei. *J. Phys. Chem. A*, 108(34):7112–7120, 2004.

[217] R. Siegel, T. T. Nakashima, and R. E. Wasylishen. Application of multiple-pulse experiments to characterize broad NMR chemical-shift powder patterns from spin-1/2 nuclei in the solid state. *J. Phys. Chem. B*, 108(7):2218–2226, 2004.

[218] R. Siegel, T. T. Nakashima, and R. E. Wasylishen. Signal-to-noise enhancement of NMR spectra of solids using multiple-pulse spin-echo experiments. *Conc. Magn. Reson. A*, 26(2):62–77, 2005.

[219] K. K. Dey, J. T. Ash, N. M. Trease, and P. J. Grandinetti. Trading sensitivity for information: Carr-Purcell-Meiboom-Gill acquisition in solid-state NMR. *J. Chem. Phys.*, 133(5):054501, 2010.

[220] J. Z. Hu and R. A. Wind. Sensitivity-enhanced phase-corrected ultra-slow magic angle turning using multiple-echo data acquisition. *J. Magn. Reson.*, 163(1):149–162, 2003.

[221] D. Lu and P. M. Joseph. A matched filter echo summation technique for MRI. *Magn. Reson. Imaging*, 13(2):241–249, 1995.

[222] R. Wangsness and F. Bloch. The dynamical theory of nuclear induction. *Phys. Rev.*, 89(4):728–739, 1953.

[223] A. G. Redfield. On the theory of relaxation processes. *IBM J. Res. Dev.*, 1(1):19–31, 1957.

[224] C. L. Mayne and S. A. Smith. *Encyclopedia of NMR*, volume 7, chapter Relaxation processes in coupled-spin systems, pages 4117–4135. John Wiley and Sons, Ltd., Chichester, U.K., 2nd edition, 2012.

[225] G. Pileio. Singlet state relaxation via scalar coupling of the second kind. *J. Chem. Phys.*, 135(17):174502, 2011.

[226] G. Pileio. Relaxation theory of nuclear singlet states in two spin-1/2 systems. *Prog. Nucl. Magn. Reson. Spectrosc.*, 56(3):217–231, 2010.

[227] I. Kuprov. Spin dynamics lecture course. Semester 2, 2012–2013, University of Southampton, U.K. Website. `http://www.spindynamics.org`.

[228] N. C. Pyper. Theory of symmetry in nuclear magnetic relaxation including applications to high resolution N.M.R. line shapes. *Mol. Phys.*, 21(1):1–33, 1971.

[229] D. A. Varshalovich, A. N. Moskalev, and V. K. Khersonskii. *Quantum theory of angular momemtum.* World Scientific Publishing, Singapore, 1988.

[230] M. C. D. Tayler and M. H. Levitt. Paramagnetic relaxation of nuclear singlet states. *Phys. Chem. Chem. Phys.*, 13(20):9128–9130, 2011.

[231] G. Pileio. Spin dynamics lecture course. Semester 2, 2012–2013, University of Southampton, U.K. Website. `http://www.spindynamics.org`.

[232] R. Kimmich and E. Anoardo. Field-cycling NMR relaxometry. *Prog. Nucl. Magn. Reson. Spectrosc.*, 44(3-4):257–320, 2004.

[233] C. J. Jameson, A. K. Jameson, D. Oppusunggu, S. Wille, P. M. Burrell, and J. Mason. ^{15}N nuclear magnetic shielding scale from gas phase studies. *J. Chem. Phys.*, 74(1):81–88, 1981.

[234] C. J. Jameson, A. K. Jameson, J. K. Hwang, and N. C. Smith. Cross sections for the anisotropic interaction of NNO with various molecules. *J. Chem. Phys.*, 89:5642–5649, 1988.

[235] C. J. Jameson, M. A. ter Horst, and A. K. Jameson. Quadrupolar spin relaxation of ^{14}N in NNO in collisions with various molecules. *J. Chem. Phys.*, 109(23):10227–10237, 1998.

[236] J. M. L. J. Reinartz, W. L. Meerts, and A. Dymanus. Hyperfine structure, electric and magnetic properties of ^{14}N$_2$^{16}O in the ground and first excited bending vibrational state. *Chem. Phys.*, 31(1):19–29, 1978.

[237] A. Tal and L. Frydman. Single-scan multidimensional magnetic resonance. *Prog. Nucl. Magn. Reson. Spectrosc.*, 57(3):241–292, 2010.

[238] P. Le Roux, G. McKinnon, Y.-F. Yen, and B. Fernandez. Realignment capability of the nCPMG sequence. *J. Magn. Reson.*, 211(2):121–133, 2011.

[239] N. Khaneja, T. Reiss, B. Luy, and S. J. Glaser. Optimal control of spin dynamics in the presence of relaxation. *J. Magn. Reson.*, 162(2):311–319, 2003.

[240] D. P. Frueh, T. Ito, J.-S. Li, G. Wagner, S. J. Glaser, and N. Khaneja. Sensitivity enhancement in NMR of macromolecules by application of optimal control theory. *J. Biomol. NMR*, 32(1):23–30, 2005.

[241] N. Khaneja, T. Reiss, C. Kehlet, T. Schulte-Herbrüggen, and S. J. Glaser. Optimal control of coupled spin dynamics: design of NMR pulse sequences by gradient ascent algorithms. *J. Magn. Reson.*, 172(2):296–305, 2005.

[242] P. de Fouquieres, S. G. Schirmer, S. J. Glaser, and I. Kuprov. Second order gradient ascent pulse engineering. *J. Magn. Reson.*, 212(2):296–305, 2011.

[243] P. L. Corio. *Structure of high-resolution NMR spectra.* Academic Press Inc., London, U.K., 1966.

[244] E. Merzbacher. *Quantum mechanics*. John Wiley and Sons, Inc., New York, U.S.A., 3rd edition, 1998.

[245] P. Bevington and D. K. Robinson. *Data reduction and error analysis for the physical sciences*. McGraw-Hill Higher Education, New York, U.S.A., 3rd edition, 2003.

PCCP

Cite this: *Phys. Chem. Chem. Phys.*, 2012, **14**, 16032–16040

www.rsc.org/pccp

PAPER

Sensitivity enhancement and low-field spin relaxation in singlet NMR

Jiri Bocan, Giuseppe Pileio and Malcolm H. Levitt*

Received 25th July 2012, Accepted 19th October 2012
DOI: 10.1039/c2cp42553j

The singlet states of nuclear spin-1/2 pairs often display extended lifetimes that can be an order of magnitude longer than conventional relaxation times. We show that, in favourable circumstances, acquisition of the NMR signal during an extended multiple spin-echo train, followed by suitable data processing, enhances the signal-to-noise ratio of singlet NMR by up to an order of magnitude. The achievable enhancement depends on the transverse relaxation time constant, the magnetic field inhomogeneity, and the acceptable degradation in digital spectral resolution. We use the combination of singlet NMR and multiple spin-echo data acquisition to study the low-field nuclear relaxation processes of ^{15}N-labelled nitrous oxide ($^{15}N_2O$) in solution. A general relaxation theory for coupled 2-spin-1/2 systems in low magnetic field is developed. Experimental trajectories of the nuclear spin observables are compared with theoretical expressions, including dipole–dipole and spin-rotation relaxation mechanisms. The estimated values of the spin-rotation tensors are compared with previous estimations from NMR and molecular beam electric resonance.

1. Introduction

When a molecule contains two nuclear spins-1/2, the spins may combine to generate three states with total nuclear spin $I = 1$ (the nuclear triplet states) and a state with total nuclear spin $I = 0$ (the nuclear singlet state). Due to its immunity against relaxation processes symmetric with respect to exchange of the two nuclei, *e.g.*, the intramolecular dipole–dipole mechanism, singlet spin order often displays an extended lifetime T_S, which may be more than an order of magnitude longer compared to the conventional longitudinal relaxation time T_1. In magnetically inequivalent systems, the long singlet lifetime is normally concealed by rapid singlet–triplet transitions induced by the chemical shift difference. However, recent experiments have shown that it is possible to suppress the singlet–triplet transitions, revealing the long lifetime of singlet spin order.[1–7] The long-lived nuclear singlet order may be exploited to study slow motional processes,[8–12] local molecular geometry,[13,14] or to transport hyperpolarized nuclear spin order.[15–17]

A remarkable example of long-lived nuclear singlet order is displayed by the coupled ^{15}N-pair in doubly-labelled nitrous oxide $^{15}N_2O$. The singlet lifetime T_S exceeds 25 minutes for $^{15}N_2O$ dissolved in a deuterated solvent.[5] The T_S value is reduced in protonated solvents, but still exceeds 7 minutes for $^{15}N_2O$ dissolved in blood.[18] This time constant is much longer than that of any other known agent when dissolved in blood, and suggests the prospect of clinical NMR imaging investigations employing $^{15}N_2O$. A step in this direction was taken with the development of an experimental procedure for converting nuclear magnetization into nuclear singlet order outside the NMR magnet.[5,7]

The study of the $^{15}N_2O$ singlet state and the optimization of experimental protocols is hampered by the weak nuclear magnetism of ^{15}N nuclei and the limited solubility of nitrous oxide in common solvents. In principle, the nuclear polarization may be enhanced by many orders of magnitude by hyperpolarization techniques such as dissolution-DNP (dynamic nuclear polarization).[19] However, at the time of writing, such hyperpolarization methods have not been successful for the case of $^{15}N_2O$ in solution.

For small molecules in solution, the decay of the NMR signal is often dominated by reversible dephasing under the inhomogeneity of the static magnetic field, rather than the irreversible decay associated with the transverse relaxation time T_2. Multiple refocussing using trains of π pulses[20,21] extends the duration of the NMR signal and hence increases the available signal energy, leading to an enhanced signal-to-noise ratio (SNR) after appropriate data processing. The NMR signal may be acquired during the entire spin-echo train, and processed to obtain the ordinary NMR spectrum.[22–28] We now show that the singlet NMR experiments are also amenable to SNR enhancement by MSE signal acquisition.

The enhancement of signal-to-noise by MSE signal acquisition allows a detailed study of the low-field relaxation processes for $^{15}N_2O$ in solution, at low magnetic field. The peak amplitudes observed in singlet NMR experiments have a characteristic dependence on the low-field relaxation interval, which may be analysed to estimate the three distinct transition probabilities between the nuclear singlet and triplet states. These transition probabilities are analysed using a relaxation model, involving

---

*School of Chemistry, University of Southampton, SO17 1BJ, UK.
E-mail: mhl@soton.ac.uk; Fax: +44 (0)23 8059 3781;
Tel: +44 (0)23 8059 6753*

dipole–dipole relaxation caused by rotational modulation of the ^{15}N–^{15}N dipole–dipole coupling, as well as coupling between the ^{15}N nuclear spins and the fluctuating molecular angular momentum.

2. Multiple spin echoes

2.1 Pulse sequence

A basic MSE timing sequence is shown in Fig. 1. The transverse magnetization is excited by a $\pi/2$ pulse, oscillates and decays for a time $\tau/2$, and is subjected to a series of π pulses, which have equal spacing τ, and a phase shift of $\pi/2$ with respect to the initial pulse (CPMG procedure).[20,21] The NMR signal is acquired continuously during the entire sequence, except for the short blanking intervals during and after each pulse. This leads to an NMR signal of total duration $T_{\mathrm{MSE}} \approx (N + \frac{1}{2})\tau$, where N is the number of echoes. For maximal SNR enhancement, T_{MSE} should be several multiples of the intrinsic relaxation time T_2.

Singlet NMR involves the spectroscopy of coupled nuclear spins. It is well-known that in such cases, spin echoes are often modulated by spin–spin couplings – indeed the existence of the *J*-coupling interaction was first demonstrated through the modulation of a spin echo.[29] Such effects can be very complicated for MSE trains[30–33] and may involve resonances with zero-quantum transitions.[6,7,34] In the current work, echo modulation is suppressed by using weak, long, π pulses, with enough frequency selectivity to avoid perturbation of the coupling partner. This allows the full SNR enhancement to be achieved on the selected nuclear site while observing undistorted NMR spectra. The frequency selectivity could be further enhanced, if required, by using shaped radiofrequency pulses.[35]

2.2 Multiple spin-echo signal

Several methods exist for acquiring and processing the MSE signal to achieve a SNR enhancement.[22–24] We used a procedure adapted from the *superposition method* of Hu *et al.*[24] by including a matched weighting function and a variable phase parameter, to obtain the optimum SNR. For completeness, a brief but explicit description is now given.

The complex MSE signal corresponding to a single NMR peak, excluding echo-modulation effects, finite duration of the radiofrequency pulses and the subsequent receiver blanking intervals, may be described by:

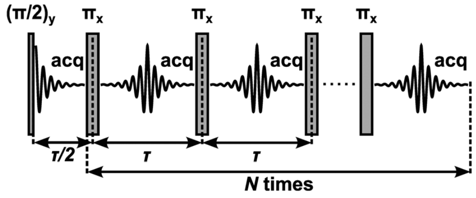

Fig. 1 MSE timing sequence. The first excitation pulse is followed by train of N equidistant refocusing pulses spaced by intervals τ. The NMR signal is acquired between the pulses during the entire pulse sequence.

$$s_{\mathrm{MSE}}(t) = h_{\mathrm{MSE}}(t)s^{0}_{\mathrm{MSE}}(t) \tag{1}$$

h_{MSE} is the signal envelope and s^{0}_{MSE} is the undecaying NMR signal.

The signal envelope is given by a superposition of the homogeneous decay and the reversible effect of magnetic field inhomogeneity. If diffusion effects are neglected,[20,21] the homogeneous transverse relaxation is approximately exponential with time constant T_2, leading to the following signal envelope function during the MSE train:

$$h_{\mathrm{MSE}}(t) \simeq \exp\{-t/T_2\}g(|t - n_{\mathrm{e}}(t)\tau|) \tag{2}$$

where the inhomogeneous broadening is described by a decaying function $g(t)$ with $g(0) = 1$ and $g(\infty) = 0$, and the integer $n_{\mathrm{e}}(t)$ is the index of the echo appropriate for time point t:

$$n_{\mathrm{e}}(t) = \left\lfloor \frac{t}{\tau} + \frac{1}{2} \right\rfloor \tag{3}$$

Here the brackets $\lfloor \cdots \rfloor$ denote the *floor* function, which rounds any real number to the nearest smaller integer.

For simplicity, we assume an exponential decay model for inhomogeneous dephasing with time constant T_2^{inh}:

$$g(t) = \exp\{-t/T_2^{\mathrm{inh}}\} \tag{4}$$

so that the decay of the unrefocussed NMR signal is described as a single exponential with a time constant T_2^{*}:

$$\{T_2^{*}\}^{-1} = \{T_2\}^{-1} + \{T_2^{\mathrm{inh}}\}^{-1} \tag{5}$$

The idealised form of s^{0}_{MSE} for a single peak with resonance offset Ω, in the absence of dephasing or relaxation, may be written as follows:

$$s^{0}_{\mathrm{MSE}}(t) = |a(0)|\exp\{i[\Omega(t - n_{\mathrm{e}}(t)\tau) + (-1)^{n_{\mathrm{e}}(t)}\phi_0 + \phi_{\mathrm{inst}}]\} \tag{6}$$

This includes the alternation of the signal phase ϕ_0 induced by the π pulses, and a constant instrumental phase shift ϕ_{inst}. The complex signal amplitude at the start of the echo train is denoted $a(0)$.

2.3 Signal processing

The MSE signal is corrected for a constant instrumental offset, multiplied by a weighting function $h_{\mathrm{proc}}(t)$, and split into half-echoes each of duration $\tau/2$. The increasing half-echoes are time-reversed and complex-conjugated before adding to the combined set of decaying half-echoes. This provides a processed signal of duration $\tau/2$ of the form:

$$\begin{aligned} s_{\mathrm{proc}}(t) = {} & \sum_{j=0}^{N} s_{\mathrm{MSE}}(j\tau + t)h_{\mathrm{proc}}(j\tau + t)\exp\{i\phi_{\mathrm{proc}}\} \\ & + \sum_{j=1}^{N} \{s_{\mathrm{MSE}}(j\tau - t)\}^{*} h_{\mathrm{proc}}(j\tau - t)\exp\{-i\phi_{\mathrm{proc}}\} \end{aligned} \tag{7}$$

where $0 \leq t \leq \tau/2$. The optimum is attained when the processing phase ϕ_{proc} compensates the initial phase of the signal (including the instrumental phase shift ϕ_{inst}), and the weighting function matches the signal envelope:[36,37]

$$\phi_{\mathrm{proc}} = -\phi_0 - \phi_{\mathrm{inst}}$$

$$h_{\text{proc}}(t) = h_{\text{MSE}}(t) \tag{8}$$

The resultant signal s_{proc} resembles a free-induction decay (FID) signal obtained after a single excitation pulse in the usual way, but truncated at time $\tau/2$. The spectrum is obtained by Fourier transformation of the signal after apodisation and zero-filling.

The frequency resolution of the final spectrum is given by the inverse of the echo spacing, and may be severely compromised if the echoes are too closely spaced. Truncation of the signal can also result in spectral distortions such as sinc-function oscillations. The bandwidth of the final spectrum, on the other hand, is determined by the inverse of the sampling interval, which is independent of the MSE acquisition procedure. However, for very long echo trains, the data capacity of the acquisition processor may limit the number of complex points that may be accommodated in a single acquisition, requiring a compromise to be made on the sampling rate.

In the context of MSE-enhanced singlet NMR, the digital resolution of the processed MSE spectrum should be sufficient to resolve the components of the *J*-coupled doublet. A processed MSE spectrum of the central ^{15}N site of ^{15}N$_2$O is shown in Fig. 2b.

2.4 SNR enhancement

The maximum achievable SNR enhancement ε_{MSE} of the Fourier transformed MSE signal with respect to the ordinary FID may be estimated by comparing the signal energies.[37] Assuming complete decay of the both signals during acquisition, this leads to:

$$\varepsilon_{\text{MSE}} = \sqrt{\frac{\int_0^\infty h_{\text{MSE}}(t)^2 \mathrm{d}t}{\int_0^\infty h_{\text{FID}}(t)^2 \mathrm{d}t}} \tag{9}$$

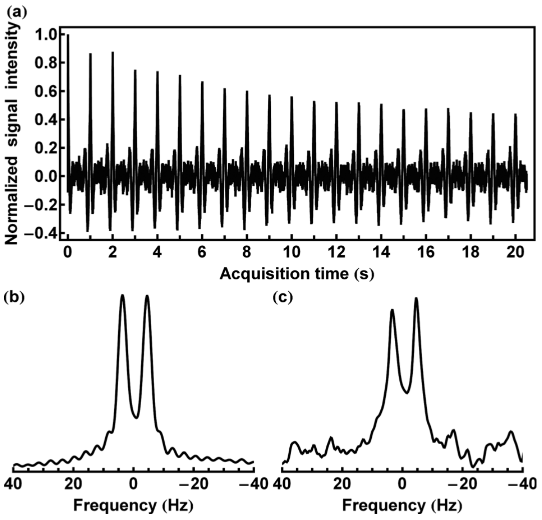

Fig. 2 (a) Initial part of the MSE signal after selective excitation of transverse magnetization of the central ^{15}N site of ^{15}N$_2$O, using weak rectangular pulses with a nutation frequency of 235 Hz. The π pulses were spaced by 1 s. The displayed signal is the average of 64 transients. (b) Processed MSE signal showing the central ^{15}N doublet of ^{15}N$_2$O. The MSE echo train consisted of 402 echoes spaced by 0.52 s, SNR = 188.7 ± 12.2. Signal processing involved a matched weighting function described by (2) with T_2 = 46.2 s and T_2^{inh} = 219 ms. (c) Signal acquired with a single π/2 pulse for comparison, SNR = 18.5 ± 1.2. The spectra (b) and (c) result from single transients. Further experimental details are provided in Section 4.

Equations (2) and (4) lead to the following expression:

$$\varepsilon_{\text{MSE}} = \sqrt{1 + \frac{2(\mathrm{e}^{\alpha-\alpha/\beta} - 1)}{(\mathrm{e}^{2\alpha} - 1)(\beta - 1)}} \tag{10}$$

where $\alpha = \tau/T_2$ and $\beta = T_2^{\text{inh}}/T_2$. The variable α corresponds to the echo spacing in units of T_2, while β quantifies the relative contributions of the inhomogeneous and homogeneous decay. Small values of α represent closely-spaced echoes, while small values of β imply large amounts of inhomogeneous dephasing.

The SNR enhancement is maximised when the inhomogeneous dephasing is strong and a short echo spacing is used, $\{\alpha, \beta\} \rightarrow 0$. However, this rapid-echo regime is often undesirable due to the heavily compromised frequency resolution, the introduction of truncation artefacts, and the accumulation of pulse imperfections over large numbers of echoes. In practice, the appropriate value of the π pulse spacing τ is a compromise between SNR enhancement, the effect of pulse imperfections and acceptable spectral resolution.

Spectra of ^{15}N$_2$O obtained by MSE signal acquisition and conventional single-pulse signal acquisition are compared in Fig. 2. The enhancement of SNR is obvious, although the MSE spectrum does show the limited digital resolution and oscillatory distortions associated with signal truncation.

Theoretical and experimental estimates of SNR enhancement by MSE data acquisition are compared for ^{15}N$_2$O in Fig. 3, as a function of the number N and spacing τ of the refocusing pulses. The agreement is generally good, with enhancements of around 10 being observed when a large number of closely-spaced π pulses are used. However, the observed SNR enhancement tends to be less than that anticipated from theory for $\tau > 1$ s and $N < 200$. This might be due to molecular diffusion in an inhomogeneous magnetic field,[38] which has not currently been included.

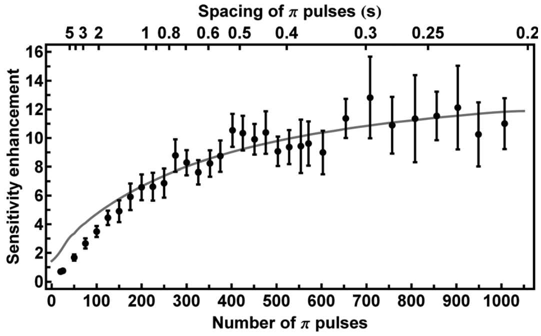

Fig. 3 Sensitivity enhancement for ^{15}N$_2$O dissolved in DMSO-d$_6$ as a function of the number and spacing of refocusing π pulses in the MSE sequence. The experimental SNR enhancement was estimated from the ratio of the mean SNR for all four ^{15}N$_2$O peaks in the case of MSE acquisition and for a single fully-decayed NMR signal. The solid line is the maximal theoretical SNR enhancement ε_{MSE}.

3. Multiple spin-echo singlet NMR

3.1 Pulse sequence

The SNR of field-cycling singlet NMR[2,5,39] may be enhanced by incorporating MSE data acquisition. The experimental procedure is shown in Fig. 4. The method applies to systems of spin-1/2 pairs with a large difference in chemical shifts between the coupling partners, so that the spin system is weakly-coupled in high magnetic field (HF):[40]

$$|\gamma B_{\mathrm{HF}}(\delta_1 - \delta_2)| \gg |\pi J_{12}| \qquad (11)$$

The value of the low magnetic field (LF) satisfies:

$$|\gamma B_{\mathrm{LF}}(\delta_1 - \delta_2)| \lesssim |\pi J_{12}| \qquad (12)$$

so that the low-field spin Hamiltonian eigenstates are given, to a good approximation, by the singlet state and the three triplet states.[2,39]

In the current implementation, the change in static magnetic field is accomplished by transporting the sample out of the NMR magnet. Fig. 4 shows the trajectory of the sample vertical position H and the resulting trajectory of the static magnetic field B_0, calculated using the known field profile of the spectrometer magnet and the transportation rate.

All radiofrequency pulses are sufficiently weak to be selective on nuclear spins in one of the coupled molecular sites. The carrier frequency may be switched before both the first π pulse and the read-out MSE train so as to switch the resonant site between the preparation stage of the sequence (the initial π pulse) and the read-out stage (the $\pi/2$ pulse and the spin echo train).

The FT spectrum of the processed MSE signal is a doublet due to spin–spin coupling with the passive nucleus. As shown in Fig. 5, the doublet peak intensities vary with the duration of the low-field interval τ_{LF}, due to relaxation processes occurring in low magnetic field. The right-hand component of the doublet decays rapidly as a function of the τ_{LF} interval, while the left-hand doublet component initially increases in intensity, decaying slowly at long times.

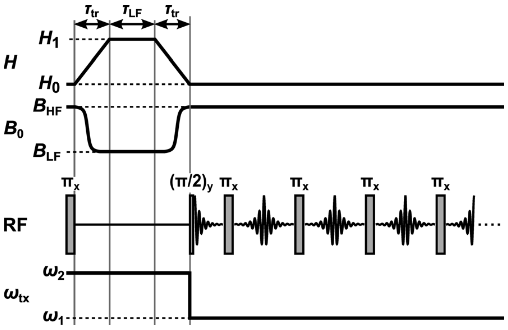

Fig. 4 Timing sequence for field-cycling MSE singlet NMR experiment, showing the transport intervals τ_{tr} and the low-field relaxation interval τ_{LF}. Trajectories are shown for the vertical sample position measured from the spectrometer centre (H), the corresponding static magnetic field (B_0), and the sequence of site-selective radiofrequency pulses (RF). The radio-frequency carrier (ω_{tx}) may be switched before both the first π pulse and the read-out MSE train so that the pulses are resonant with different molecular sites.

3.2 Principles of low-field relaxation

The data shown in Fig. 5 indicate multi-exponential relaxation dynamics in low magnetic field, with a rich kinetic structure. Previous analyses of low field relaxation for spin-1/2 pairs[39,41] have concentrated on the decay of only one spin order term (singlet order). We now provide a fuller analysis, including the relaxation properties of the nuclear spin magnetization and the rank-2 spin order, which are all significant for a detailed understanding of the relaxation trajectories shown in Fig. 5.

The energy eigenstates of the nuclear spin system in low magnetic field are the singlet state $|S_0\rangle$ and the three triplet states $|T_M\rangle$ with $M \in \{-1,0,1\}$ defined as follows:

$$\begin{aligned}|S_0\rangle &= (|\alpha\beta\rangle - |\beta\alpha\rangle)/\sqrt{2}\\ |T_{+1}\rangle &= |\alpha\alpha\rangle\\ |T_0\rangle &= (|\alpha\beta\rangle + |\beta\alpha\rangle)/\sqrt{2}\\ |T_{-1}\rangle &= |\beta\beta\rangle\end{aligned} \qquad (13)$$

The populations of the states are exchanged according to transition probabilities per unit time denoted W_M^{TT} for triplet–triplet

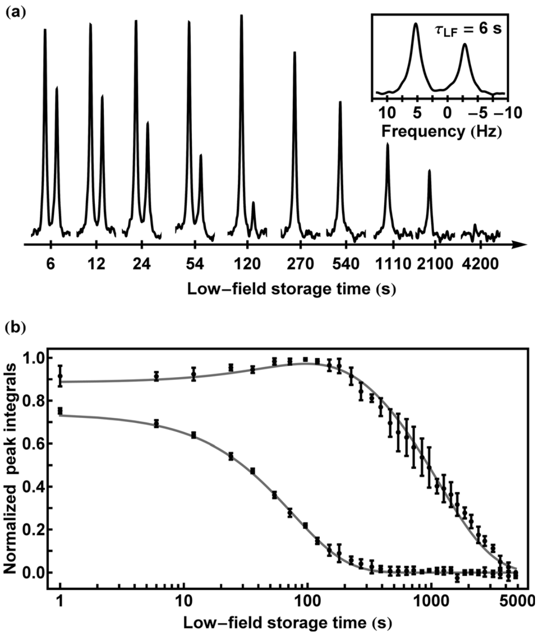

Fig. 5 (a) MSE NMR spectra of the central ^{15}N site, as a function of the low-field interval τ_{LF} in the MSE singlet NMR experiment. All radiofrequency pulses, including the preparation pulse, were selective for the central ^{15}N site. The displayed τ_{LF} intervals are approximately equally-spaced on a logarithmic scale. (b) Integrated amplitudes of the two ^{15}N peaks as a function of τ_{LF} interval. The experimental data is the mean of four different experimental series, obtained using the MSE sequence in Fig. 4 with $N = 104$ and $\tau = 2$ s, selectively exciting all possible combinations of ^{15}N sites. The solid lines are theoretical curves calculated using the relaxation model described in the text.

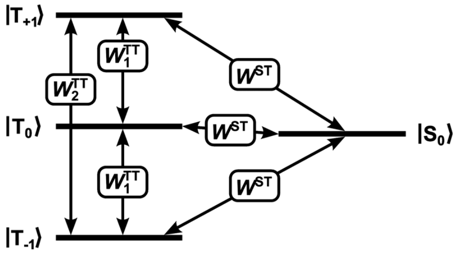

Fig. 6 Energy level scheme of the two spin-1/2 system in low field. Individual populations exchange with the indicated transition probabilities per unit time.

transitions and W_M^{ST} for singlet–triplet transitions (Fig. 6). The transition probabilities in opposite directions are assumed to be equal, since the low-field energy differences are very small with respect to thermal energy. In addition, the relaxation superoperator is rigorously isotropic in low magnetic field, providing the physical phase of the material is also isotropic. As shown in the Appendix, this leads to the following equalities:

$$\begin{aligned} W_{+1}^{TT} &= W_{-1}^{TT} \\ W_{+1}^{ST} &= W_0^{ST} = W_{-1}^{ST} \end{aligned} \tag{14}$$

The population kinetics of the system is therefore described, with high generality, using only three transition probabilities, namely the singlet–triplet transition probability W^{ST} (which is the same for all three transitions), the single-quantum triplet–triplet transition probability W_1^{TT}, and the double-quantum triplet–triplet transition probability W_2^{TT}.

In general, the populations of the singlet and triplet states evolve in low magnetic field according to the first-order homogeneous differential equations

$$\frac{\mathrm{d}}{\mathrm{d}t}\boldsymbol{P}_{\mathrm{L}}(t) = \boldsymbol{W}\cdot\boldsymbol{P}_{\mathrm{L}}(t) \tag{15}$$

where $\boldsymbol{W}$ is the kinetic matrix:

$$\boldsymbol{W} = \begin{pmatrix} \Delta^{S} & W^{ST} & W^{ST} & W^{ST} \\ W^{ST} & \Delta_{-1}^{T} & W_1^{TT} & W_2^{TT} \\ W^{ST} & W_1^{TT} & \Delta_0^{T} & W_1^{TT} \\ W^{ST} & W_2^{TT} & W_1^{TT} & \Delta_{+1}^{T} \end{pmatrix} \tag{16}$$

and the diagonal terms, required for detailed balance, are defined as follows:

$$\begin{aligned} \Delta^{S} &= -3W^{ST} \\ \Delta_{\pm 1}^{T} &= -(W^{ST} + W_1^{TT} + W_2^{TT}) \\ \Delta_0^{T} &= -(W^{ST} + 2W_1^{TT}) \end{aligned} \tag{17}$$

The elements of the low-field population vector $\boldsymbol{P}_{\mathrm{L}}$ are given by the singlet and triplet state populations:

$$\boldsymbol{P}_{\mathrm{L}}(t) = \begin{pmatrix} \langle S_0|\rho(t)|S_0\rangle \\ \langle T_{-1}|\rho(t)|T_{-1}\rangle \\ \langle T_0|\rho(t)|T_0\rangle \\ \langle T_{+1}|\rho(t)|T_{+1}\rangle \end{pmatrix} \tag{18}$$

where $\rho(t)$ is the spin density operator. Note that in low magnetic field, where the spin order vanishes at thermal equilibrium, no term for the equilibrium density operator is required in (15).

The four eigenvalues of the kinetic matrix $\boldsymbol{W}$ include one zero and three negative eigenvalues $\{-R_0, -R_1, -R_2\}$ given as follows:

$$\begin{aligned} R_0 &= 4W^{ST} \\ R_1 &= W^{ST} + W_1^{TT} + 2W_2^{TT} \\ R_2 &= W^{ST} + 3W_1^{TT} \end{aligned} \tag{19}$$

The eigenvector related to the zero eigenvalue corresponds to a uniform distribution of populations, *i.e.*, {1,1,1,1}, as required by the conservation of the total state population. The other three eigenvectors are as follows:

$$\begin{aligned} \boldsymbol{V}_0 &= \{-3,1,1,1\} \\ \boldsymbol{V}_1 &= \{0,1,0,-1\} \\ \boldsymbol{V}_2 &= \{0,1,-2,1\} \end{aligned} \tag{20}$$

The eigenvector $\boldsymbol{V}_0$ corresponds to singlet spin order (a difference between the singlet state population and the mean of the three triplet populations). The eigenvector $\boldsymbol{V}_1$ corresponds to longitudinal magnetization. Therefore, the rate constants R_0 and R_1 may be identified with the inverse of the singlet relaxation time T_S and the low-field magnetization relaxation time T_1, respectively. The eigenvector $\boldsymbol{V}_2$ corresponds to rank-2 order (a population deviation of the central triplet state with respect to the two outer states). The corresponding relaxation time constant is denoted $T_{\#2}$, in order to avoid confusion with the conventional symbol T_2 for the transverse relaxation time:

$$\begin{aligned} R_0 &= T_S^{-1} \\ R_1 &= T_1^{-1} \\ R_2 &= T_{\#2}^{-1} \end{aligned} \tag{21}$$

The three relaxation eigenvalues R, and hence all of the transition probabilities W, may be obtained by conducting a set of experiments, in which the relaxation of at least three independent population distributions are followed as a function of storage time in low magnetic field.

Initial low-field population vectors $\boldsymbol{P}_{\mathrm{L}}$ are constructed by thermal equilibration of the spin system in high magnetic field, followed by a radiofrequency pulse sequence to manipulate the population distribution and consequent adiabatic transport into low magnetic field. The population distribution of the weakly-coupled spin system in high magnetic field, before transport, may be described in a similar way to (18):

$$\boldsymbol{P}_{\mathrm{H}} = \begin{pmatrix} \langle\alpha\alpha|\rho(t)|\alpha\alpha\rangle \\ \langle\alpha\beta|\rho(t)|\alpha\beta\rangle \\ \langle\beta\alpha|\rho(t)|\beta\alpha\rangle \\ \langle\beta\beta|\rho(t)|\beta\beta\rangle \end{pmatrix} \tag{22}$$

Ideal adiabatic transport transforms the populations from the high-field to the corresponding low-field eigenstates without loss. In the case of $^{15}N_2O$, where the ^{15}N–^{15}N scalar coupling constant is positive, the ^{15}N magnetogyric ratio is negative, and the chemical shifts of the terminal and central ^{15}N comply $\delta_1 < \delta_2$, an ideal adiabatic transport from high to low field may be described as follows:

$$\boldsymbol{P}_{\mathrm{L}} = \boldsymbol{A}_{\mathrm{LH}} \cdot \boldsymbol{P}_{\mathrm{H}} \tag{23}$$

where the adiabatic transport matrix is given by:

$$\boldsymbol{A}_{\mathrm{LH}} = \begin{pmatrix} 0 & 1 & 0 & 0 \\ 0 & 0 & 0 & 1 \\ 0 & 0 & 1 & 0 \\ 1 & 0 & 0 & 0 \end{pmatrix} \tag{24}$$

At the end of the low-field evolution, adiabatic transport in the opposite sense takes place, leading to the following idealised correspondence between low-field and high-field populations:

$$\boldsymbol{P}_{\mathrm{H}} = \boldsymbol{A}_{\mathrm{HL}} \cdot \boldsymbol{P}_{\mathrm{L}} \tag{25}$$

where the matrix $\boldsymbol{A}_{\mathrm{HL}}$ is given by transpose of $\boldsymbol{A}_{\mathrm{LH}}$.

The final population distribution is read out by applying a selective $\pi/2$ pulse and the following MSE train to generate NMR signals. Each spectral peak is proportional to the population difference across a pair of high-field eigenstates. The amplitude of a single NMR peak in a general field-cycling NMR experiment, and its dependence on the low-field interval τ_{LF}, may therefore be described as follows:

$$a_{\mathrm{p}}(\tau_{\mathrm{LF}}) = \boldsymbol{Q}_{\mathrm{p}}^{\mathrm{T}} \cdot \boldsymbol{A}_{\mathrm{HL}} \cdot \exp\{\boldsymbol{W}\tau_{\mathrm{LF}}\} \cdot \boldsymbol{A}_{\mathrm{LH}} \cdot \boldsymbol{P}_{\mathrm{H}}(0) \tag{26}$$

where the row vector $\boldsymbol{Q}_{\mathrm{p}}^{\mathrm{T}}$ represents the pattern of high-field spin state populations giving rise to a particular NMR peak p after selective excitation. In the case of $^{15}N_2O$, there are four such peaks, one for each of the doublet components of the two ^{15}N sites. The vectors associated with the four ^{15}N peaks in $^{15}N_2O$, reading from left-to-right in a conventionally presented NMR spectrum, are as follows:

$$\begin{aligned} \boldsymbol{Q}_1^{\mathrm{T}} &= \{1,-1,0,0\} \\ \boldsymbol{Q}_2^{\mathrm{T}} &= \{0,0,1,-1\} \\ \boldsymbol{Q}_3^{\mathrm{T}} &= \{1,0,-1,0\} \\ \boldsymbol{Q}_4^{\mathrm{T}} &= \{0,1,0,-1\} \end{aligned} \tag{27}$$

A variety of initial high-field population distributions $\boldsymbol{P}_{\mathrm{H}}(0)$ may be prepared. For example, if the system is allowed to establish thermal equilibrium in high field, and no manipulations are applied before transport, the high-field population vector is given as follows (omitting constant numerical factors):

$$\boldsymbol{P}_{\mathrm{H}}(\mathrm{eq}) = \{-1,0,0,1\} \tag{28}$$

This indicates excess population in the low-energy $|\beta\beta\rangle$ state and depleted population in the high-energy $|\alpha\alpha\rangle$ state (this applies to ^{15}N which has a negative magnetogyric ratio). After adiabatic transport, the low-field population distribution is as follows:

$$\boldsymbol{P}_{\mathrm{L}}(\text{no initial pulse}) = \boldsymbol{A}_{\mathrm{LH}} \cdot \boldsymbol{P}_{\mathrm{H}}(\mathrm{eq}) = \{0,1,0,-1\} \tag{29}$$

which indicates preparation of the $\boldsymbol{V}_1$ population eigenvector. Since $\boldsymbol{V}_1$ is the eigenvector of the kinetic matrix $\boldsymbol{W}$, all peak amplitudes decay in a uniform way, characterized by the common exponential decay time constant T_1, and it does not matter which doublet is observed. A series of field-cycling experiments performed without the initial selective π pulse, varying the low-field interval τ_{LF}, therefore allows a straightforward estimate of the low-field relaxation time constant T_1.

More complex behaviour is observed when a selective π pulse is used before transport to low field. Assuming, for example, application of selective inversion on the terminal ^{15}N site, the high-field population vector is given as:

$$\boldsymbol{P}_{\mathrm{H}}(\pi^{(1)}) = \{0,-1,1,0\} \tag{30}$$

The corresponding low-field vector is a superposition of the two population eigenvectors $\boldsymbol{V}_0$ and $\boldsymbol{V}_2$:

$$\boldsymbol{P}_{\mathrm{L}}(\pi^{(1)}) = \boldsymbol{A}_{\mathrm{LH}} \cdot \boldsymbol{P}_{\mathrm{H}}(\pi^{(1)}) = \{-1,0,1,0\} = (\boldsymbol{V}_0 - \boldsymbol{V}_2)/3 \tag{31}$$

indicating a superposition of singlet and rank-2 spin order. These two forms of spin order decay independently during the low-field interval τ_{LF} with rate constants R_0 and R_2, so that the populations at the end of the low-field interval are given by:

$$\boldsymbol{P}_{\mathrm{L}}(\pi^{(1)},\tau_{\mathrm{LF}}) = (\boldsymbol{V}_0 \exp\{-R_0\tau_{\mathrm{LF}}\} - \boldsymbol{V}_2 \exp\{-R_2\tau_{\mathrm{LF}}\})/3 \tag{32}$$

The four peak amplitudes observed after adiabatic transport to high field and selective excitation of the appropriate coupled site are given by:

$$a_{\mathrm{p}}(\pi^{(1)},\tau_{\mathrm{LF}}) = \boldsymbol{Q}_{\mathrm{p}}^{\mathrm{T}} \cdot \boldsymbol{A}_{\mathrm{HL}} \cdot \boldsymbol{P}_{\mathrm{L}}(\pi^{(1)},\tau_{\mathrm{LF}}) \tag{33}$$

Observation of the two central ^{15}N site doublet components yields the following trajectories:

$$\begin{aligned} a_1(\pi^{(1)},\tau_{\mathrm{LF}}) &= \tfrac{4}{3}\exp\{-R_0\tau_{\mathrm{LF}}\} - \tfrac{1}{3}\exp\{-R_2\tau_{\mathrm{LF}}\} \\ a_2(\pi^{(1)},\tau_{\mathrm{LF}}) &= \exp\{-R_2\tau_{\mathrm{LF}}\} \end{aligned} \tag{34}$$

whereas observation of the two terminal ^{15}N site doublet components gives:

$$\begin{aligned} a_3(\pi^{(1)},\tau_{\mathrm{LF}}) &= -\exp\{-R_2\tau_{\mathrm{LF}}\} \\ a_4(\pi^{(1)},\tau_{\mathrm{LF}}) &= -\tfrac{4}{3}\exp\{-R_0\tau_{\mathrm{LF}}\} + \tfrac{1}{3}\exp\{-R_2\tau_{\mathrm{LF}}\} \end{aligned} \tag{35}$$

Apart from the sign change, the trajectories in (35) are identical to those in (34). In fact, all combinations of selective inversion pulses and observed sites generate the same pair of trajectories, except for the sign, which was also experimentally verified. The experimental trajectories shown in Fig. 5 were derived by combining the results from all four equivalent experiments.

3.3 Relaxation analysis

In the current case of $^{15}N_2O$ dissolved in DMSO-d$_6$, fitting the decay curves led to the following estimates of the relaxation time constants:

$$\begin{aligned} T_{\mathrm{S}} &= 1155 \pm 23\ \mathrm{s} \\ T_1 &= 207 \pm 7\ \mathrm{s} \\ T_{\#2} &= 76 \pm 4\ \mathrm{s} \end{aligned} \tag{36}$$

The corresponding rate constants, evaluated according to (21), are:

$$R_0 = (0.87 \pm 0.02) \times 10^{-3}\ \mathrm{s}^{-1}$$
$$R_1 = (4.83 \pm 0.16) \times 10^{-3}\ \mathrm{s}^{-1}$$
$$R_2 = (13.1 \pm 0.7) \times 10^{-3}\ \mathrm{s}^{-1} \qquad (37)$$

and the transition probabilities per unit time, using (19), are as follows:

$$W^{\mathrm{ST}} = (0.216 \pm 0.004) \times 10^{-3}\ \mathrm{s}^{-1}$$
$$W_1^{\mathrm{TT}} = (4.32 \pm 0.23) \times 10^{-3}\ \mathrm{s}^{-1}$$
$$W_2^{\mathrm{TT}} = (0.14 \pm 0.14) \times 10^{-3}\ \mathrm{s}^{-1} \qquad (38)$$

Note that the singlet–triplet transition probability W^{ST} is small, but is determined with good precision. The double-quantum transition probability W_2^{TT} is also very small but is poorly defined by the data. The best-fit relaxation curves are compared to the experimental data in Fig. 5b.

The only relaxation mechanism that leads to double-quantum transitions is the dipole–dipole (DD) mechanism deriving from motional modulation of the dipolar coupling between the two ^{15}N nuclei. Dipole–dipole relaxation does not induce singlet–triplet transitions, and is associated with the following ratio of triplet–triplet transition probabilities:

$$W_2^{\mathrm{TT}}(\mathrm{DD}) = 2W_1^{\mathrm{TT}}(\mathrm{DD}) \qquad (39)$$

The dipole–dipole contributions may therefore be subtracted from (38), leading to:

$$W^{\mathrm{ST}}(\text{no DD}) = (0.216 \pm 0.004) \times 10^{-3}\ \mathrm{s}^{-1}$$
$$W_1^{\mathrm{TT}}(\text{no DD}) = (4.25 \pm 0.24) \times 10^{-3}\ \mathrm{s}^{-1}$$
$$W_2^{\mathrm{TT}}(\text{no DD}) \equiv 0 \qquad (40)$$

The ratio of the triplet–triplet and singlet–triplet transition probabilities (excluding dipole–dipole contributions) is given by:

$$W_1^{\mathrm{TT}}(\text{no DD})/W^{\mathrm{ST}} = 19.7 \pm 1.2 \qquad (41)$$

It is instructive to compare this ratio with that expected for spin-rotation relaxation, which dominates for ^{15}N$_2$O in the gas phase.[42,43] The linear geometry of the nitrous oxide molecule constrains the spin-rotation tensors of the two ^{15}N sites, and also the molecular inertial tensor, to be uniaxial and colinear. In this case, the local magnetic field fluctuations caused by changes in the molecular angular momentum are completely correlated, and the theoretical transition probabilities generated by the fluctuations of molecular angular momentum are as follows:[41]

$$W^{\mathrm{ST}}(\mathrm{SR}) = \tfrac{1}{2}(C_1 - C_2)^2 J_{\mathrm{rms}}^2 \tau_J$$
$$W_1^{\mathrm{TT}}(\mathrm{SR}) = \tfrac{1}{2}(C_1 + C_2)^2 J_{\mathrm{rms}}^2 \tau_J \qquad (42)$$

where C_1 and C_2 are the largest principal values of the spin-rotation tensors for the terminal and central ^{15}N sites, respectively. The fluctuating molecular angular momentum has a root-mean-square value denoted J_{rms} and a correlation time τ_J. The spin-rotation mechanism leads to the following theoretical ratio of transition probabilities:[41,44]

$$\frac{W_1^{\mathrm{TT}}(\mathrm{SR})}{W^{\mathrm{ST}}(\mathrm{SR})} = \frac{(C_1 + C_2)^2}{(C_1 - C_2)^2} \qquad (43)$$

There is disagreement in the literature about the magnitudes of the spin-rotation tensors in ^{15}N$_2$O. The estimates $C_1 = 1.829 \pm 0.065$ kHz and $C_2 = 3.06 \pm 0.12$ kHz were obtained by molecular beam electric resonance experiments[45] on the ground vibrational state of ^{14}N^{14}N^{16}O. Assuming that the spin-rotation constants are in proportion to the nuclear magnetic moments, these estimates correspond to the following ratio of transition probabilities in ^{15}N$_2$O: $W_1^{\mathrm{TT}}(\mathrm{SR})/W^{\mathrm{ST}}(\mathrm{SR}) = 15.8 \pm 3.1$, which is in good agreement with the experimental estimate in (41). However, Jameson *et al.*[42,43,46] proposed a revised estimate for the central ^{15}N site of $C_2 = 3.35$ kHz, based on nuclear spin-lattice relaxation data. She found that the molecular beam estimates conflicted with measurements of nuclear spin-lattice relaxation rates and chemical shift data, and concluded that the molecular beam data had been misinterpreted. The revised figures[42,43] of $\{C_1, C_2\} = \{2.48, 3.35\}$ kHz (no confidence limits provided) correspond to a transition probability ratio of $W_1^{\mathrm{TT}}(\mathrm{S}R)/W^{\mathrm{ST}}(\mathrm{S}R) = 44.9$. This exceeds the experimentally determined transition probability ratio (eqn (41)) by a factor of more than 2.

A similar conclusion may be drawn from the ratio of T_{S} and T_1, excluding DD contribution:

$$\frac{T_{\mathrm{S}}(\mathrm{SR})}{T_1(\mathrm{SR})} = \frac{C_1{}^2 + C_2{}^2}{2(C_1 - C_2)^2} \qquad (44)$$

Values of the spin-rotation tensor components C_1 and C_2 determined by Reinartz *et al.*[45] give rise to a value 4.19 ± 0.78, while results of Jameson *et al.*[42,43] lead to 11.5. The experimental value of 5.14 ± 0.30 is in better agreement with the molecular beam measurement.[45]

Further study is needed to resolve this issue. If the spin-rotation tensors proposed by Jameson are correct, then pure spin-rotation relaxation would give rise to singlet relaxation rates which are more than twice those observed experimentally. The discrepancy may be due to the existence of small additional mechanisms, such as intermolecular interactions with solvent nuclei and paramagnetic impurities, such as O$_2$ or NO, which contribute to an acceleration of the singlet relaxation.

4. Experimental

The NMR experiments were performed on a 300 MHz Varian NMR spectrometer equipped with a 10 mm direct-detection liquid-state probe. The sample was a 0.3 M solution of ^{15}N$_2$O gas (CK-gas, UK) dissolved in DMSO-d$_6$ under a pressure of 3.5 bar. The ^{15}N resonance frequency was 30.3879 MHz. The isotropic chemical-shift difference of the ^{15}N sites and their scalar coupling were 83.19 ± 0.03 ppm (2528 ± 1 Hz) and 8.20 ± 0.06 Hz, respectively.

The sample transport system was the same as used in previous works.[5,47] The field at the magnet centre ($H_0 = 0$) was $B_{\mathrm{HF}} = 7.0461$ T. Low-field relaxation was observed in a field $B_{\mathrm{LF}} = 3.3 \pm 0.1$ mT at a distance $H_1 = 145 \pm 2$ cm above the magnet centre. The sample was transported between the two positions during transport intervals $\tau_{\mathrm{tr}} = 10$ s.

All radiofrequency pulses were rectangular in shape and employed an rf field corresponding to a ^{15}N nutation frequency of 235 ± 1 Hz. The $\pi/2$ and π pulses had durations of 1066 ± 6 μs and 2132 ± 12 μs, respectively.

Multiple-spin echo signals were obtained for up to 1007 π pulses with spacings varying between 0.208 and 10.228 s. The low-field interval τ_{LF} varied between 1 and 4800 s. The MSE signals contained up to 256 k complex points with a total acquisition time τ_{acq} up to 210 s.

The processing of all MSE signals was performed using Mathematica[48] software. The time constants for the matched weighting functions were $T_2 = 46.2 \pm 3.4$ s and $T_2^{\mathrm{inh}} = 219 \pm 18$ ms. The phase correction ϕ_{proc} was $150° \pm 1°$ for all signals and no further phase correction was needed. Zero-filling up to 16 k samples was applied before Fourier transformation.

5. Discussion

Multiple-spin echo data acquisition, followed by optimised data processing, can lead to considerable enhancement in SNR for singlet NMR experiments on small molecules. We have observed enhancements in SNR of around an order of magnitude in a single scan, although the achievable degree of enhancement is often limited by the required spectral resolution. Nevertheless, we performed MSE-enhanced singlet NMR experiments in which the doublet peaks of ^{15}N$_2$O were clearly resolved and in which SNR was enhanced by a factor of 4 (Fig. 5) or a factor of 10 (Fig. 2) relative to conventional single-pulse acquisition.

We anticipate that this method will be useful for systems other than ^{15}N$_2$O. The main requirement is that the system has a long T_2 relaxation time. The case of ^{15}N$_2$O is particularly favourable since there are no other magnetic nuclei in the most abundant isotopologue besides ^{15}N.

We exploited the sensitivity enhancement offered by MSE data acquisition to perform a detailed study of the low-field relaxation of ^{15}N$_2$O in solution. The experimental curves were fitted well by a developed relaxation model involving three distinct transition probabilities, as expected for relaxation of a spin-1/2 pair system in low magnetic field. The double-quantum transition probability W_2^{TT} showed to be very small, indicating that dipole–dipole relaxation is of negligible importance in this case. The ratio of the two other transition probabilities, $W_1^{\mathrm{TT}}/W^{\mathrm{ST}}$ was compared with that expected for fully correlated spin-rotation relaxation. The ratio agrees reasonably well with that predicted from experimental estimates of the spin-rotation tensors obtained by microwave spectroscopy. However, there is a discrepancy by a factor of more than two using revised estimates of the spin-rotation tensors. Provided that the revised values are correct, additional contributions to the singlet relaxation need to be taken into account.

We expect to use MSE-enhanced field-cycling NMR to study signals from ^{15}N$_2$O and other small biologically significant molecules, dissolved under atmospheric pressure in blood and other substances, in order to observe ongoing transport or metabolic processes. Performing the experiment in magnetic fields of different strength and at different temperatures should quantify the mechanisms of ^{15}N$_2$O relaxation. MSE data acquisition may be combined with other hyperpolarization techniques to further enhance the detection sensitivity.

Appendix: symmetry properties of low-field relaxation

In this appendix we show that in low magnetic field and isotropic material phase, the three singlet–triplet transition probabilities are equal, and that the two single-quantum triplet–triplet transition probabilities are also equal.

Denote the singlet and triplet states using the notation $|I,M\rangle$, where I is the total spin quantum number:

$$|S_0\rangle = |0,0\rangle$$

$$|T_M\rangle = |1,M\rangle \tag{45}$$

with $M \in \{-1,0,1\}$. The transition probability per unit time between the singlet state and one of the triplet states is given by:

$$W_M^{\mathrm{ST}} = (|0,0\rangle\langle 0,0||\hat{\Gamma}||1,M\rangle\langle 1,M|) \tag{46}$$

where $\hat{\Gamma}$ is the relaxation superoperator and $(A|B)$ denotes the Liouville bracket,[49] defined as:

$$(A|B) = \mathrm{Tr}\{A^{\dagger}B\} \tag{47}$$

In an isotropic material phase, and low magnetic field, the relaxation superoperator is isotropic, *i.e.* invariant to rotations of the system in space, which implies:

$$\hat{\Gamma} = \hat{R}^{\dagger}(\Omega)\hat{\Gamma}\hat{R}(\Omega) \tag{48}$$

where $\hat{R}(\Omega)$ is the superoperator for an arbitrary three-dimensional rotation Ω. This may be combined with (46) to obtain:

$$W_M^{\mathrm{ST}} = (|0,0\rangle\langle 0,0||\hat{R}^{\dagger}(\Omega)\hat{\Gamma}\hat{R}(\Omega)||1,M\rangle\langle 1,M|) \tag{49}$$

Rotation superoperators have the following property:[49]

$$\hat{R}(\Omega)|A) = |R(\Omega)AR^{\dagger}(\Omega)) \tag{50}$$

where $R(\Omega)$ is a rotation operator. Spin states transform under rotations as follows:

$$R(\Omega)|I,M\rangle = \sum_{M'=-I}^{+I} |1,M'\rangle D_{M'M}^{I}(\Omega) \tag{51}$$

where $D_{M'M}^{I}(\Omega)$ are Wigner matrix elements. These equations may be combined to obtain:

$$W_M^{\mathrm{ST}} = \sum_{M'=-1}^{+1} (|0,0\rangle\langle 0,0||\hat{\Gamma}||1,M'\rangle\langle 1,M''|)D_{M'M}^{1}(\Omega)D_{M''M}^{1}(\Omega)^{*} \tag{52}$$

Both sides of the equation may be integrated over the space of all three-dimensional orientations Ω. Wigner functions are orthogonal when integrated over the entire 3D rotational space:[50]

$$\int_{\mathrm{all}\,\Omega} D_{M'M}^{I}(\Omega)D_{M''M}^{I}(\Omega)^{*}\mathrm{d}\Omega = \frac{8\pi^2}{2I+1}\delta_{M'M''} \tag{53}$$

where $\delta_{M'M''}$ is the Kronecker delta. This leads to

$$\begin{aligned} W_M^{\mathrm{ST}} &= \frac{1}{3}\sum_{M'=-1}^{+1}(|0,0\rangle\langle 0,0||\hat{\Gamma}||1,M'\rangle\langle 1,M'|) \\ &= \frac{1}{3}\sum_{M'=-1}^{+1} W_{M'}^{\mathrm{ST}} \end{aligned} \tag{54}$$

Hence all three transition probabilities W_M^{ST} are equal.

A similar argument may be used to prove that the two single-quantum triplet–triplet transition probabilities $W_{\pm 1}^{\mathrm{TT}}$ are equal. These probabilities are given by

$$W_M^{\mathrm{TT}} = (|1,0\rangle\langle 1,0||\hat{\Gamma}||1,M\rangle\langle 1,M|) \tag{55}$$

For the spin-1 triplet manifold, a rotation by π around the x-axis has the following effect:

$$R(\pi)|1,M\rangle = -|1,-M\rangle \tag{56}$$

Since the relaxation superoperator is isotropic, a π rotation may be inserted in (55), which leads to the desired result:

$$\begin{aligned} W_M^{\mathrm{TT}} &= (|1,0\rangle\langle 1,0|\hat{R}_x^{\dagger}(\pi)\hat{\Gamma}\hat{R}_x(\pi)||1,M\rangle\langle 1,M|) \\ &= (R_x(\pi)|1,0\rangle\langle 1,0|R_x^{\dagger}(\pi)|\hat{\Gamma}|R_x(\pi)|1,M\rangle\langle 1,M|R_x^{\dagger}(\pi)) \\ &= W_{-M}^{\mathrm{TT}} \end{aligned} \tag{57}$$

These results apply to any relaxation mechanism in low magnetic field and isotropic material phase.

Acknowledgements

This research was funded by EPSRC (UK) and the Leverhulme Foundation (UK). We are grateful to M. C. D. Tayler for discussions and O. G. Johannessen for experimental help.

References

1 M. H. Levitt, *Ann. Rev. Phys. Chem.*, 2012, **63**, 89–105.
2 M. H. Levitt, in *Encyclopedia of Magnetic Resonance*, ed. D. M. Grant and R. K. Harris, John Wiley & Sons, Ltd., Chichester, UK, 1st edn, 2010, vol. 9, ch. Singlet and Other States with Extended Lifetimes.
3 M. Carravetta, O. G. Johannessen and M. H. Levitt, *Phys. Rev. Lett.*, 2004, **92**, 153003.
4 M. Carravetta and M. H. Levitt, *J. Am. Chem. Soc.*, 2004, **126**, 6228–6229.
5 G. Pileio, M. Carravetta, E. Hughes and M. H. Levitt, *J. Am. Chem. Soc.*, 2008, **130**, 12582–12583.
6 M. C. D. Tayler and M. H. Levitt, *Phys. Chem. Chem. Phys.*, 2011, **13**, 5556–5560.
7 G. Pileio, M. Carravetta and M. H. Levitt, *Proc. Natl. Acad. Sci. U. S. A.*, 2010, **107**, 17135–17139.
8 S. Cavadini, J. Dittmer, S. Antonijevic and G. Bodenhausen, *J. Am. Chem. Soc.*, 2005, **127**, 15744–15748.
9 R. Sarkar, P. R. Vasos and G. Bodenhausen, *J. Am. Chem. Soc.*, 2007, **129**, 328–334.
10 R. Sarkar, P. Ahuja, P. R. Vasos and G. Bodenhausen, *ChemPhysChem*, 2008, **9**, 2414–2419.
11 P. Ahuja, R. Sarkar, P. R. Vasos and G. Bodenhausen, *J. Am. Chem. Soc.*, 2009, **131**, 7498–7499.
12 A. Bornet, P. Ahuja, R. Sarkar, L. Fernandes, S. Hadji, S. Y. Lee, A. Haririnia, D. Fushman, G. Bodenhausen and P. R. Vasos, *ChemPhysChem*, 2011, **12**, 2729–2734.
13 P. Ahuja, R. Sarkar, P. R. Vasos and G. Bodenhausen, *J. Chem. Phys.*, 2007, **127**, 134112.
14 M. C. D. Tayler, S. Marie, A. Ganesan and M. H. Levitt, *J. Am. Chem. Soc.*, 2010, **132**, 8225–8227.
15 P. R. Vasos, A. Comment, R. Sarkar, P. Ahuja, S. Jannin, J. P. Ansermet, J. A. Konter, P. Hautle, B. van den Brandt and G. Bodenhausen, *Proc. Natl. Acad. Sci. U. S. A.*, 2009, **106**, 18469–18473.
16 W. S. Warren, E. Jenista, R. T. Branca and X. Chen, *Science*, 2009, **323**, 1711–1714.
17 M. C. D. Tayler, I. Marco-Rius, M. I. Kettunen, K. M. Brindle, M. H. Levitt and G. Pileio, *J. Am. Chem. Soc.*, 2012, **134**, 7668–7671.
18 R. K. Ghosh, S. J. Kadlecek, J. H. Ardenkjaer-Larsen, B. M. Pullinger, G. Pileio, M. H. Levitt, N. N. Kuzma and R. R. Rizi, *Magn. Reson. Med.*, 2011, **66**, 1177–1180.
19 J. H. Ardenkjaer-Larsen, B. Fridlund, A. Gram, G. Hansson, L. Hansson, M. H. Lerche, R. Servin, M. Thaning and K. Golman, *Proc. Natl. Acad. Sci. U. S. A.*, 2003, **100**, 10158–10163.
20 H. Carr and E. Purcell, *Phys. Rev.*, 1954, **94**, 630–638.
21 S. Meiboom and D. Gill, *Rev. Sci. Instrum.*, 1958, **29**, 688–691.
22 A. Allerhand and D. W. Cochran, *J. Am. Chem. Soc.*, 1970, **92**, 4482–4484.
23 A. Bax, A. F. Mehlkopf and J. Smidt, *J. Magn. Reson.*, 1979, **35**, 373–377.
24 J. Z. Hu and R. A. Wind, *J. Magn. Reson.*, 2003, **163**, 149–162.
25 F. H. Larsen, H. J. Jakobsen, P. D. Ellis and N. C. Nielsen, *J. Phys. Chem. A*, 1997, **101**, 8597–8606.
26 R. Lefort, J. W. Wiench, M. Pruski and J.-P. Amoureux, *J. Chem. Phys.*, 2002, **116**, 2493–2501.
27 I. Hung, A. J. Rossini and R. W. Schurko, *J. Phys. Chem. A*, 2004, **108**, 7112–7120.
28 R. Siegel, T. T. Nakashima and R. E. Wasylishen, *Concepts Magn. Reson., Part A*, 2005, **26**, 62–77.
29 E. L. Hahn and D. E. Maxwell, *Phys. Rev.*, 1951, **84**, 1246–1247.
30 A. Allerhand, *J. Chem. Phys.*, 1966, **44**, 1–9.
31 T. F. Segawa, B. Baishya and G. Bodenhausen, *ChemPhysChem*, 2010, **11**, 3343–3354.
32 B. Baishya, T. F. Segawa and G. Bodenhausen, *J. Magn. Reson.*, 2011, **211**, 240–242.
33 J. A. Aguilar, M. Nilsson, G. Bodenhausen and G. A. Morris, *Chem. Commun.*, 2012, **48**, 811–813.
34 V. A. Norton, PhD thesis, California Institute of Technology, 2010.
35 R. Freeman, *Prog. NMR Spectrosc.*, 1998, **32**, 59–106.
36 M. H. Levitt, G. Bodenhausen and R. R. Ernst, *J. Magn. Reson.*, 1984, **58**, 462–472.
37 R. Ernst, G. Bodenhausen and A. Wokaun, *Principles of Nuclear Magnetic Resonance in One and Two Dimensions*, Clarendon Press, Oxford, UK, Reprint edn, 1988.
38 A. Abragam, *The Principles of Nuclear Magnetism*, Claredon Press, Oxford, UK, 1st edn, 1961.
39 M. Carravetta and M. H. Levitt, *J. Chem. Phys.*, 2005, **122**, 214505.
40 M. H. Levitt, *Spin Dynamics: Basics of Nuclear Magnetic Resonance*, Wiley, Chichester, 2nd edn, 2007.
41 G. Pileio, *Prog. Nucl. Magn. Reson. Spectrosc.*, 2010, **56**, 217–231.
42 C. J. Jameson, A. K. Jameson, J. K. Hwang and N. C. Smith, *J. Chem. Phys.*, 1988, **89**, 5642–5649.
43 C. J. Jameson, M. A. ter Horst and A. K. Jameson, *J. Chem. Phys.*, 1998, **109**, 10227–10237.
44 P. S. Hubbard, *Phys. Rev.*, 1963, **131**, 1155–1165.
45 J. M. L. J. Reinartz, W. L. Meerts and A. Dymanus, *Chem. Phys.*, 1978, **31**, 19–29.
46 C. J. Jameson, A. K. Jameson, D. Oppusunggu, S. Wille, P. M. Burrell and J. Mason, *J. Chem. Phys.*, 1981, **74**, 81–88.
47 G. Pileio, M. Carravetta and M. H. Levitt, *Phys. Rev. Lett.*, 2009, **103**, 083002.
48 Wolfram Research, *Mathematica* 8, 2011, http://www.wolfram.com/mathematica/.
49 J. Jeener, *Adv. Magn. Reson.*, 1982, **10**, 1–51.
50 D. Varshalovich, A. Moskalev and V. Khersonskii, *Quantum Theory of Angular Momentum*, World Scientific, Singapore, 1988.